LIQUID-VAPOR PHASE CHANGE PHENOMENA FOR HEAT EXCHANGERS AND ELECTRONICS COOLING

BY

PATRICK BIRBARAH

DISSERTATION

Submitted in partial fulfillment of the requirements
for the degree of Doctor of Philosophy in Mechanical Engineering
in the Graduate College of the
University of Illinois at Urbana-Champaign, 2019

Urbana, Illinois

Doctoral Committee:

Professor Nenad Miljkovic, Chair, Director of Research
Professor Anthony Jacobi
Professor Andrew Alleyne
Professor William King
Professor Robert Pilawa

ABSTRACT

Phase change heat transfer is an attractive heat transfer process due to its superior heat transfer coefficients as compared to single phase heat transfer. Among the fluids used as refrigerants, water is of interest for its good thermodynamic properties. It is in addition widely available, inexpensive and of no health hazards. In particular, liquid vapor phase change of water is widely observed. Water vapor condensation is vital to many natural and industrial processes such as building environmental control, power generation, and water desalination. Jumping-droplet condensation of water has recently been shown to have a 10X heat transfer enhancement compared to state-of-the-art filmwise condensation due to the removal of condensate at much smaller length scales (~ 1μm) than what is capable with gravitational shedding (~ 1mm). However, the efficient removal of jumping droplets can be limited by droplet return to the surface due to gravity, entrainment in bulk convective vapor flow, and entrainment in local condensing vapor flow. If used appropriately, convective condensation has the potential to entrain droplets, hence impeding their return to the surface. In addition, obtaining droplet size distributions is critical to determine the heat flux on these surfaces and is still lacking in literature. On the other hand, evaporation of these droplets can provide a cooling mechanism for small electronics components at high flux. Demand for enhanced cooling technologies within various commercial and consumer applications has increased in recent decades due to electronic devices becoming more energy dense. In this work, laminar boundary layer theory was used to model the vapor flow and jumping droplet behavior on a plate and inside the tube with condensation modeled as vapor suction. The droplet size distribution for jumping-droplet condensation is also investigated for a stagnant flow. On the other hand, the cooling potential of these droplets is studied for hot spots in electronics, and is compared to a higher heat flux approach of immersion cooling in water.

ACKNOWLEDGEMENT

This work would not have been possible without the support my academic adviser Professor Nenad Miljkovic, who continuously encouraged me (both on the academic and personal levels) to perform at my best all throughout my journey as a graduate student.

I am thankful for the financial, logistic and emotional support of the Power Optimization of Electro-Thermal Systems (POETS) Engineering Research Center presided by Professor Andrew Alleyne at the University of Illinois Urbana Champaign.

I am thankful for my doctoral committee members who provided guidance and support for my thesis work.

I am thankful for my labmates at the Energy Transfer Research Lab (ETRL) and collaborators who are numerous to list, with a special thanks to Tarek Gebrael and Shreyas Chavan who provided some help for this work.

I would like to thank the University of Illinois at Urbana Champaign staff and professors for their logistic and technical support.

Lastly, I am deeply grateful for my family, my wife and my (expected) daughter. I have been blessed to be surrounded by God's love through these people.

Patrick Birbarah

TABLE OF CONTENTS

LIST OF FIGURES

LIST OF TABLES

NOMENCLATURE

Symbols

A	Area
a	Pipe radius, geometrical distance
b	Geometrical distance
Bi	Biot number
Bo	Bond number
C	Coefficient of proportionality
c	Specific heat, geometrical distance
Ca	Capillary number
D	Drain of transistor
d	Distance, diameter
dt	Time step
$\vec{e}$	Unitary vector
F	Force magnitude
$\vec{F}$	Force vector
f	Droplet size distribution, non-dimensional stream function, similarity function, friction factor, fraction (between 0 and 1)
G	Mass flux, Gate of transistor
g	Earth gravitational constant
$\vec{g}$	Earth gravitational vector
h	Heat transfer coefficient, jumping height, enthalpy

I	Electric current
i	Index, electric current
$\vec{\imath}$	Unitary vector along x
$\vec{\jmath}$	Unitary vector along y
k	Thermal conductivity
L	Side length of square condensing surface, droplet traveled length, characteristic length
m	Mass
$\dot{m}$	Mass flux
Ma	Mach number
N	Number (of drops)
Nu	Nusselt number
P	Pressure
Pr	Prandtl number
q	Heat flow, heat flux
q''	Heat flux
R	Droplet radius, Rotation matrix, suction-based Reynolds number, thermal resistance, thermal resistance per area, ideal gas constant
Ra	Rayleigh number
Re	Reynolds number
r	Radial coordinate, correlation parameter (Rohsenow)
S	Source of transistor
s	average nucleation site spacing, correlation parameter (Rohsenow)

T	Temperature
t	Time, thickness
U	Velocity
u	(Vapor) velocity tangential to plate, axial velocity for a pipe
$\vec{V}$	Velocity vector
V	Suction velocity, Voltage
v	(vapor) velocity perpendicular to plate, radial velocity (pipe)
w	Width of plate,
We	Weber number
x	Cartesian coordinate tangent to horizontal plate
y	Cartesian coordinate perpendicular to vertical plate
z	Cartesian coordinate, axial coordinate (pipe)

Greek letters

α	Condensation accommodation coefficient, void fraction, thermal diffusivity
β	Thermal expansion coefficient
γ	Surface tension
Δ	Change, hysteresis
δ	Hydrophobic coating thickness, hydrodynamic boundary layer thickness
η	Non dimensional similarity variable
θ	Contact angle, angle between tangential and perpendicular relative velocities, angle between vector and x-axis in xy plane
μ	Dynamic viscosity

ν	Kinematic viscosity
ρ	Density
σ	Surface tension, standard deviation, Boltzmann constant
τ	Wall shear stress
$\bar{\tau}$	Average wall shear stress
ϕ	Multiplier, angle between vector and Cartesian z-axis
φ	Dimensional stream function
ψ	Angle of plate inclination (CCW), thermal resistance

Subscripts

0	Initial, inlet (pipe)
a	Advancing
amb	Ambient
avg	Average
B	Backside, bottom side (transistor)
b	Boiling
Bot	Bottom side (transistor)
c	Covered, condensation, convection, center
cc	Convection cold
ch	Convection hot
coa,2D	2D coalescence
coa,3D	3D coalescence
coalesce	Average of coalescing drops

coat	Hydrophobic coating
cond	Condensation
Cu	Copper
D	Drag
d	Droplet
drop	Droplet
ds,ON	drain-source, during operation
end	End of droplet trajectory
eq	Equivalent electric circuit
evap	Evaporation
f	front, free stream, flow
fg	difference between vapor and liquid
FR4	Relating to PCB material FR4
G	Gallium Nitride,Gravitational, based on velocity gradient
g	Geometrical, specific gas constant
GaN	Gallium Nitride
hom	Homogeneous
i	Interfacial
i+drop	Interfacial and droplet
j	Jumps
J	Junction (transistor)
jump,max	Maximum jumping
jump,min	Minimum jumping

l	liquid
lo	liquid only
losses	Relating to thermal losses
m	Maximum
max	Maximum
nat	Natural convection
p	Projected, constant pressure, plate, Parylene C
p,film	Plate with liquid film
pad	Thermal pad
PCB	Portable circuit board
r	Receding, position
rad	Radiation
rel	Relative
S	Saffman
s	Sample, condensing surface
sat	Saturation
SB	Solder balls (transistor)
sf	Surface
SL	Saffman lift
sp	Spreading
T	Top side (transistor)
t	Tangential, total
Top	Top side (transistor)

tp	Two-phase
v	Vapor, velocity
w	Water, wall
x	Projected on x-axis
x^1	Projected on x^1 axis
y	Projected on y-axis
y^1	Projected on y^1 axis
σ	Adhesion

Superscripts

1	In frame 1 (relative to x^1 and y^1)
app	Apparent
$'$	Derivative

Chapter 1- Introduction

Phase change heat transfer is an attractive heat transfer process due to its superior heat transfer coefficients as compared to single phase heat transfer. Among the fluids used as refrigerants (hydrocarbons, CO2, water-ammonia…) water is of interest since it has good thermodynamic properties (latent heat of vaporization, heat capacity, thermal conductivity and viscosity). It is in addition widely available, inexpensive and of no health hazards.

Water vapor condensation is an important industrial and natural process. In an effort to more rapidly remove condensate for enhanced phase-change heat transfer, researchers have created non-wetting surfaces for dropwise [1] and jumping-droplet condensation [2], whereby millimetric droplets shed due to gravity or micrometric droplets spontaneously jump away from the surface [3], respectively. A number of recent works have fabricated superhydrophobic surfaces to achieve jumping-droplet condensation [4-14] for a variety of applications including self-cleaning [15-17], thermal diodes [18], anti-icing [19-22], vapor chambers [23, 24], energy harvesting [25-27], and heat transfer enhancement [28-43].

The efficient removal of jumping droplets along with the heat transfer enhancement can be limited by droplet return to the surface due to (1) gravitational force (2) entrainment in a bulk convective vapor flow, and (3) entrainment in the local condensing vapor flow toward the surface [23, 44]. The first two return mechanisms can be mitigated with suitable geometric design of the macroscale condensing surface and vapor supply. However, local vapor flow driven droplet return is more difficult to eliminate due to the need to conserve mass of the condensing vapor flowing towards the surface.

While the removal of the droplets by electric fields offers a method to remove condensate [27, 45], practical difficulties exist, mainly related to the need for energized electrodes that require condensate to be removed from their surfaces [41]. Here, we present a solution to the aforementioned limitations by utilizing forced bulk vapor flow to remove jumping-droplets, in what we term convective jumping-droplet condensation.

In order to quantify the heat transfer, the droplet size distribution is needed. The overall heat flux through the condensing surface is a weighted average of the heat fluxes through individual droplets, with the weights relating to the number density of droplets per size range.

For dropwise condensation on hydrophobic surfaces, the steady state distribution of droplet sizes has been studied by Rose et al. [46] for the case of droplets growing mainly by coalescence. The droplet distribution has been verified experimentally and with numerical simulations [47]. While the Rose distribution was originally derived through empirical observations, it has also been derived separately through the fractal theory [48]. For droplets smaller than the coalescence radius, Abu Orabi devised the analytical population balance model to predict the size distribution function [49,50]. The derivation relied on the Rose distribution for the boundary conditions at the coalescence radius. However, the population balance theory has not been verified experimentally or computationally. As for the distribution provided by Rose, although valid for classical dropwise condensation, it cannot be applied to and does not reflect the physics governing jumping droplet condensation. Specifically: 1) sweeping does not take place and droplet jumping is the only mechanism for droplet removal, 2) for larger apparent contact angles that are observed on superhydrophobic surfaces ($\theta > 150°$), small droplets can grow in the geometric shadow of larger droplets, a process not observed on hydrophobic surfaces ($\theta \approx 90°$), and 3) the main growth

mechanism of droplets is via direct condensation with only a fraction of growth occurring via coalescence.

Prior works have attempted to derive an analytical expression for the droplet size distribution for jumping droplet condensation [43]. In addition to the uncertainty related to the population balance theory on which these derivations relied, three main limitations exist: 1) the assumption that droplets are removed exactly when their radius reaches half the coalescence radius defined by the average spacing between nucleation sites. Although the coalescence radius assumption is exact for non-random nucleation site distributions (*e.g.* square lattices, close-packed arrays, etc…), the effective departure radius for randomly distributed droplets differs from that of well-ordered distributions. 2) Droplet size mismatch is an important parameter that determines whether droplets jump or coalesce and remain on the condensing surface, a physical phenomenon currently not tractable with analytical solutions. 3) For jumping droplet condensation, characterized by droplets having large apparent contact angles ($\theta > 150°$), small droplets can grow in the geometric shadow of larger droplets, a process not captured by past analytical solutions.

On the other hand, droplets can be used to evaporatively cool devices such as electronics. Recent advances in electronic materials and circuit architectures have catalyzed an increase in power density (power-to-volume ratio) and the specific power (power-to-weight ratio) of both stationary and mobile systems.[51, 52] The trend of replacing bulky pneumatic and mechanical systems with smaller electrical systems in more-electric and fully-electric vehicles ranging from automobiles to aircrafts has created a demand for lighter and more compact power electronics. Yet, the ability to remove heat from internal hot spots constrains the design of converters and inverters.[53] Phase change heat transfer offers a platform to efficiently remove heat from electronic devices and transfer it via the generated vapor phase (evaporation in heat pipes and

vapor chambers) to the outside environment.[54] However, recent advances utilizing wide bandgap semiconductors have shown that the majority of heat can be generated locally near spatially distributed hot spots.[55, 56] Traditional cooling schemes can also be stymied by the temporal variation in hot spot locations concurrent with electro-thermal optimization and novel circuit architectures.[57]

For high heat flux applications (>50 W/cm^2), however, jumping-droplets are not a viable solution. Instead, immersion cooling has emerged as a potential solution to overcome these barriers by enabling the boiling of a cooling fluid directly from the electronics module, thereby removing thermal interface materials [58, 59] and packaging constraints. Except for the use of treated, deionized water for some systems [60], state of the art (SOA) immersion cooling systems [61] utilize non-conductive dielectric heat transfer liquids due to electrical considerations [62, 63]. The use of these fluids presents three fundamental disadvantages: 1) the low boiling point of non-polar fluids at atmospheric pressure means that electronics components cannot exceed the boiling temperature (≈ 50°C) by an appreciable amount due to the formation of a vapor blanket and critical heat flux. 2) The maximum heat flux attainable in the system is equal to the critical heat flux of the working fluid, which for non-polar dielectric fluids is much smaller (< 20 W/cm^2) than what is needed for next generation high power density systems (> 100 W/cm^2). 3) The dielectric fluid has relatively poor thermophysical properties such as thermal conductivity, latent heat, and surface tension, when compared to ideal conducting fluids such as water.

References

[1.1] E. Schmidt, W. Schurig, W. Sellschopp, Condensation of water vapour in film- and drop form, Zeitschrift Des Vereines Deutscher Ingenieure, 74 (1930) 544-544.
[1.2] N. Miljkovic, R. Enright, Y. Nam, K. Lopez, N. Dou, J. Sack, E.N. Wang, Jumping-droplet-enhanced condensation on scalable superhydrophobic nanostructured surfaces, Nano Lett, 13(1) (2013) 179-187.
[1.3] J.B. Boreyko, C.H. Chen, Self-Propelled Dropwise Condensate on Superhydrophobic Surfaces, Phys Rev Lett, 103(18) (2009) 184501.
[1.4] X. Chen, J. Wu, R. Ma, M. Hua, N. Koratkar, S. Yao, Z. Wang, Nanograssed Micropyramidal Architectures for Continuous Dropwise Condensation, Advanced Functional Materials, 21 (2011) 4617–4623.
[1.5] J. Feng, Y. Pang, Z. Qin, R. Ma, S. Yao, Why Condensate Drops Can Spontaneously Move Away on Some Superhydrophobic Surfaces but Not on Others, ACS Applied Materials & Interfaces, 4 (2012) 6618−6625.
[1.6] J. Feng, Z.Q. Qin, S.H. Yao, Factors Affecting the Spontaneous Motion of Condensate Drops on Superhydrophobic Copper Surfaces, Langmuir, 28(14) (2012) 6067-6075.
[1.7] C.J. Lv, P.F. Hao, Z.H. Yao, Y. Song, X.W. Zhang, F. He, Condensation and jumping relay of droplets on lotus leaf, Appl Phys Lett, 103 (2013) 021601.
[1.8] K. Rykaczewski, Microdroplet Growth Mechanism during Water Condensation on Superhydrophobic Surfaces, Langmuir, 28(20) (2012) 7720-7729.
[1.9] K. Rykaczewski, W.A. Osborn, J. Chinn, M.L. Walker, J.H.J. Scott, W. Jones, C. Hao, S. Yaod, Z. Wang, How nanorough is rough enough to make a surface superhydrophobic during water condensation?, Soft Matter, 8 (2012) 8786-8794.
[1.10] J. Tian, J. Zhu, H.Y. Guo, J. Li, X.Q. Feng, X.F. Gao, Efficient Self-Propelling of Small-Scale Condensed Microdrops by Closely Packed ZnO Nanoneedles, J Phys Chem Lett, 5(12) (2014) 2084-2088.
[1.11] M. McCarthy, K. Gerasopoulos, S.C. Maroo, A.J. Hart, Materials, Fabrication, and Manufacturing of Micro/Nanostructured Surfaces for Phase-Change Heat Transfer Enhancement, Nanosc Microsc Therm, 18(3) (2014) 288-310.
[1.12] G.Q. Li, M.H. Alhosani, S.J. Yuan, H.R. Liu, A. Al Ghaferi, T.J. Zhang, Microscopic Droplet Formation and Energy Transport Analysis of Condensation on Scalable

Superhydrophobic Nanostructured Copper Oxide Surfaces, Langmuir, 30(48) (2014) 14498-14511.
[1.13] K. Yanagisawa, M. Sakai, T. Isobe, S. Matsushita, A. Nakajima, Investigation of droplet jumping on superhydrophobic coatings during dew condensation by the observation from two directions, Appl Surf Sci, 315 (2014) 212-221.
[1.14] C.W. Lo, C.C. Wang, M.C. Lu, Scale Effect on Dropwise Condensation on Superhydrophobic Surfaces, ACS Applied Materials & Interfaces, 6(16) (2014) 14353-14359.
[1.15] K.M. Wisdom, J.A. Watson, X. Qua, F. Liua, G.S. Watson, C.H. Chen, Self-cleaning of superhydrophobic surfaces by self-propelled jumping condensate, Proceedings of the National Academy of Sciences of the United States of America, 110(20) (2013) 7992–7997.
[1.16] G.S. Watson, L. Schwarzkopf, B.W. Cribb, S. Myhra, M. Gellender, J.A. Watson, Removal mechanisms of dew via self-propulsion off the gecko skin, J R Soc Interface, 12(105) (2015).
[1.17] G.S. Watson, M. Gellender, J.A. Watson, Self-propulsion of dew drops on lotus leaves: a potential mechanism for self cleaning, Biofouling, 30(4) (2014) 427-434.
[1.18] J.B. Boreyko, Y.J. Zhao, C.H. Chen, Planar jumping-drop thermal diodes, Appl Phys Lett, 99(23) (2011) 234105.
[1.19] J.B. Boreyko, P.C. Collier, Delayed Frost Growth on Jumping-Drop Superhydrophobic Surfaces, Acs Nano, 7(2) (2013) 1618-1627.
[1.20] X.M. Chen, R.Y. Ma, H.B. Zhou, X.F. Zhou, L.F. Che, S.H. Yao, Z.K. Wang, Activating the Microscale Edge Effect in a Hierarchical Surface for Frosting Suppression and Defrosting Promotion, Sci Rep-Uk, 3 (2013).
[1.21] J.Y. Lv, Y.L. Song, L. Jiang, J.J. Wang, Bio-Inspired Strategies for Anti-Icing, ACS Nano, 8(4) (2014) 3152-3169.
[1.22] Q.L. Zhang, M. He, J. Chen, J.J. Wang, Y.L. Song, L. Jiang, Anti-icing surfaces based on enhanced self-propelled jumping of condensed water microdroplets, Chem Commun, 49(40) (2013) 4516-4518.
[1.23] J.B. Boreyko, C.H. Chen, Vapor chambers with jumping-drop liquid return from superhydrophobic condensers, International Journal of Heat and Mass Transfer, 61 (2013) 409-418.

[1.24] J. Oh, P. Birbarah, T. Foulkes , S.L. Yin, M. Rentauskas, J. Neely, R.P. Podgurski, N. Miljkovic, Jumping-Droplet Electronics Hot Spot Cooling, Appl Phys Lett, in press (2017).
[1.25] D.J. Preston, N. Miljkovic, R. Enright, E.N. Wang, Jumping Droplet Electrostatic Charging and Effect on Vapor Drag, J Heat Trans-T Asme, 136(8) (2014).
[1.26] N. Miljkovic, D.J. Preston, R. Enright, E.N. Wang, Jumping-droplet electrostatic energy harvesting, Appl Phys Lett, 105(1) (2014).
[1.27] N. Miljkovic, D.J. Preston, R. Enright, E.N. Wang, Electrostatic charging of jumping droplets, Nat Commun, 4 (2013).
[1.28] R. Enright, N. Miljkovic, J.L. Alvarado, K. Kim, J.W. Rose, Dropwise Condensation on Micro- and Nanostructured Surfaces, Nanosc Microsc Therm, 18(3) (2014) 223-250.
[1.29] N. Miljkovic, E.N. Wang, Condensation heat transfer on superhydrophobic surfaces, Mrs Bull, 38(5) (2013) 397-406.
[1.30] R. Enright, N. Miljkovic, N. Dou, Y. Nam, E.N. Wang, Condensation on Superhydrophobic Copper Oxide Nanostructures, J Heat Transf, 135(9) (2013) 091304.
[1.31] N. Miljkovic, R. Enright, E.N. Wang, Effect of Droplet Morphology on Growth Dynamics and Heat Transfer during Condensation on Superhydrophobic Nanostructured Surfaces, Acs Nano, 6(2) (2012) 1776–1785.
[1.32] N. Miljkovic, R. Enright, E.N. Wang, Growth Dynamics During Dropwise Condensation on Nanostructured Superhydrophobic Surfaces, 3rd Micro/Nanoscale Heat & Mass Transfer International Conference, (2012).
[1.33] J. Cheng, A. Vandadi, C.L. Chen, Condensation heat transfer on two-tier superhydrophobic surfaces, Appl Phys Lett, 101 (2012) 131909-131901 - 131909-131904.
[1.34] E. Olceroglu, C.Y. Hsieh, M.M. Rahman, K.K.S. Lau, M. McCarthy, Full-Field Dynamic Characterization of Superhydrophobic Condensation on Biotemplated Nanostructured Surfaces, Langmuir, 30(25) (2014) 7556-7566.
[1.35] E. Olceroglu, S.M. King, M.M. Rahman, M. McCarthy, Biotemplated Superhydrophobic Surfaces for Enhanced Dropwise Condensation, Proceedings of the Asme International Mechanical Engineering Congress and Exposition - 2012, Vol 7, Pts a-D, (2013) 2809-2815.
[1.36] D. Attinger, C. Frankiewicz, A.R. Betz, T.M. Schutzius, R. Ganguly, A. Das, C.-J. Kim, C.M. Megaridis, Surface engineering for phase change heat transfer: A review, MRS Energy & Sustainability, 1 (2014).

[1.37] X.M. Chen, J.A. Weibel, S.V. Garimella, Exploiting Microscale Roughness on Hierarchical Superhydrophobic Copper Surfaces for Enhanced Dropwise Condensation, Adv Mater Interfaces, 2(3) (2015).
[1.38] Y.M. Hou, M. Yu, X.M. Chen, Z.K. Wang, S.H. Yao, Recurrent Filmwise and Dropwise Condensation on a Beetle Mimetic Surface, ACS Nano, 9(1) (2015) 71-81.
[1.39] H. Cha, C. Xu, J. Sotelo, J.M. Chun, Y. Yokohama, R. Enright, N. Miljkovic, Coalescence-Induced Nanodroplet Jumping, Physical Review Fluids, In press (2016).
[1.40] S. Chavan, H. Cha, D. Orejon, K. Nawaz, N. Singla, Y.F. Yeung, D. Park, D.H. Kang, Y.J. Chang, Y. Takata, N. Miljkovic, Heat Transfer through a Condensate Droplet on Hydrophobic and Nanostructured Superhydrophobic Surfaces, Langmuir, 32(31) (2016) 7774-7787.
[1.41] A. Shahriari, P. Birbarah, J. Oh, N. Miljkovic, V. Bahadur, Electric-Field Based Control and Enhancement of Boiling and Condensation, Nanosc Microsc Therm, in press (2017).
[1.42] P. Birbarah, Z.E. Li, A. Pauls, N. Miljkovic, A Comprehensive Model of Electric-Field-Enhanced Jumping-Droplet Condensation on Superhydrophobic Surfaces, Langmuir, 31(28) (2015) 7885-7896.
[1.43] N. Miljkovic, R. Enright, E.N. Wang, Modeling and Optimization of Superhydrophobic Condensation, J Heat Trans-T Asme, 135(11) (2013).
[1.44] N. Miljkovic, R. Enright, Y. Nam, K. Lopez, N. Dou, J. Sack, E.N. Wang, Jumping-Droplet-Enhanced Condensation on Scalable Superhydrophobic Nanostructured Surfaces, Nano Letters, 13(1) (2013) 179-187.
[1.45] N. Miljkovic, D.J. Preston, R. Enright, E.N. Wang, Electric-Field-Enhanced Condensation on Superhydrophobic Nanostructured Surfaces, ACS Nano, 7(12) (2013) 11043-11054.
[1.46] Rose, J. W.; Glicksma.Lr. Dropwise Condensation - Distribution of Drop Sizes. *International Journal of Heat and Mass Transfer* **1973,** *16* (2), 411-425.
[1.47] Glicksman, L. R.; Hunt, A. W. Numerical Simulation of Dropwise Condensation. *International Journal of Heat and Mass Transfer* **1972,** *15* (11), 2251-+.
[1.48] Mei, M. F.; Yu, B. M.; Cai, J. C.; Luo, L. A fractal analysis of dropwise condensation heat transfer. *International Journal of Heat and Mass Transfer* **2009,** *52* (21-22), 4823-4828.
[1.49] Kim, S.; Kim, K. J. Dropwise Condensation Modeling Suitable for Superhydrophobic Surfaces. *J Heat Trans-T Asme* **2011,** *133* (8).

[1.50] AbuOrabi, M. Modeling of heat transfer in dropwise condensation. *International Journal of Heat and Mass Transfer* **1998,** *41* (1), 81-87.
[1.51] P.T. Krein, Elements of power electronics, Oxford University Press, New York, 1998.

[1.52] J.G. Kassakian, T.M. Jahns, Evolving and Emerging Applications of Power Electronics in Systems, Ieee J Em Sel Top P, 1(2) (2013) 47-58.

[1.53] Y. Lei, C. Barth, S. Qin, W. Liu, I. Moon, A. Stillwell, D. Chou, T. Foulkes, Z. Ye, Z. Liao, R.C. Pilawa-Podgurski, A single-phase, 7-level, gan inverter with an active energy buffer achieving 216 w/in3 power density and 97.6% peak efficiency, in: IEEE (Ed.) Applied Power Electronics Conference and Exposition (APEC), IEEE, Long Beach, CA, 2016.

[1.54] A. Faghri, Heat pipe science and technology, 2nd ed., Global Digital Press, Columbia, MO, 2010.

[1.55] C.B. Barth, T. Foulkes, W. Chung, T. Modeer, P. Assem, Y. Lei, R.C.N. Pilawa-Podgurski, Design and control of a GaN-based, 13-level, flying capacitor multilevel inverter, in: IEEE (Ed.) 2016 IEEE 17th Workshop on Control and Modeling for Power Electronics (COMPEL), IEEE, Trondheim, Norway, 2016, pp. 1-6.

[1.56] J. Doty, K. Yerkes, L. Byrd, J. Murthy, A. Alleyne, M. Wolff, S. Heister, T.S. Fisher, Dynamic Thermal Management for Aerospace Technology: Review and Outlook, J Thermophys Heat Tr, 0(0) (2016) 1-13

[1.57] W.L. Qu, I. Mudawar, Measurement and prediction of pressure drop in two-phase micro-channel heat sinks, International Journal of Heat and Mass Transfer, 46(15) (2003) 2737-2753.
[1.58] F. Sarvar, D.C. Whalley, P.P. Conway, Thermal Interface Materials - A review of the State of the Art, in: Electronics System Integration Technology Conference, 1st. IEEE, Dresden, Germany, 2006.
[1.59] S. Narumanchi, Thermal Interface Materials for Power Electronics Applications, in: Itherm, Orlando, FL, USA, 2008.
[1.60] L. Zhu, R.F. Boehm, Y.P. Wang, C. Halford, Y. Sun, Water immersion cooling of PV cells in a high concentration system, Sol Energ Mat Sol C, 95(2) (2011) 538-545.

[1.61] E. Baker, Liquid Immersion Cooling of Small Electronic Devices, Microelectron Reliab, 12(2) (1973) 163-173.
[1.62] P.J. Marto, V.J. Lepere, Pool Boiling Heat-Transfer from Enhanced Surfaces to Dielectric Fluids, J Heat Trans-T Asme, 104(2) (1982) 292-299.
[1.63] T.L. Chen, S.V. Garimella, Measurements and high-speed visualizations of flow boiling of a dielectric fluid in a silicon microchannel heat sink, Int J Multiphas Flow, 32(8) (2006) 957-971.

Chapter 2- External Convective Jumping-Droplet Condensation

2.1. Introduction

Water vapor condensation, whether industrially driven or occurring in nature, is a critical process for the sustainability of ecosystems and advancement of economies. Due to the reduced energy barrier for vapor-to-liquid nucleation, condensation preferentially occurs on high surface energy substrates [1], forming a thermally-insulating liquid blanket, termed filmwise condensation [2]. In an effort to shed the liquid layer and enhance heat transfer, engineers and researchers have devised techniques for creating non-wetting surfaces to enable dropwise [3] or jumping-droplet condensation [4], whereby non-wetting droplets shed due to gravity at millimetric length scales or spontaneously jump away from the surface at micrometric length scales [5], respectively. Specifically, jumping-droplet condensation, whereby microdroplets (~10-100 μm) condensing and coalescing on suitably designed superhydrophobic surfaces undergo surface-to-kinetic energy transfer and result in the merged droplet jumping away from the surface [5-10], has recently been shown to have a 10X heat transfer enhancement compared to state-of-the-art filmwise condensing surfaces [11-20]. A number of works have since fabricated superhydrophobic nanostructured surfaces to achieve spontaneous droplet removal [21-31] for a variety of applications including self-cleaning [32-34], thermal diodes [33, 35], anti-icing [36-39], vapor chambers [40], electrostatic energy harvesting [41-43], and heat transfer enhancement [44-55].

However, the efficient removal of jumping droplets along with the heat transfer enhancement can be limited by droplet return to the surface due to (1) gravitational force (2) entrainment in a bulk convective vapor flow, and (3) entrainment in the local condensing vapor flow toward the surface [40, 56]. The first two return mechanisms (gravity and bulk vapor flow) can be mitigated with suitable geometric design of the macroscale condensing surface and vapor

supply. However, the third return mechanism (local vapor flow) is more difficult to eliminate due to the need to conserve mass of the condensing vapor flowing towards the surface. Although previous studies have experimentally characterized the effects of gravitational return, [57, 58] further study of local vapor flow entrainment on droplet return and methods to limit this process are needed.

One avenue to enhance droplet removal after jumping is by exploiting the fact that jumping droplets attain a positive charge (~ +10fC) after departing the superhydrophobic surface due to electric-double-layer charge separation at the coating-droplet interface [43]. This discovery has allowed for the development of electric-field-enhanced (EFE) condensation, whereby an external electric field was used to enhance the removal of jumping droplets from a radial (tube) condensing surface by counteracting the three droplet return mechanisms described above [59]. Through the elimination of droplet return, a heat transfer enhancement of 20X was experimentally demonstrated, compared to state-of-the-art filmwise condensing surfaces.

While the removal of the droplets by external electric fields offers a method remove condensate, practical difficulties exist. For example, the need for energized external electrodes presents critical safety concerns. Furthermore, the need to remove the condensate from the external electrode has not been addressed. Lastly, the added complexity associated with the design and manufacture of EFE system equates to higher probability of failure once integrated into real life applications.

Here, we present a solution to the aforementioned limitations by utilizing forced bulk vapor flow to remove jumping-droplets, in what we term convective jumping-droplet condensation. We provide a comprehensive modeling framework of convective jumping-droplet condensation over a flat plate. Utilizing hydrodynamic boundary layer analysis, we couple the droplet motion to the

external vapor flow fields to calculate droplet trajectories and surface interactions. We study the jumping droplet traveled length along the plate and maximum jumping height as a function of the condensation heat flux, free stream vapor velocity, jumping droplet size, location of droplets along the plate, and plate inclination. By linking droplet return with droplet jumping (multi-hop), we develop a framework to predict macroscopic droplet motion along the condensing plate, and offer guidelines for the minimization of drag force and maximization of overall condensation heat transfer. The modeling framework shown here outlines the first treatment of convective jumping-droplet condensation which has the potential to be implemented in both water cooled and air-cooled steam condensers for energy and water applications.

2.2. Theory

2.2.1. Laminar External Convective Jumping-Droplet Condensation on a Flat Plate

Figure 2.1 shows a schematic of the laminar external flow over a flat plate with condensation at the wall. The wall is assumed to be superhydrophobic, having a condensed droplet-surface adhesion less than the critical threshold for droplet jumping [6]. As saturated water vapor condenses on the plate, droplets merge and jump normal to the plate surface into the flow domain.

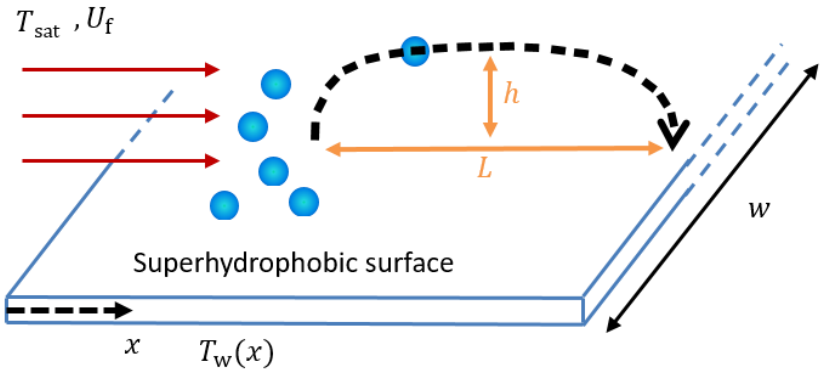

Figure 2.1. Schematic of external convective jumping-droplet condensation on a flat plate. Saturated water vapor (T_{sat}) flows at a free stream velocity, U_f, parallel to the cooled superhydrophobic surface with wall temperature T_w. As droplets nucleate, grow, coalesce and jump away from the surface, they are entrained by the vapor flow, travel a distance, L, along the plate (x-direction) and jump to maximum heights, h, normal to the plate prior to returning to the

surface due to surface and body forces. The depth of the plate (w) is much larger than the distances considered in the x -direction, allowing for a 2-dimensional analysis of the problem (the flow being laminar).

Condensation at the wall results in the loss of water vapor from the bulk vapor flow with a negligible added liquid volume at the wall (liquid density $\rho_{\mathrm{l}} \gg$ vapor density ρ_{v}). Hence mathematically we can model the condensation process by assuming a permeable wall with a suction velocity (V_{w}) that obeys the conservation of mass loss by condensation:

$$q = \dot{m}_{\mathrm{c}} h_{\mathrm{fg}} = \rho_{\mathrm{v}} V_{\mathrm{w}} h_{\mathrm{fg}} \,, \tag{2.1}$$

where q represents the condensation heat flux, $\dot{m}_c$ is the mass-loss of condensate per unit time per unit area, ρ_{v} is the density of water vapor and h_{fg} the latent heat of vaporization . Therefore we can obtain the vapor velocity at the wall by relating it to the heat flux by rearranging Eq. 2.1:

$$V_{\mathrm{w}} = \frac{q}{\rho_{\mathrm{v}} h_{\mathrm{fg}}} \tag{2.2}$$

The continuity and x-momentum equations of the flow in terms of the horizontal velocity $u(x, y)$ and the vertical velocity $v(x, y)$, respectively, are [60]:

$$\frac{\partial u}{\partial x} + \frac{\partial v}{\partial y} = 0 \,, \tag{2.3}$$

$$u \frac{\partial u}{\partial x} + v \frac{\partial u}{\partial y} = \nu_{\mathrm{v}} \frac{\partial^2 u}{\partial y^2} \,, \tag{2.4}$$

where the water vapor is assumed to be a Newtonian, incompressible fluid (Mach number Ma < 0.3), and the flow is assumed laminar ($Re_x = U_{\mathrm{f}} x / \nu_{\mathrm{v}}$ < 5 x10^5) and two-dimensional. The equations are valid sufficiently far away from the leading edge of the plate as long as the boundary layer thickness, $\delta(x) \ll x$.

We use a similarity solution to solve for the horizontal and vertical velocity profiles. Using the Blasius transformation, the non-dimensional independent variable η is defined as:

$$\eta = \frac{1}{2}\sqrt{\frac{U_\mathrm{f}}{\nu_\mathrm{v} x}}\, y\,, \tag{2.5}$$

and the dimensional stream function φ is defined in terms of the non-dimensional stream function $f(\eta)$ by:

$$\varphi = (\nu_\mathrm{v} U_\mathrm{f} x)^{1/2} f\,. \tag{2.6}$$

The horizontal and vertical velocities of the flow can be determined in terms of f and its derivatives. Note, we use the prime symbol " $'$ " to represent derivatives with respect to the independent variable, in this case η, as follows:

$$u = \frac{\partial \varphi}{\partial y} = \frac{1}{2} U_\mathrm{f} f'\,, \tag{2.7}$$

$$v = -\frac{\partial \varphi}{\partial x} = \frac{1}{2}\sqrt{\frac{U_\mathrm{f}\nu_\mathrm{v}}{x}}\,(\eta f' - f)\,. \tag{2.8}$$

Replacing u and v from equations 2.7 and 2.8 into 2.3 and 2.4 and simplifying, we obtain a non-dimensional non-linear third order ODE for f:

$$f''' + f f'' = 0\,. \tag{2.9}$$

The boundary conditions for the problem are:

$$\begin{aligned} u|_{y=0} &= 0\,, \\ u|_{y\to\infty} &= U_\mathrm{f}\,, \\ v|_{y=0} &= V_w\,, \end{aligned} \tag{2.10}$$

which respectively translates to in the non-dimensional formulation:

$$f'(0) = 0\,, \tag{2.11}$$

$$f'(\infty) = 2\,,$$

$$-\frac{1}{2}\sqrt{\frac{U_f \nu}{x}} f(0) = V_w\,.$$

By combining Eq. 2.9 with the boundary conditions defined by Eq. 2.11, the problem can be solved numerically using an iterative Runge-Kutta scheme with a shooting method [61].

The velocity profiles are expected to converge to the asymptotic solution [62] far downstream of the flow, where the profiles are fully developed and do not depend on x, as shown in Eq. 2.12, resulting in a constant boundary layer thickness.

$$u = U_f(1 - e^{\frac{V_w y}{\nu_v}}) \tag{2.12}$$

Note, a key assumption of our model is that the bulk vapor free stream consists of pure saturated vapor, allowing us to forgo analysis of both concentration and thermal boundary layer development and focus only on the hydrodynamics of the flow. This assumption can be deemed appropriate since in the hydrodynamic fully developed regime, no change in vertical vapor velocity exists, resulting in a constant pressure in the surface normal direction. If any temperature decrease exited as we approach the wall, condensation with a corresponding pressure decrease would occur,

not consistent with our previous argument. Hence we can say that condensation occurs at a constant temperature equal to the saturation temperature of the free stream and no thermal boundary layer is present. For the entrance region, the effect of pressure change in the direction normal to the plate is minimal such that this assumption still hold. In addition, the work done by the jumping microdroplets on the vapor flow is assumed to be have a negligible effect on the velocity profiles.

2.2.2. Plate Inclination

In order to develop a more comprehensive model of convective jumping-droplet condensation, we also analyzed the case where the condenser plate is inclined by an arbitrary angle, ψ, relative to the horizontal plane (Figure 2.2).

To develop a solution for the inclined plate case, we use two reference frames: the fixed frame (xy) and a frame attached to the plate (x^1y^1), that is rotated counter-clockwise from the fixed frame by an angle ψ. Any vector expressed in the (xy) coordinate frame can be related to equivalent coordinates in the (x^1y^1) frame by:

$$\begin{pmatrix} x \\ y \end{pmatrix} = R \begin{pmatrix} x^1 \\ y^1 \end{pmatrix}, \tag{2.13}$$

where

$$R = \begin{pmatrix} \cos\psi & -\sin\psi \\ \sin\psi & \cos\psi \end{pmatrix}. \tag{2.14}$$

Note, the inverse transformation can be applied by multiplying Eq. 2.13 by R^{-1}.

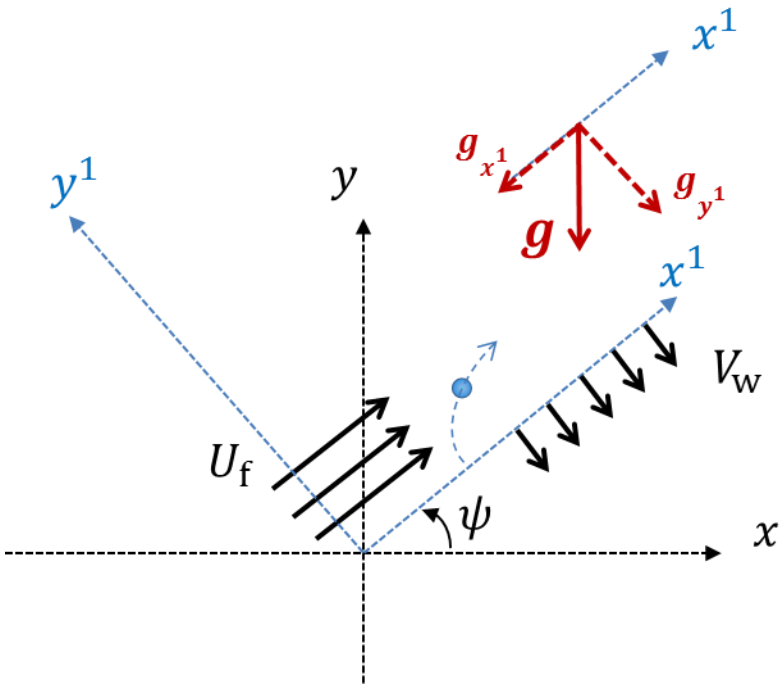

Figure 2.2. Schematic of convective jumping-droplet condensation on an inclined superhydrophobic surface. The free stream and suction velocities are represented by U_f and V_w, respectively. The schematic depicts the two simulation reference frames: reference (xy) represents the fixed frame while reference (x^1y^1) represents the inclined frame attached to the plate rotated by an angle ψ counterclockwise from (xy). Droplet jumping dynamics are affected by the projection of gravity (g) onto the tangential and perpendicular components (g_{x^1} and g_{y^1} respectively) representing directions along the plate and normal to the plate.

2.2.3. Jumping-Droplet Equations of Motion

Figure 2.3 shows the free body diagram on a jumping droplet during convective condensation on a superhydrophobic surface. The forces acting on the droplet are: the drag force $\overrightarrow{F_D}$, the gravitational force $\overrightarrow{F_G}$, and the Saffman lift force [63, 64], $\overrightarrow{F_{SL}}$, due to the horizontal velocity gradient. The drag and gravitational forces can, respectively, be expressed in magnitude and direction as:

$$\overrightarrow{F_D} = \frac{1}{2}\rho_v {V_{rel}}^2 C_D(Re_d)\pi {R_d}^2 \frac{\overrightarrow{V_{rel}}}{|V_{rel}|}, \tag{2.15}$$

$$\overrightarrow{F_G} = \frac{4}{3}\pi {R_d}^3 \rho_l \vec{g}\,, \tag{2.16}$$

where $\overrightarrow{V_{rel}} = \overrightarrow{V_f} - \overrightarrow{V_d}$ represents the relative velocity vector between the vapor flow $\overrightarrow{V_f}$ and droplet $\overrightarrow{V_d}$ velocity vectors, C_D is the Reynolds number dependent drag coefficient [65, 66] $\mathrm{Re}_d = |V_{rel}|(2R_d)/\upsilon_v$, and ρ_l is the density of liquid water.

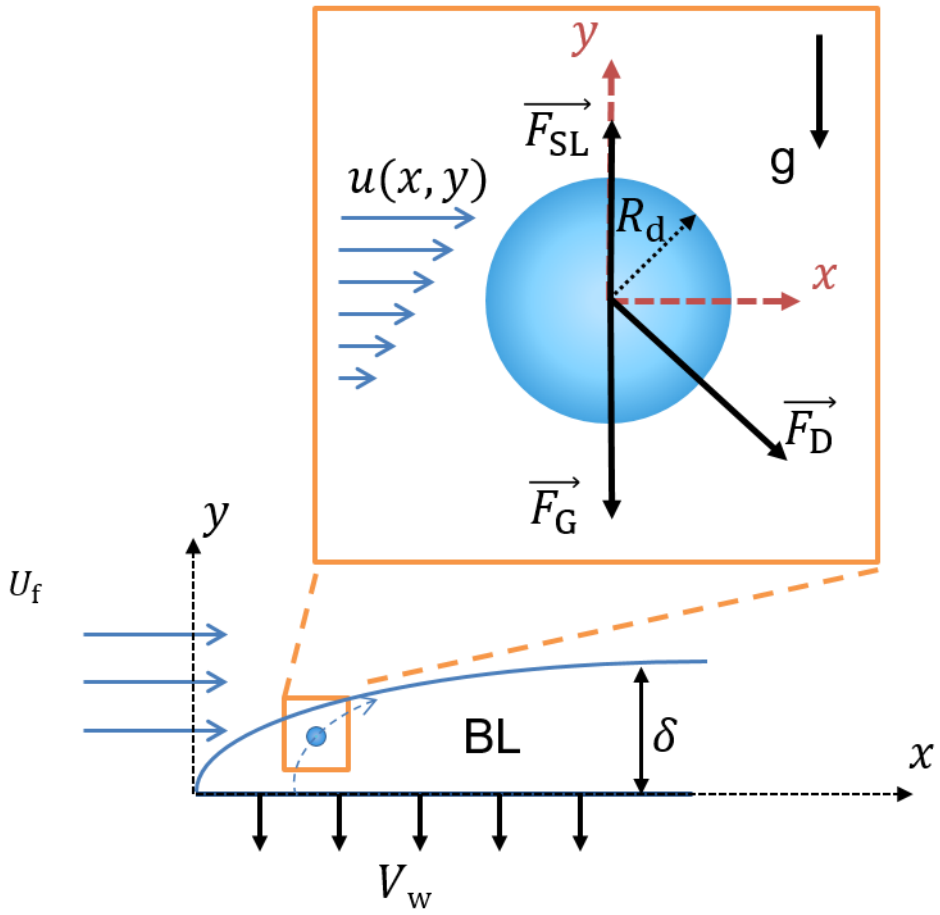

Figure 2.3. Free body diagram on a droplet of radius R_d jumping against gravity from a flat plate during convective jumping-droplet condensation on a superhydrophobic surface. The saturated vapor flow has a uniform and horizontal free stream velocity U_f prior to reaching the leading edge of the plate. Close to the wall, a boundary layer (BL) of thickness δ is formed as the horizontal velocity profile (u) is developed in the y-direction (BL profile shown in the figure not to scale). Vapor mass loss due to condensation is modeled as suction at the wall with suction velocity, V_w. The forces experienced by the droplet include the vapor drag force (F_D), the gravitational body force (F_G), and the Saffman lift force (F_{SL}) due to the velocity gradient in the boundary layer.

The Saffman lift force is expressed as:

$$\overrightarrow{F_{\mathrm{SL}}} = \phi_{\mathrm{S}}(Re_{\mathrm{G}}, Re_{\mathrm{d}}) \left[6.46 {R_{\mathrm{d}}}^2 \left(\mu_{\mathrm{v}} \rho_{\mathrm{v}} \left| \frac{\partial u^1}{\partial y^1} \right| \right)^{0.5} sgn\left(\frac{\partial u^1}{\partial y^1} \right) (u^1 - {u_{\mathrm{d}}}^1) \right] \overrightarrow{j^1} . \tag{2.17}$$

The velocity gradient can be determined by:

$$\frac{\partial u^1}{\partial y^1} = \frac{\partial \eta}{\partial y^1} \frac{\partial u^1}{\partial \eta} , \tag{2.18}$$

$$\frac{\partial u^1}{\partial y^1} = \frac{1}{4} \sqrt{\frac{{U_{\mathrm{f}}}^3}{\nu_{\mathrm{v}} x^1}} \, f'' , \tag{2.19}$$

where ϕ_{S} is the Saffman multiplier that extends the lift force to higher droplet Reynolds number flows [67]. The multiplier ϕ_{S} is a function of the droplet Reynolds number $\mathrm{Re_d}$ and the gradient Reynolds number $\mathrm{Re_G} = |\partial u^1/\partial y^1|(2R_{\mathrm{d}})^2/\nu_{\mathrm{v}}$. The symbol *sgn* is used to define the sign function ($sgn(\partial u^1/\partial y^1) = +1$ for $\partial u^1/\partial y^1 > 0$, and $sgn(\partial u^1/\partial y^1) = -1$ for $\partial u^1/\partial y^1 < 0$). The droplet horizontal velocity is represented by ${u_{\mathrm{d}}}^1$, and $\overrightarrow{j^1}$ is the elementary vector in the y^1-direction. The equations of motion in the (xy) frame for the center of mass of the droplet are hence:

$$\frac{\partial u_{\mathrm{d}}}{\partial t} = \frac{1}{m} \left[F_{\mathrm{D}} \cos\theta + F_{\mathrm{SL},x} \right] , \tag{2.20}$$

$$\frac{\partial v_{\mathrm{d}}}{\partial t} = \frac{1}{m} \left[-mg + F_{\mathrm{D}} \sin\theta + F_{\mathrm{SL},y} \right] , \tag{2.21}$$

where $\theta = \tan^{-1}(v_{\mathrm{rel}}/u_{\mathrm{rel}})$ is the angle between the relative velocity vector and the x-axis, and $F_{\mathrm{SL},x}$ and $F_{\mathrm{SL},y}$ are obtained using the transformation shown in Eq. 2.14. Due to the relatively small size of departing droplets (~10-100 μm), we assume that the shape of droplets remained spherical during flight. This assumption is justified given that the Bond, Webber, and Capillary numbers are all much less than one ($\mathrm{Bo} = \rho_{\mathrm{l}} g {R_{\mathrm{d}}}^2/\gamma \ll 1, \mathrm{We} = \rho_{\mathrm{v}} u^2 R_{\mathrm{d}}/\gamma \ll 1, \mathrm{Ca} = \mu_{\mathrm{v}} u/\gamma \ll 1$, where γ = 73 mN/m is the water surface tension and μ_{v} is vapor dynamic viscosity). The effect of residual surface charge on the trajectories of the droplets was assumed to be negligible away from the wall.

The initial position coordinates of the center of mass of the droplet are: $x_0^1 = 10$ cm, $y_0^1 = R_\mathrm{d}$. The initial velocity of the center of mass is obtained by balancing the excess surface energy and kinetic energy of the jumping droplet, with a proportionality constant $C \approx 0.23$ that accounts for the efficiency of this energy conversion and that best fits the experimental data [6]. For a droplet jumping perpendicular to the plate we can write:

$$u_{\mathrm{d},0}^1 = 0\,,$$
$$v_{\mathrm{d},0}^1 = 0.23\sqrt{\frac{\gamma}{\rho_\mathrm{l} R_\mathrm{d}}}\,. \tag{2.22}$$

2.2.4. Droplet Considerations

In order to determine whether stationary condensing droplets are removed prior to jumping by the vapor flow induced shear force, we compare the magnitude of the droplet-surface adhesion via contact line pinning to the horizontal drag force on the droplet. Due to the relatively low apparent contact angle hysteresis ($\Delta\theta^{\mathrm{app}} \sim 10°$) required to ensure droplet jumping, the adhesion force is very low and needs to be compared to the vapor shear force. For the case of a horizontal plate where gravitational force acts transverse to the shear force [68, 69], the contact line pinning force F_σ can be determined by [49]

$$F_\sigma = 2\gamma R_\mathrm{d} \sin\theta_\mathrm{e}^{\mathrm{app}} (\cos\theta_\mathrm{r}^{\mathrm{app}} - \cos\theta_\mathrm{a}^{\mathrm{app}}) \tag{2.23}$$

Where $\theta_\mathrm{r}^{\mathrm{app}}$ and $\theta_\mathrm{a}^{\mathrm{app}}$ are the apparent advancing and receding contact angles, respectively, and $\theta_\mathrm{e}^{\mathrm{app}} = \cos^{-1}(0.5\cos\theta_\mathrm{r}^{\mathrm{app}} + 0.5\cos\theta_\mathrm{a}^{\mathrm{app}})$ is the apparent equilibrium contact angle on the superhydrophobic surface.

The droplet drag force (Eq. 2.15) can be approximated by using the boundary layer velocity at the droplet center location, $y_c = R_d\sqrt{1-\sin^2\theta_e}$. We use the general expression of the projected area A_p of a stationary droplet in terms of θ_e^{app}, defined as $A_p = {R_d}^2(\theta_e^{app} + \sin\theta_e^{app}\sqrt{1-\sin^2\theta_e^{app}})$. Figure 2.4 shows the ratio F_D/F_σ as a function of the stationary droplet radius for $U_f = 20$ m/s, q = 1 W/cm^2, at $x = x_0$. The results show that adhesion force is dominant for R_d < 100 μm with $150^o < \theta_a^{app} < 170^o$, and $140^o < \theta_r^{app} < 160^o$, indicating that individual droplet sweeping due to vapor shear is not likely during convective jumping-droplet condensation. The relative magnitude of the drag force increases at higher droplet radii since the flow velocity u_c reach higher values at elevated heights away from the plate. Increased contact angle hysteresis acts to increase adhesion and thus reduce the likelihood of a droplet being swept off by vapor flow. As the droplet departure location moves downstream, we expect a decreased drag force because the velocity profile becomes less steep whereas increased suction (heat flux) would have the opposite effect.

We also investigate whether the granularity of the droplet affects the numerical results, since the droplet was modeled as a point mass, and the finite size of the droplet was neglected. The highest gradients occur as the droplet experiences a horizontal velocity gradient along the y^1-direction. Numerically, the most significant value of the relative velocity change across the radius of the droplet is $\partial u^1/u^1 \approx 50\%$ near the wall. However, the gradient is close to linear at the wall ($\partial^2 u^1/u^1 \approx 0.5\%$), making the center of mass velocity an acceptable average velocity between the bottom and top values of the flow velocity across the droplet. Furthermore, variations in the vertical velocities are < 1% for the microscale droplets considered here, resulting in negligible error in the numerical simulations due to the point mass approximation.

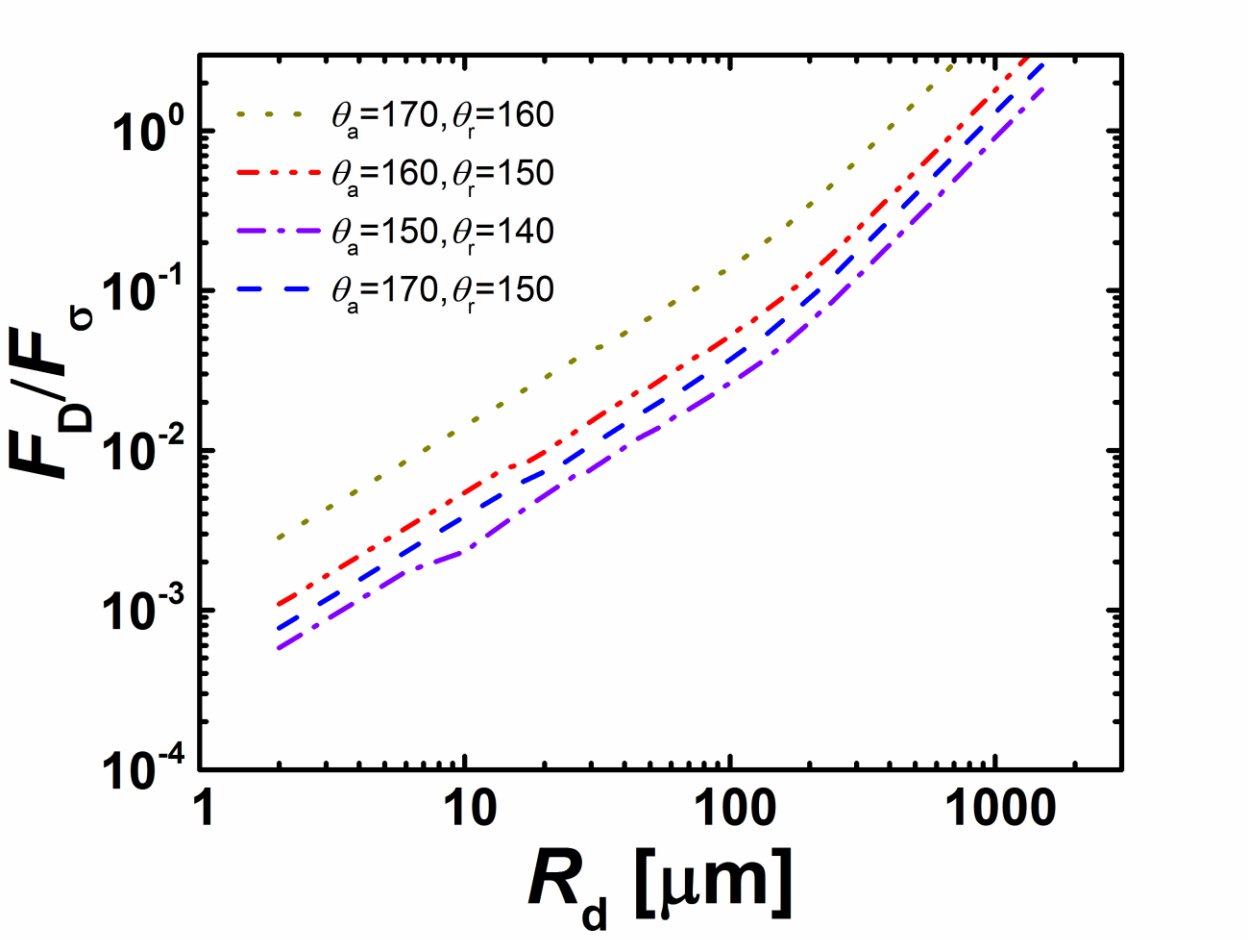

Figure 2.4. Relative magnitude of the drag force $\boldsymbol{F_D}$ to the adhesion force $\boldsymbol{F_\sigma}$ between a stationary droplet of radius $\boldsymbol{R_d}$ and the solid horizontal surface. Different combinations of advancing and receding contact angles ($\boldsymbol{\theta_a^{app}}$ and $\boldsymbol{\theta_r^{app}}$ respectively), in degrees, are considered. $\boldsymbol{U_f}$ = 20 m/s, q = 1 W/cm^2, and $\boldsymbol{x = x_0}$. It is clear that for droplets less than 100 μm in radius the adhesion force is dominant whereas the drag force becomes more important as the radius increases (the horizontal flow velocity reaches higher values). Increased contact angle hysteresis and decreased hydrophobicity both increase adhesion of the droplet to the surface.

2.2.5. Force on the Plate

To determine the force on the plate during convective jumping-droplet condensation, we computed the shear stress at the wall τ_w, defined as:

$$\tau_w = \mu_v \left.\frac{\partial u^1}{\partial y^1}\right|_{y^1=0} \tag{2.24}$$

Substituting Eq. 2.19 into Eq. 2.24, we obtain

$$\tau_{\mathrm{w}} = \frac{1}{4}\mu_{\mathrm{v}}\sqrt{\frac{{U_{\mathrm{f}}}^{3}}{\nu_{\mathrm{v}}x^{1}}}\, f''(0) \tag{2.25}$$

In order to obtain the force per unit depth (w) of the plate acting over a distance d along the plate, we integrate the shear stress along x^1:

$$F_{\mathrm{p}} = \int_{x_0^1}^{x_0^1+d} \tau_w dx^1 \tag{2.26}$$

2.3. Solution Methodology

The flow chart shown in Fig. 2.5 outlines the solution methodology adopted to solve for the coupled flow field and droplet trajectory equations. The iterative solution starts with the initial conditions in terms of position and velocity of the droplet in the fixed frame. Then we apply the frame transformation to obtain these components in the inclined frame, where we can solve for the flow field with suction (at that location). Having solved for the horizontal and vertical velocities of the flow in the inclined frame, we then apply the inverse frame transformation to obtain the velocities in the fixed frame where we apply the equations of motion and solve for the next position and velocity of the droplet. The steps outlined above are iterated until the droplet reaches the surface ($y^1 < 2R_{\mathrm{d}}$).

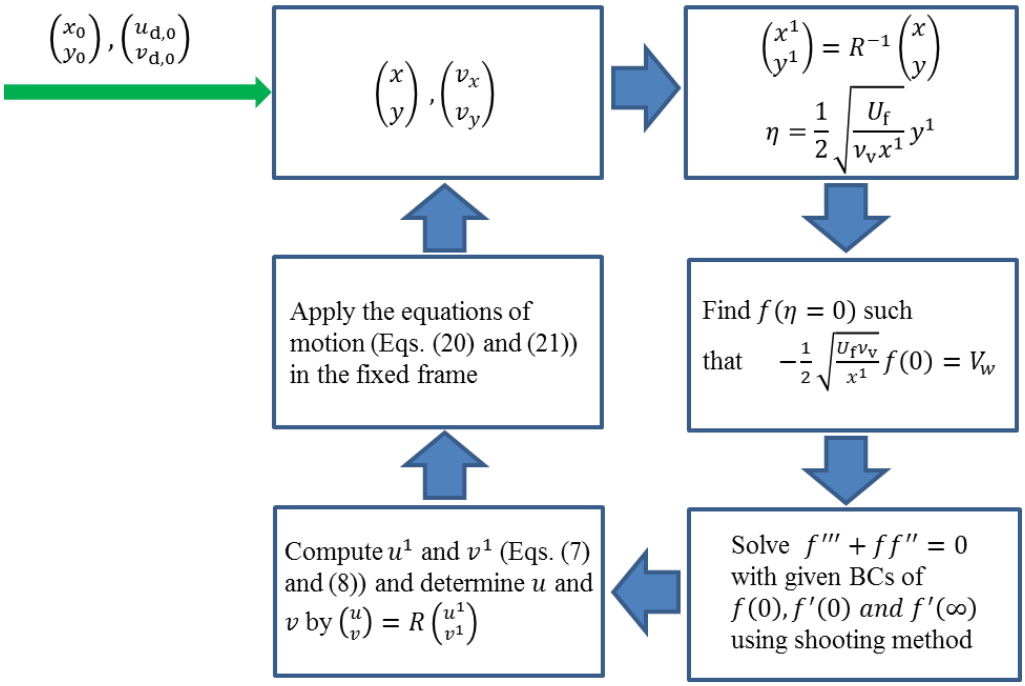

Figure 2.5. Flow chart representing the iterative algorithm used to simulate the jumping droplet trajectory. The green arrow represents the initiation step. The simulation time (~1 s) is longer than the total flight time of the droplet (~1-100 ms). The time step considered is 100 μs. The algorithm was implemented using MATLAB software. The stopping condition was the droplet reaching the surface ($\boldsymbol{y^1} < R_d$).

2.4. Simulation Results

Due to the large number of independent variables governing convective jumping-droplet condensation, we first performed parameter identification (Table 1) along with default value selection for each critical parameter based on previous experiments and theory.

Table 2.1. List of independent parameters governing the numerical simulation of the jumping droplet trajectory. Each parameter is attributed a default value that is maintained when the designated parameter is not explicitly varied. The default values have been chosen based on previous experimental observations to provide realistic physical quantities.

Parameter	**Symbol**	**Default value**	**References**
Droplet Radius	R_{d}	10 µm	[4]
Initial position along the plate	x_0^1	10 cm	Sufficiently large for Blasius to be valid $\left(\frac{\delta_0}{x_0} \ll 1\right)$ where δ_0 is the boundary layer thickness at x_0 [62]
Initial speed	$\left\|\overrightarrow{V_{\mathrm{d}}}\right\|$	$0.23\sqrt{\frac{\gamma}{\rho_{\mathrm{l}} R_{\mathrm{d}}}}$	[6]
Initial jumping direction	-	Perpendicular to the plate	[70]
Heat Flux	q	1 W/cm^2	Industrial condensers [71-74]
Free stream velocity	U_{f}	20 m/s	Industrial condenser flow rate [71-74]

2.4.1. Velocity profiles

To verify our flow solution, we computed the saturated vapor velocity profiles and compared them to well established results for laminar boundary layer flow over horizontal plate with suction at the wall. Figure 2.6 shows the horizontal and vertical velocity profiles near the wall ($y < \delta$), at different horizontal locations from the leading edge of the plate, for a free stream velocity U_{f} = 20 m/s and a heat flux q = 1 W/cm^2. It can be seen that the profiles converge to the asymptotic solution

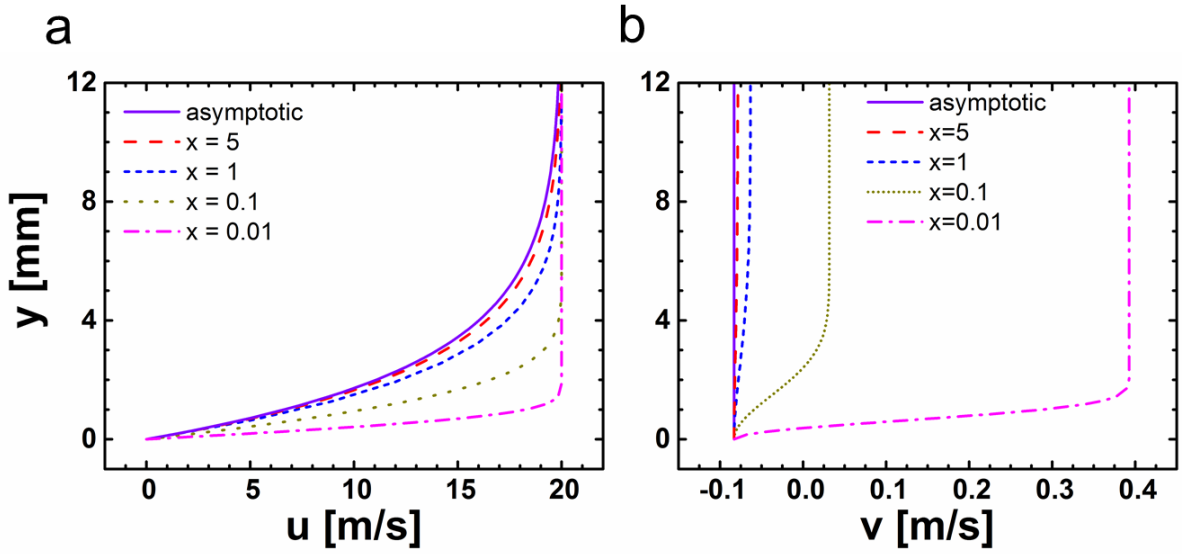

Figure 2.6. Water vapor (a) horizontal velocity, $\boldsymbol{u}$ and (b) vertical velocity, $\boldsymbol{v}$ as a function of the vertical distance $\boldsymbol{y}$ from the horizontal plate, for a free stream velocity $\boldsymbol{U_f}$ = 20 m/s, and a heat flux of 1 W/cm^2. The velocity profiles are shown for different horizontal locations ($\boldsymbol{x}$) along the plate in meters. Far downstream from the leading edge ($\boldsymbol{x} \approx 5$ m) the velocity profiles converge to the asymptotic suction solution (dashed line) presented in equation 2.12. The boundary layer thickness, δ, increases from ≈ 1.3 mm to 11 mm for $\boldsymbol{x}$ = 1 cm to $\boldsymbol{x} \rightarrow \infty$. We note that the length of the entrance region would also depend on the heat flux.

for a laminar flow over a flat plate with suction (Eq. 2.12), in agreement with previous studies. We note that the hydrodynamic entrance length is dependent on the condensation heat flux. Larger heat fluxes result in increased boundary layer suction and decreased entrance lengths.

2.4.2. Droplet Trajectories

Figure 2.7 shows the trajectories of 5, 10, 20, 30, 50 and 80 μm radii umping droplets (q = 1 W/cm^2) on a horizontal superhydrophobic surface with convection (U_f = 20 m/s, flow from left to right). The droplets jump initially perpendicular to the plate, 10 cm away from the leading edge. The trajectories are parabolic, and it can be seen that the traveled distance L and the maximum jumping height h can be ≈ 4.5x and ≈ 4x greater, respectively, for a 50 μm-radius droplet when

compared to its 10 µm counterpart. The jumping height was ~1 mm, while the travel distance was as ~10 cm,

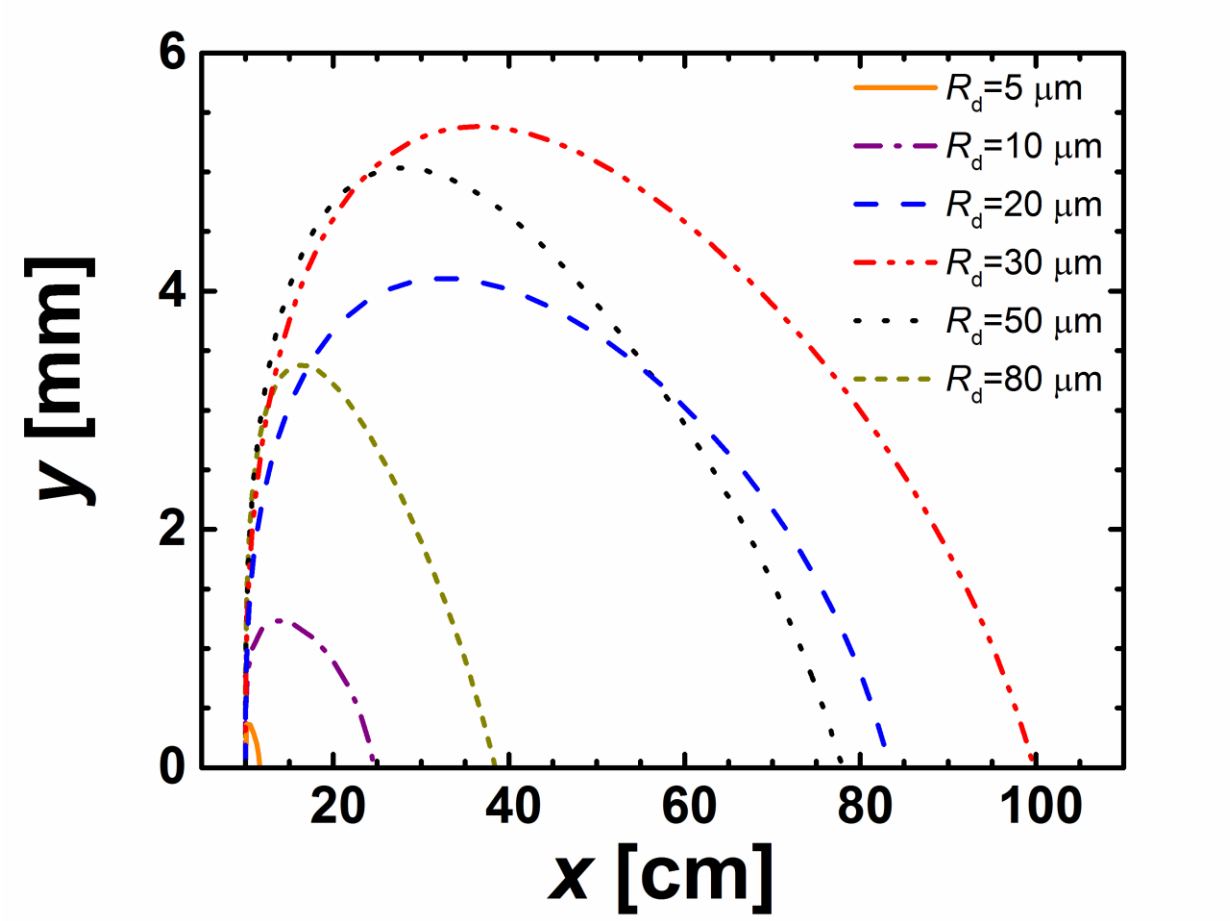

Figure 2.7. Trajectories of 5, 10, 20, 30, 50 and 80 µm radii ($\boldsymbol{R_d}$) jumping droplets for a condensation heat flux of 1 W/cm^2 on a horizontal superhydrophobic surface with convective condensation and free stream velocity $\boldsymbol{U_f}$ = 20 m/s (flow from left to right). The droplets jump perpendicular to the plate, 10 cm away from the leading edge, and are entrained in the vapor flow resulting in lateral motion parallel to the plate prior to returning to the surface.

showing the promise of convective vapor flow to effectively remove droplets laterally down the condensing surface, and potentially avoid flooding due to droplet return[59, 75]. Interestingly, the travel distance down the plate shows a non-linear behavior, with an optimum droplet size for the maximum travel distance. This is attributed to the balance between the gravitational body force at

large droplet length scales ($F_G \sim R_d^3$) and the Stokes drag force due to boundary layer suction at small droplet length scales ($F_D \sim R_d$).

2.4.3. Effect of droplet size

The forces acting on the droplet (Eqns. 2.15, 2.16 and 2.17) all have size dependence with varying exponents, leading to different trajectories for droplets having different sizes. Figures 2.8 and 2.9 show the traveled length and the maximum jumping height, respectively, as a function of the droplet radius for heat fluxes ranging from 0.1 to 5 W/cm^2. For any heat flux, the curves have a concave shape, with an optimal droplet radius $R_d \approx 30$ μm, which varies negligibly with heat flux. As droplets approach the limit of infinitesimal size ($R_d \to 0$), Stokes drag becomes dominant and droplet travel distance decreases. Conversely, as droplets become large ($R_d \to \infty$), gravitational body forces dominate and droplet travel distances diminishes. Between these two limits ($0 < R_d < \infty$), a delicate balance between drag, gravity, and Saffman lift force yields the observed optimum behavior for both jumping height and travel distance. For most cases, increasing the condensation heat flux acted to reduce the travel length as suction to the wall is increased at higher heat fluxes (Eq. 2.2).

To better understand the relative breakdown between the three fundamental forces in the optimum travel distance regime, we analyzed the results to determine the horizontal and vertical forces on the droplets as a function of the horizontal distance (Fig. 2.10). As shown in Fig. 2.10 b,d and f, the net vertical force on departing droplets is negative, resulting in a vertical deceleration throughout their trajectories. For small droplets ($R_d = 10$ μm), inertia is reduced and surface forces are elevated, resulting in short droplet trajectories along the flat plate. For large droplets

($R_d = 80$ μm), gravity begins to dominate, as can be seen from the relative sharp decline in the horizontal

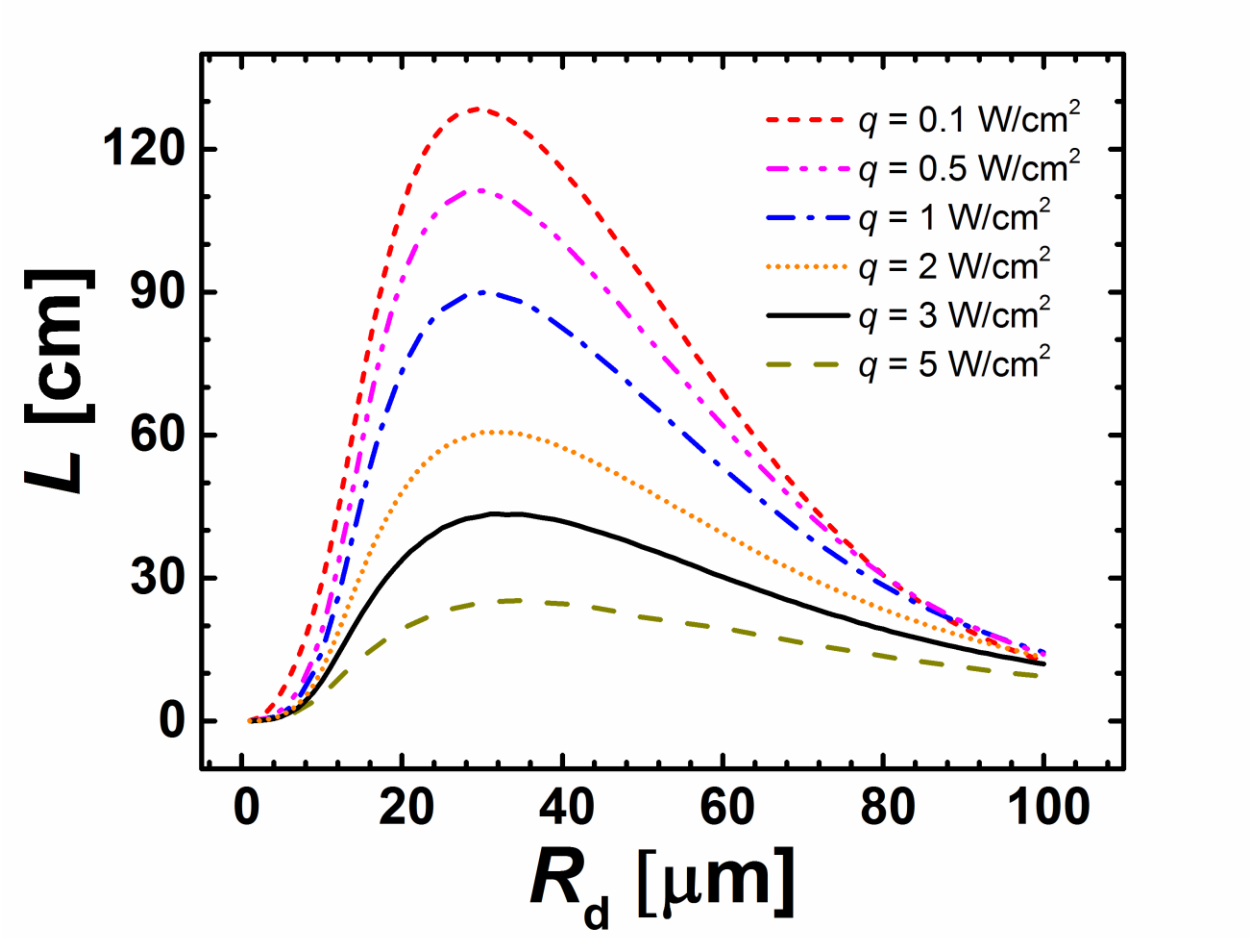

Figure 2.8. Droplet horizontal distance traveled ($\boldsymbol{L}$) as a function of jumping droplet radius ($\boldsymbol{R_d}$) for jumping upward against gravity, $\boldsymbol{U_f}$ = 20 m/s, 0.1 < $\boldsymbol{q}$ < 5 W/cm^2, and $\boldsymbol{x_0}$ = 10 cm. The results show that an optimal value of $\boldsymbol{R_d}$ exists capable of obtaining the maximum traveled length. In the small droplet regime ($\boldsymbol{R_d \to 0}$), droplets have reduced inertia and are sucked to the plate rapidly after jumping by the suction drag, resulting in a small travel length. In the large droplet regime ($\boldsymbol{R_d \to \infty}$), gravitational force dominates, resulting in rapid return of jumping droplet to the surface. In between the low and high droplet regimes, an optimal droplet size exists ($\boldsymbol{R_d} \approx 30$ μm) where the droplet strikes a balance between inertia, drag force, and adverse gravitational force. For the majority of droplets, the net effect of the increasing $\boldsymbol{q}$ is to decrease $\boldsymbol{L}$ due to increased suction drag force perpendicular to the surface. However, increased $\boldsymbol{q}$ can also increase $\boldsymbol{L}$ for specific conditions ($\boldsymbol{R_d}$ = 84 μm, 0.1 < $\boldsymbol{q}$ < 1 W/cm^2) as increased suction acts to bring faster moving fluid closer to the wall and enhance horizontal momentum transfer to the droplet.

forces in a and e. For the intermediate droplet size ($R_d = 50$ μm), the horizontal forces decline at a slower rate (c). The curves a, c and e are in general self-similar since the droplet experiences the same stages of flight. This behavior also applies to the vertical forces b, d and f. The Saffman lift force has a net effect of increasing the traveled distance as the greatest product of relative velocity

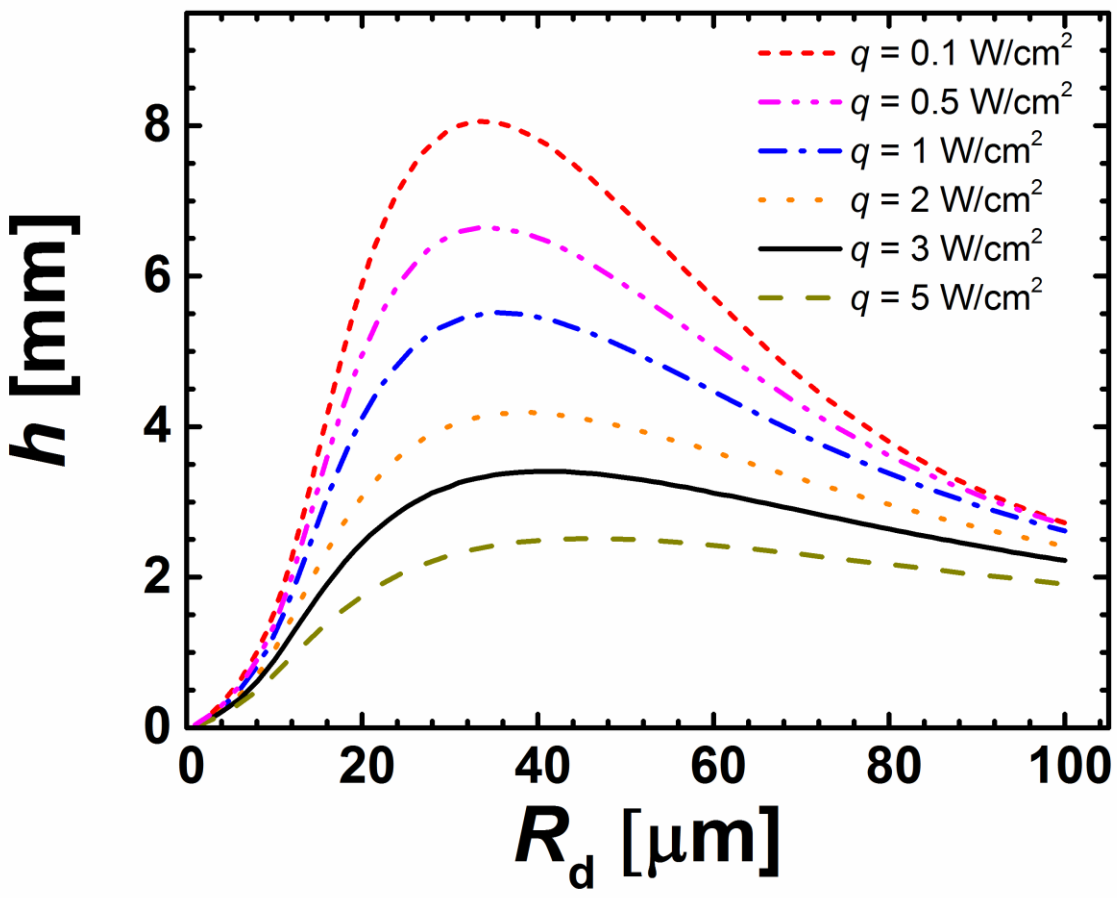

Figure 2.9. Jumping droplet height ($\boldsymbol{h}$) relative to the horizontal superhydrophobic surface as a function of droplet radius, $\boldsymbol{R_d}$ for a free stream velocity $\boldsymbol{U_f}$ = 20 m/s, initial jumping location of 10 cm from the leading edge of the plate, and condensation heat flux 0.1 < $\boldsymbol{q}$ < 5 W/cm^2. The behavior of small droplets ($\boldsymbol{R_d}$ < 10 μm) is dictated by their small inertia and the suction drag force despite the increased initial velocity with respect to larger droplets (Eq. 2.22), which results in the lowest jumping height. For large droplets ($\boldsymbol{R_d}$ > 60 μm), the smaller initial velocity and increased gravitational force result in low jumping heights. Within these asymptotic limits, an optimal droplet size exists ($\boldsymbol{R_d} \approx$ 30 μm) for which the jumping height is maximum.

and velocity gradient occurs during the first part (ascending from the plate) of the flight. However, the Saffman lift force is a surface force that has optimal performance for the intermediate-sized droplet.

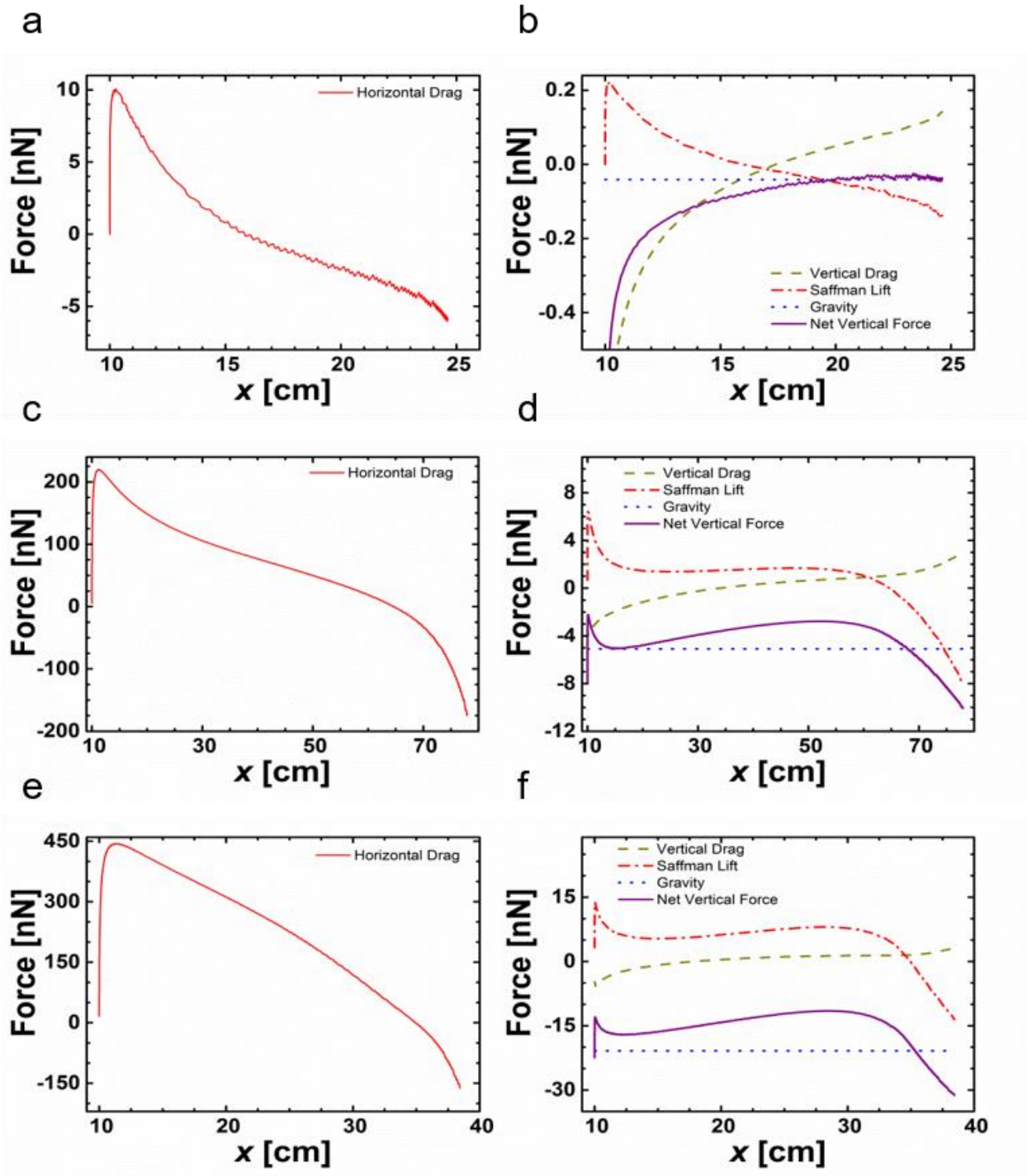

Figure 2.10. Forces acting on a droplet jumping from a horizontal plate during jumping-droplet condensation (q = 1 W/cm^2, U_f = 20 m/s, x_0 = 10 cm) as a function of the distance from the leading edge of the plate. (a) and (b) represent the horizontal (x-direction) and vertical (y-direction) forces on a 10 µm-radius droplet, respectively. (c) and (d) represent the horizontal and vertical forces on a 50 µm-radius droplet, respectively. (e) and (f) represent the horizontal and vertical forces on an 80 µm-radius droplet, respectively. For the horizontal direction (a, c and e), the drag force (projection of Eq.2. 15 on the x-axis) is the only force acting in the x-

direction. The results show that the horizontal drag on the droplets peak rapidly as the droplet jumps away from the surface to regions where the horizontal velocity of the flow is much larger than the horizontal velocity of the droplet (initially zero). As the droplet is accelerated, it reaches a the horizontal velocity of the flow, which reduces the net force to zero in the x-direction. Further downstream, as the droplet returns to the surface after reaching a horizontal velocity close to free stream conditions, the net relative velocity of the flow in the x-direction becomes negative, resulting in a net negative force that decelerates the droplet until it reaches the wall. For the vertical direction (b, d and f), the relevant forces include the vertical drag force (projection of Eq. 2.15 on the y-axis), the Saffman lift force (Eq. 2.17), and gravitational body force (Eq. 2.16). Vertical drag initially acts against the motion of the droplet (negative y-direction). As the droplet reaches the velocity of the vapor flow in the x-direction, the vertical force becomes zero due to the small relative vertical velocity. Further downstream, the velocity of the flow in the y-direction lags behind the negative velocity of the droplet that is being accelerated downwards as shown by the negative total net force. The Saffman lift force changes direction from positive to negative as the relative velocity between the flow and the droplet becomes negative. The shape of the horizontal velocity gradient as a function of distance is parabolic as the droplet climbs up and down the velocity profile, whereas the relative velocity decreases monotonically with distance, explaining the shape of the Saffman curve and the secondary peaks observed in d and f. Results a-f demonstrate that as the droplet increases in size (10 μm to 80 μm) the ratio of the average horizontal force to the average vertical force goes through a maximum (Figs. 2.8 and 2.9).

2.4.4. Effect of initial position along the plate

Due to the uniform rate of condensation along the plate, droplets do not only jump from the leading edge, hence it was important to analyze droplet trajectories initiating further down the flat plate where the flow field approach the asymptotic limit (Eq. 2.12). The effect of the starting position (x_0) of the droplet horizontal travel distance along the horizontal plate is shown in Fig. 2.11. As the jumping location approaches the leading edge (x_0 decreased from 50 cm to 0), the distance traveled increases by a factor up to 5 (for the case of U_f = 20 m/s and q = 1 W/cm^2). The enhanced travel distance can be explained by the change in the velocity profiles along the length of the plate in the developing region which affects the trajectory in a non-linearly fashion. It can be observed that the dependence on x_0 decays at large x_0 (> 50 cm) which is consistent with the development of the asymptotic velocity profile (Fig. 2.6). We note that as $x_0 \rightarrow 0$ the boundary layer equations

used (Eqns. 2.3 and 2.4) are no longer valid since the ratio of the boundary layer thickness to starting position is no longer much less than 1. As expected, lower condensation heat fluxes resulted in longer travel distances for all x_0 due to the lower suction drag force.

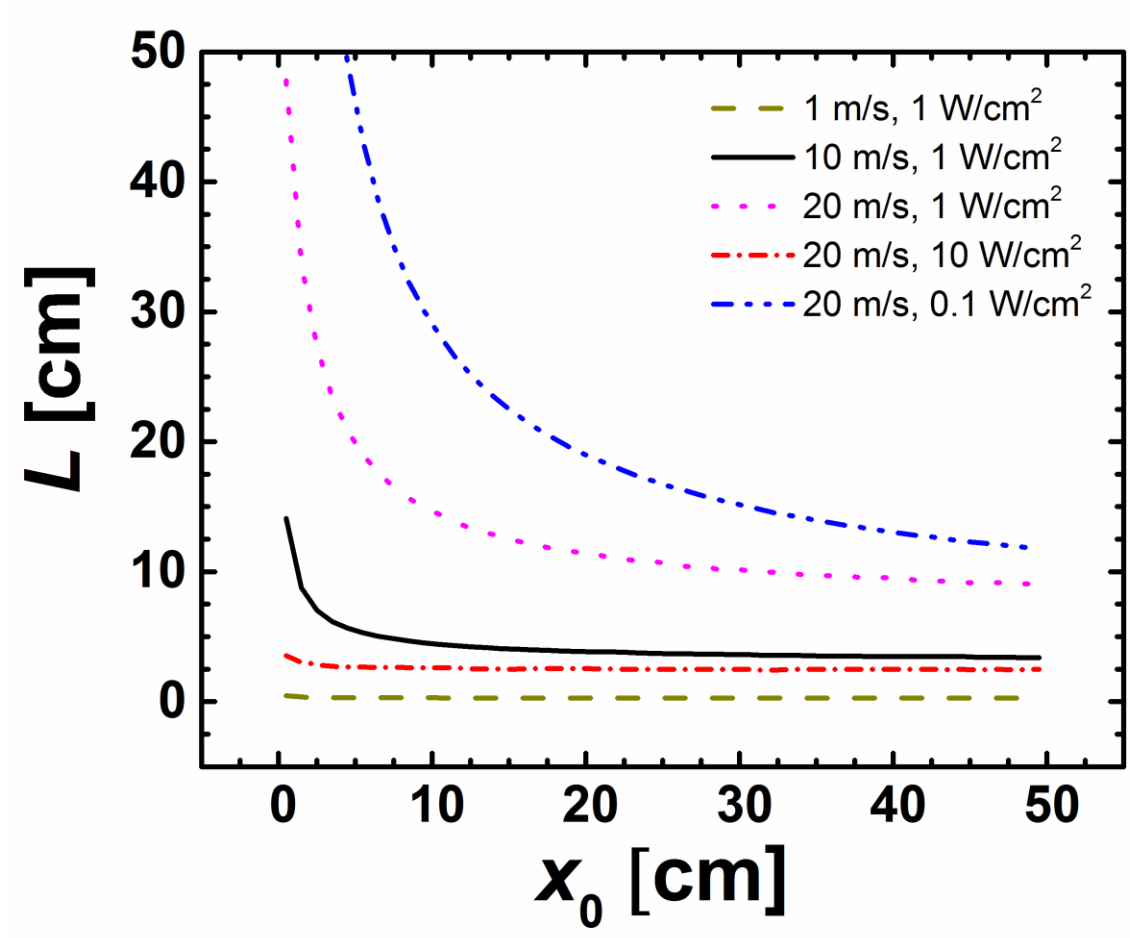

Figure 2.11. Droplet horizontal travel distance ($\boldsymbol{L}$) as a function of the initial jumping position ($\boldsymbol{x_0}$) along the horizontal plate for a 10 μm radius droplet jumping upward against gravity. The simulation results are obtained for a range of free stream velocities ($1 < \boldsymbol{U_f} < 20$ m/s) and condensation heat fluxes ($0.1 < \boldsymbol{q} < 10$ W/cm^2) that span the realistic parameter space. While the effect of the initial jumping position depends on the free stream velocity and condensation heat flux, for sufficiently large distances from the plate leading edge ($\boldsymbol{x_0} > 50$ cm), the hydrodynamic boundary layer becomes location independent as the boundary layer thickness and velocity profiles approach the asymptotic solution (Eq. 2.12, Fig.2.6).

2.4.5. Effect of free stream velocity

To study the effects of horizontal free stream velocity, and its effect on droplet trajectory, we computed the horizontal travel distance (Fig. 2.12) and jumping height (Fig. 2.13) for $1 < U_f < 30$ m/s, and $0.1 < q < 5$ W/cm^2. We observe a quadratic dependence of the free stream velocity on both the horizontal travel length and jumping height due to the quadratic drag force dependence (Eq. 2.15) on the free stream velocity. At increased heat fluxes, increased suction at the wall acts to shifts the curves down due to larger suction drag force towards the wall.

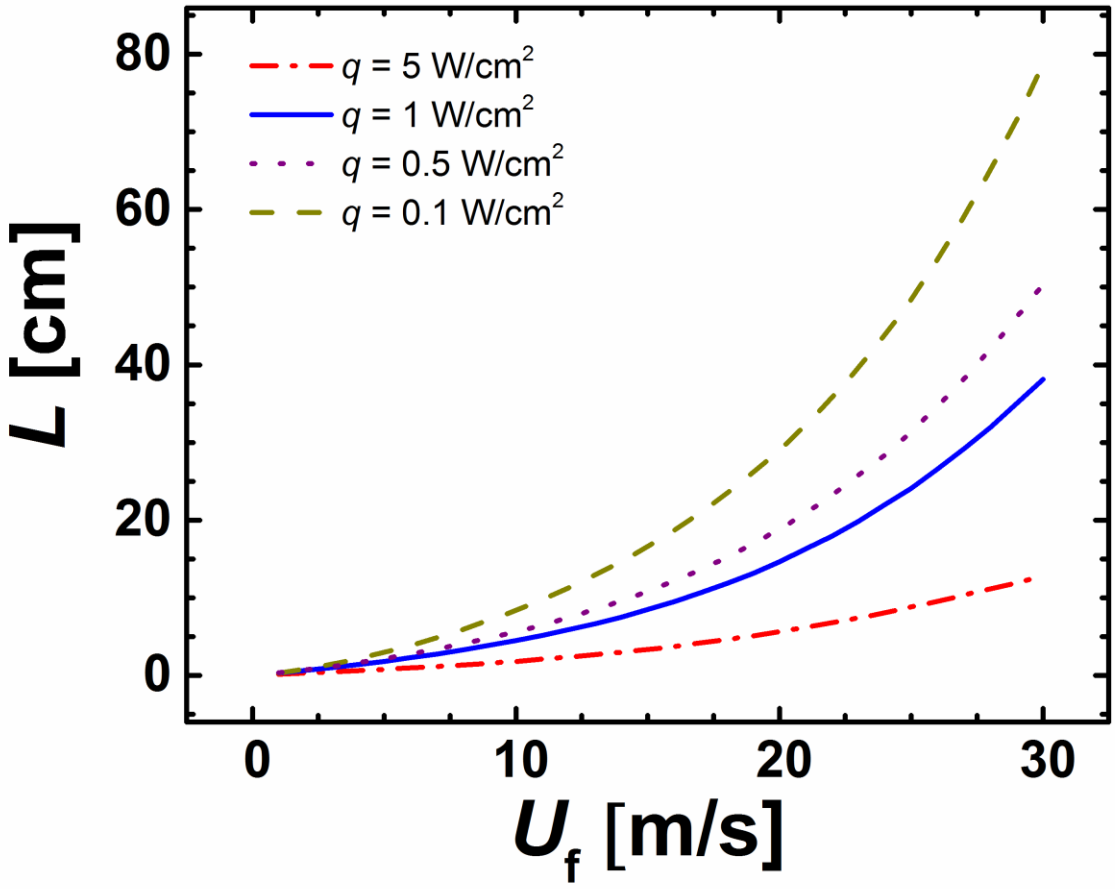

Figure 2.12. Droplet horizontal travel distance along the flat plate ($\boldsymbol{L}$) as a function of free stream velocity ($\boldsymbol{U_f}$) for a 10 μm radius droplet jumping upward against gravity at and $\boldsymbol{x_0}$ = 10 cm. The non-linear increase in $\boldsymbol{L}$ arises due to the increased horizontal drag at elevated $\boldsymbol{U_f}$. The net effect of increasing heat flux ($\boldsymbol{q}$) from 0.1 to 5 W/cm^2 decreases $\boldsymbol{L}$ due to the increased downward drag (~$\boldsymbol{R_d}$) exceeding the effect of the reduced boundary layer thickness and steeper velocity profiles (higher Saffman force) at elevated suction velocities.

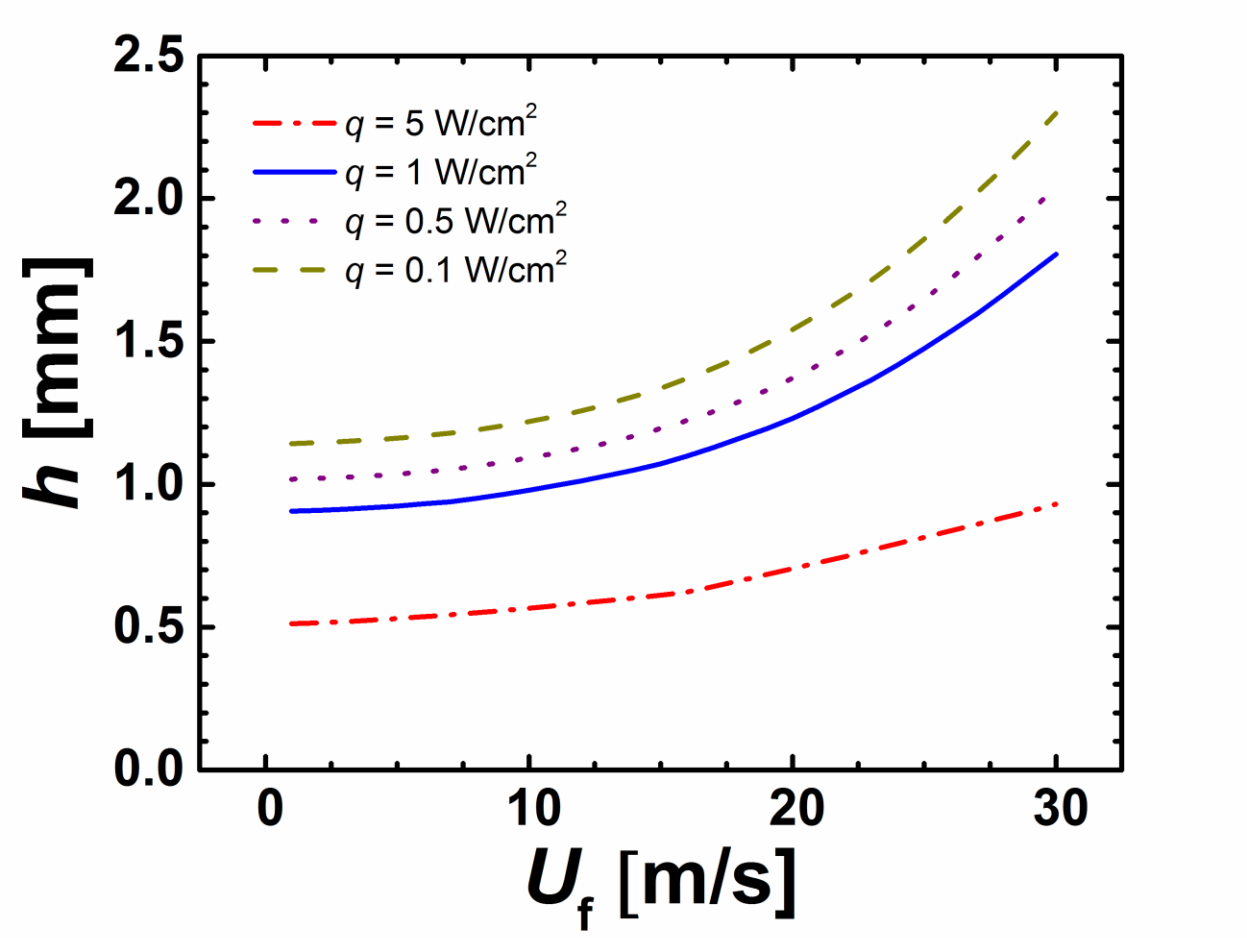

Figure 2.13. Droplet jumping height, $\boldsymbol{h}$, as a function of the free stream velocity, $\boldsymbol{U_f}$ for 0.1 < $\boldsymbol{q}$ < 5 W/cm^2 and $\boldsymbol{x_0}$ = 10 cm. As $\boldsymbol{U_f}$ increases, the velocity gradient in the boundary layer increases due to the no slip boundary condition at the wall, resulting in an increase in the Saffman lift force (Eq. 2.17). As the condensation heat flux increases, the vertical drag force on the droplet increases, resulting in lower jumping height.

2.4.6. Effect of plate inclination

Due to the fact that not all condensing surfaces are horizontal with the gravitational force directed normal towards the plate, we studied the effect of plate inclination, ψ (Fig. 2.2) on the droplet jumping dynamics. Figure 2.14 shows the case of droplets jumping downwards from a horizontal plate (ψ= 180°) for 10 μm < R_d < 50 μm. The results show that smaller droplets return to the

surface (R_d = 10 μm, R_d = 15 μm), while larger droplets (R_d = 20 μm, R_d = 50 μm) are completely removed from the plate. The effect of plate inclination has great sensitivity to the distance traveled, especially at radii where the fundamental forces approach one another in magnitude. As the droplet size increases from 10 to 15 μm, the distance traveled is increased from 30 cm to 200 cm. The results indicate that for certain plate orientations, surface engineering to favor the departure of larger droplets with higher gravitational body force, although detrimental to overall condensation heat transfer, is beneficial for the aversion of progressive flooding due to droplet return.

In the case of convective jumping-droplet condensation on inclined plates having orientation between the limits of right side up and upside down, we computed the travel distance as a function of the inclination angle (Fig. 2.15). As expected, the maximum travel length for 10 μm and 15 μm droplets occurs when droplets jump directly downwards ($\psi = 180°$) with gravity.

The sensitivity of the travel length to the inclination angle increases with increasing droplet radius due to the fact that inclination reflects the projection of gravity on the travel distance direction, which is increased as the droplet size increases. Intersection between curves of different droplet radii occurs due to the trade-off between optimal droplet size (Figs. 2.8 and 2.9) and inclination angle. The distance traveled by the droplet can span orders of magnitude as the plate is tilted, especially for $R_d > 15$ μm.

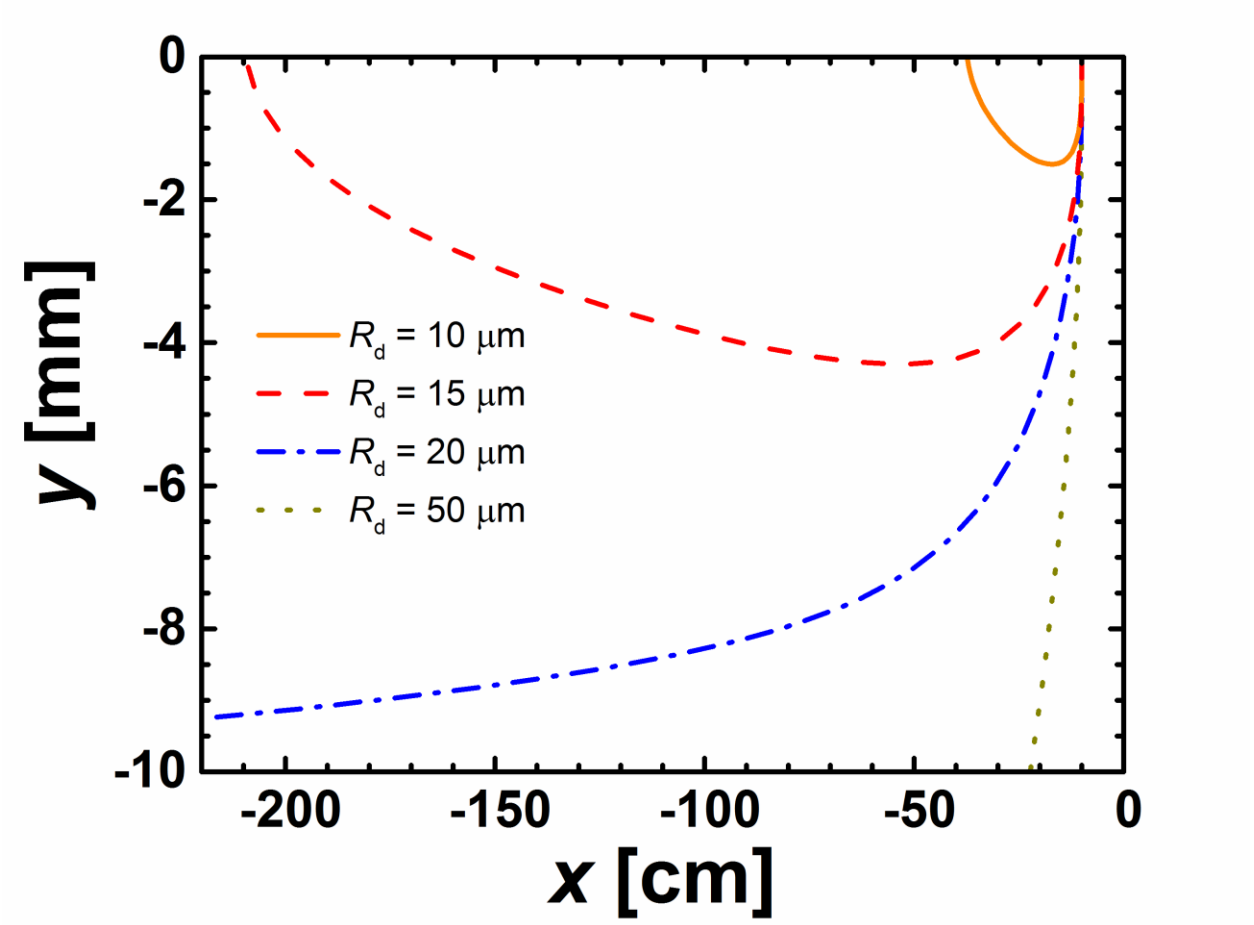

Figure 2.14. Droplet trajectories of 10, 15, 20 and 50 µm radii droplets jumping downward ($\boldsymbol{q}$ = 1 W/cm^2) on a horizontal superhydrophobic surface undergoing convective condensation ($\boldsymbol{U_f}$ = 20 m/s, vapor flow from right to left). The droplets jump initially perpendicular to the plate, 10 cm away from the leading edge. For these forced convection conditions, droplets having a radii larger than 19 µm leave the surface with no return.

Figure 2.15 shows that for larger droplets, there exists a critical inclination angle , ψ_{crit}, beyond which the droplet no longer return to the plate. Figure 2.16 shows ψ_{crit} as a function of the jumping droplet size, R_d. For R_d < 19 µm, ψ_{crit} is not defined as droplets always return to the surface. Note, this return threshold is valid for a heat flux of 1 W/cm^2 and will vary for differing heat fluxes as the vapor drag returning the droplet changes. For R_d > 19 µm, as the droplet size increases, ψ_{crit} decreases in absolute value demonstrating the effect of the increased projected gravitational pull along the inclined plate.

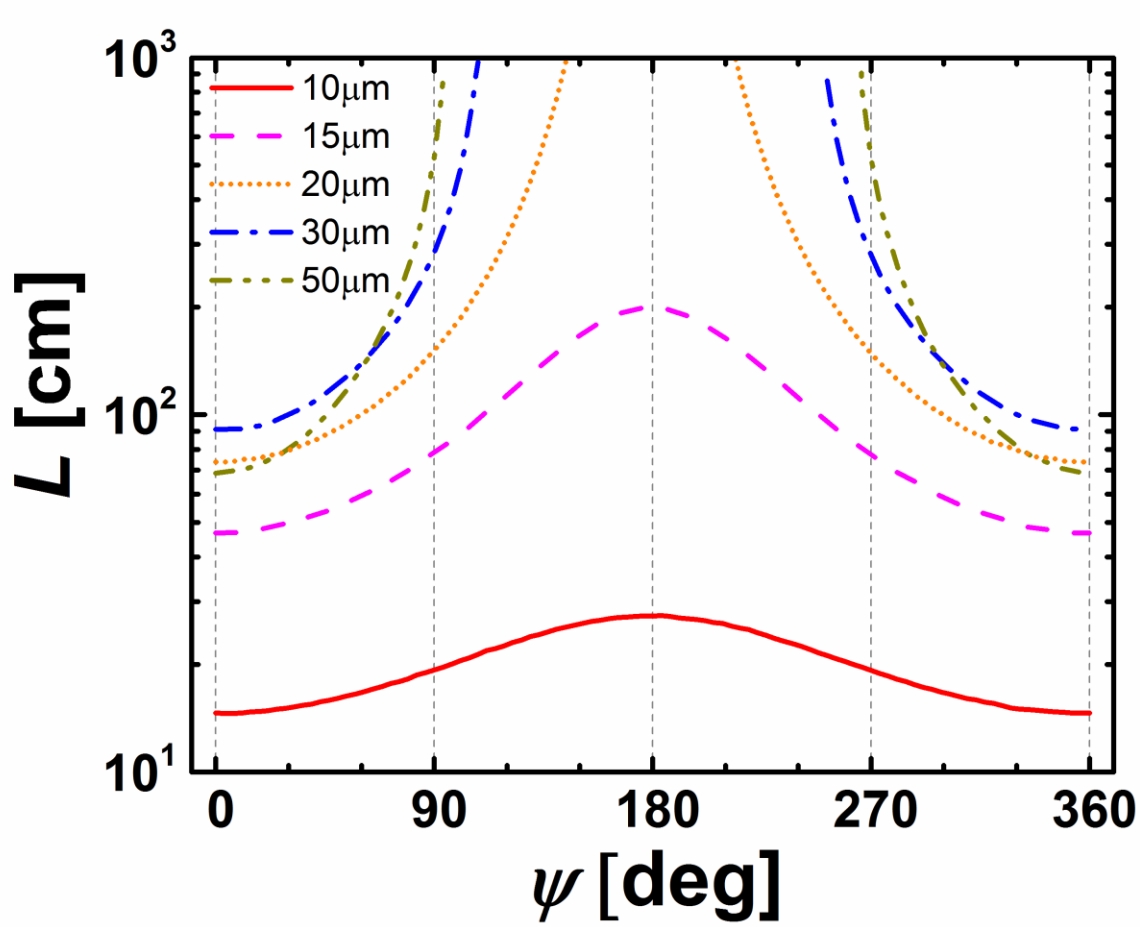

Figure 2.15. Effect of plate inclination angle $\boldsymbol{\psi}$ on the droplet travel length ($\boldsymbol{L}$) along the plate for 10, 30, and 50 μm radii droplets jumping perpendicular to the surface. $\boldsymbol{U_f}$ = 20 m/s, q = 1 W/cm^2, $\boldsymbol{x_0^1}$ = 10 cm. The sensitivity of the travel length to the inclination angle increases with increasing droplet radius due to the fact that inclination reflects the effect of gravity which is increased as the droplet size increases.

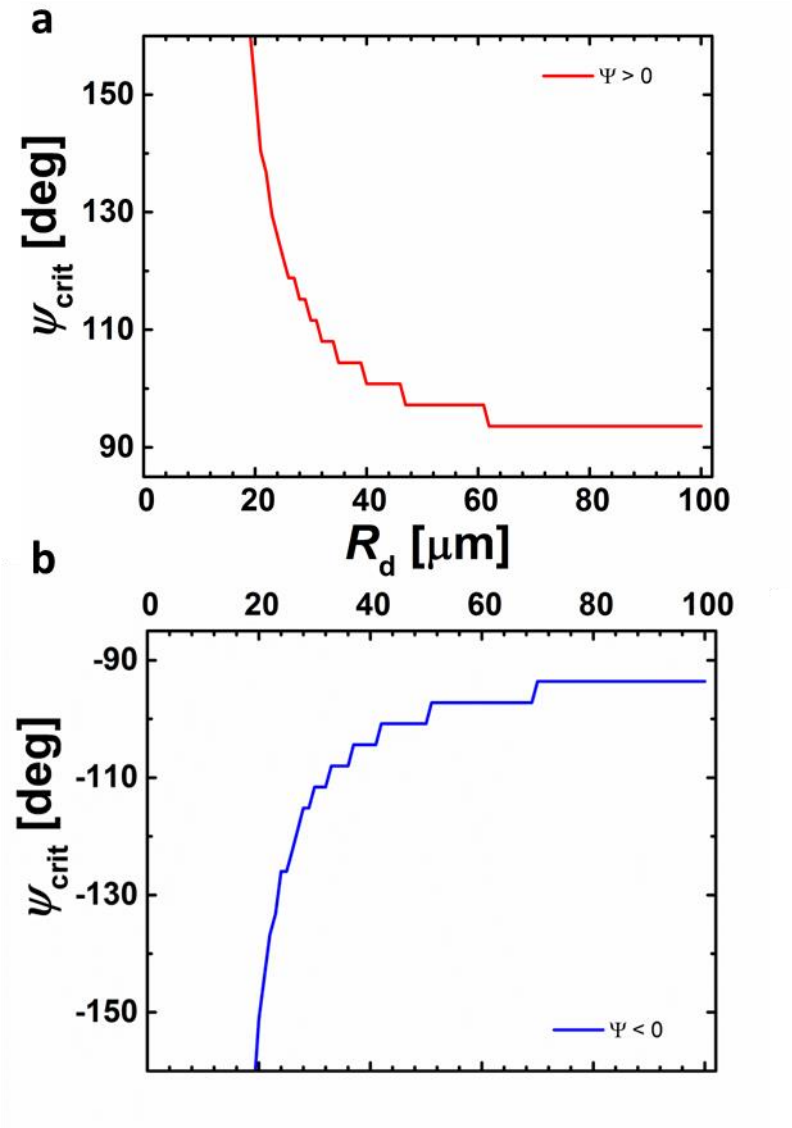

Figure 2.16. Critical angle of plate inclination ($\boldsymbol{\psi_{crit}}$) as a function of droplets radius (1 μm < $\boldsymbol{R_d}$ < 100 μm) jumping from the superhydrophobic surface with $\boldsymbol{U_f}$ = 20 m/s, $\boldsymbol{x_0^1}$ = 10 cm, and $\boldsymbol{q}$ = 1 W/cm^2. The critical angle, $\boldsymbol{\psi_{crit}}$, represents the angle beyond which the droplet does not return to surface for (a) counterclockwise plate rotation ($\boldsymbol{\psi}$ > 0) and (b) clockwise ($\boldsymbol{\psi}$ < 0) plate rotation (corresponding to $\boldsymbol{\psi}$ > 180° in Fig. 2.2). For $\boldsymbol{R_d}$ < 19 μm, $\boldsymbol{\psi_{crit}}$ is not defined as droplets always return to the surface. For $\boldsymbol{R_d}$ > 19 μm, as the droplet size increases, $\boldsymbol{\psi_{crit}}$ decreases in absolute value demonstrating the effect of the increased gravitational pull.

2.4.7. Force on the plate

To gain an understanding of the hydrodynamic forces on the condensing plate during convective jumping-droplet condensation, we computed the force on the plate per unit depth (F_p) acting on a distance d from a starting position of 10 cm away from the leading edge (Fig. 2.17). As expected,

higher condensation rates increase the force on the plate due to larger velocity gradients closer to the wall. The force increase can be as much as one order of magnitude when comparing the no-heat flux case (q = 0) to moderate heat fluxes (q = 5 W/cm^2). Verification of our calculations showed that the results for q = 0 are consistent with the analytical solution of the flow over a flat plate [76] ($\bar{\tau} = 0.664\rho_{\mathrm{v}}{U_{\mathrm{f}}}^2/{Re_{\mathrm{L}}}^{1/2}$), where $\bar{\tau}$ is the average shear stress on the plate.

To compare convective jumping-droplet condensation to state-of-the-art (SOA) condensation, we computed the equivalent laminar forced convection filmwise condensation skin friction coefficient on a horizontal plate [77, 78]. The force on the plate, $F_{\mathrm{p,film}}$ for SOA condensation is $\sim 10^3$ times larger than convective jumping-droplet condensation due to two main contributions. First, the ratio of liquid to vapor dynamic viscosities, μ_{l} and μ_{v} respectively, is $\mu_{\mathrm{l}}/\mu_{\mathrm{v}} \sim 10^2$. Second, we can think of the film boundary layer to be thinner than the vapor boundary layer for a given mass flow rate due to the large density difference between the two phases, leading to a higher velocity gradient at the wall for when boundary conditions on velocity do not differ much. It is important to note that our analysis is approximate due to the fact that the external vapor flow experiences additional resistance due to work done by the jumping droplets on the flow. The incorporation of droplet work will diminish the difference between the SOA and convective jumping-droplet condensation.

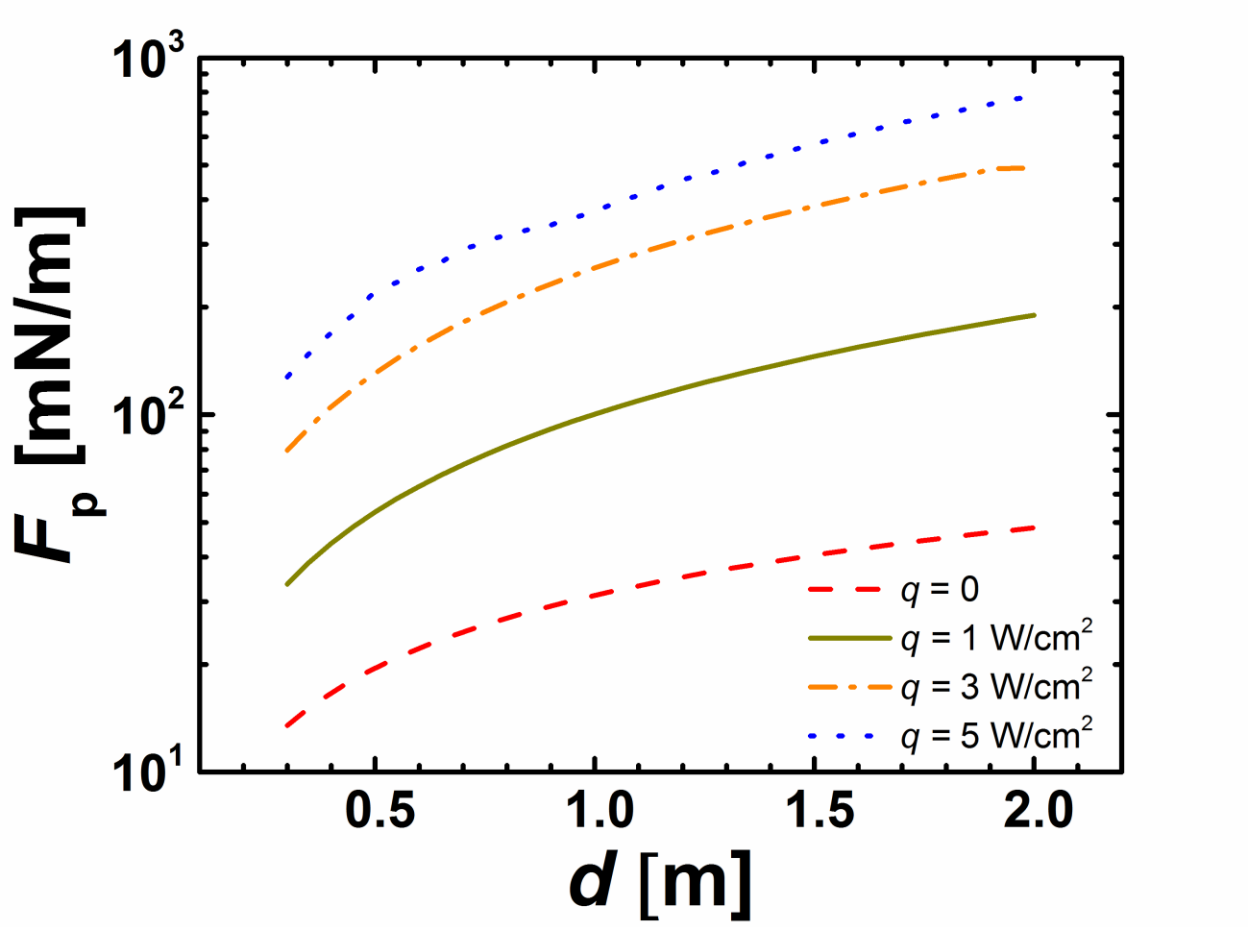

Figure 2.17. Shear force on the condenser plate per unit depth, $\boldsymbol{F_p}$, as a function of the distance $\boldsymbol{d}$ from a starting position of 10 cm from the leading edge. The heat flux, $\boldsymbol{q}$, is varied from 0 W/cm^2 (no suction case) to 5 W/cm^2. With increased suction, the horizontal velocity gradient at the wall is increased (thinner boundary layer), which increases the shear stress on the plate.

2.4.8. Multi-Hop Dynamics

Up to this point, the developed model has focused solely on the coupled dynamics between individual jumping droplets and the external saturated vapor flow. To gain a more holistic picture of the jumping droplet process in the presence of vapor flows, we must consider the effects of multi-hop droplet dynamics. Recent studies have shown that droplets departing from a jumping droplet surface, if returned, will in fact re-coalesce and jump again in a serial manner until they either pin to the surface at local defect sites, or become too large ($R_d \approx 250$ μm) to overcome the

gravitational body force acting on them. These multiple-jumping or multi-hop effects become crucial when estimating the total travel distance of individual droplets. To estimate the total multi-hop travel distance, we computed the distance traveled by the droplet after successive jumps until the droplet reaches a size where it is too heavy to jump (R_{d} = 250 μm). To more rigorously compute the droplet trajectory, we took into account the returning droplet momentum on the next droplet in x and y-direction just prior to jumping. Applying the conservation of linear momentum, the initial velocities of the i$^{\mathrm{th}}$ jump in the x and y- directions, $\left[u_{\mathrm{d},0}^{1}\right]_i$ and $\left[v_{\mathrm{d},0}^{1}\right]_i$ respectively, are modified from Eq. 2.22 with incorporated momentum of the previous droplet just prior to touching the surface (y =0.5 ± 0.1 mm).

$$\begin{aligned}\left[u_{\mathrm{d},0}^{1}\right]_{\mathrm{i}} &= \frac{1}{2}\left[u_{\mathrm{d,end}}^{1}\right]_{\mathrm{i}-1}. \\ \left[v_{\mathrm{d},0}^{1}\right]_{\mathrm{i}} &= 0.23\sqrt{\frac{\gamma}{\rho_{\mathrm{l}}[R_{\mathrm{d}}]_{\mathrm{i}}}} + \frac{1}{2}\left[v_{\mathrm{d,end}}^{1}\right]_{\mathrm{i}-1}.\end{aligned} \tag{27}$$

The ratio of $1/2$ results from the initial-to-next jumping event droplet mass ratio, $m_{\mathrm{i}-1}/m_{\mathrm{i}}$, assuming that coalescence happens between two equally sized droplets. The final x and y velocities of the returning droplet from the $(i-1)^{\mathrm{th}}$ jump are $\left[u_{\mathrm{d,end}}^{1}\right]_{\mathrm{i}-1}$ and $\frac{1}{2}\left[v_{\mathrm{d,end}}^{1}\right]_{\mathrm{i}-1}$, respectively, while $[R_{\mathrm{d}}]_{\mathrm{i}}$ represents the droplet radius of the current (i^{th}) jump. The velocities are expressed in the coordinate frame fixed to the plate (as shown by the superscript "1"). By conservation of mass, $[R_{\mathrm{d}}]_{\mathrm{i}} = 2^{1/3}[R_{\mathrm{d}}]_{\mathrm{i}-1}$.

Figure 2.18 depicts trajectories of droplets that initially jump with a radius $R_{\mathrm{d},0}$ and that are assumed to coalesce with droplets of the same size upon return prior to the next jump. The results clearly show that the combined trajectory (dashed lines) present a much larger effective traveled distance (~100 cm) when compared to individual droplet jumping lengths (~10 cm).

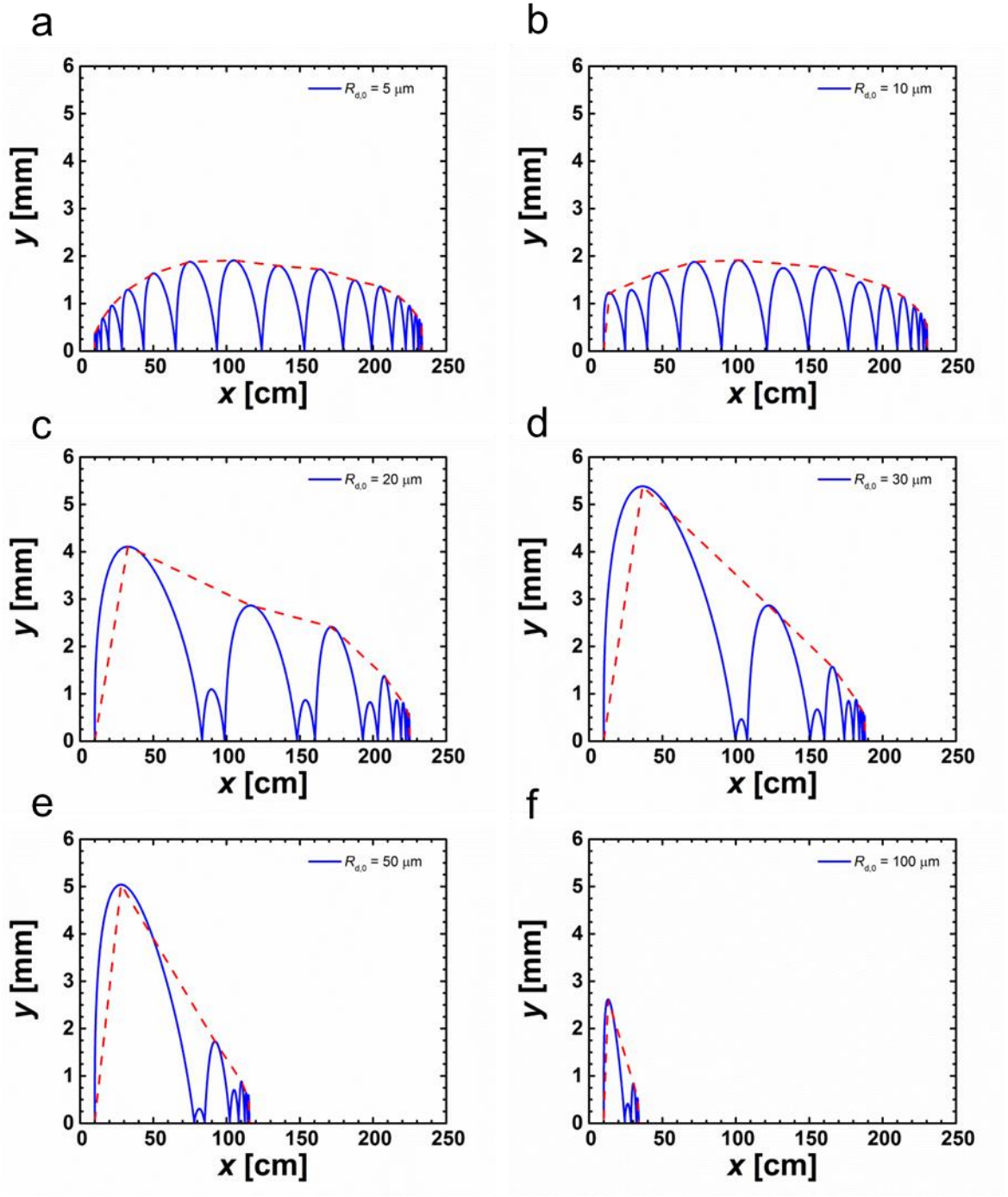

Figure 2.18. Successive jumps of droplets of different starting radius $\boldsymbol{R_{d,0}}$, on a horizontal plate ($\boldsymbol{\psi}$= 0) with $\boldsymbol{q}$ = 1 W/cm^2 , $\boldsymbol{U_f}$ = 20 m/s and $\boldsymbol{x_0^1}$ = $\boldsymbol{x_0}$= 10 cm. (a) $\boldsymbol{R_{d,0}}$ = 5 µm. (b) $\boldsymbol{R_{d,0}}$ = 10 µm. (c) $\boldsymbol{R_{d,0}}$ = 20 µm. (d) $\boldsymbol{R_{d,0}}$ = 30 µm. (e) $\boldsymbol{R_{d,0}}$ = 50 µm. (f) $\boldsymbol{R_{d,0}}$ = 100 µm. For all droplets, as observed in Eq. 2.27, two main parameters affect the behavior: the decrease in initial vertical velocity due to the momentum of the previous jump and the decrease in initial vertical velocity

due to the increased droplet size for the successive jump. For smaller droplets ($\boldsymbol{R_{d,0}}$ = 5 μm, $\boldsymbol{R_{d,0}}$ = 10 μm), these two effects nearly balance each other, without any large differences in consecutive jumps until the droplet becomes too heavy. For larger droplets, (20, 30, 50 and 100 μm), the negative momentum of the previous jump strongly affects the successive jump. The latter, because of the smaller jumping height (or flight time), has a sufficiently small final vertical velocity, hence negligibly impacts the successive jump. We can hence see alternating high and low jumps until the initial vertical velocity is decreased due to the large droplet size. The dashed lines show the effective trajectory of the droplet resulting from the successive jumps.

It is interesting to note that successive jumps with alternating low-high jumping heights has been observed before experimentally [79]. Although not as pronounced as in Figure 2.18c-f due to low condensation heat fluxes, the previous experiment offer an excellent verification of this interesting multi-hop alternating jumping behavior.

At elevated condensation heat fluxes (q > 0.1 W/cm^2), the larger suction velocity acts to bring faster moving fluid closer to the wall. The higher momentum at the wall results in larger momentum transfer to jumping droplets and longer overall multi-hop travel distance. Figure 2.19 shows the multi-hop droplet trajectory for three different condensation heat fluxes (q = 0.1, 0.5, and 1 W/cm^2). The velocity profiles have been overlaid as dashed lines to underscore the effect of suction of the horizontal velocity profile, which is the main factor affecting the total trajectory of the droplet. The results indicate that although higher condensation rates act to decrease individual droplet jumping height, multi-hop dynamics act to lengthen the overall droplet trajectory. It is important to note, the assumption used here of returning multi-hop droplets coalescing with identically sized droplets for each serial event is valid only for surface undergoing progressive flooding along the length of the condenser plate with gradually increasing droplet sizes. If the droplet distribution was uniform (≈10 μm), Eq. 2.27 would need to be altered to account for re-coalescence with constant sized droplets residing on the surface.

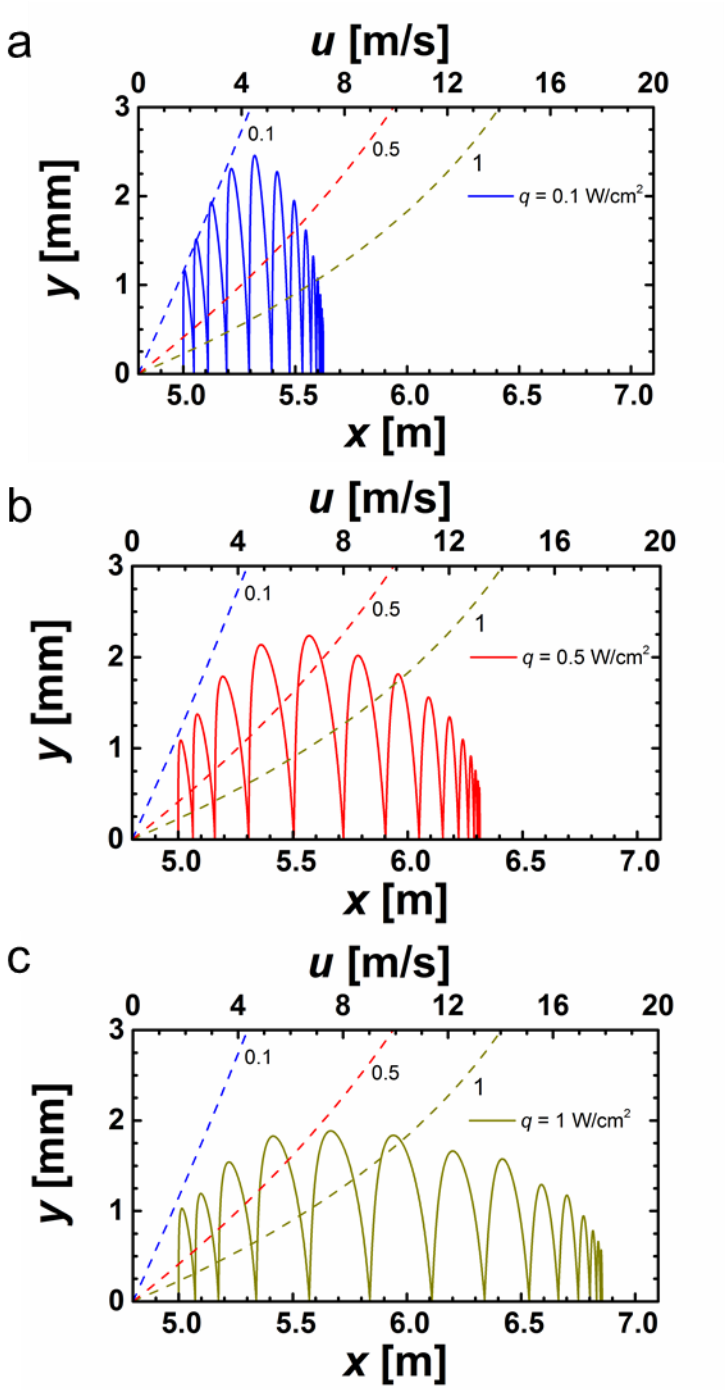

Figure 2.19. Effect of heat flux $\boldsymbol{q}$ on the multi-hop trajectory of a droplet initially jumping with a radius of 10 µm. (a) $\boldsymbol{q}$ = 0.1 W/cm^2. (b) $\boldsymbol{q}$ = 0.5 W/cm^2. (c) $\boldsymbol{q}$ = 1 W/cm^2. In order to mitigate the effects of the entrance region, the droplet is assumed to start jumping far from the leading edge ($\boldsymbol{x_0}$ = 5 m). The horizontal velocity ($\boldsymbol{u}$) profile is shown for all three cases of 0.1, 0.5 and 1 W/cm^2 in dashed lines, with the scale on the top axis, for a free stream velocity $\boldsymbol{U_f}$ = 20 m/s. It should be noted that these profiles are not the asymptotic profiles described by Eq. 2.12 because of the heat flux dependence of the entrance length.

2.5. Discussion

2.5.1. Heat Transfer Performance

Prior studies of jumping droplet condensation from quiescent saturated water vapor have shown heat transfer coefficients approaching ≈100 kW/m^{2}K. As previously developed for both dropwise and filmwise condensation [80, 81], the presence of forced vapor convection acts to enhance the condensed liquid removal mechanism and does little to enhance heat transfer due to single phase convection. The modeling results shown here indicate that convective jumping-droplet condensation has the potential to enhance droplet removal and prevent return to the surface for length scales approaching ~1 m. For efficient operation, the maximum droplet travel distance presents a geometric design guideline for the development of enhanced jumping droplet condensers. If condensers are larger than the maximum droplet travel distance, condensate accumulation at the end of the plate is possible, and the condenser becomes ineffective.

Future cases considering non-uniform condensation heat fluxes can be implemented using our model by discretizing the plate and solving for a stepwise varying heat flux, which is physically analogous to a larger number of condensing droplets per unit time emanating from the surface.

Furthermore, in the entrance region, where an acceleration of the vapor towards the surface exists, a pressure decrease occurs as we approach the wall. The decreased pressure corresponds to a decrease in vapor saturation temperature. However, this change of vapor pressure is negligible for the suction velocities considered (q < 1 W/cm^2), such that a negligible pressure and temperature gradient, and hence thermal boundary layer, exist.

It is important to note that although convective jumping-droplet condensation can delay progressive flooding, nucleation mediated flooding still poses a limitation to the outlined approach. The coupled dynamics of convective condensation with nucleation mediated flooding need to be

investigated as droplet shear of microscale Wenzel state droplets have been shown to induce droplet motion and result in enhanced flow condensation heat transfer [82].

2.5.2. Interpretation

The present work presents a comprehensive model for individual and multi-hop droplet trajectories and dynamics during convective condensation. Future models should make an effort to more holistically integrate multi-droplet events in the vapor flow. For example, individual droplet charging has the potential to separate droplets mid-flight and alter the droplet trajectories[43]. In addition, the presence of vigorous droplet jumping at elevated heat fluxes has the potential to disturb the laminar hydrodynamic boundary layer, and induce turbulence and mixing at reduced Reynolds numbers. Future models need to take this into account.

The use of convective jumping-droplet condensation has much potential to enhance the performance of condensation in the presence of non-condensable gases (NCGs). Much work has been done to show the importance of vapor flow and droplet shedding on condensation heat transfer enhancement in the presence of NCGs via boundary layer mixing [83-85]. In the future, a more comprehensive analysis is needed that can couple the hydrodynamic and concentration boundary layer equations in order to predict overall performance. In addition, even no-flow jumping droplet condensation presents an opportunity to enhance condensation in the presence of NCGs due to the potential for significant boundary layer mixing created by high-frequency droplet jumping. The outlined convective jumping-droplet condensation approach therefore has high promise for applications such as water harvesting, desalination or dehumidification, where the relative driving potential for condensation is low and NCGs are present [86].

The analysis outlined here presents a stepping stone for the development of more advanced models which are representative of more complex condenser geometries. In the future, it would be interesting to extend the developed external flow model to more advanced surface topologies such as tubes or parallel fins, where surface-surface interactions may dominate droplet trajectory and vapor flow dynamics. Furthermore, the present analysis provides a modeling methodology capable of extension to internal condensing flows commonly seen in air-cooled condensers. This work provides quantitative guidelines for future experimental measurements of droplet trajectories in a convective vapor flow.

2.6. Conclusions

We have developed a comprehensive physical model of external convective jumping-droplet condensation a flat plate. A boundary layer approach was used to model the vapor flow over the plate with condensation modeled as a suction at the wall. The jumping droplet trajectories were simulated accounting for the Saffman lift force of the shear flow. Using our model, we showed that the distance traveled by the droplets can range from millimeters to meters whereas the jumping height was less than a centimeter for the parameters considered. The results indicated that a delicate balance between drag, lift and gravitational force leads to optimum trajectories in terms of both height and distance traveled for a droplet radius of ≈ 30 μm. Increasing condensation heat flux acts to shortens the trajectory of the droplet as it leads to an increased suction, however it can have the opposite effect for very small ($\sim$1 μm) or very big droplets ($\sim$100 μm) as it can cause a downward shift of the horizontal velocity profile and greater transverse momentum transfer. Using our individual droplet model, we then incorporated multi-hop jumping, showing that multi-hop jumping droplet condensation has the potential to increase the total travel distances along the plate

by a factor of 10X. The present analysis outlines a condensation methodology to delay progressive flowing and enable the steady heat transfer coefficients of >100 kW/m^2K at low supersaturations. The findings presented here have significant relevance to the applications of convective jumping-droplet condensation for efficient phase change heat transfer applications. Furthermore, the developed boundary layer based modeling approach presents a design framework for future models and designs of jumping droplet condensers having more complex geometries, flow conditions, and heat fluxes.

2.7. References

[2.1] D. Kashchiev, Nucleation : basic theory with applications, Butterworth Heinemann, Oxford ; Boston, 2000.
[2.2] W. Nusselt, The surface condensation of water vapour., Zeitschrift Des Vereines Deutscher Ingenieure, 60 (1916) 541-546.
[2.3] E. Schmidt, W. Schurig, W. Sellschopp, Condensation of water vapour in film- and drop form, Zeitschrift Des Vereines Deutscher Ingenieure, 74 (1930) 544-544.
[2.4] N. Miljkovic, R. Enright, Y. Nam, K. Lopez, N. Dou, J. Sack, E.N. Wang, Jumping-droplet-enhanced condensation on scalable superhydrophobic nanostructured surfaces, Nano Lett, 13(1) (2013) 179-187.
[2.5] J.B. Boreyko, C.H. Chen, Self-Propelled Dropwise Condensate on Superhydrophobic Surfaces, Phys Rev Lett, 103(18) (2009) 184501.
[2.6] R. Enright, N. Miljkovic, J. Sprittles, K. Nolan, R. Mitchell, E.N. Wang, How Coalescing Droplets Jump, ACS Nano, 8(10) (2014) 10352-10362.
[2.7] F.J. Liu, G. Ghigliotti, J.J. Feng, C.H. Chen, Numerical simulations of self-propelled jumping upon drop coalescence on non-wetting surfaces, J Fluid Mech, 752 (2014) 39-65.
[2.8] F.J. Liu, G. Ghigliotti, J.J. Feng, C.H. Chen, Self-propelled jumping upon drop coalescence on Leidenfrost surfaces, J Fluid Mech, 752 (2014) 22-38.
[2.9] Y. Nam, H. Kim, S. Shin, Energy and hydrodynamic analyses of coalescence-induced jumping droplets, Appl Phys Lett, 103(16) (2013).
[2.10] Y. Nam, D. Seo, C. Lee, S. Shin, Droplet coalescence on water repellant surfaces, Soft Matter, 11(1) (2015) 154-160.
[2.11] J.W. Rose, Dropwise condensation theory and experiment: a review, P I Mech Eng a-J Pow, 216(A2) (2002) 115-128.
[2.12] E. Schmidt, W. Schurig, W. Sellschopp, Versuche über die Kondensation von Wasserdampf in Film- und Tropfenform, Forsch. Ingenieurwes, 1(2) (1930) 53–63.
[2.13] E.J. Le Fevre, J.W. Rose, Heat-Transfer Measurements During Dropwise Condensation of Steam, International Journal of Heat and Mass Transfer, 7 (1964) 272-273.

[2.14] E.J. Le Fevre, J.W. Rose, A Theory af Heat Transfer by Dropwise Condensation, in: Proceedings of the Third International Heat Transfer Conference, ASME, Chicago, IL, 1966, pp. 362-375.
[2.15] J.L. McCormick, E. Baer, On Mechanism of Heat Transfer in Dropwise Condensation, J Coll Sci Imp U Tok, 18(3) (1963) 208-216.
[2.16] B.B. Mikic, On Mechanism of Dropwise Condensation, International Journal of Heat and Mass Transfer, 12 (1969) 1311-1323.
[2.17] D.W. Tanner, D. Pope, C.J. Potter, D. West, Heat Transfer in Dropwise Condensation, International Journal of Heat and Mass Transfer, 8 (1965) 427-436.
[2.18] A. Umur, P. Griffith, Mechanism of Dropwise Condensation, J Heat Transf, 87(2) (1965) 275–282.
[2.19] W.H. Wu, J.R. Maa, On the Heat Transfer in Dropwise Condensation, Chemical Engineering Journal, 12(3) (1976) 225–231.
[2.20] S. Kim, K.J. Kim, Dropwise Condensation Modeling Suitable for Superhydrophobic Surfaces, J Heat Transf, 133(8) (2011) 081502.
[2.21] X. Chen, J. Wu, R. Ma, M. Hua, N. Koratkar, S. Yao, Z. Wang, Nanograssed Micropyramidal Architectures for Continuous Dropwise Condensation, Advanced Functional Materials, 21 (2011) 4617–4623.
[2.22] J. Feng, Y. Pang, Z. Qin, R. Ma, S. Yao, Why Condensate Drops Can Spontaneously Move Away on Some Superhydrophobic Surfaces but Not on Others, ACS Applied Materials & Interfaces, 4 (2012) 6618−6625.
[2.23] J. Feng, Z.Q. Qin, S.H. Yao, Factors Affecting the Spontaneous Motion of Condensate Drops on Superhydrophobic Copper Surfaces, Langmuir, 28(14) (2012) 6067-6075.
[2.24] C.J. Lv, P.F. Hao, Z.H. Yao, Y. Song, X.W. Zhang, F. He, Condensation and jumping relay of droplets on lotus leaf, Appl Phys Lett, 103 (2013) 021601.
[2.25] K. Rykaczewski, Microdroplet Growth Mechanism during Water Condensation on Superhydrophobic Surfaces, Langmuir, 28(20) (2012) 7720-7729.
[2.26] K. Rykaczewski, W.A. Osborn, J. Chinn, M.L. Walker, J.H.J. Scott, W. Jones, C. Hao, S. Yaod, Z. Wang, How nanorough is rough enough to make a surface superhydrophobic during water condensation?, Soft Matter, 8 (2012) 8786-8794.
[2.27] J. Tian, J. Zhu, H.Y. Guo, J. Li, X.Q. Feng, X.F. Gao, Efficient Self-Propelling of Small-Scale Condensed Microdrops by Closely Packed ZnO Nanoneedles, J Phys Chem Lett, 5(12) (2014) 2084-2088.
[2.28] M. McCarthy, K. Gerasopoulos, S.C. Maroo, A.J. Hart, Materials, Fabrication, and Manufacturing of Micro/Nanostructured Surfaces for Phase-Change Heat Transfer Enhancement, Nanosc Microsc Therm, 18(3) (2014) 288-310.
[2.29] G.Q. Li, M.H. Alhosani, S.J. Yuan, H.R. Liu, A. Al Ghaferi, T.J. Zhang, Microscopic Droplet Formation and Energy Transport Analysis of Condensation on Scalable Superhydrophobic Nanostructured Copper Oxide Surfaces, Langmuir, 30(48) (2014) 14498-14511.
[2.30] K. Yanagisawa, M. Sakai, T. Isobe, S. Matsushita, A. Nakajima, Investigation of droplet jumping on superhydrophobic coatings during dew condensation by the observation from two directions, Appl Surf Sci, 315 (2014) 212-221.
[2.31] C.W. Lo, C.C. Wang, M.C. Lu, Scale Effect on Dropwise Condensation on Superhydrophobic Surfaces, ACS Applied Materials & Interfaces, 6(16) (2014) 14353-14359.

[2.32] K.M. Wisdom, J.A. Watson, X. Qua, F. Liua, G.S. Watson, C.H. Chen, Self-cleaning of superhydrophobic surfaces by self-propelled jumping condensate, Proceedings of the National Academy of Sciences of the United States of America, 110(20) (2013) 7992–7997.
[2.33] G.S. Watson, L. Schwarzkopf, B.W. Cribb, S. Myhra, M. Gellender, J.A. Watson, Removal mechanisms of dew via self-propulsion off the gecko skin, J R Soc Interface, 12(105) (2015).
[2.34] G.S. Watson, M. Gellender, J.A. Watson, Self-propulsion of dew drops on lotus leaves: a potential mechanism for self cleaning, Biofouling, 30(4) (2014) 427-434.
[2.35] J.B. Boreyko, Y.J. Zhao, C.H. Chen, Planar jumping-drop thermal diodes, Appl Phys Lett, 99(23) (2011) 234105.
[2.36] J.B. Boreyko, P.C. Collier, Delayed Frost Growth on Jumping-Drop Superhydrophobic Surfaces, Acs Nano, 7(2) (2013) 1618-1627.
[2.37] X.M. Chen, R.Y. Ma, H.B. Zhou, X.F. Zhou, L.F. Che, S.H. Yao, Z.K. Wang, Activating the Microscale Edge Effect in a Hierarchical Surface for Frosting Suppression and Defrosting Promotion, Sci Rep-Uk, 3 (2013).
[2.38] J.Y. Lv, Y.L. Song, L. Jiang, J.J. Wang, Bio-Inspired Strategies for Anti-Icing, ACS Nano, 8(4) (2014) 3152-3169.
[2.39] Q.L. Zhang, M. He, J. Chen, J.J. Wang, Y.L. Song, L. Jiang, Anti-icing surfaces based on enhanced self-propelled jumping of condensed water microdroplets, Chem Commun, 49(40) (2013) 4516-4518.
[2.40] J.B. Boreyko, C.H. Chen, Vapor chambers with jumping-drop liquid return from superhydrophobic condensers, International Journal of Heat and Mass Transfer, 61 (2013) 409-418.
[2.41] D.J. Preston, N. Miljkovic, R. Enright, E.N. Wang, Jumping Droplet Electrostatic Charging and Effect on Vapor Drag, J Heat Trans-T Asme, 136(8) (2014).
[2.42] N. Miljkovic, D.J. Preston, R. Enright, E.N. Wang, Jumping-droplet electrostatic energy harvesting, Appl Phys Lett, 105(1) (2014).
[2.43] N. Miljkovic, D.J. Preston, R. Enright, E.N. Wang, Electrostatic charging of jumping droplets, Nat Commun, 4 (2013).
[2.44] R. Enright, N. Miljkovic, J.L. Alvarado, K. Kim, J.W. Rose, Dropwise Condensation on Micro- and Nanostructured Surfaces, Nanosc Microsc Therm, 18(3) (2014) 223-250.
[2.45] N. Miljkovic, E.N. Wang, Condensation heat transfer on superhydrophobic surfaces, Mrs Bull, 38(5) (2013) 397-406.
[2.46] R. Enright, N. Miljkovic, N. Dou, Y. Nam, E.N. Wang, Condensation on Superhydrophobic Copper Oxide Nanostructures, J Heat Transf, 135(9) (2013) 091304.
[2.47] N. Miljkovic, R. Enright, E.N. Wang, Effect of Droplet Morphology on Growth Dynamics and Heat Transfer during Condensation on Superhydrophobic Nanostructured Surfaces, Acs Nano, 6(2) (2012) 1776–1785.
[2.48] N. Miljkovic, R. Enright, E.N. Wang, Growth Dynamics During Dropwise Condensation on Nanostructured Superhydrophobic Surfaces, 3rd Micro/Nanoscale Heat & Mass Transfer International Conference, (2012).
[2.49] N. Miljkovic, R. Enright, E.N. Wang, Modeling and Optimization of Condensation Heat Transfer on Micro and Nanostructured Superhydrophobic Surfaces, J Heat Transf, (2013) doi: 10.1115/1111.4024597.
[2.50] J. Cheng, A. Vandadi, C.L. Chen, Condensation heat transfer on two-tier superhydrophobic surfaces, Appl Phys Lett, 101 (2012) 131909-131901 - 131909-131904.

[2.51] E. Olceroglu, C.Y. Hsieh, M.M. Rahman, K.K.S. Lau, M. McCarthy, Full-Field Dynamic Characterization of Superhydrophobic Condensation on Biotemplated Nanostructured Surfaces, Langmuir, 30(25) (2014) 7556-7566.
[2.52] E. Olceroglu, S.M. King, M.M. Rahman, M. McCarthy, Biotemplated Superhydrophobic Surfaces for Enhanced Dropwise Condensation, Proceedings of the Asme International Mechanical Engineering Congress and Exposition - 2012, Vol 7, Pts a-D, (2013) 2809-2815.
[2.53] D. Attinger, C. Frankiewicz, A.R. Betz, T.M. Schutzius, R. Ganguly, A. Das, C.-J. Kim, C.M. Megaridis, Surface engineering for phase change heat transfer: A review, MRS Energy & Sustainability, 1 (2014).
[2.54] X.M. Chen, J.A. Weibel, S.V. Garimella, Exploiting Microscale Roughness on Hierarchical Superhydrophobic Copper Surfaces for Enhanced Dropwise Condensation, Adv Mater Interfaces, 2(3) (2015).
[2.55] Y.M. Hou, M. Yu, X.M. Chen, Z.K. Wang, S.H. Yao, Recurrent Filmwise and Dropwise Condensation on a Beetle Mimetic Surface, ACS Nano, 9(1) (2015) 71-81.
[2.56] N. Miljkovic, R. Enright, Y. Nam, K. Lopez, N. Dou, J. Sack, E.N. Wang, Jumping-Droplet-Enhanced Condensation on Scalable Superhydrophobic Nanostructured Surfaces, Nano Letters, 13(1) (2013) 179-187.
[2.57] C.J. Lv, P.F. Hao, Z.H. Yao, F.L. Niu, Departure of Condensation Droplets on Superhydrophobic Surfaces, Langmuir, 31(8) (2015) 2414-2420.
[2.58] K. Rykaczewski, A.T. Paxson, S. Anand, X. Chen, Z. Wang, K.K. Varanasi, Multimode Multidrop Serial Coalescence Effects during Condensation on Hierarchical Superhydrophobic Surfaces, Langmuir, 29(3) (2013) 881–891.
[2.59] N. Miljkovic, D.J. Preston, R. Enright, E.N. Wang, Electric-Field-Enhanced Condensation on Superhydrophobic Nanostructured Surfaces, ACS Nano, 7(12) (2013) 11043-11054.
[2.60] B. Thwaites, An Exact Solution of the Boundary-layer Equations Under Particular Conditions of Porous Surface Suction, 2241, National Physical Laboratory (NPL), United Kingdom, London, United Kingdom, 1946.
[2.61] J. Stoer, R. Bulirsch, Introduction to numerical analysis, 3rd ed., Springer, New York, 2002.
[2.62] H. Schlichting, K. Gersten, Boundary-layer theory, 8th rev. and enl. ed., Springer, Berlin ; New York, 2000.
[2.63] P.G. Saffman, Lift on a Small Sphere in a Slow Shear Flow, J Fluid Mech, 22 (1965) 385-&.
[2.64] H.A. Stone, Philip Saffman and viscous flow theory, J Fluid Mech, 409 (2000) 165-183.
[2.65] F.M. White, Fluid mechanics, 6th ed., McGraw-Hill, New York, 2008.
[2.66] F.A. Morrison, Data Correlation for Drag Coefficient for Sphere, Michigan Technological University, Houghton Michigan, 2013.
[2.67] R. Mei, An Approximate Expression for the Shear Lift Force on a Spherical-Particle at Finite Reynolds-Number, Int J Multiphas Flow, 18(1) (1992) 145-147.
[2.68] H.Y. Kim, H.J. Lee, B.H. Kang, Sliding of liquid drops down an inclined solid surface, J Colloid Interf Sci, 247(2) (2002) 372-380.
[2.69] P. Dimitrakopoulos, J.J.L. Higdon, On the gravitational displacement of three-dimensional fluid droplets from inclined solid surfaces, J Fluid Mech, 395 (1999) 181-209.
[2.70] J.M.C. H. Cha, J. Sotelo, N. Miljkovic, Focal Plane Shift Imaging for the Analysis of Dynamic Wetting Processes, ACS Nano, (2016).
[2.71] The Water-Energy Nexus: Challenges and Opportunities, U.S. Department of Energy, 2014.

[2.72] Estimating Freshwater Needs to Meet Future Thermoelectric Generation, National Energy Technology Laboratory, 2011.
[2.73] Water for Energy - Advanced Dry Cooling for Power Plants, in, NSF/EPRI, 2013.
[2.74] B. Owens, The Rise Of Distributed Power, General Electric, 2014.
[2.75] P. Birbarah, Z.E. Li, A. Pauls, N. Miljkovic, A Comprehensive Model of Electric-Field-Enhanced Jumping-Droplet Condensation on Superhydrophobic Surfaces, Langmuir, 31(28) (2015) 7885-7896.
[2.76] P.K. Kundu, I.M. Cohen, D.R. Dowling, Fluid mechanics, 5th ed., Academic Press, Waltham, MA, 2012.
[2.77] J.C.Y. KOH, Film Condensation in a Forced-Convection Boundary-Layer Flow, International Journal of Heat and Mass Transfer, 5(10) (1962) 941-954.
[2.78] R.D. Cess, Laminar-Film Condensation on a Flat Plate in the Absence of a Body Force, Zeitschrift fur angewandte Mathematik und Physik ZAMP, 11(5) (1960) 426-433.
[2.79] D.P. N. Miljkovic, R. Enright, E. Wang, Dynamics of Coalescence-Induced Jumping Water Droplets, in: arXiv.org, Cornell University Library, 2013.
[2.80] J.G. Collier, J.R. Thome, Convective boiling and condensation, 3rd ed., Clarendon Press ;

Oxford University Press, OxfordNew York, 1994.

[2.81] J.W. Rose, Condensation heat transfer fundamentals, Chem Eng Res Des, 76(A2) (1998) 143-152.
[2.82] D. Torresin, M.K. Tiwari, D. Del Col, D. Poulikakos, Flow Condensation on Copper-Based Nanotextured Superhydrophobic Surfaces, Langmuir, 29(2) (2013) 840-848.
[2.83] X.H. Ma, X.D. Zhou, Z. Lan, Y.M. Li, Y. Zhang, Condensation heat transfer enhancement in the presence of non-condensable gas using the interfacial effect of dropwise condensation, International Journal of Heat and Mass Transfer, 51(7-8) (2008) 1728-1737.
[2.84] J.W. Rose, Approximate Equations for Forced-Convection Condensation in the Presence of a Non-Condensing Gas on a Flat-Plate and Horizontal Tube, International Journal of Heat and Mass Transfer, 23(4) (1980) 539-546.
[2.85] N.K. Maheshwari, D. Saha, R.K. Sinha, M. Aritomi, Investigation on condensation in presence of a noncondensable gas for a wide range of Reynolds number, Nucl Eng Des, 227(2) (2004) 219-238.
[2.86] G.P. Thiel, J.H. Lienhard, Entropy generation in condensation in the presence of high concentrations of noncondensable gases, International Journal of Heat and Mass Transfer, 55(19-20) (2012) 5133-5147.

Chapter 3- Internal Convective Jumping Droplet Condensation

3.1. Introduction

Water vapor condensation is an important industrial and natural process. In an effort to more rapidly remove condensate for enhanced phase-change heat transfer, researchers have created non-wetting surfaces for dropwise [1] and jumping-droplet condensation [2], whereby millimetric droplets shed due to gravity or micrometric droplets spontaneously jump away from the surface [3], respectively. A number of recent works have fabricated superhydrophobic surfaces to achieve jumping-droplet condensation [4-14] for a variety of applications including self-cleaning [15-17], thermal diodes [18], anti-icing [19-22], vapor chambers [23, 24], energy harvesting [25-27], and heat transfer enhancement [28-43].

The efficient removal of jumping droplets along with the heat transfer enhancement can be limited by droplet return to the surface due to (1) gravitational force (2) entrainment in a bulk convective vapor flow, and (3) entrainment in the local condensing vapor flow toward the surface [23, 44]. The first two return mechanisms can be mitigated with suitable geometric design of the macroscale condensing surface and vapor supply. However, local vapor flow driven droplet return is more difficult to eliminate due to the need to conserve mass of the condensing vapor flowing towards the surface.

While the removal of the droplets by electric fields offers a method to remove condensate [27, 45], practical difficulties exist, mainly related to the need for energized electrodes that require condensate to be removed from their surfaces [41]. Here, we present a solution to the aforementioned limitations by utilizing forced bulk vapor flow to remove jumping-droplets, in what we term convective jumping-droplet condensation. We provide a comprehensive modeling framework of internal convective jumping-droplet condensation inside a tube. Utilizing

hydrodynamic boundary layer analysis, we couple the droplet motion to the internal vapor flow fields to calculate droplet trajectories and surface interactions. We study the jumping droplet traveled length along the tube as a function of the condensation heat flux, tube entrance vapor velocity, jumping droplet size, location of droplets along the tube, and radial location of jumping. By linking droplet return with droplet jumping (multi-hop), we develop a framework to predict macroscopic droplet motion along the tube axis, and offer guidelines for the minimization of drag force and maximization of overall condensation heat transfer. We also develop a framework for analyzing internal flow jumping-droplet condensation pressure drop and compare it to conventional two-phase flow pressure drop calculations for homogeneous and separated flows. The modeling framework shown here outlines the first treatment of internal convective jumping-droplet condensation which has the potential to be implemented in air-cooled steam condensers for energy and water applications.

3.2. Internal Convective Jumping Droplet Condensation Model

3.2.1. Assumptions

Our model for the convective jumping droplet condensation in a tube is based on several assumptions:

1) Jumping droplets are much smaller (R_d < 250 μm) than the radius of the pipe (a > 1 cm), hence the droplets have a negligible effect on the vapor velocity field in the pipe.
2) The condensation at the pipe inner wall can be modeled mathematically as a suction velocity (equivalent to a porous pipe) due to the negligible change in volume during the process ($\rho_v \ll \rho_l$) [46, 47]. The suction velocity V_w can be expressed in terms of the heat flux q, vapor density ρ_v and latent heat of vaporization of water h_{fg} as:

$$V_{\mathrm{w}} = \frac{q}{\rho_{\mathrm{v}} h_{\mathrm{fg}}} \tag{3.1}$$

3) The flow is laminar. Although we consider transitional Reynolds numbers (Re ≈ 11,000) at the pipe inlet, the wall suction is assumed to retard transition to turbulence [48].
4) The flow is fully developed, meaning the axial velocity of the vapor has a self-similar profile along the tube, and the radial velocity does not depend on the axial location.
5) Heat flux is assumed to be uniform along the circumference of the pipe and along the axial location. Because of constant velocity around the circumference of the pipe, the flow is axisymmetric.

3.2.2. Velocity Field

Figure 3.1 shows a schematic of the internal flow problem coupled with jumping droplet condensation. The problem is treated in cylindrical coordinates, z and r representing the axial and radial coordinates, respectively. The pipe considered has a radius a and the axial and radial velocities are represented by u and v, respectively. The suction velocity at the wall due to vapor condensation and the circular droplet (blue circle) are contributions from jumping droplet condensation.

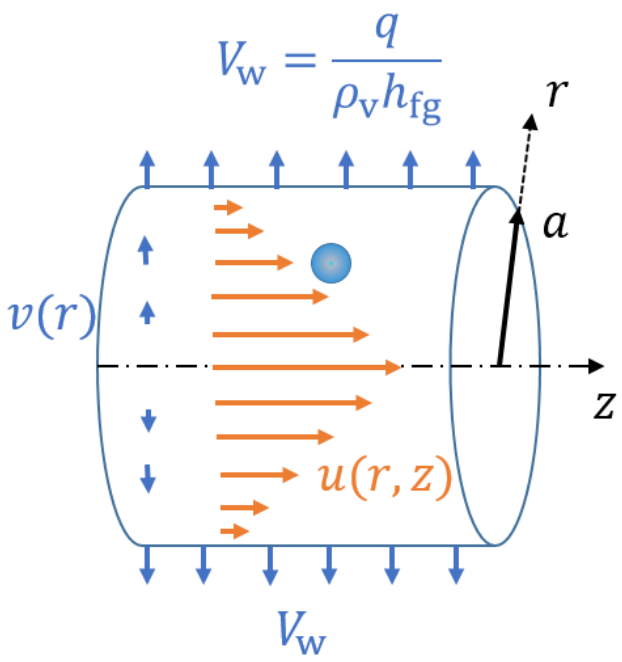

Figure 3.1. Schematic representation of the fully developed laminar flow in a pipe of radius a, with jumping droplet condensation on the inner surface (orange arrows). The heat flux q is assumed to be constant, creating a vapor flow with constant velocity at the wall due to mass conservation (blue arrows). The depicted velocity profiles (orange and blue arrows) are schematics only and do not represent realistic results. The vapor velocity at the wall $\boldsymbol{V_w}$ can be related to the heat flux, vapor density $\boldsymbol{\rho_v}$ and the latent heat of vaporization $\boldsymbol{h_{fg}}$. In the fully developed regime, the axial velocity u is considered to be self-similar along the pipe, and the radial velocity v is only a function of radial position r.

The problem of a fully developed laminar flow in a tube has been solved analytically and numerically via series solutions by R.M. Terrill and P.W. Thomas [49]. We will present only the main findings here. Considering the non-dimensional similarity variable:

$$\eta = \frac{r^2}{a^2}\,, \tag{3.2}$$

the axial and radial velocities can be expressed as:

$$u = \left(U_0 - \frac{2V_w z}{a}\right) f'(\eta)\,, \tag{3.3}$$

$$v = \frac{V_w f(\eta)}{\eta^{1/2}}\,, \tag{3.4}$$

where f is the similarity function, and the symbol prime denotes the derivative with respect to the independent variable, η in this case.

The Navier- Stokes equations reduce to the following 4th order non-linear ordinary differential equation (ODE):

$$\eta f^{\mathrm{iv}} + 2f''' + \frac{R}{2}(f'f'' - ff''') = 0\,, \tag{3.5}$$

where *R* is the (suction based) Reynolds number (based on pipe radius a):

$$R = \frac{V_{\mathrm{w}} a}{\nu_{\mathrm{v}}}, \tag{3.6}$$

with ν_{v} representing the kinematic viscosity of water vapor.

The boundary values for this ODE are as follows:

$$\begin{cases} f(0) = 0 \\ f(1) = 1 \\ f'(1) = 0 \\ \lim_{\eta \to 0} \eta^{1/2} f''(\eta) = 0\,. \end{cases} \tag{3.7}$$

The conditions represent the: 1) zero radial velocity v at the center of the tube (in order to get continuity of the function at r=0), 2) suction velocity at the wall; 3) no slip condition for the axial velocity u; and 4) symmetry of the radial profile with respect to the z-axis, obtained by setting $\partial u/\partial r$ to be zero at r = 0, respectively.

In the original paper, Terrill et. al. present a series solution to the problem [49]. In the current study, we solve directly for the similarity function f using an iterative numerical scheme via MATLAB. Since the problem is a boundary value problem, we use a shooting method [50] to turn it into an initial value problem. Figure 3.2 shows $f'(\eta)$ as a function of $\eta^{1/2} = r/a$, which

represents the non-dimensional profile of the axial velocity normalized by the mass averaged velocity u/u_{avg}, for different suction based Reynolds numbers, R. We can see from the case of $R = 0$ (no suction case) that the velocity at the center of the pipe (r=0) is twice as large as the average velocity. This is consistent with the classical result of the Poiseuille flow in a pipe [51]. Beyond the R = 0 case, we observe three different regimes. The first regime ($0 < R < 2.3$) is characterized by a decrease in the velocity gradient at the wall and an increase in the concavity of the profile showing increased laminar-like behavior. The second regime ($2.3 < R < 10$) is a region of instability. Mathematically, the ODE does not have a solution for the range of $2.3 < R < 9.1$ [49]. We were able to find a solution the value of $R = 10$, which shows patterns of instability as an inflexion point is observed in the profile rendering the maximum velocity at a location different from the center. The third regime, which is for values of $R > 10$, represents an increased turbulent-like behavior where the velocity profile is mostly uniform along the radial direction, the gradient at the wall increasing as R is increased.

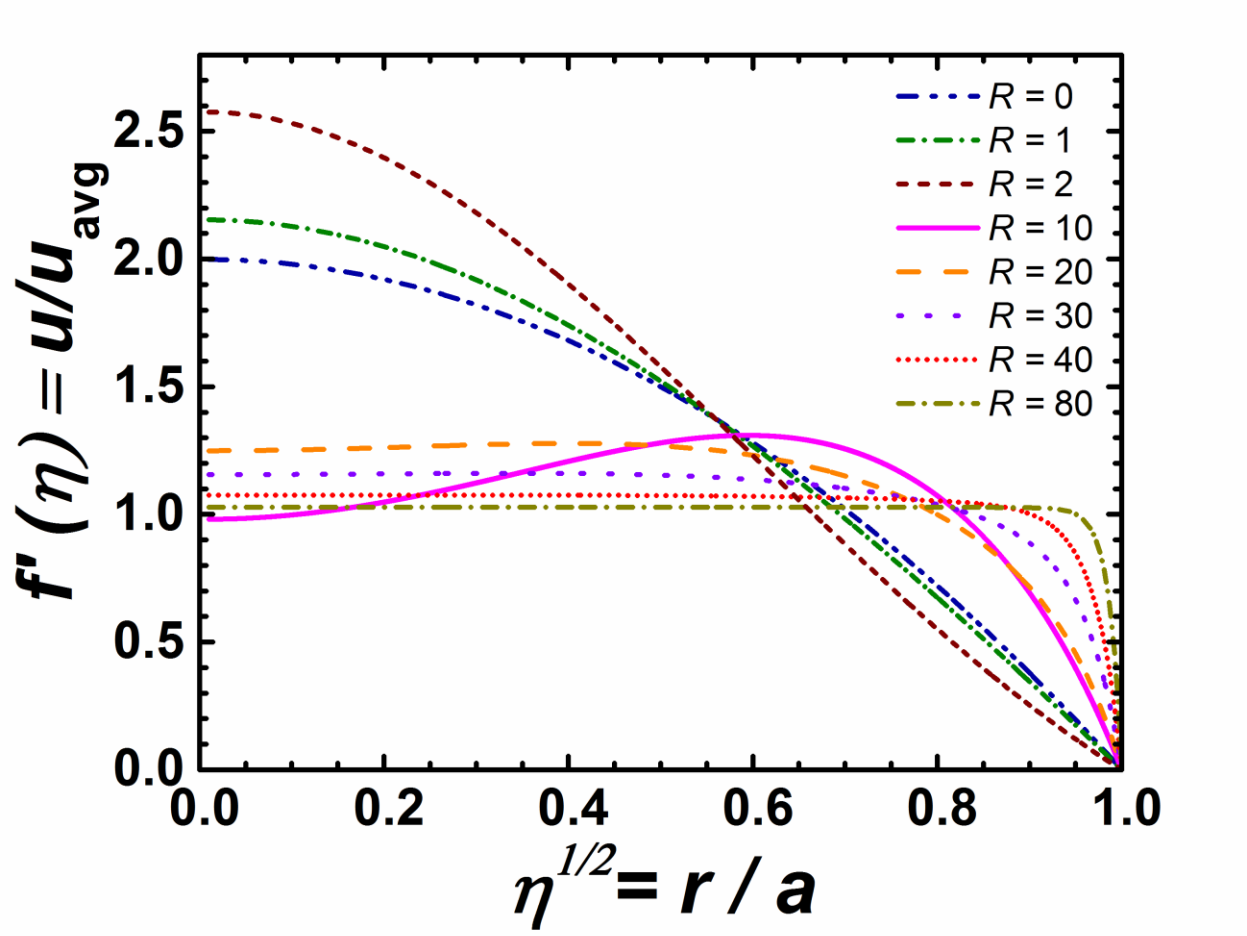

Figure 3.2. Normalized axial velocity ($\boldsymbol{u/u_{avg}}$) as a function of the non-dimensional radial position along the pipe (r/a). The solution for $\boldsymbol{f'}$ is obtained by numerically solving equation 3.5, for different suction Reynolds numbers, R. For the no suction case (R = 0), $\boldsymbol{u/u_{avg}}$ = 2, which corresponds to Poiseuille flow in a pipe. The flow experiences 3 regimes as the suction parameter R is increased. For 0 < R < 2.3, the velocity gradient at the wall decreases as R is increased. This trend breaks down for R > 2.3. Mathematically, no solution is possible for 2.3 < R < 9.1, as the numerical scheme does not converge [49], which is indicative of a regime of flow instability. Beyond the transition regime (R > 10), we observe a regime that exhibits turbulent-like behavior as the profile shows increasing uniformity with increasing R. We note that R = 80 represents the upper bound for the R values for which numerical convergence was obtained.

The results for the normalized radial velocity v/V_w profiles are shown in Fig.3.3. The same regimes observed in Fig.2.2 illustrate a transition from a parabolic-like to linear profile passing through a region of instability as R is increased. The linear profile is evidence of mixing as it represents the fastest route between the boundary conditions.

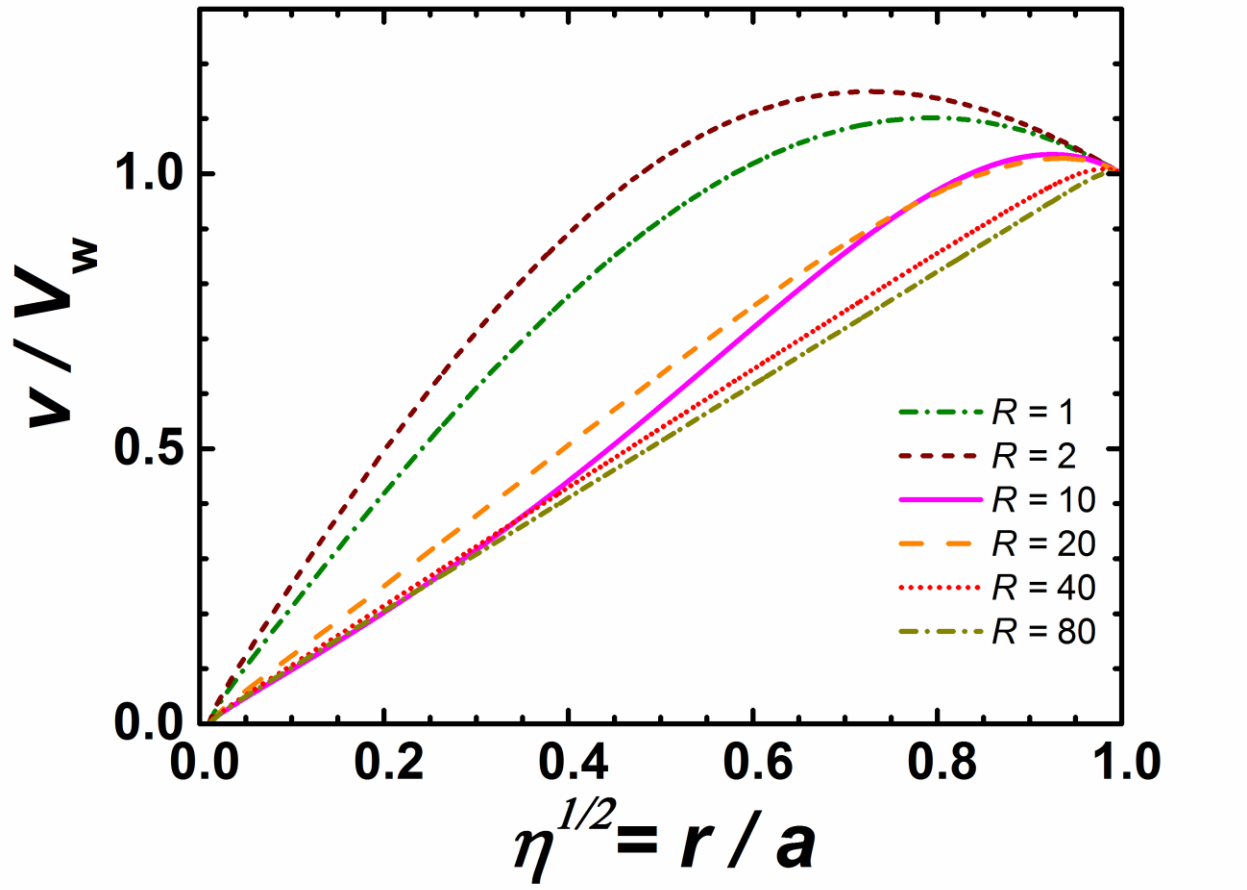

Figure 3.3. Normalized radial velocity (v/V_w) as a function of the normalized radial position along the pipe (r/a), as obtained from Eq. 3.4. As the suction Reynolds number, R, increases to 2.3, the radial velocity profile looks concave. Above R = 9.1, convergence to a linear behavior is observed. The curve R = 10 reflects instability that is observed mathematically by the non-convergence of the numerical scheme for 2.3 < R < 9.1.

To gain more physical insight about the effect of the droplet location along the z-axis, we assume an average velocity of U_0= 15 m/s (a representative value of actual velocities in large industrial condensers [52-54]), a pipe radius a = 10 cm typical for air-cooled condensers, and different heat fluxes at the wall (q = 0.03, 0.5 and 1 W/cm^2). Figure 3.4 shows the axial velocity profile (Eq. 3.3) at different locations along the pipe (z = 0, 4, 8 m). We observe that the axial velocity is

increasingly affected in magnitude as the heat flux is increased, since additional mass is converted to liquid.

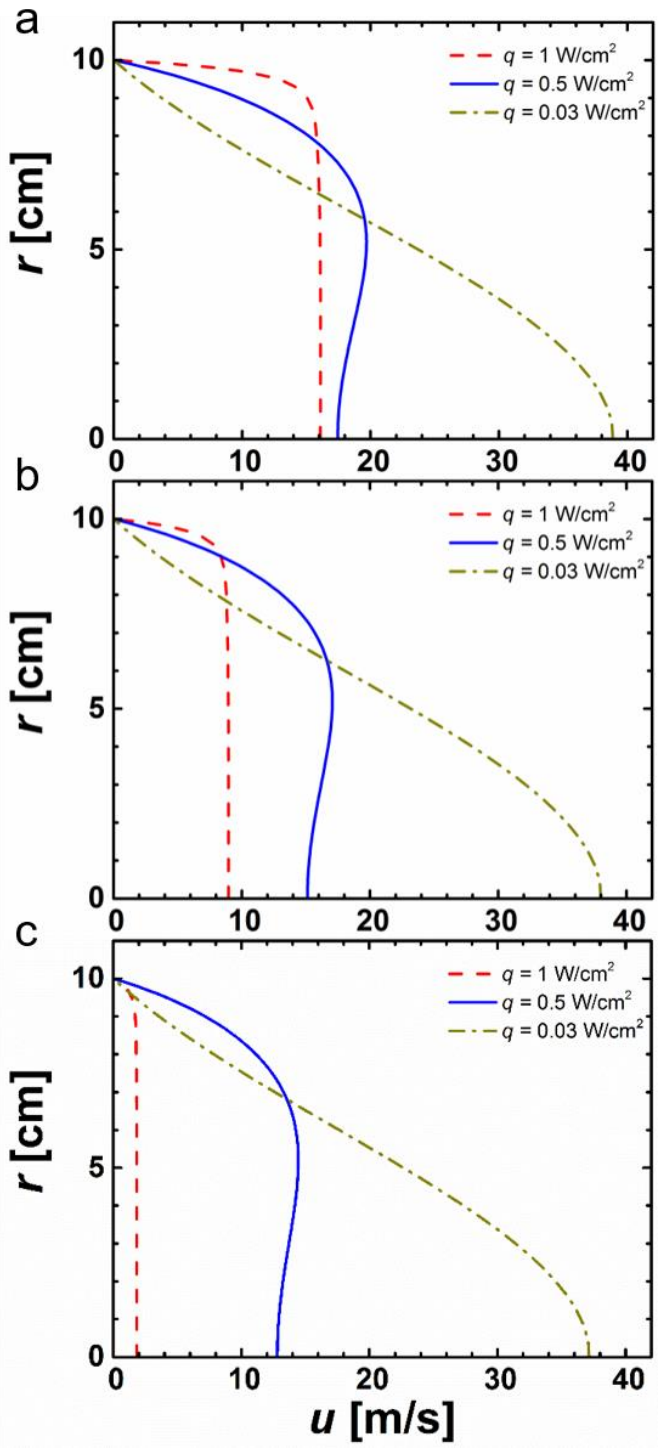

Figure 3.4. Axial velocity (u) profiles for a pipe of radius 10 cm at: (a) z = 0, (b) z = 4 m, and (c) z = 8 m axial locations along the pipe. As expected, for small heat fluxes (q = 0.03 W/cm^2) the

magnitude of the velocity is affected negligibly due to the small condensation rates. However, the vapor velocity decreases significantly for larger heat fluxes (q = 1 W/cm^2) along the pipe. We note that the self-similar profile results from the fully developed flow.

3.2.3. Droplet Equations of Motion

In order to solve for the trajectories of droplets having radii R_{d} in the presence of the vapor flow, we consider the free body diagram on the jumping droplet. The acting forces include the gravitational force $\overrightarrow{F_{\mathrm{G}}} = (4/3)\pi {R_{\mathrm{d}}}^3 \rho_{\mathrm{l}} \vec{g}$, the drag force $\overrightarrow{F_{\mathrm{D}}}$ and the Saffman lift force $\overrightarrow{F_{\mathrm{SL}}}$ [55]. The buoyancy force has been neglected since the vapor density is much smaller than the liquid density. The drag force can be determined by assuming the generalized drag equation on a sphere:

$$\overrightarrow{F_{\mathrm{D}}} = \frac{1}{2}\rho_{\mathrm{v}} {V_{\mathrm{rel}}}^2 C_D\left(Re_{\mathrm{d,t}}\right)\pi {R_{\mathrm{d}}}^2 \frac{\overrightarrow{V_{\mathrm{rel}}}}{|V_{\mathrm{rel}}|}, \tag{3.8}$$

where $\overrightarrow{V_{\mathrm{rel}}}$ is the relative velocity vector between the vapor flow velocity and the droplet velocity, which can be expressed in Cartesian coordinates (x, y, z), with x is into the page and y vertical (based on Fig.3.1), using the position polar angle θ_{r} as

$$\overrightarrow{V_{\mathrm{rel}}} \begin{cases} V_{\mathrm{rel},x} = v\cos\theta_{\mathrm{r}} - v_{\mathrm{d},x} \\ V_{\mathrm{rel},y} = v\sin\theta_{\mathrm{r}} - v_{\mathrm{d},y} \\ V_{\mathrm{rel},z} = u - u_{\mathrm{d}}\,. \end{cases} \tag{3.9}$$

The drag coefficient C_D is dependent on the Reynolds number based on the total velocity vector $\mathrm{Re}_{\mathrm{d,t}} = |V_{\mathrm{rel}}|(2R_{\mathrm{d}})/\nu_{\mathrm{v}}$ [56].

The Saffman lift force arises when the fluid surrounding the droplet has a velocity gradient (shear flow). Qualitatively, it can be seen as a difference in pressure between higher and lower velocity regions, or by the moment created on the droplet due to unequal forces at the top and at the bottom of the droplet, similar to the Magnus effect [57]. The Saffman force is derived for low Reynolds

numbers based on the droplet size, and can be extended for arbitrary Reynolds numbers by incorporating a pre-multiplying factor:

$$\overrightarrow{F_{\mathrm{SL}}} = \phi_{\mathrm{S}}(\mathrm{Re_G}, \mathrm{Re_d}) \left[6.46 {R_{\mathrm{d}}}^2 \left(\mu_{\mathrm{v}} \rho_{\mathrm{v}} \left| \frac{\partial u}{\partial r} \right| \right)^{0.5} \mathrm{sgn}\left(\frac{\partial u}{\partial r} \right) (u - u_{\mathrm{d}}) \right] \overrightarrow{e_{\mathrm{r}}} , \tag{3.10}$$

where ϕ_{S} is the Saffman multiplier that extends the lift force to higher droplet Reynolds number flows [58]. The multiplier ϕ_{S} is a function of the droplet Reynolds number $\mathrm{Re_d} = (u - u_{\mathrm{d}})(2R_{\mathrm{d}})/\nu_{\mathrm{v}}$ and the gradient Reynolds number $\mathrm{Re_G} = |\partial u/\partial r|(2R_{\mathrm{d}})^2/\nu_{\mathrm{v}}$. The symbol sgn is used to define the sign function ($\mathrm{sgn}(\partial u/\partial r) = +1$ for $\partial u/\partial r > 0$, and $\mathrm{sgn}(\partial u/\partial r) = -1$ for $\partial u/\partial r < 0$). The droplet axial velocity is represented by u_{d}, and $\overrightarrow{e_{\mathrm{r}}}$ is the unitary vector in the radial direction, where the main velocity gradient is present.

Having considered the forces applied on the droplet, we can now write the equations of motion at the droplet center of mass in Cartesian coordinates:

$$\begin{aligned} m_{\mathrm{d}} \frac{\partial v_{\mathrm{d,x}}}{\partial t} &= F_{\mathrm{D}} \cos\phi \cos\theta_{\mathrm{v}} + F_{\mathrm{SL}} \cos\theta_{\mathrm{r}} , \\ m_{\mathrm{d}} \frac{\partial v_{\mathrm{d,y}}}{\partial t} &= -m_{\mathrm{d}} g + F_{\mathrm{D}} \cos\phi \sin\theta_{\mathrm{v}} + F_{\mathrm{SL}} \sin\theta_{\mathrm{r}} , \\ m_{\mathrm{d}} \frac{\partial u_{\mathrm{d}}}{\partial t} &= F_{\mathrm{D}} \sin\phi , \end{aligned} \tag{3.11}$$

where ϕ and θ_{v} are the angles formed by $\overrightarrow{V_{\mathrm{rel}}}$ and z-axis, and the projection of $\overrightarrow{V_{\mathrm{rel}}}$ on the xy-plane and the x-axis, respectively. These angles can be found from the components of the relative velocity vector.

Equation 3.11 represents a system of differential equations that can be solved using a Runge-Kutta numerical scheme with initial conditions of position and velocity. The initial speed of the center of mass is obtained by balancing the excess surface energy and kinetic energy of the jumping

droplet, with a proportionality constant $C \approx 0.23$ that accounts for the efficiency of this energy conversion and that best fits the experimental data [59]. The droplets are assumed to jump perpendicular to the surface [60] leading to a radial initial speed of $v = 0.23\sqrt{\gamma/\rho_l R_d}$ where γ = 73 mN/m is the water surface tension. Due to the relatively small size of departing droplets (~10-100 μm), we assume that the shape of droplets remained spherical during flight. This assumption is justified given that the Bond, Webber, and Capillary numbers are all much less than one ($\mathrm{Bo} = \rho_l g {R_d}^2/\gamma \ll 1, \mathrm{We} = \rho_v u^2 R_d/\gamma \ll 1, \mathrm{Ca} = \mu_v u/\gamma \ll 1$, where μ_v is the vapor dynamic viscosity). The effect of residual electrostatic surface charge [27] on the trajectories of the droplets was assumed to be negligible away from the wall. The relative magnitude of drag and adhesion in during droplet jumping has been studied in previous works [61]. It has been shown that unless droplets are in the order of millimeters in diameter, adhesion to the surface dominates, rendering growing droplets on the surface to be stationary in the vapor flow conditions. Numerically, the most significant value of the relative velocity change across the radius of the droplet $\partial u/u$ may reach values of ≈ 50% near the wall. However, the gradient is close to linear at the wall ($\partial^2 u/u^2 <$ 1%), making the center of mass velocity an acceptable average velocity between the bottom and top values of the flow velocity across the droplet.

3.3. Effect of Flow and Geometry on Internal Jumping-Droplet Condensation

It is important at this stage to list the parameters studied herein and their respective default values that are not changed unless specified. Table 3.1 summarizes the parameters considered in this study, which have been chosen from representative A-frame air-cooled condenser (ACC) applications due to the use of internal-flow convective condensation.

Table 3.1. List of independent parameters governing the numerical simulation of the jumping droplet trajectory. Each parameter is attributed a default value that is maintained when the designated parameter is not explicitly varied.

Parameter	**Symbol**	**Default value**	**References and Quantification**
Droplet Radius	R_{d}	10 μm	[2-8]
Pipe radius	a	10 cm	Industrial ACC condensers [52-54, 62]
Heat flux	q	1 W/cm^2	Industrial ACC condensers [52-54, 62]
Inlet average velocity	U_0	15 m/s	Industrial ACC condensers [52-54, 62]
Initial droplet position along z- direction	z_0	0	Fully developed flow
Jumping direction	-	Downward/upward	Limiting cases

3.3.1. Droplet Trajectories

Figure 3.5 shows a few representative cases of the numerically simulated droplet trajectories. Figure 3.5(a) represents droplets jumping upward (emanating from the bottom of the tube inner surface), whereas Figs. 3.5(b) and (c) show downward jumping droplets (emanating from the top of the tube inner surface). The results show that smaller droplets ($R_{\mathrm{d}} < 20$ μm) jumping downwards return to the surface due to drag and lift dominated motion. Droplets having $R_{\mathrm{d}} > 20$ μm fall downward due to gravity while traveling very large distances (meters) in the axial direction as compared to centimeters (Fig. 3.5a). Figures 3.5(d) and 3.5(e) show droplets jumping from arbitrary radial locations (side and front view respectively).

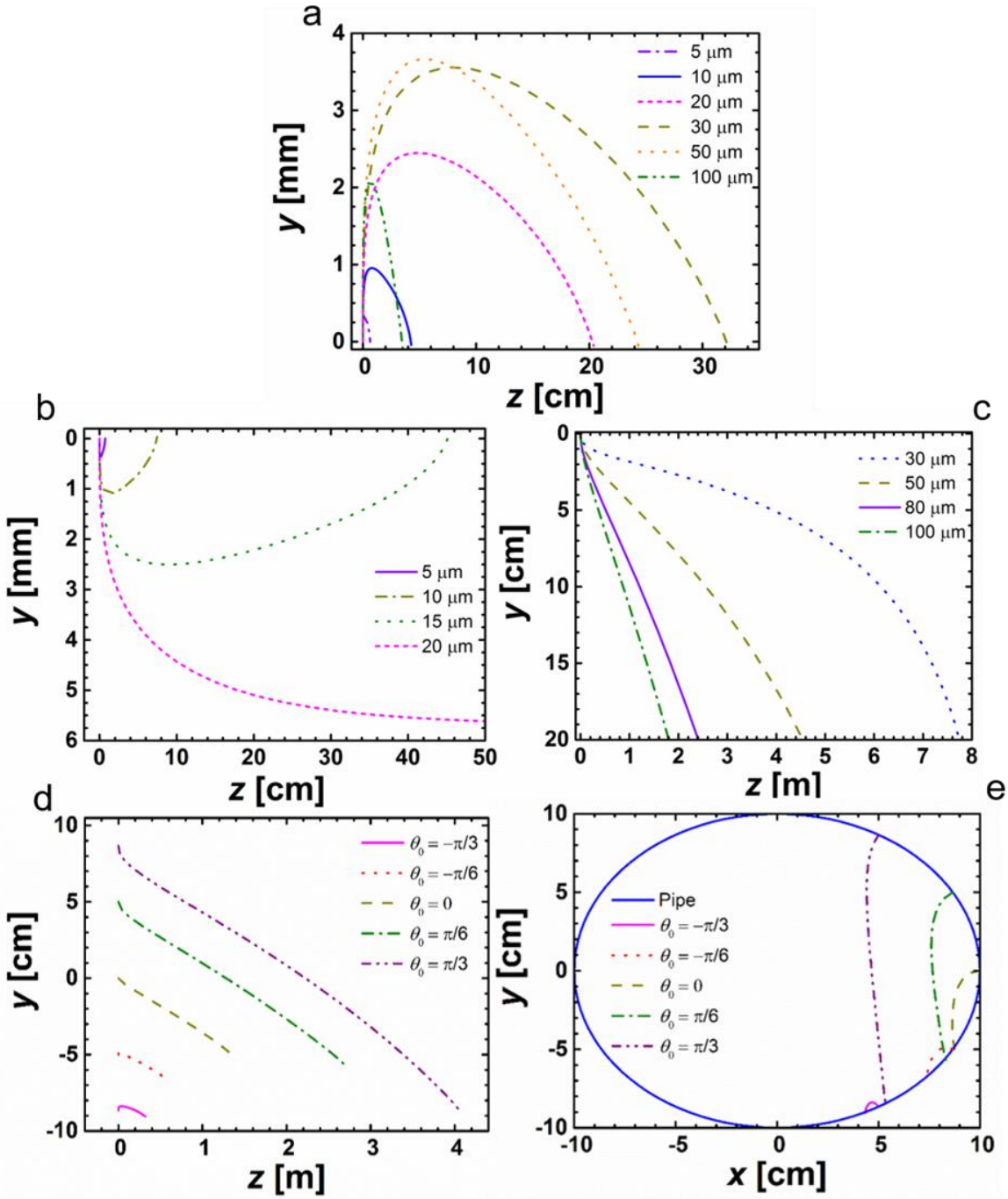

Figure 3.5. Jumping droplet trajectories in a pipe of radius 10 cm, with a saturated vapor average velocity at the inlet of 15 m/s and heat flux of 1 W/cm^2. Trajectories show droplets jumping from the pipe inlet (z = 0) with a radial initial velocity given by the capillary-inertial scaling, for (a) jumping upward, and (b) jumping downwards and returning to the surface, with drag dominated motion (droplet radius $\boldsymbol{R_d} \leq 20$ μm). (c) Bigger droplets ($\boldsymbol{R_d} \geq 20$ μm) jumping downwards travel large distances (meters in contrast to centimeters) as gravity pulls them down slowly towards the bottom of the tube. (d) Side and (e) front view of droplets jumping at angles $\boldsymbol{\theta_0}$ with respect to horizontal, experiencing intermediate behavior between the two cases of jumping downward and upward. Note, the aspect ratio is not 1:1 in (e).

3.3.2. Effect of Pipe Radius

By varying the pipe radius a, the main parameter affected is the suction based Reynold number R since it is directly proportional to a. We can see this effect in Fig. 3.6, where we plot the axial distance traveled by the droplet before landing back on the surface, L, and the time of arrival t_a as a function of a, for both jumping upward (Fig. 3.6a) and jumping downward (Fig. 3.6b). For both cases, the effect of the channel size is only important in the regime where large boundary layer effects are observed ($0 < R < 2.3$). This dependence becomes increasingly negligible for large R. The concave shape of the distance traveled curve is due to the transition between the two opposing trends (Figs. 3.2 and 3.3): parabolic-like behavior of the velocity profile for $R < 2.3$ and turbulent-like behavior for $R > 10$. We can see that the time of arrival and traveled length are almost perfectly correlated. We also observe that droplets jumping downward travel longer distances since gravity is pulling them away from the surface while suction and drag keep them in a quasi-equilibrium in their radial position.

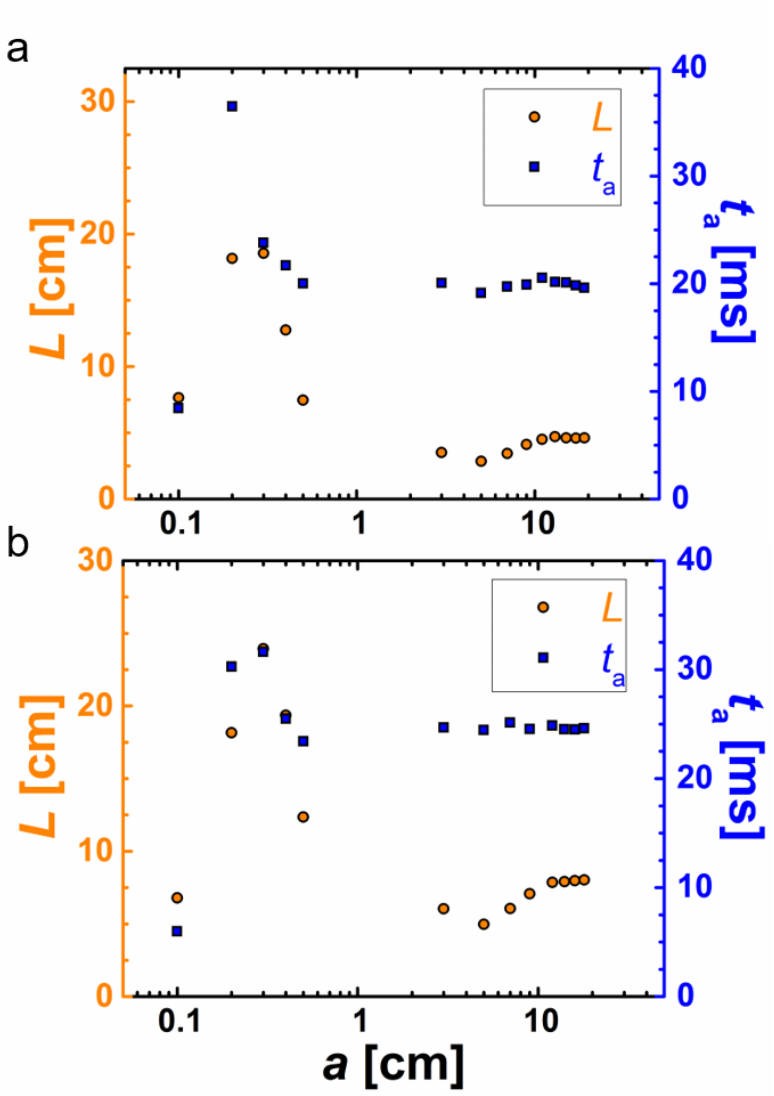

Figure 3.6. Distance traveled, L (left axis, circles), and time of travel, t_a (right axis, squares), of a droplet of radius 10 µm jumping (a) upward and (b) downward as a function of the pipe radius a. The vapor velocity at the inlet and heat flux are 15 m/s and 1 W/cm^2, respectively. Although the effect of the pipe radius is important for small channels (a < 1 cm), the effect becomes negligible for larger pipes (a > 5 cm). This is attributed to the large deviations in the velocity profiles for laminar flows as compared to turbulent-like flow (Fig. 2).

3.3.3. Effect of Droplet Size

Figure 3.7 shows the effect of droplet size on the distance traveled *L* for heat fluxes of 0.05, 0.3 and 1 W/cm^2. The result curves have a concave shape, leading to an optimal droplet radius for maximum traveled length. This occurs when surface forces (drag and lift) balance with

gravitational forces, and is consistent with previous studies on external convective flow jumping-droplet condensation on a flat plate [61]. The jumping downward case (Fig. 3.7b) shows a jump of order of magnitude in the distance traveled between small (< 20 μm) and large (> 20 μm) droplets, which is the result of a droplets transitioning from returning to the top surface to returning to the lower surface, respectively.

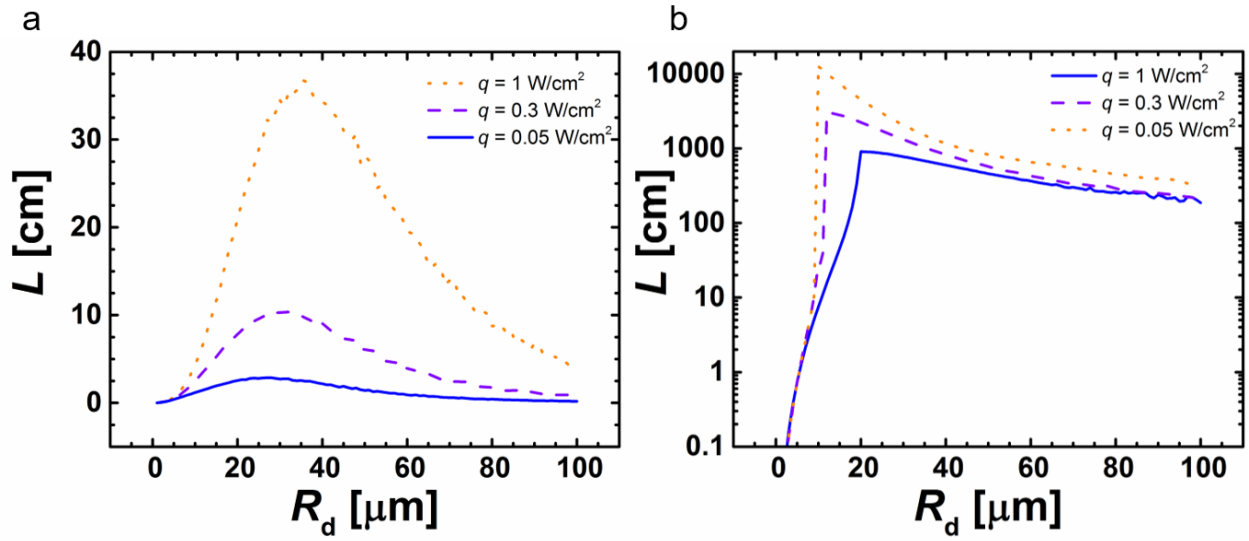

Figure 3.7. Droplet axial travel length L as a function of droplet radius $\boldsymbol{R_d}$ for a vapor flow entering the tube at an average velocity of 15 m/s and droplets jumping (a) upward and (b) downward. For upward jumping, an optimal size exists ($\boldsymbol{R_d} \approx 30$ μm) for which the traveled length is maximum. The optimum is due to the balance between surface forces such as drag and lift and volumetric forces such as gravity. Decreasing the heat flux, q, from 1 to 0.05 W/cm^2 reduces the velocity gradient at the wall and hence decreases the overall distance traveled. For downward jumping droplets, the distance traveled increases by orders of magnitude suddenly as droplets reach the size where they fall back down due to gravity ($\boldsymbol{R_d} \approx 20$ μm).

3.3.4. Effect of Inlet Velocity and Axial Position

Figure 3.8 depicts the effects of the mass averaged velocity at the inlet U_0 (a) and the axial position of the droplet before jumping (b) on the maximum droplet axial travel distance. From Fig. 3.8(a), we observe that the travel length increases due to increased axial drag and lift forces (for both upward and downward jumping) carrying the droplet down the tube. However, Fig 3.8(b) shows that the droplet travel length decreases as a function of initial axial jumping location for both

upward and downward jumping due to the decrease in the bulk vapor velocity caused by the wall suction and conservation of mass.

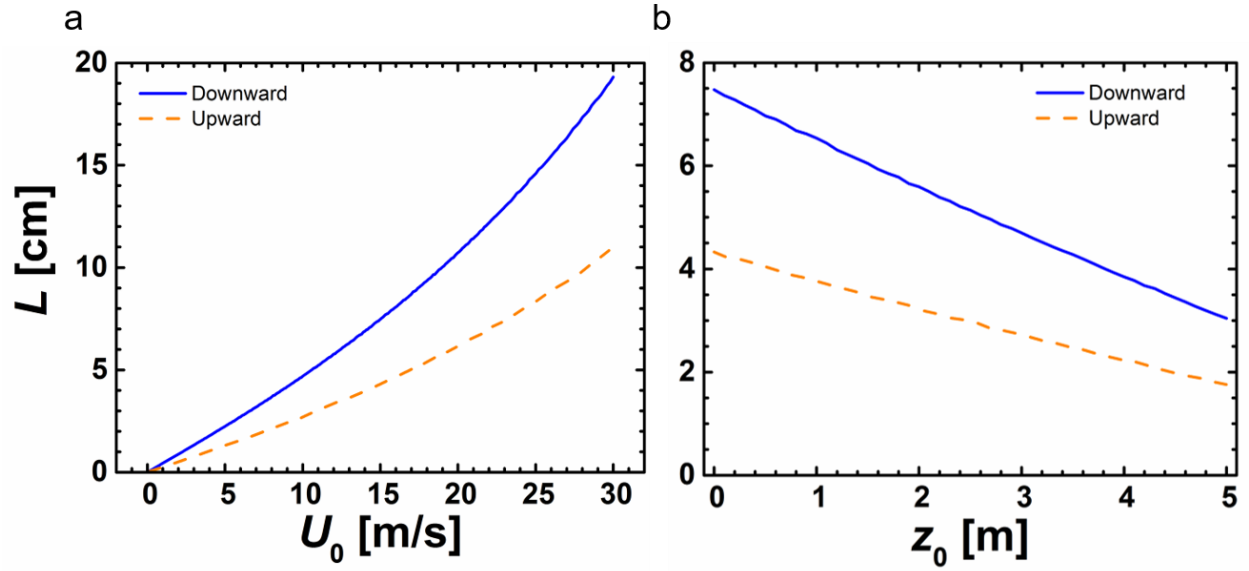

Figure 3.8. Droplet axial travel length L as a function (a) average vapor velocity at the inlet ($\boldsymbol{U_0}$) and (b) position of initial droplet jumping along the tube for a 10 μm radius droplet and heat flux of 1 W/cm^2. The effect of free stream velocity acts to increase the drag and lift forces causing the droplet to travel farther. Droplets jumping downward experience a gravitational push away from the surface causing L to be higher than in the jumping upward case. Further down the tube, as vapor condenses, vapor velocity decreases due to expansion, causing lower drag force on the droplets and hence lower travel length.

3.4. Multi-hop

The aforementioned results have shown droplet trajectory dynamics for a single jumping event. However, in reality, droplets can jump more than once due to coalescence with other droplets upon landing[7, 63, 64], leading to an overall trajectory of multiple jumps or "Multi – hop". To account for this behavior, we simulate the case of the droplet merging with another droplet of the same size, before jumping again. We adjust the initial position and velocity of the next jump by accounting for the position and momentum of the previous jump upon landing. Applying the conservation of linear momentum, the initial velocities of the ith jump in the x, y and z- directions are modified as follows:

$$\left[v_{\mathrm{d,x,0}}\right]_{\mathrm{i}} = 0.23\sqrt{\frac{\gamma}{\rho_{\mathrm{l}}[R_{\mathrm{d}}]_{\mathrm{i}}}}[\cos\theta_{\mathrm{r}}]_{\mathrm{i}} + \frac{1}{2}\left[v_{\mathrm{d,x,end}}\right]_{\mathrm{i}-1},$$

$$\left[v_{\mathrm{d,y,0}}\right]_{\mathrm{i}} = 0.23\sqrt{\frac{\gamma}{\rho_{\mathrm{l}}[R_{\mathrm{d}}]_{\mathrm{i}}}}[\sin\theta_{\mathrm{r}}]_{\mathrm{i}} + \frac{1}{2}\left[v_{\mathrm{d,y,end}}\right]_{\mathrm{i}-1}, \quad \textbf{(3.12)}$$

$$[u_{\mathrm{d}}]_{\mathrm{i}} = \frac{1}{2}\left[u_{\mathrm{d,end}}\right]_{\mathrm{i}-1},$$

where the ratio of 1/2 results from the initial-to-next jumping event droplet mass ratio, $m_{\mathrm{i}-1}/m_{\mathrm{i}}$, and the subscripts "0" and "end" denote initial and final terms, respectively. Figure 3.9 shows droplet trajectories that initially jump upward with a radius $R_{\mathrm{d,0}}$ and that coalesce with droplets of the same size upon return prior to the next jump, the maximum jumping radius being set to 250 μm. It is interesting to note that successive jumps with alternating low-high jumping heights has been observed before experimentally [65]. Although not as pronounced as in Figure 3.9(d-f) due to low condensation heat fluxes, the previous experiments offer an excellent verification of this interesting multi-hop alternating jumping behavior.

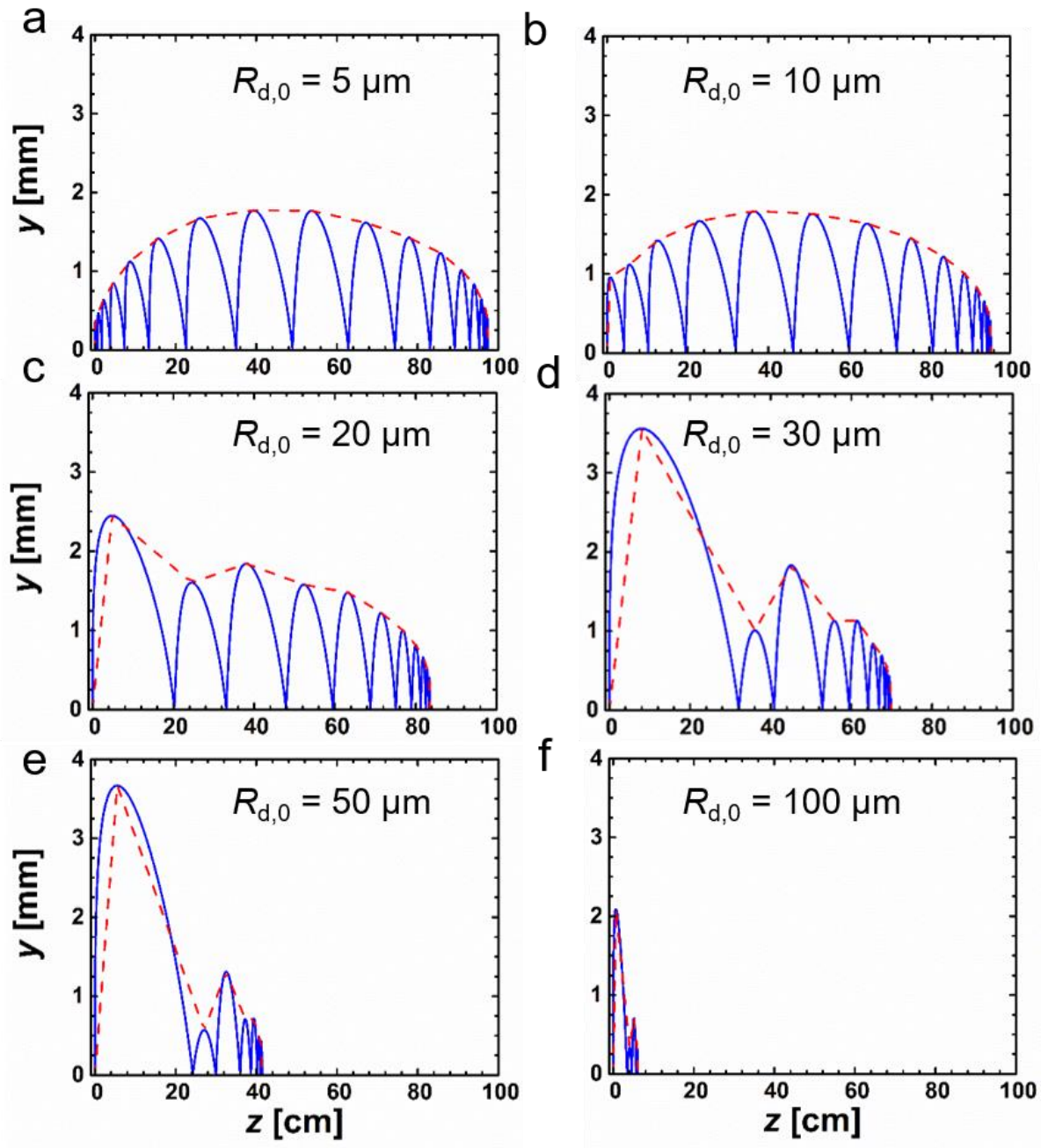

Figure 3.9. Droplet vertical travel distance, y, as a function of axial location z down the tube for multi-hop upward jumping droplets having initial radii of: (a) $\boldsymbol{R_{d,0}}$ = 5 μm, (b) $\boldsymbol{R_{d,0}}$ = 10 μm, (c) $\boldsymbol{R_{d,0}}$ = 20 μm, (d) $\boldsymbol{R_{d,0}}$ = 30 μm, (e) $\boldsymbol{R_{d,0}}$ = 50 μm, and (f) $\boldsymbol{R_{d,0}}$ = 100 μm. The multi-hop phenomena was modeled as sequential coalescence of landing droplets with droplets of the same mass for q = 1 W/cm^2 and $\boldsymbol{U_0}$ = 15 m/s. The droplets eventually become too heavy to jump (~250 μm). For larger droplets ($\boldsymbol{R_{d,0}}$ > 20 μm), the negative momentum of the returning droplet becomes relevant and results in lower jumping heights. Jump events with lower heights do now impart as much negative momentum on the sequential, hence creating the observed pattern of alternating high and low jumps until the droplet becomes sessile.

Droplets jumping downwards can also exhibit multi-hop behavior (Fig. 3.10) up to radii of approximately 20 μm, before they fall down to the bottom of the tube from the first jump. In Figs. 3.9 and 3.10 we can see that multi hop increases the overall travel distance of the droplets, especially for downward- jumping droplets, since the droplets grow to a size that enables gravity to overcome lift and drag forces, pulling droplets towards the core flow. Hence the droplets travel large distances (meters) before returning to the bottom of the tube, as compared to upward-jumping distances of tens of centimeters.

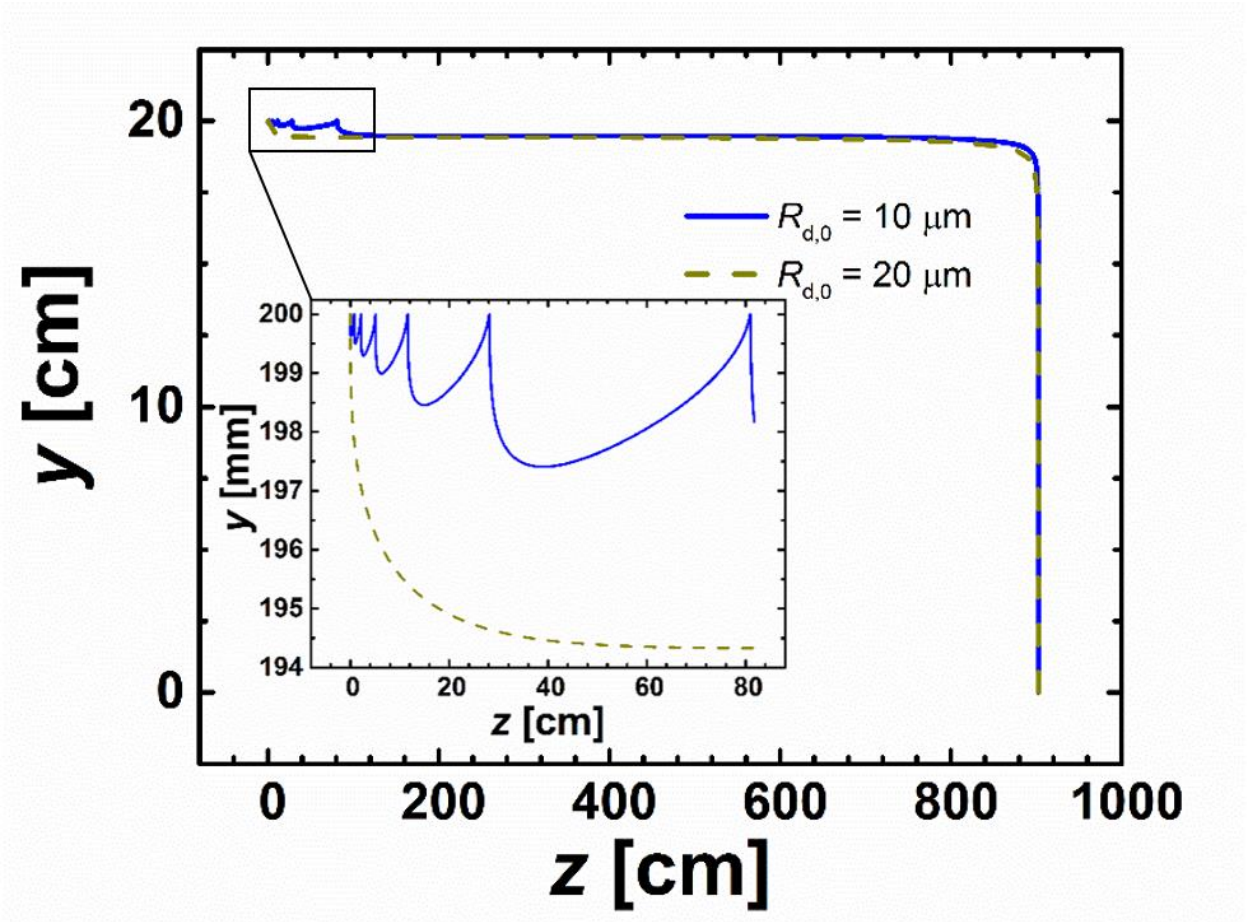

Figure 3.10. Multi-Hop trajectory of a droplet jumping downward having an initial radius $\boldsymbol{R_{d,0}}$ = 10 μm. As the droplet reaches a critical radius of ≈ 20 μm (at z ≈ 0.8 m), it does not return to the upper wall of the pipe, resulting in a large axial travel distance (Fig. 3.7). The large axial travel distance from 100 < z < 800 cm results from a balance of gravitational and drag forces due to radial vapor flow.

3.5. Hydraulic Performance

In order to gain a better understanding of the thermal-hydraulic performance of internal convective jumping-droplet condensation, we focused on determining the pressure drop along the axial direction of the tube geometries and condensation conditions considered in this study.

3.5.1. Flow Characteristics

Convective internal jumping droplet condensation represents a particular regime of two-phase flows, since it lies somewhere between the homogeneous flow case, where the droplets travel at a terminal velocity equal to the velocity of the flow (mist flow), and the separated flow case such as annular and stratified flow where the vapor and liquid phases are completely separated with two different velocities [66]. We therefore developed a pressure drop analysis different than the classical two-phase flows approach. Figure 3.11 shows the vapor quality (x) and the void fraction (α) variation along the pipe length. The void fraction represents the cross-sectional area of the vapor divided by the cross-sectional area of the pipe, and is calculated from the Lockhart-Martinelli correlation assuming a separated flow [66]. Curves are plotted for heat fluxes of 0.5, 1 and 5 W/cm^2. We can see that the void fraction stays very close to 1 whereas the quality decreases linearly with the axial length z, reflecting the negligible change in volume of the vapor after condensation due to a large difference in densities between the vapor and the liquid. We note that the discontinuity in the void fraction in Fig. 3.11 is due to the transition from laminar to turbulent flow. Increasing heat fluxes (0.5 – 5 W/cm^2) impose a faster decay of the vapor quality as a function of the axial distance along the pipe (from 18m to 2m), since more condensation occurs on the walls and mathematically higher suction velocity is imposed on the surface (Eq. 3.3).

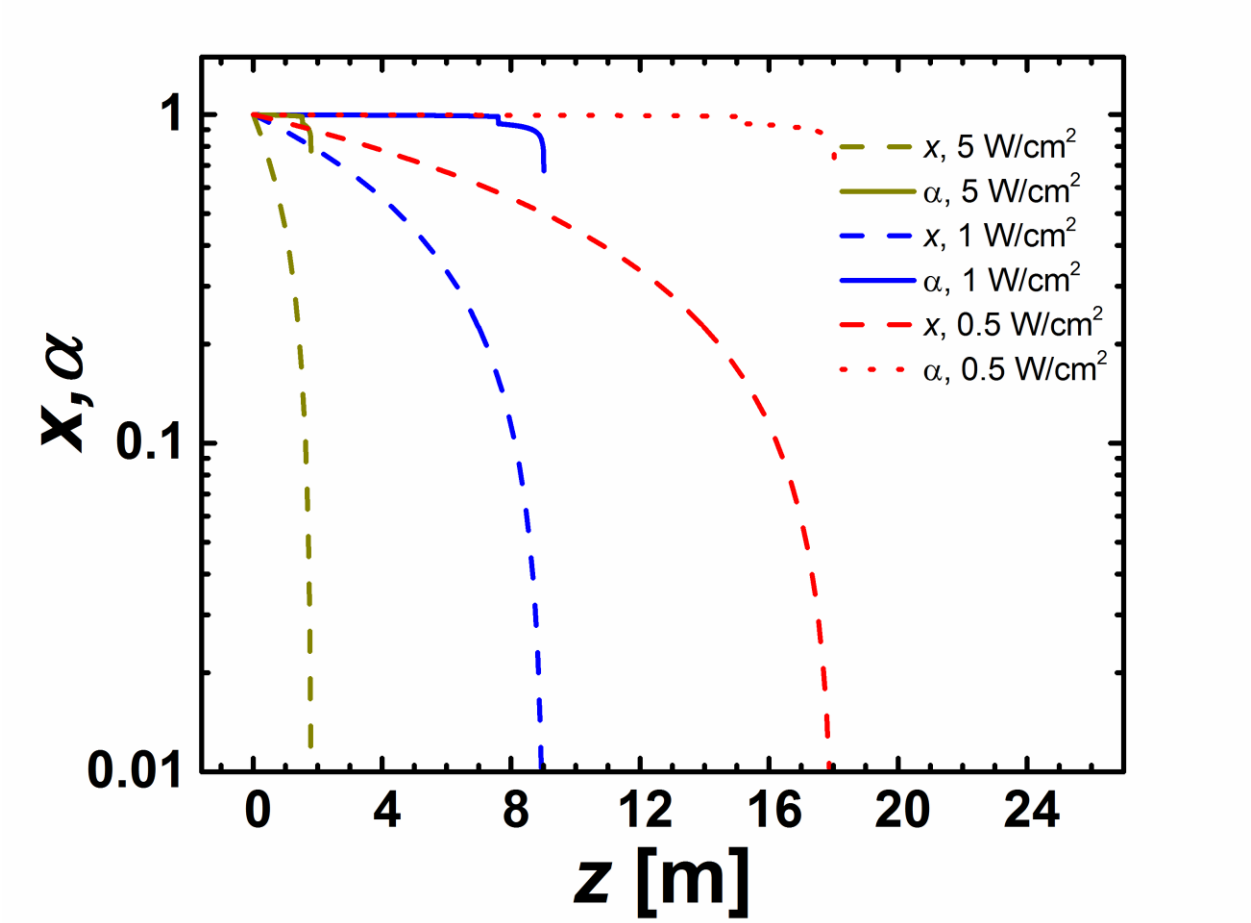

Figure 3.11. Vapor quality (x, dashed lines) and void fraction ($\boldsymbol{\alpha}$, solid/dotted lines) as a function of the axial distance z along the pipe. The quality was calculated from the heat flux similar to Eq.3.3 and the void fraction was calculated using the Lockhart-Martinelli correlation for a separated flow. The results illustrate the large gap between the quality and void fraction decays, also giving the limiting pipe lengths for different heat fluxes. The discontinuities observed in $\boldsymbol{\alpha}$ correspond to transition to turbulence.

Figure 3.12 shows the vapor (u_{v}) and the liquid (u_{l}) bulk velocities as a function of axial location, z, for the quality and void fraction shown in Fig. 3.11. The fluid velocities can be expressed as:

$$\boldsymbol{u_{\mathrm{v}} = \frac{Gx}{\rho_{\mathrm{v}}\alpha}} \tag{3.13}$$

$$u_{\mathrm{l}} = \frac{G(1-x)}{\rho_{\mathrm{l}}(1-\alpha)}, \tag{3.14}$$

where $G = \rho_v U_0$ is the mass flux. The results show that the vapor velocity is orders of magnitude higher than the liquid velocity for a steady mass flux. In addition to underscoring the relative density effect, the velocity behavior helps us understand the different pressure drop behavior for homogeneous and separated flow.

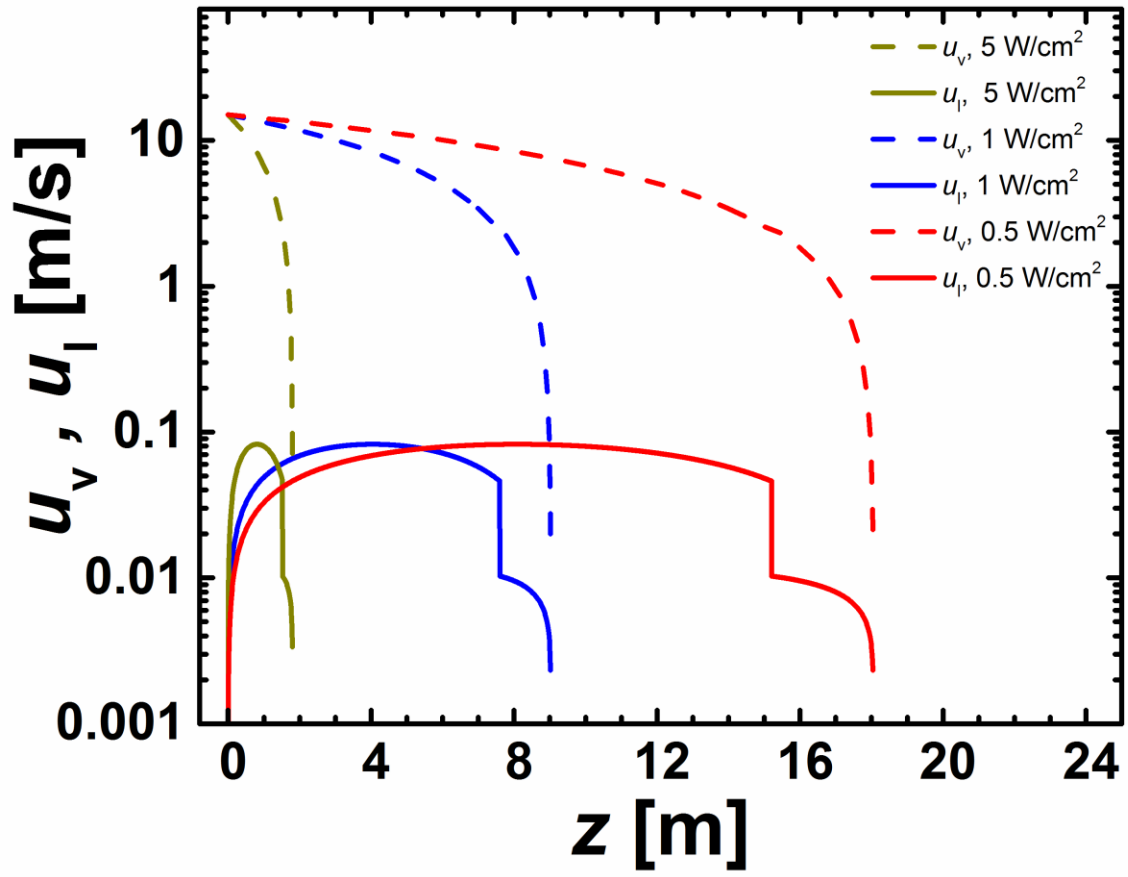

Figure 3.12. Vapor velocity $\boldsymbol{u_v}$ and liquid velocity $\boldsymbol{u_l}$ as a function of the axial distance z along the pipe. The velocities are calculated from the quality and the void fractions (Fig. 3.11). The discontinuities observed correspond to transition to turbulence. We can observe that the velocities differ by order of magnitudes which is consistent with the large difference in density between water vapor and liquid water.

3.5.2. Energy Analysis for Pressure Drop

The approach adopted for determining the pressure drop for the jumping droplet case is based on the conservation of energy applied on the vapor stream. Vapor energy is lost either by friction at the wall (since droplets will be jumping and not sticking to the surface) or by work done on the droplets (acceleration/deceleration). The shear stress on the wall can be determined by:

$$\tau = \mu_{\mathrm{v}} \left.\frac{\partial u}{\partial r}\right|_{r=a} \tag{3.15}$$

Eq. 3.13 can be rewritten in terms of f with the use of the chain rule as:

$$\tau(z) = \frac{2\mu_v}{a}\left(U_0 - 2V_w \frac{z}{a}\right) f''(1) \tag{3.16}$$

We can obtain the change in pressure due to shear at the wall, ΔP_{v}, as:

$$\Delta P_{\mathrm{v}}(z) = 2\pi a \int_0^z \tau(z')dz' \tag{3.17}$$

Figure 3.13 shows a schematic of the approach used to determine the energy decrease due to work done by the vapor on the liquid (jumping droplets). We consider the work done on a monodisperse distribution of droplets of radius R_{d} (mass m_{d}), traveling a distance L, in a time Δt. By considering a section L of the pipe, and decomposing it into *n* segments of length dl, we can calculate the pressure drop by computing the work done on the droplets jumping within this section, from each of the segments. For each segment, we multiply the work done on the droplet by the number of droplets of this size $N_{\mathrm{d,i}}$ that nucleate within the time Δt, expressed as :

$$N_{\mathrm{d,i}} = \frac{q\Delta t}{m_{\mathrm{d}} h_{\mathrm{fg}}} dl \tag{3.18}$$

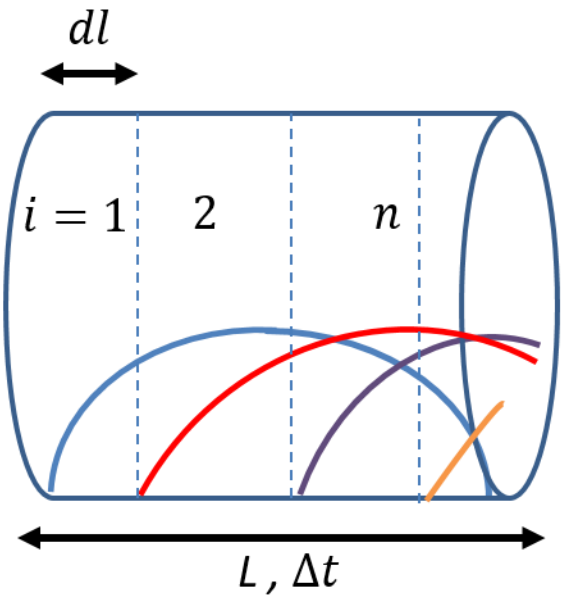

Figure 3.13. Schematic of analysis of the work done by the vapor on the droplets within a section L of the pipe representing the length traveled by the droplet size of the monodisperse distribution considered. The time taken to travel the distance L is represented by $\Delta \boldsymbol{t}$. The pipe section is divided to n segments of length $\boldsymbol{dl}$ from which trajectories are shown up to L, and work is accounted along these portions of the trajectories.

The pressure drop due to vapor flow work on jumping droplets, $\Delta P_{\mathrm{d,L}}$, can be expressed as:

$$\Delta P_{\mathrm{d,L}} = \frac{\sum_i N_{d,i} \int_{z_i}^{L} F_D dz}{L(\pi a^2)}, \tag{3.19}$$

where z_{i} is the center of each segment i.

Since the mass of the liquid increases linearly with L, we can consider an upper bound for the pressure drop in the following section as $2\Delta P_{\mathrm{L}}$, $3\Delta P_{\mathrm{L}}$, and so forth. In reality, vapor flow decreases, resulting in smaller differential quantities of work being extracted. However the following analysis can be taken as a conservative estimate of an upper bound of pressure drop. The sum of the differential pressure drops represents the sum of an arithmetic series, which can be written in terms of the total length as:

$$\Delta P_{\mathrm{d,z}} = \Delta P_{\mathrm{L}} \frac{z}{L} \frac{1 + \frac{z}{L}}{2} \tag{3.20}$$

We note that this approximation is also based on the fact that droplets are jumping independent of gravitational orientation which is true for small droplets (up to 20 μm). Also, vertical work on the droplet has been assumed negligible compared to the horizontal work (higher force, longer distance).

Figure 3.14 shows the results of the pressure drop calculation ($-\Delta P$) as a function of distance z based on 3 different droplet sizes considered (R_d =10, 30 and 50 μm). We can see that the vapor shear stress increases almost linearly with distance since heat flux is constant. The work done on droplets increases with droplet size, since droplets have increased inertia, showing curves monotonically increasing as determined from Eq. (3.20).

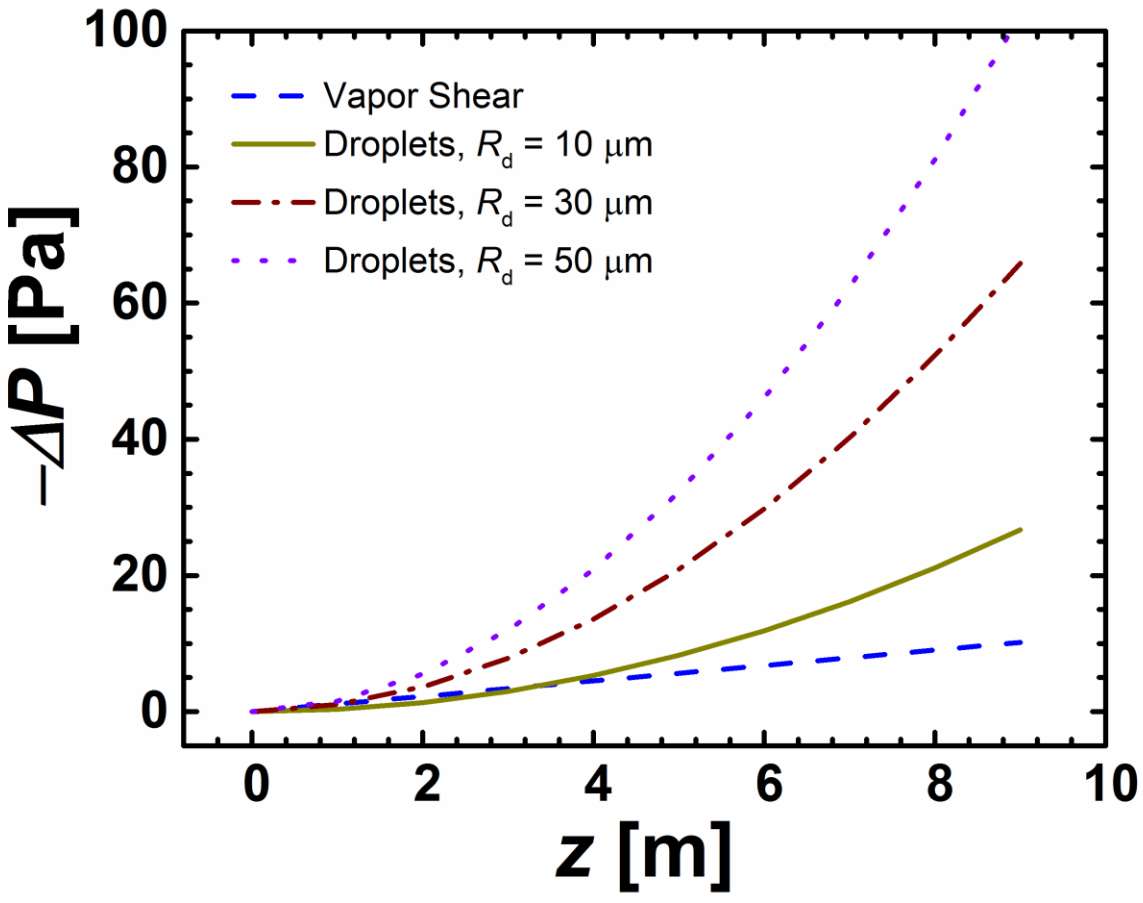

Figure 3.14. Pressure drop (-Δ***P*** = $P_{inlet} - P_{outlet}$) in the pipe as a function of the pipe length, z. The pressure drop consists of the vapor shear stress at the wall and the work done by the vapor

flow on the jumping droplets. The pressure drop due to acceleration/deceleration of droplets (Eq. 3.20) is shown for monodisperse radii of 10, 30 and 50 μm. As expected, bigger droplets result in larger pressure drops due to the higher acceleration force from the flow.

Figure 3.14 shows that the jumping-droplet pressure drop is bounded by the two theoretical limits defined by Eqns. (3.21-23) (homogeneous and separated flow), closer to the homogeneous flow case,

$$-\left(\frac{dP}{dz}\right)_{\mathrm{hom}} = \frac{\left[{\phi_{lo}}^2\left(\frac{2f_{\mathrm{lo}}G^2v_{\mathrm{l}}}{d}\right) + G^2v_{\mathrm{lv}}\frac{dx}{dz}\right]}{1 + G^2x\frac{dv_{\mathrm{v}}}{dP}}, \tag{3.21}$$

where ${\phi_{lo}}^2 = (f_{\mathrm{tp}}/f_{\mathrm{lo}})[1 + (\rho_{\mathrm{l}}/\rho_{\mathrm{v}} - 1)x]$ is the multiplier written in terms of the friction factors of the two-phase flow f_{tp} (using average properties) and the friction factor of the liquid only case f_{lo} as if the liquid was flowing by itself in the pipe with the same mass flux, d represents the diameter of the pipe, v_{v}, v_{l} and v_{lv} represent the specific volumes of the liquid, vapor and their difference ($v_{\mathrm{lv}} = v_{\mathrm{v}} - v_{\mathrm{l}}$), respectively. Using the ideal gas law, we can write:

$$\boldsymbol{\frac{dv_{\mathrm{v}}}{dP} = -R_{\mathrm{g}}\frac{T_{\mathrm{sat}}}{{P_{\mathrm{sat}}}^2}}, \tag{3.22}$$

where T_{sat} and P_{sat} are the saturation temperature and pressure taken at 40°C for this calculation. The separated flow pressure gradient is:

$$-\left(\boldsymbol{\frac{dP}{dz}}\right)_{\mathbf{sep}} = \left(\boldsymbol{{\phi_l}^2\frac{2f_{\mathrm{l}}G^2(1-x)^2v_{\mathrm{l}}}{d}}\right) + \boldsymbol{G^2\frac{dx}{dz}\left[\left(\frac{2xv_{\mathrm{v}}}{\alpha} - \frac{2(1-x)v_{\mathrm{l}}}{1-\alpha}\right) + \frac{d\alpha}{dx}\left(\frac{(1-x)^2v_{\mathrm{l}}}{(1-\alpha)^2} - \frac{x^2v_{\mathrm{v}}}{\alpha^2}\right)\right]}, \tag{3.23}$$

where f_l is the friction factor of the liquid flowing in its own cross-section area at the liquid flow rate, and compressibility effects have been neglected. Equation (3.21) and (3.23) can be integrated to obtain the pressure drop within any section of the pipe.

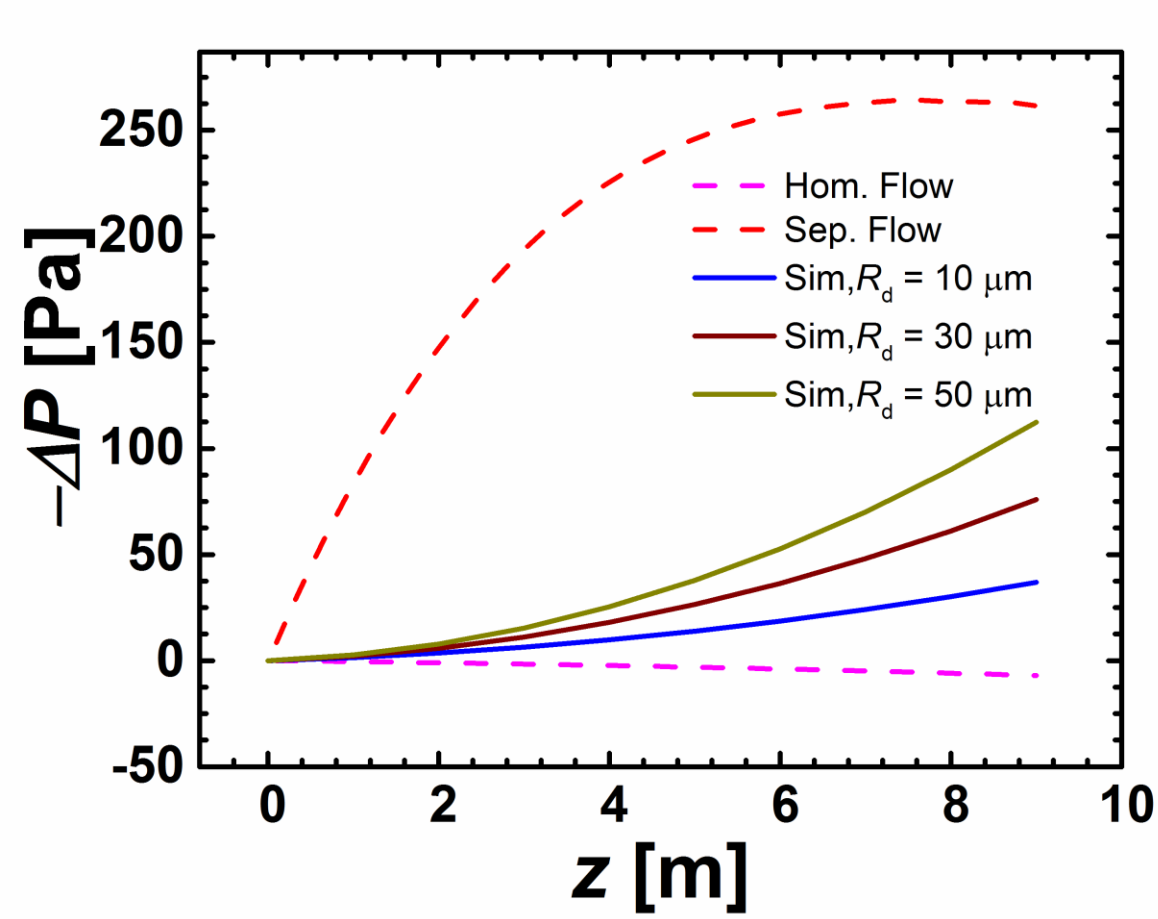

Figure 3.15. Pressure drop ($-\Delta P$) in the pipe as a function of the pipe length z for homogeneous flow (Eq. 3.21), separated flow (Eq. 3.23) and an upper bound for the pressure drop given by an analysis of the work done by the flow on droplets with a monodisperse radii of 10, 30 and 50 μm (Eq. 3.20). As expected, the calculated jumping-droplet pressure drop is bounded by the two limiting cases of homogeneous and separated flow.

3.6. Discussion

The presence of internal flow during jumping droplet condensation is assumed to enhance the condensation heat transfer measured in quiescent condensation conditions (h > 100,000 W/m^{2}K

[2]). Vapor flow will enhance vapor mixing, and will convect departing droplet away from the surface and down the tube where they can be collected in a liquid reservoir. As shown through the results of Figs. (3.6-8), proper consideration of the droplet jumping location, direction, heat flux, and tube geometry, will have large effects on the droplet trajectory. With careful design, tube geometries can be made such that all departing droplet are convected to the end of the tube, avoiding progressive flooding from returning droplets [45]. Although nucleation mediated flooding will still exist and poses a problem for the maximum attainable heat flux available for condensation, post-flooding performance has the potential to reach ultra-high heat transfer coefficients due to the shearing effect of vapor on the growing condensate droplets [67]. Furthermore, if non-condensable gases (NCGs) are present in the vapor, convection will disrupt the buildup of the NCG boundary layer and should enhance thermal performance [68, 69]. In addition, the removal of the condensate from the surface at micrometric length scales reduces the required subcooling towards the end of the tube (typically seen in internal-flow convective filmwise condensation), increasing the ratio of latent heat to sensible cooling, rendering the condensation more efficient.

We anticipate that the easier removal of droplets from the top as compared to the bottom surface will most likely lead to the bottom region of the pipe having larger droplet distributions over time, resulting in a radially dependent heat flux along the tube length, particularly for applications having long internal flow passages ($a << L$).

Thus far, our analysis has focused on calculations involving geometries and fluid flow parameters characteristic of air-cooled A-frame condensers (ACCs). The main barrier for ACC heat transfer is the air side and not the internal steam condensation side [52-54, 70]. Enhancing the air-side heat transfer coefficients sufficiently for the desired condenser performance is extremely challenging

due to the low heat capacity and thermal conductivity of air, as well as limited opportunities to significantly modify air flow while maintaining a low air side pressure drop and fan power consumption [70]. However, the internal convective jumping-droplet condensation approach developed here can enable the reduction in cross-sectional area of the steam channel without minimal penalty in pressure drop. Therefore, a larger number of steam tubes can be used, thereby increasing the exterior fin area and improving the performance of the system through decreased steam condensation temperatures, which can translate to increased net power production.

3.7. Future Work

The results presented in this paper construct a quantitative framework for the investigation of internal convective jumping-droplet condensation. Our simulations have considered the case of single droplet behavior inside a tube. Although the single-droplet analysis provides insight into the physics of the problem, a more holistic approach should consider: 1) multiple droplets simultaneously jumping from different radial locations with possible fluidic and electrostatic interactions between the droplets [27], 2) the droplets' effect on the vapor flow at high heat fluxes, and 3) the effects of polydisperse droplet distributions on the thermal-hydraulic performance. In the future, the effects of vapor flow turbulence should be modeled, as many internal condensing applications have turbulent flow conditions. Although in some cases the Reynolds number in our simulations was on the order of several thousand, which lies in the transitional region between laminar and turbulent single phase flows in tubes, future work should focus on investigating the retardation of the laminar-to-turbulent transition due to wall suction, as observed in external flow where the boundary layer is drawn closer to the surface when suction at the wall is imposed [71]. The developed model and concept of internal jumping-droplet convective condensation has much potential for unique and enhanced thermal-hydraulic applications. It would be interesting to utilize

convective jumping-droplet condensation for humidification and dehumidification systems. By properly designing the tube or channel for an inlet flow of moist air, jumping droplet can be collected in the core flow, developing a central humid stream, and a near-wall dry stream that can be separated and distributed at the exit.

3.8. Conclusions

Our work presents a comprehensive analysis of the laminar, fully developed flow jumping-droplet condensation inside tubes. The dynamics of the droplets jumping from the inner superhydrophobic surface of the pipe were determined in the context of constant heat flux at the wall. With condensation modeled as a suction velocity boundary condition at the wall, the velocity profiles of the saturated vapor were solved via numerical simulation with a careful examination of the problem parameters such as pipe radius, droplet size, initial jumping droplet location (radial and axial), heat flux, and inlet vapor mass flow rate. The possibility of the droplets undergoing multiple jumps inside the tube (multi-hop process) was considered and effective traveled lengths of the droplets quantified. An analysis of the pressure drop was developed, based on energy conservation, showing that forced convection internal jumping-droplet condensation is bounded by the two limiting cases of homogeneous and separated flow. The modeling framework developed here has the potential to be implemented for the design of advanced condensers for energy and water applications.

3.9. References

[3.1] E. Schmidt, W. Schurig, W. Sellschopp, Condensation of water vapour in film- and drop form, Zeitschrift Des Vereines Deutscher Ingenieure, 74 (1930) 544-544.
[3.2] N. Miljkovic, R. Enright, Y. Nam, K. Lopez, N. Dou, J. Sack, E.N. Wang, Jumping-droplet-enhanced condensation on scalable superhydrophobic nanostructured surfaces, Nano Lett, 13(1) (2013) 179-187.
[3.3] J.B. Boreyko, C.H. Chen, Self-Propelled Dropwise Condensate on Superhydrophobic Surfaces, Phys Rev Lett, 103(18) (2009) 184501.
[3.4] X. Chen, J. Wu, R. Ma, M. Hua, N. Koratkar, S. Yao, Z. Wang, Nanograssed Micropyramidal Architectures for Continuous Dropwise Condensation, Advanced Functional Materials, 21 (2011) 4617–4623.
[3.5] J. Feng, Y. Pang, Z. Qin, R. Ma, S. Yao, Why Condensate Drops Can Spontaneously Move Away on Some Superhydrophobic Surfaces but Not on Others, ACS Applied Materials & Interfaces, 4 (2012) 6618−6625.
[3.6] J. Feng, Z.Q. Qin, S.H. Yao, Factors Affecting the Spontaneous Motion of Condensate Drops on Superhydrophobic Copper Surfaces, Langmuir, 28(14) (2012) 6067-6075.
[3.7] C.J. Lv, P.F. Hao, Z.H. Yao, Y. Song, X.W. Zhang, F. He, Condensation and jumping relay of droplets on lotus leaf, Appl Phys Lett, 103 (2013) 021601.
[3.8] K. Rykaczewski, Microdroplet Growth Mechanism during Water Condensation on Superhydrophobic Surfaces, Langmuir, 28(20) (2012) 7720-7729.
[3.9] K. Rykaczewski, W.A. Osborn, J. Chinn, M.L. Walker, J.H.J. Scott, W. Jones, C. Hao, S. Yaod, Z. Wang, How nanorough is rough enough to make a surface superhydrophobic during water condensation?, Soft Matter, 8 (2012) 8786-8794.
[3.10] J. Tian, J. Zhu, H.Y. Guo, J. Li, X.Q. Feng, X.F. Gao, Efficient Self-Propelling of Small-Scale Condensed Microdrops by Closely Packed ZnO Nanoneedles, J Phys Chem Lett, 5(12) (2014) 2084-2088.
[3.11] M. McCarthy, K. Gerasopoulos, S.C. Maroo, A.J. Hart, Materials, Fabrication, and Manufacturing of Micro/Nanostructured Surfaces for Phase-Change Heat Transfer Enhancement, Nanosc Microsc Therm, 18(3) (2014) 288-310.
[3.12] G.Q. Li, M.H. Alhosani, S.J. Yuan, H.R. Liu, A. Al Ghaferi, T.J. Zhang, Microscopic Droplet Formation and Energy Transport Analysis of Condensation on Scalable Superhydrophobic Nanostructured Copper Oxide Surfaces, Langmuir, 30(48) (2014) 14498-14511.
[3.13] K. Yanagisawa, M. Sakai, T. Isobe, S. Matsushita, A. Nakajima, Investigation of droplet jumping on superhydrophobic coatings during dew condensation by the observation from two directions, Appl Surf Sci, 315 (2014) 212-221.
[3.14] C.W. Lo, C.C. Wang, M.C. Lu, Scale Effect on Dropwise Condensation on Superhydrophobic Surfaces, ACS Applied Materials & Interfaces, 6(16) (2014) 14353-14359.
[3.15] K.M. Wisdom, J.A. Watson, X. Qua, F. Liua, G.S. Watson, C.H. Chen, Self-cleaning of superhydrophobic surfaces by self-propelled jumping condensate, Proceedings of the National Academy of Sciences of the United States of America, 110(20) (2013) 7992–7997.

[3.16] G.S. Watson, L. Schwarzkopf, B.W. Cribb, S. Myhra, M. Gellender, J.A. Watson, Removal mechanisms of dew via self-propulsion off the gecko skin, J R Soc Interface, 12(105) (2015).
[3.17] G.S. Watson, M. Gellender, J.A. Watson, Self-propulsion of dew drops on lotus leaves: a potential mechanism for self cleaning, Biofouling, 30(4) (2014) 427-434.
[3.18] J.B. Boreyko, Y.J. Zhao, C.H. Chen, Planar jumping-drop thermal diodes, Appl Phys Lett, 99(23) (2011) 234105.
[3.19] J.B. Boreyko, P.C. Collier, Delayed Frost Growth on Jumping-Drop Superhydrophobic Surfaces, Acs Nano, 7(2) (2013) 1618-1627.
[3.20] X.M. Chen, R.Y. Ma, H.B. Zhou, X.F. Zhou, L.F. Che, S.H. Yao, Z.K. Wang, Activating the Microscale Edge Effect in a Hierarchical Surface for Frosting Suppression and Defrosting Promotion, Sci Rep-Uk, 3 (2013).
[3.21] J.Y. Lv, Y.L. Song, L. Jiang, J.J. Wang, Bio-Inspired Strategies for Anti-Icing, ACS Nano, 8(4) (2014) 3152-3169.
[3.22] Q.L. Zhang, M. He, J. Chen, J.J. Wang, Y.L. Song, L. Jiang, Anti-icing surfaces based on enhanced self-propelled jumping of condensed water microdroplets, Chem Commun, 49(40) (2013) 4516-4518.
[3.23] J.B. Boreyko, C.H. Chen, Vapor chambers with jumping-drop liquid return from superhydrophobic condensers, International Journal of Heat and Mass Transfer, 61 (2013) 409-418.
[3.24] J. Oh, P. Birbarah, T. Foulkes , S.L. Yin, M. Rentauskas, J. Neely, R.P. Podgurski, N. Miljkovic, Jumping-Droplet Electronics Hot Spot Cooling, Appl Phys Lett, in press (2017).
[3.25] D.J. Preston, N. Miljkovic, R. Enright, E.N. Wang, Jumping Droplet Electrostatic Charging and Effect on Vapor Drag, J Heat Trans-T Asme, 136(8) (2014).
[3.26] N. Miljkovic, D.J. Preston, R. Enright, E.N. Wang, Jumping-droplet electrostatic energy harvesting, Appl Phys Lett, 105(1) (2014).
[3.27] N. Miljkovic, D.J. Preston, R. Enright, E.N. Wang, Electrostatic charging of jumping droplets, Nat Commun, 4 (2013).
[3.28] R. Enright, N. Miljkovic, J.L. Alvarado, K. Kim, J.W. Rose, Dropwise Condensation on Micro- and Nanostructured Surfaces, Nanosc Microsc Therm, 18(3) (2014) 223-250.
[3.29] N. Miljkovic, E.N. Wang, Condensation heat transfer on superhydrophobic surfaces, Mrs Bull, 38(5) (2013) 397-406.
[3.30] R. Enright, N. Miljkovic, N. Dou, Y. Nam, E.N. Wang, Condensation on Superhydrophobic Copper Oxide Nanostructures, J Heat Transf, 135(9) (2013) 091304.
[3.31] N. Miljkovic, R. Enright, E.N. Wang, Effect of Droplet Morphology on Growth Dynamics and Heat Transfer during Condensation on Superhydrophobic Nanostructured Surfaces, Acs Nano, 6(2) (2012) 1776–1785.
[3.32] N. Miljkovic, R. Enright, E.N. Wang, Growth Dynamics During Dropwise Condensation on Nanostructured Superhydrophobic Surfaces, 3rd Micro/Nanoscale Heat & Mass Transfer International Conference, (2012).
[3.33] J. Cheng, A. Vandadi, C.L. Chen, Condensation heat transfer on two-tier superhydrophobic surfaces, Appl Phys Lett, 101 (2012) 131909-131901 - 131909-131904.
[3.34] E. Olceroglu, C.Y. Hsieh, M.M. Rahman, K.K.S. Lau, M. McCarthy, Full-Field Dynamic Characterization of Superhydrophobic Condensation on Biotemplated Nanostructured Surfaces, Langmuir, 30(25) (2014) 7556-7566.

[3.35] E. Olceroglu, S.M. King, M.M. Rahman, M. McCarthy, Biotemplated Superhydrophobic Surfaces for Enhanced Dropwise Condensation, Proceedings of the Asme International Mechanical Engineering Congress and Exposition - 2012, Vol 7, Pts a-D, (2013) 2809-2815.
[3.36] D. Attinger, C. Frankiewicz, A.R. Betz, T.M. Schutzius, R. Ganguly, A. Das, C.-J. Kim, C.M. Megaridis, Surface engineering for phase change heat transfer: A review, MRS Energy & Sustainability, 1 (2014).
[3.37] X.M. Chen, J.A. Weibel, S.V. Garimella, Exploiting Microscale Roughness on Hierarchical Superhydrophobic Copper Surfaces for Enhanced Dropwise Condensation, Adv Mater Interfaces, 2(3) (2015).
[3.38] Y.M. Hou, M. Yu, X.M. Chen, Z.K. Wang, S.H. Yao, Recurrent Filmwise and Dropwise Condensation on a Beetle Mimetic Surface, ACS Nano, 9(1) (2015) 71-81.
[3.39] H. Cha, C. Xu, J. Sotelo, J.M. Chun, Y. Yokohama, R. Enright, N. Miljkovic, Coalescence-Induced Nanodroplet Jumping, Physical Review Fluids, In press (2016).
[3.40] S. Chavan, H. Cha, D. Orejon, K. Nawaz, N. Singla, Y.F. Yeung, D. Park, D.H. Kang, Y.J. Chang, Y. Takata, N. Miljkovic, Heat Transfer through a Condensate Droplet on Hydrophobic and Nanostructured Superhydrophobic Surfaces, Langmuir, 32(31) (2016) 7774-7787.
[3.41] A. Shahriari, P. Birbarah, J. Oh, N. Miljkovic, V. Bahadur, Electric-Field Based Control and Enhancement of Boiling and Condensation, Nanosc Microsc Therm, in press (2017).
[3.42] P. Birbarah, Z.E. Li, A. Pauls, N. Miljkovic, A Comprehensive Model of Electric-Field-Enhanced Jumping-Droplet Condensation on Superhydrophobic Surfaces, Langmuir, 31(28) (2015) 7885-7896.
[3.43] N. Miljkovic, R. Enright, E.N. Wang, Modeling and Optimization of Superhydrophobic Condensation, J Heat Trans-T Asme, 135(11) (2013).
[3.44] N. Miljkovic, R. Enright, Y. Nam, K. Lopez, N. Dou, J. Sack, E.N. Wang, Jumping-Droplet-Enhanced Condensation on Scalable Superhydrophobic Nanostructured Surfaces, Nano Letters, 13(1) (2013) 179-187.
[3.45] N. Miljkovic, D.J. Preston, R. Enright, E.N. Wang, Electric-Field-Enhanced Condensation on Superhydrophobic Nanostructured Surfaces, ACS Nano, 7(12) (2013) 11043-11054.
[3.46] T.P. Cotter, Theory of Heat Pipes, LA-3426-MS, Los Alamos Scientific Laboratory, UC, Los Alamos, New Mexico, 1965.
[3.47] S.W. Yuan, A.B. Finkelstein, Laminar Pipe Flow With Injection and Suction Through a Porous Wall, Tr. ASME, 78 (1956) 719.
[3.48] W.M. Kays, M.E. Crawford, B. Weigand, Convective heat and mass transfer, 4th ed., McGraw-Hill Higher Education, Boston, 2005.
[3.49] R.M. Terrill, P.W. Thomas, On Laminar Flow through a Uniformly Porous Pipe, Appl Sci Res, 21(1) (1969) 37.
[3.50] J. Stoer, R. Bulirsch, Introduction to numerical analysis, 3rd ed., Springer, New York, 2002.
[3.51] F.M. White, Fluid mechanics, 6th ed., McGraw-Hill, New York, 2008.
[3.52] Water for Energy - Advanced Dry Cooling for Power Plants, in, NSF/EPRI, 2013.
[3.53] The Water-Energy Nexus: Challenges and Opportunities, U.S. Department of Energy, 2014.
[3.54] Estimating Freshwater Needs to Meet Future Thermoelectric Generation, National Energy Technology Laboratory, 2011.

[3.55] P.G. Saffman, Lift on a Small Sphere in a Slow Shear Flow, J Fluid Mech, 22 (1965) 385-&.
[3.56] F.A. Morrison, Data Correlation for Drag Coefficient for Sphere, Michigan Technological University, Houghton Michigan, 2013.
[3.57] C.T. Crowe, Multiphase flows with droplets and particles, 2nd ed., CRC Press, Boca Raton, 2012.
[3.58] R. Mei, An Approximate Expression for the Shear Lift Force on a Spherical-Particle at Finite Reynolds-Number, Int J Multiphas Flow, 18(1) (1992) 145-147.
[3.59] R. Enright, N. Miljkovic, J. Sprittles, K. Nolan, R. Mitchell, E.N. Wang, How Coalescing Droplets Jump, ACS Nano, 8(10) (2014) 10352-10362.
[3.60] H. Cha, J.M. Chun, J. Sotelo, N. Miljkovic, Focal Plane Shift Imaging for the Analysis of Dynamic Wetting Processes, Acs Nano, 10(9) (2016) 8223-8232.
[3.61] P. Birbarah, N. Miljkovic, External Convective Jumping-Droplet Condensation on a Flat Plate, International Journal of Heat and Mass Transfer, 107 (2017) 74-88.
[3.62] B. Owens, The Rise Of Distributed Power, General Electric, 2014.
[3.63] M.K. Kim, H. Cha, P. Birbarah, S. Chavan, C. Zhong, Y.H. Xu, N. Miljkovic, Enhanced Jumping-Droplet Departure, Langmuir, 31(49) (2015) 13452-13466.
[3.64] K. Rykaczewski, A.T. Paxson, S. Anand, X. Chen, Z. Wang, K.K. Varanasi, Multimode Multidrop Serial Coalescence Effects during Condensation on Hierarchical Superhydrophobic Surfaces, Langmuir, 29(3) (2013) 881–891.
[3.65] D.P. N. Miljkovic, R. Enright, E. Wang, Dynamics of Coalescence-Induced Jumping Water Droplets, in: arXiv.org, Cornell University Library, 2013.
[3.66] V.P. Carey, Liquid-vapor phase-change phenomena : an introduction to the thermophysics of vaporization and condensation processes in heat transfer equipment, 2nd ed., Taylor and Francis, New York, 2008.
[3.67] D. Torresin, M.K. Tiwari, D. Del Col, D. Poulikakos, Flow Condensation on Copper-Based Nanotextured Superhydrophobic Surfaces, Langmuir, 29(2) (2013) 840-848.
[3.68] J.W. Rose, Condensation of a Vapour in Presence of a Non-Condensing Gas, International Journal of Heat and Mass Transfer, 12(2) (1969) 233.
[3.69] W.C. Lee, J.W. Rose, Forced-Convection Film Condensation on a Horizontal Tube with and without Non-Condensing Gases, International Journal of Heat and Mass Transfer, 27(4) (1984) 519-528.
[3.70] J.R. Thome, Engineering Data Book III, Wolverine Tube, Inc, 2004.
[3.71] H. Schlichting, K. Gersten, Boundary-layer theory, 8th rev. and enl. ed., Springer, Berlin ; New York, 2000.

Chapter 4- Numerical Simulation of Jumping-Droplet Condensation

4.1. Introduction

Dropwise condensation has been widely studied since its discovery in 1930[1]. Dropwise condensation on non-wetting surfaces has the potential to enhance heat transfer performance by up to 2000% when compared to filmwise condensation on wetting surfaces[2-5]. A more recent study revealed that dropwise condensation on suitably-designed low-adhesion superhydrophobic surfaces has the potential to achieve even higher heat transfer coefficients, approaching 100% higher than observed on hydrophobic dropwise condensing substrates [6,7]. The heat transfer enhancement stems from the coalescence-induced jumping of condensate droplets from the surface [8,9]. Termed "jumping-droplet condensation", the coalescence-induced removal of condensate leads to a lower average droplet size on the condensing surface, and hence lower vapor to surface thermal resistance [10,11]. For thin hydrophobic coatings (< 1 μm, $k \approx 0.2$ W/m·K), smaller droplets (100 nm to 10 μm in radii) contribute to a higher heat transfer coefficient since their conduction thermal resistance is lower as compared to larger droplets (>10 μm to 1mm in radii). However, the overall heat flux through the condensing surface is a weighted average of the heat fluxes through individual droplets, with the weights relating to the number density of droplets per size range. Hence, in order to characterize the overall surface heat transfer for dropwise and jumping droplet condensation, the droplet size distribution must be known.

For dropwise condensation on hydrophobic surfaces, the steady state distribution of droplet sizes has been studied by Rose et al. [12] for the case of droplets growing mainly by coalescence. The droplet distribution has been verified experimentally and with numerical simulations [13].

While the Rose distribution was originally derived through empirical observations, it has also been derived separately through the fractal theory [14]. For droplets smaller than the coalescence radius, Abu Orabi devised the analytical population balance model to predict the size distribution function [15,16]. The derivation relied on the Rose distribution for the boundary conditions at the coalescence radius. However, the population balance theory has not been verified experimentally or computationally. As for the distribution provided by Rose, although valid for classical dropwise condensation, it cannot be applied to and does not reflect the physics governing jumping droplet condensation. Specifically: 1) sweeping does not take place and droplet jumping is the only mechanism for droplet removal, 2) for larger apparent contact angles that are observed on superhydrophobic surfaces ($\theta > 150°$), small droplets can grow in the geometric shadow of larger droplets, a process not observed on hydrophobic surfaces ($\theta \approx 90°$), and 3) the main growth mechanism of droplets is via direct condensation with only a fraction of growth occurring via coalescence.

Prior works have attempted to derive an analytical expression for the droplet size distribution for jumping droplet condensation [9]. In addition to the uncertainty related to the population balance theory on which these derivations relied, three main limitations exist: 1) the assumption that droplets are removed exactly when their radius reaches half the coalescence radius defined by the average spacing between nucleation sites. Although the coalescence radius assumption is exact for non-random nucleation site distributions (*e.g.* square lattices, close-packed arrays, etc…), the effective departure radius for randomly distributed droplets differs from that of well-ordered distributions. 2) Droplet size mismatch is an important parameter that determines whether droplets jump or coalesce and remain on the condensing surface, a physical phenomenon currently not tractable with analytical solutions. 3) For jumping droplet condensation, characterized by droplets

having large apparent contact angles (θ > 150°), small droplets can grow in the geometric shadow of larger droplets, a process not captured by past analytical solutions.

Here, we provide a comprehensive analysis of droplet size distributions during jumping droplet condensation. We start by rigorously examining the criteria for achieving steady state condensation. After achieving steady state, the droplet size distribution was obtained for several nucleation site densities. The effect of number of droplets simulated, droplet growth rate, apparent advancing contact angle, minimum jumping radius, and maximum jumping radius was studied. A numerical correlation for the droplet distribution function is provided and the overall heat transfer on the condensing surface is quantified.

4.2. Simulation variables

The variables considered for this work are summarized in tables 1 and 2.

Table 4.1. Simulation variables, nomenclature and values of constants

Name	Symbol (value)	Name	Symbol (value)
Total covered area	A_{c}	Area of 2D coalescences	$A_{\mathrm{coa,2D}}$
Area of 3D coalescences	$A_{\mathrm{coa,3D}}$	Total projected area	A_{p}
Constant relating coalescing droplets sizes	C_{g}	Constant expressing the ratio $R_{\max}/s$	C_{m}
Time step	$\mathrm{d}t$	Droplet size distribution density function	f
Latent heat of vaporization of water	$h_{\mathrm{fg}} \approx 2300\ \mathrm{kJ/kg}$	Liquid vapor interfacial heat transfer coefficient[17]	$h_{\mathrm{i}} \approx 0.4\ \mathrm{MW/\ (m^2 \cdot K)}$[17]
Combined interfacial and droplet heat transfer coefficient	$h_{\mathrm{i+drop}}$	Thermal conductivity of hydrophobic coating	$k_{\mathrm{coat}} \approx 0.2\ \mathrm{W/(m \cdot K)}$
Thermal conductivity of liquid water	$k_{\mathrm{w}} \approx 0.6\ \mathrm{W/(m \cdot K)}$	Side length of condensing (square) surface	L
Number of nucleation sites	N_0	Number of 2D coalescences	$N_{\mathrm{coa,2D}}$

Table 4.1. (cont)

Number of 3D coalescences	$N_{\mathrm{coa,3D}}$	Number of jumps	N_{j}
Overall condensation heat flux	q''	Droplet heat transfer	q_{d}
Droplet Radius	R	Average radius of coalescing droplets	R_{coalesce}
Specific gas constant	R_{g}	Maximum jumping droplet radius	$R_{\mathrm{jump,max}}$
Minimum jumping droplet radius	$R_{\mathrm{jump,min}}$	Maximum droplet radius on the surface	R_{max}
Time	t	Temperature of condensing surface	T_{s}
Saturation temperature	T_{sat}	Condensation accommodation coefficient	α
Surface tension (liquid-vapor)	$\gamma \approx 72\ \mathrm{mN/m}$	Thickness of hydrophobic coating	δ
Apparent advancing contact angle	θ	Liquid water density	$\rho_{\mathrm{l}} \approx 998\ \mathrm{kg/m^3}$
Water vapor density	ρ_{v}	Standard deviation (population) of the radius of coalescing droplets	$\sigma_{\mathrm{R,coalesce}}$
Thermal resistance	ψ	Coating thermal resistance	ψ_{coat}
Droplet conduction thermal resistance	ψ_{drop}	Interfacial thermal resistance	ψ_{i}

Table 4.2. Defining equations of some basic variables

Name	**Symbol (Formula)**	**Equation number**
Number density of nucleation sites	$N_{\mathrm{s}} = \frac{N_0}{L^2}$	(4.1-a)
Average spacing between random nucleation sites [18]	$s = \frac{1}{\sqrt{4N_{\mathrm{s}}}}$	(4.1-b)
Coalescence radius	$R_{\mathrm{c}} = \frac{s}{2}$	(4.1-c)
Standard deviation for site spacing [18]	$\sigma_{\mathrm{s}} = \sqrt{\frac{(4-\pi)}{4\pi N_{\mathrm{s}}}}$	(4.1-d)

Table 4.2. (cont)

Droplet radius of the largest droplet present on the surface	$R_{\min} = \frac{2\gamma T_{\text{sat}}}{\rho_{\text{l}} h_{\text{fg}} \Delta T} \approx 10 \text{ nm}$	(4.1-e)
Condensation temperature potential	$\Delta T = T_{sat} - T_{\text{s}}$	(4.1-f)
Droplet coalescence mismatch parameter	$m = \frac{\sigma_{\text{R,coalesce}}}{R_{\text{coalesce}}}$	(4.1-g)
Biot number	$\text{Bi} = \frac{h_{\text{i}}}{R \sin\theta \, k_{\text{w}}}$	(4.1-h)
Nusselt number	$\text{Nu} = \frac{h_{\text{i+drop}}}{k_{\text{w}} R \sin\theta}$	(4.1-i)

4.3. Individual Droplet Growth Rate

The growth rate of a single droplet condensing on a non-wetting surface is modeled with a thermal resistance approach[15]. The thermal resistances (ψ) include the liquid-vapor interfacial resistance (eq. 4.2), droplet conduction resistance (eq. 4.3), hydrophobic coating resistance (eq. 4.4), and temperature drop due to droplet curvature:

$$\psi_{\text{i}} = \frac{1}{h_{\text{i}} 2\pi R^2 (1 - \cos\theta)}, \tag{4.2}$$

$$\psi_{\text{drop}} = \frac{\theta}{4\pi R k_{\text{w}} \sin\theta}, \tag{4.3}$$

$$\psi_{\text{coat}} = \frac{\delta}{k_{\text{coat}} \pi R^2 \, sin^2\,\theta}. \tag{4.4}$$

Figure 1 depicts the thermal resistance breakdown. For smaller droplets (R < 100 nm), the coating thermal resistance dominates, whereas at larger length scales (R > 1 mm), the droplet conduction thermal resistance dominates. The coating thickness (δ) is an important parameter that affects the thermal resistance circuit and is chosen here to be 1 μm, with a thermal conductivity of

0.2 W/(m·K)[15]. The temperature drop due to droplet curvature is only important for very small droplets ($R \sim R_{\min} < 100$ nm) and is accounted for in the droplet growth rate calculation.

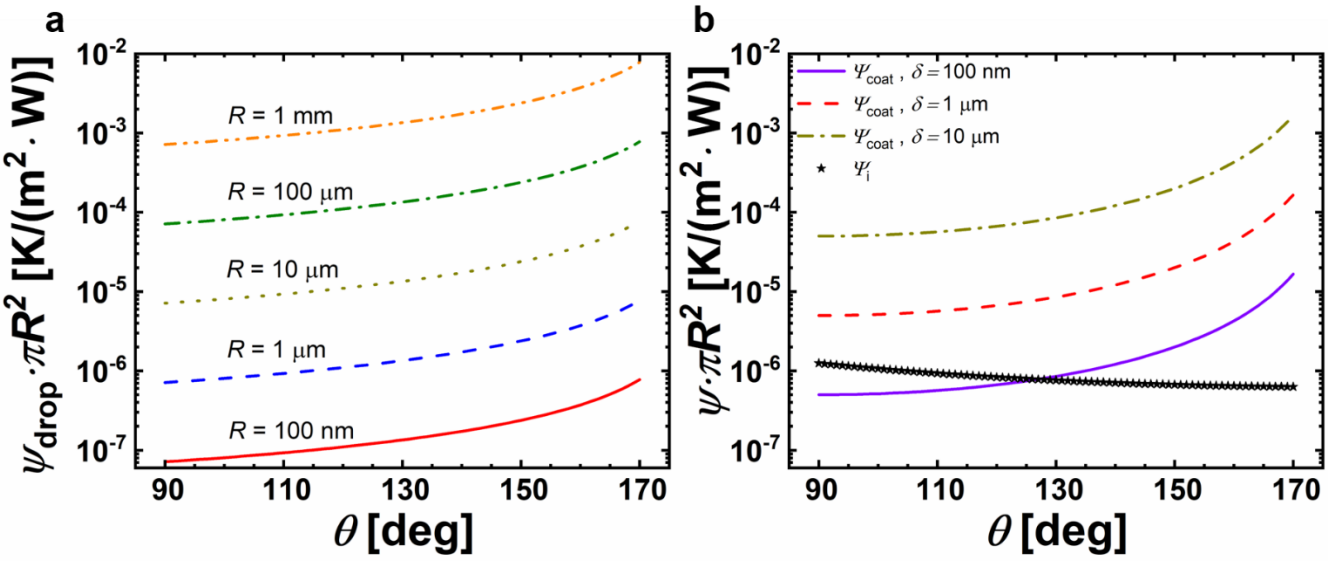

Figure 4.1. Thermal resistance ($\boldsymbol{\psi\pi R^2}$) of a droplet having radius, $\boldsymbol{R}$, condensing on a hydrophobic surface as a function of the apparent advancing contact angle, $\boldsymbol{\theta}$. The thermal resistances depicted are the (a) droplet conduction resistance ($\boldsymbol{\psi_{drop}\pi R^2}$, eq. 4.3), and (b) hydrophobic coating resistance ($\boldsymbol{\psi_{coat}\pi R^2}$, eq. 4.4) with the liquid-vapor interface resistance shown ($\boldsymbol{\psi_i\pi R^2}$, eq. 4.2).

The overall heat transfer rate through a droplet can be determined from the vapor-to-surface temperature difference (ΔT) and the thermal resistances, which has been shows previously to be [15]:

$$q_{\mathrm{d,Kim}} = \frac{\Delta T \pi R^2 (1 - R_{\min}/R)}{\left(\frac{\delta}{k_{\mathrm{coat}} \sin^2\theta} + \frac{R\theta}{4k_{\mathrm{w}} \sin\theta} + \frac{1}{2h_{\mathrm{i}}(1-\cos\theta)}\right)}. \tag{4.5}$$

The heat transfer through a droplet can also be calculated from the enthalpy dissipated by the condensing vapor:

$$q_{\mathrm{d}} = \rho_{\mathrm{l}} h_{\mathrm{fg}} \pi R^2 (1-\cos\theta)^2 (2+\cos\theta) \frac{\mathrm{d}R}{\mathrm{d}t}. \tag{4.6}$$

In order to determine the interfacial heat transfer coefficient, we used the kinetic theory formulation to obtain a close form solution presented in the past [9,17,19]

$$h_{\mathrm{i}} = \frac{2\alpha}{2-\alpha}\frac{1}{\sqrt{2\pi R_{\mathrm{g}} T_{\mathrm{s}}}}\frac{\rho_{\mathrm{v}} {h_{\mathrm{fg}}}^2}{T_{\mathrm{s}}} \tag{4.7}$$

where α is the condensation accommodation coefficient. The accommodation coefficient represents the fraction of vapor molecules that will be captured by the liquid droplet. It is often assumed that the accommodation coefficient is equal to unity [9,15]. At ambient conditions, $h_{\mathrm{i}} \approx 0.4\ \mathrm{MW/(m^2 \cdot K)}$[17], and is held constant throughout the simulations.

Recent simulations have suggested that the isotherm model provided in the aforementioned analysis for droplet conduction resistance (eq. 4.3) is inaccurate and results in an infinite heat flux at the contact line [20]. A more recent work proposed a modified correlation for the interfacial resistance and the droplet conduction thermal resistance. The non-dimensional correlation represents the Nusselt number (Nu, eq. 4.1-i) as a function of Biot number (Bi, eq. 4.1-h) and the apparent advancing contact angle (θ). The modified individual droplet heat transfer becomes:

$$q_{\mathrm{d,Chavan}} = \frac{\Delta T \pi R^2 (1 - R_{\min}/R)}{\left(\frac{\delta}{k_{\mathrm{coat}} \sin^2\theta} + \frac{1}{\mathrm{Nu}(\theta, Bi) k_{\mathrm{w}} R \sin\theta\, \pi R^2}\right)}. \tag{4.8}$$

In order to determine the individual droplet growth rate, eq. (4.5) and (4.6) were equated. The parameters used in the model were ΔT = 10 K, $R_{\min}$ = 10 nm, δ = 1 μm, k_{w} = 0.6 W/m·K, h_{i} = 0.4 MW/m^2·K, ρ_{l} = 1000 kg/m^3, h_{fg} = 2.3 MJ/kg, k_{coat} = 0.2 W/m·K. The apparent advancing contact angle was θ = 175°, unless explicitly noted.

Figure 4.2 depicts the two independent droplet growth rate calculations. While the approaches agree with each other for small droplets (R < 10 μm), they differ for larger droplets (R > 10 μm). For our current study, eq. (4.8) was used to calculate the individual growth rate during simulations.

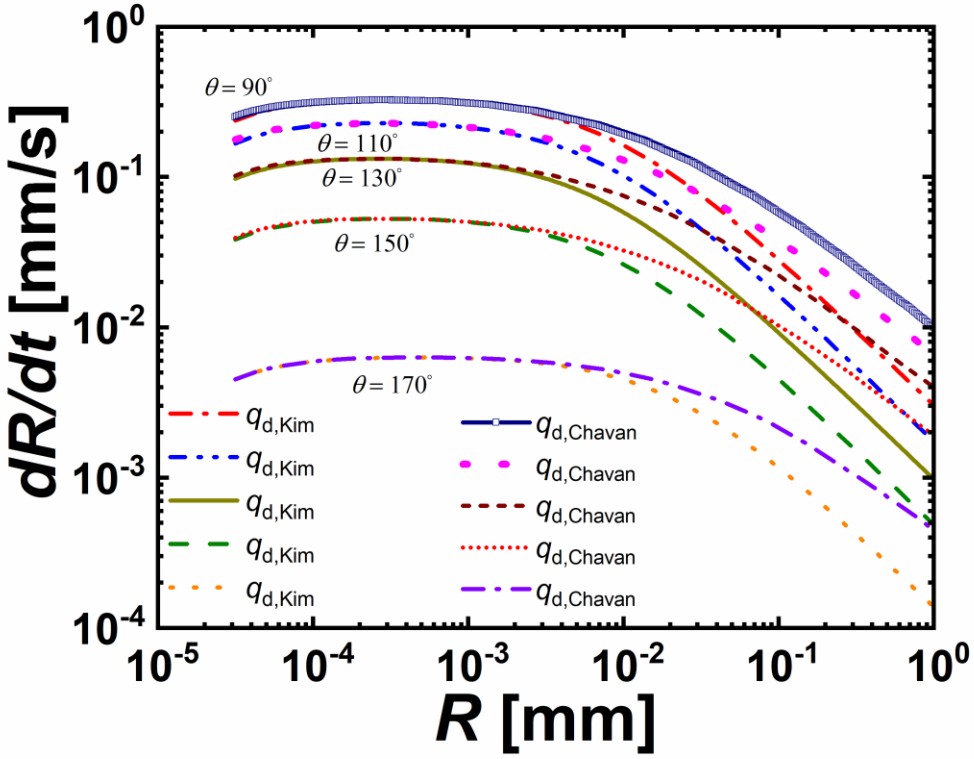

Figure 4.2. Droplet growth rate ($\boldsymbol{dR/dt}$) as a function of droplet radius $\boldsymbol{R}$. The heat transfer through the droplet was calculated via eq. (4.5) for the thermal resistance model (Kim & Kim,*[15]*) and via eq. (4.8) for the more recent model (Chavan,*[20]*). The hydrophobic coating thickness was assumed to be 1 μm.

4.4. The Simulation

The simulation begins by randomly distributing the number of condensate nucleation sites, N_0, on the surface (Fig. 4.3). Next, we initiated a droplet on each nucleation site with a size equivalent to the critical nucleation radius as specified by eq. (4.1-e). Prior to iterating in time, the time step was chosen such that the product of the maximum growth rate and the time step resulted in a change of radius equivalent to a tenth of the average spacing between droplets, or a fifth of the average coalescence radius. The finite and small time step guaranteed adequate granularity to access the

direct droplet growth mode prior to coalescence. After initiating time iteration, coalescence checks were made for each iteration such that clusters of droplets that intersect were captured. From the intersecting droplets, the radius of the resulting coalesced droplet was calculated via conservation of mass. If the calculated radius (post-coalescence) resided between the minimum jumping radius ($R_{\mathrm{jump,min}}$ = 1 μm) and the maximum jumping radius ($R_{\mathrm{jump,max}}$ = 100 μm)[21], an additional check was performed for droplet size mismatch. Past studies have observed experimentally that when two coalescing droplets merge, if one has a radius exceeding 150% of the other, there is a reduced chance of jumping [22,23]. For a multi-droplet (more than 2 droplets merging) coalescence events, we generalize the problem by setting the constraint that jumping occurs if m < 0.2, where m represents the mismatch between droplets as expressed by the ratio of the radius standard deviation (population-based) to the mean radius (eq. 4.1-g). When all of the aforementioned conditions are met, droplets jump and are hence artificially removed from the simulation domain.

At each iteration, the number of jumping events (N_{j}) was recorded. The next step in each iteration was the growth of droplets and droplet re-nucleation. For re-nucleation, we checked whether the initial nucleation sites were covered by an existing droplet. Only if a nucleation site was "free" (i.e. not covered), then a droplet with radius R_{min} was seeded at that location. The seeding step marked the end of each iteration. The algorithm was repeated until the number of jumping events had reached a specified value. Figure 4.3 shows a schematic breakdown of the algorithm steps used in the simulation. Figure 4.4 shows representative top-view snapshots of the surface at multiples of the time step $\mathrm{d}t$. The outlined regions mark jumping events that occurred due to coalescence on the superhydrophobic surface at consecutives time steps. It is important to note, although Figure 4.4 shows a top view two-dimensional projection, the numerical model was

implemented in three-dimensions. Figure 4.5 shows representative three-dimensional isometric snapshots during condensation on the superhydrophobic surface with a higher magnification than Figure 4.4.

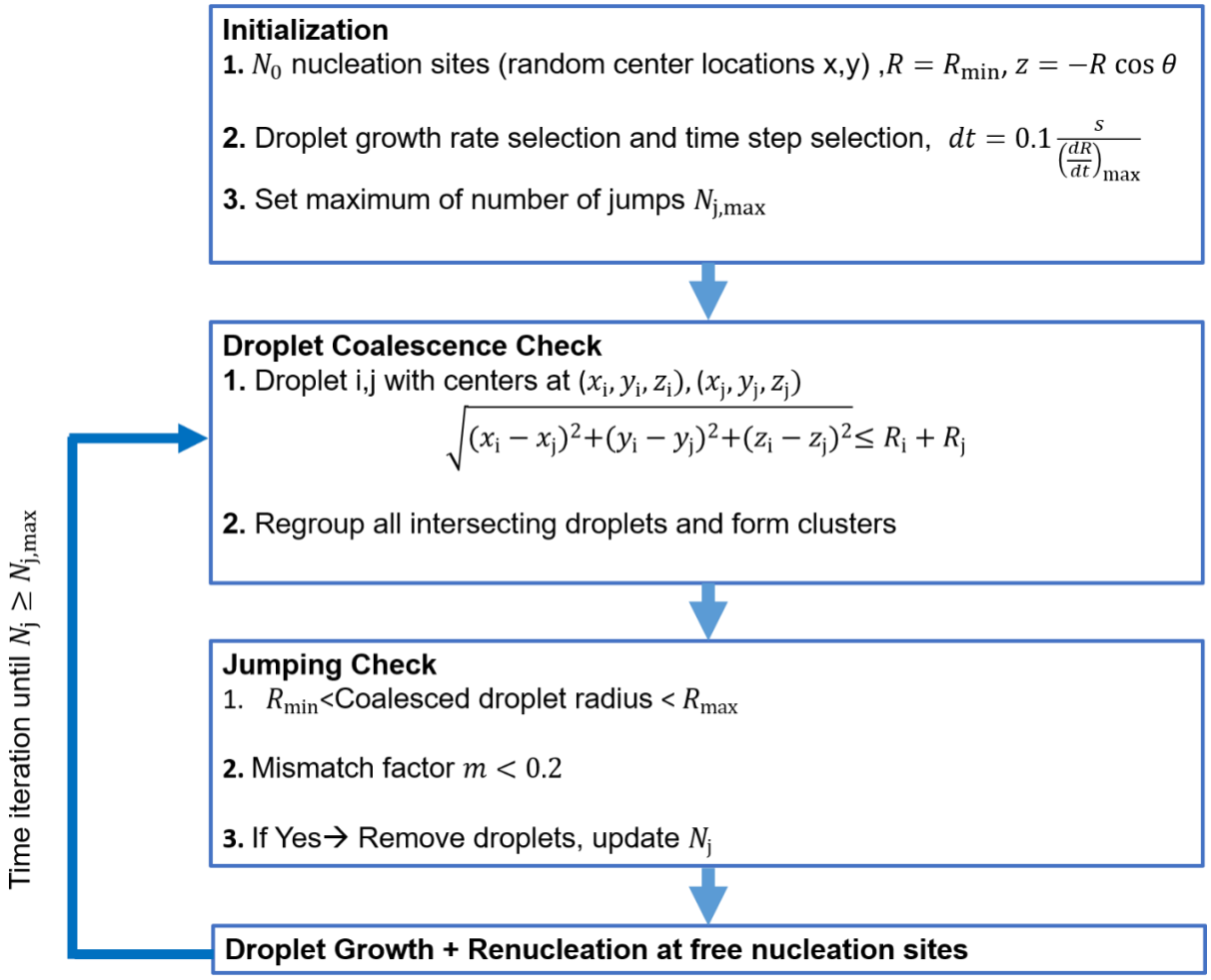

Figure 4.3. Flow chart of the numerical algorithm used to implement the jumping droplet simulation.

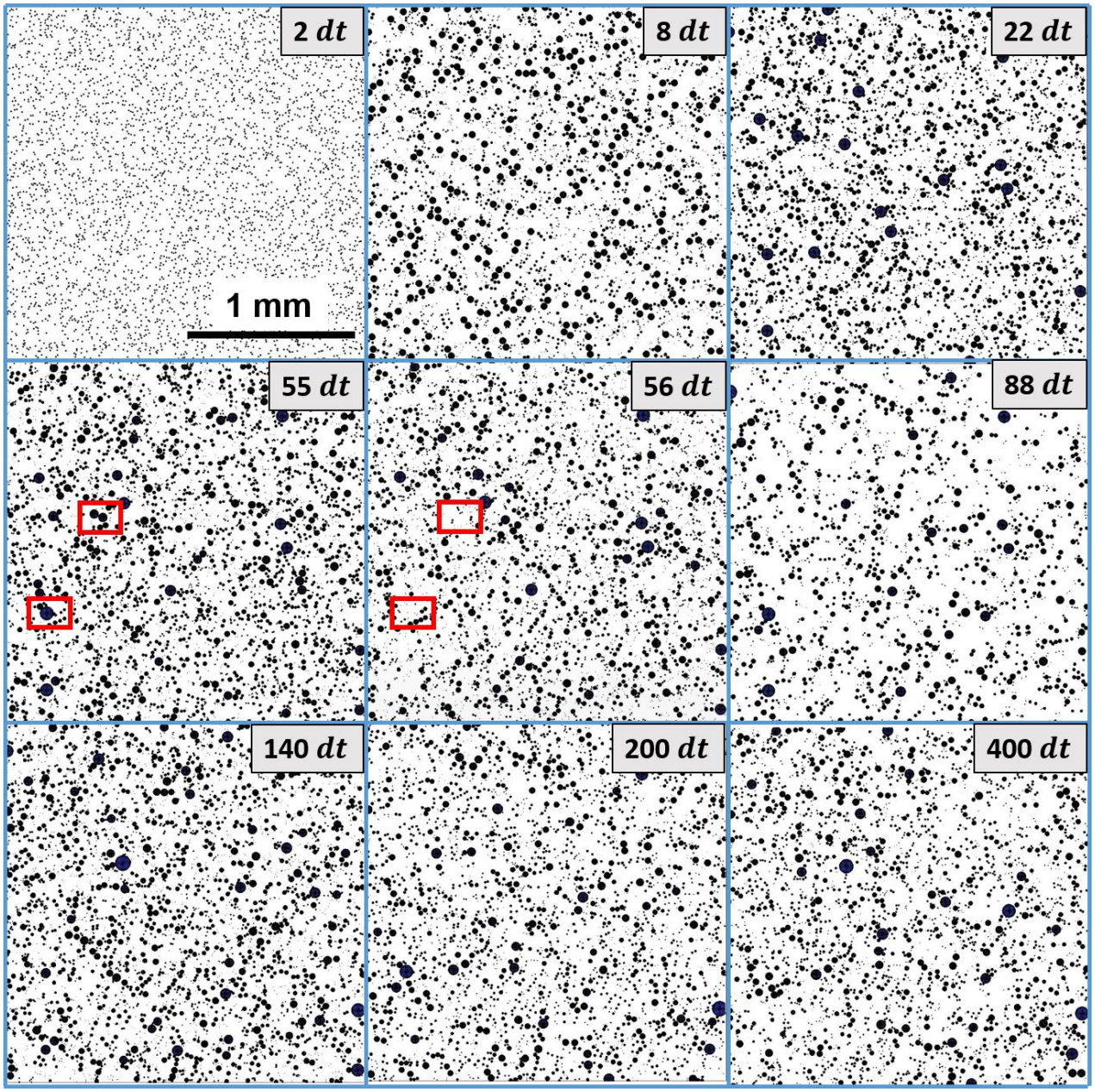

Figure 4.4. Time-lapse top-view images of simulated jumping droplet condensation. Black represents liquid condensate while white represents the superhydrophobic surface. Snapshots are taken at different multiples of the time step ($\boldsymbol{dt}$ = 0.3 ms for this simulation). Areas outlined in red boxes reveal droplet jumping. Simulation parameters: $\boldsymbol{N_0}$ = 5000 sites, $\boldsymbol{L}$ = 2.2 mm, $\boldsymbol{\theta}$ = 175°.

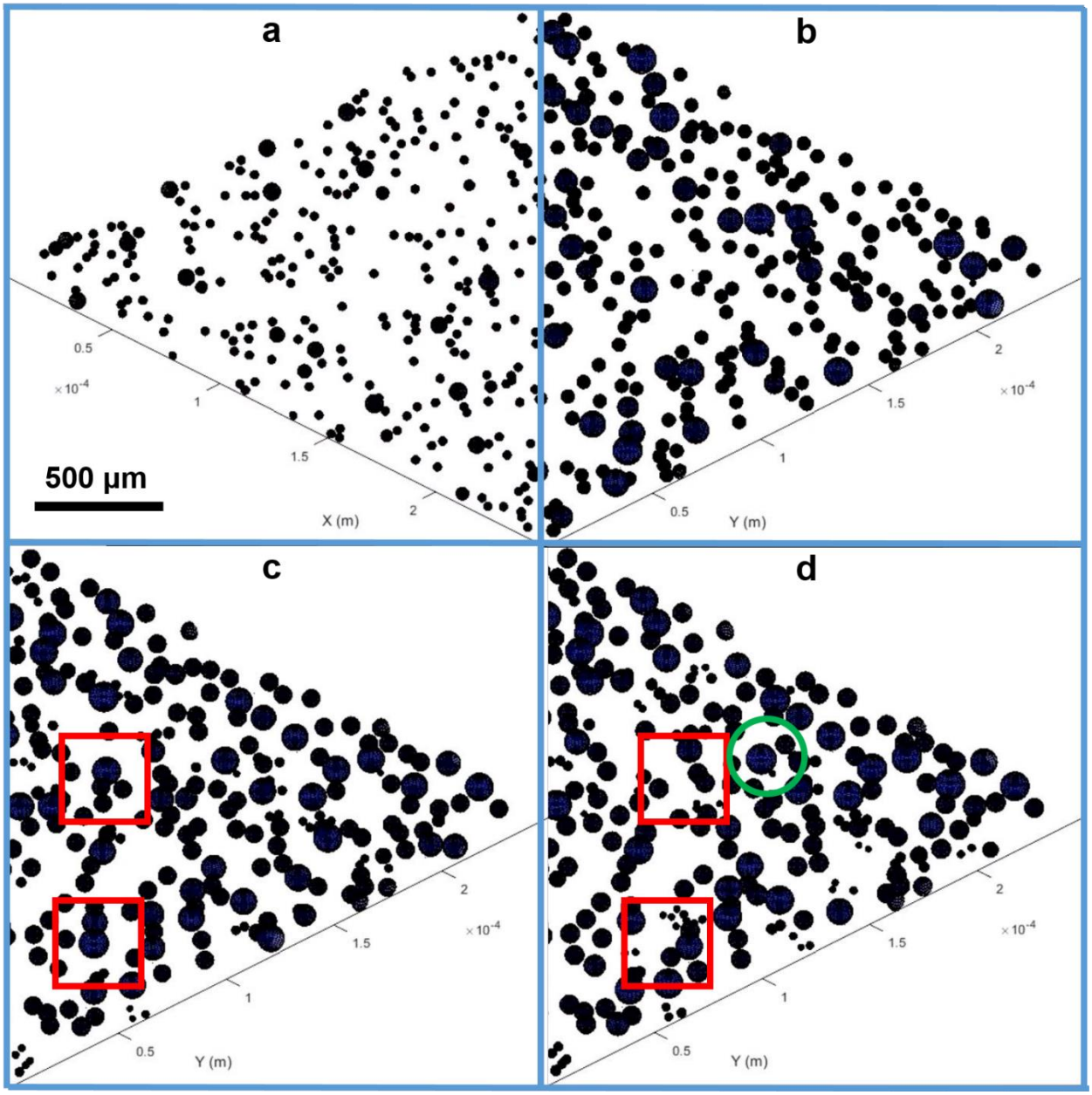

Figure 4.5. 3D time lapse images of jumping droplet condensation simulation, N_0 = 1000, L=2.5mm, $\boldsymbol{\theta}$=170° and dt = 0.3 ms. (a) Droplets are small shortly after the start of the simulation (5 dt), as compared to (b) at 20 dt. (c) and (d) are taken within 2 time steps from each other at steady state (>200 dt). Areas outlined in a red circle depict jumping droplets that disappear between (c) and (d) whereas the green circle depicts a small droplet feeding the large droplet from within the latter's geometric shadow.

4.4.1 Steady State Criterion

We hypothesize that one way of tracking whether steady state has been achieved during jumping-droplet condensation is by checking the maximum droplet radius on the surface. If the maximum radius reaches a constant value that is bounded, then we know that the droplets on average are not growing anymore. An alternate method to check steadiness is to check if the droplet distribution is changing over time, by calculating a standard cumulative error. The latter method, however, lacks physical insight compared to the former, hence we tracked the maximum radius on the surface as an indicator of achieving steady state, double checking the result with the obtained distribution.

Figure 4.6 depicts the maximum droplet size ($R_{\max}$) obtained as an ensemble average over 50 simulations as a function of the number of jumping events (N_j) that have occurred on the condensing surface (1 mm^2 with N_0 = 1,000 sites). The simulation used the droplet growth rate formulation developed in the previous section with $\theta = 175°$, and droplet mismatch not considered (*i.e.* all coalescing droplets jumped). The cumulative average and the right-half (RH) cumulative average were plotted as metrics for convergence. The RH cumulative average was calculated from half the data points taken from the right side as opposed to the whole dataset, both in cumulative terms. It was observed, as expected, that the RH cumulative average converged faster than the cumulative average since the starting set of data (left half) was dispatched during the calculation. The number of jumping events to steady state, however, was expected to vary as the number of nucleation sites vary, and possibly for different number densities. Therefore we normalized the number of jumping events by the number of initial nucleation sites, and plotted convergence curves for multiple cases. The results shown in Figure 4.6(b) prove that the unified steady state criterion could be formulated in terms of the number of jumping events, N_j, normalized by the number of

sites simulated, N_0. Simulations for N_0 = 1,000, N_s = 10^3 sites/mm^2, N_0 = 1,000, N_s = 10^5 sites/mm^2 and N_0=10,000, N_s = 10^3sites/mm^2 were performed. The simulations enabled us to change the droplet number density while keeping the number of sites constant and vice versa. The results showed that steady state was reached (within 3% error of the average of R_{max}) when the number of jumping events reached $\approx 20N_0$, independently of the number density, N_s. The number of droplets simulated did not affect the final value of R_{max}, as will be discussed in the next section.

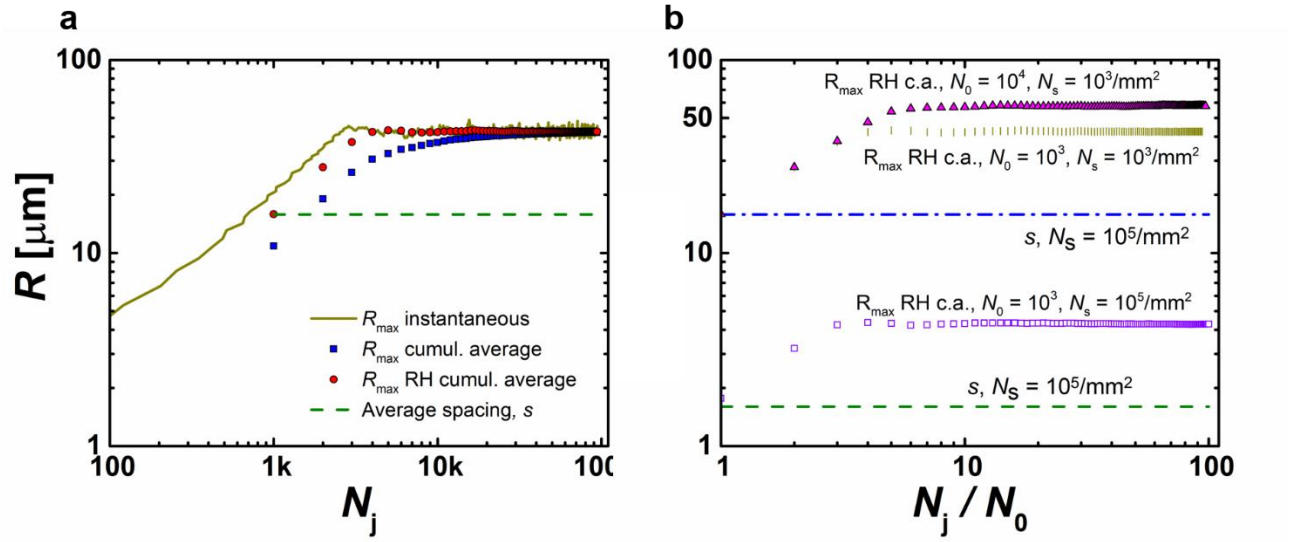

Figure 4.6. Steady state convergence of the maximum droplet size $\boldsymbol{R_{max}}$, taken as an ensemble average over 50 simulations, as a function of the (a) number of jumping events ($\boldsymbol{N_j}$) that have occurred on the condensing surface having dimensions 1 mm^2 with 1,000 nucleation sites, $\boldsymbol{\theta}$ = 175°, and droplet mismatch not considered. The cumulative and right half (RH) cumulative time averages are plotted as metrics for convergence. The RH cumulative average was calculated from half the data points taken from the right side as opposed to the whole dataset, both in cumulative terms. The average spacing, $\boldsymbol{s}$, between nucleation sites was calculated from Eq. 4.1-b. (b) The RH cumulative average (c.a.) as a function of the number of jumping events normalized by the number of sites simulated. The average value was reached within a 3% error when the number of jumping events reached $\approx 20\boldsymbol{N_0}$.

4.4.2. Effect of Number of Simulated Sites

The initial number of droplets simulated (number of nucleation sites), N_0, was varied for a constant number density (changing condensing area), in order to determine its effect on the jumping droplet distribution. We observed that increasing N_0 from 1,000 to 10,000 increased the maximum droplet

radius on the surface. Figure 4.7 shows the normalized maximum droplet radius $R_{\max}$ as a function of the normalized number of jumping events (representing the time axis). For a nucleation site density of N_s = 10^3 sites/mm^2, the steady state average of $R_{\max}$ increased by 19% as N_0 is increased from 1,000 to 5,000 nucleation sites. Furthermore, the steady state average of $R_{\max}$ increased by 35% as N_0 was increased from 1,000 to 10,000 sites. The same increasing behavior was observed at larger nucleation site densities (N_s = 10^5 sites/mm^2), where the respective increases in $R_{\max}$ were 17% and 30%. The increase in $R_{\max}$ was justifiable since $R_{\max}$ is correlated with the maximum spacing between two nearest droplets as defined by the number of nucleation sites. As the sample size was increased, a higher probability for deviation from the mean occurred. However, the distribution of nucleation site spacing becomes more narrow at higher number densities (as shown by the decreasing standard deviation in eq. 4.1-d [18]). Nevertheless, the effect of the number of sites simulated on the overall droplet size distribution was shown to be negligible even at lower nucleation densities (N_s = 10^3 sites/mm^2).

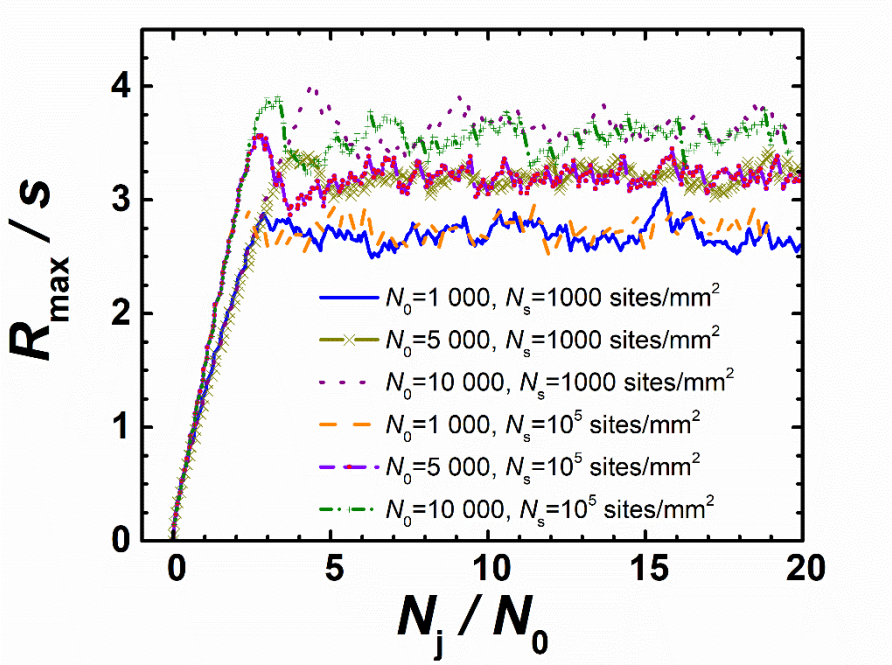

Figure 4.7. Normalized maximum droplet radius $\boldsymbol{R_{max}/s}$ as a function of time, as represented by the number of jumping events normalized by the number of nucleation sites simulated,

$\boldsymbol{N_j/N_0}$. The curves are plotted for two different number densities ($\boldsymbol{N_s}$ = 10^3 and 10^5 sites/mm^2), with variation of the number of simulated sites ($\boldsymbol{N_0}$ = 1,000, 5,000, and 10,000). For both nucleation densities, $\boldsymbol{R_{max}}$ remained below four times the average spacing, $\boldsymbol{s}$, with an increasing value correlated with the increase in sample size.

4.4.3. Steady State Considerations

As a first attempt to obtain physical insight into the validity of the developed simulation, we tested our hypothesis stating that the droplet size distribution reaches steady state when the maximum jumping radius ceases to change. For surfaces where droplet return is not present (vertical surface or horizontal facing downward with minimal vapor flow entrainment)[24-27], with droplets jumping without the droplet size mismatch constraint, the simulations demonstrated that steady state was reached for all conditions except for very low droplet number density where $R_{\max}$ exceeded the maximum jumping radius (≈100 μm). The latter was only the case for small nucleation sites densities $N_s < 600$ sites/mm^2 (assuming $R_{\max}$ is bounded by $\approx 5s$, Fig. 4.6), much lower than real life practical cases ($N_s \sim$ 50,000 sites/mm^2, [4]).

Without the droplet mismatch constraint, droplets cannot grow indefinitely as they would touch other droplets, coalesce, and jump eventually, regardless of their size compared to the coalescing droplets. In a real experiments, however, coalescing droplets do not jump regardless of their respective sizes. Droplets having large size mismatch ($R_1/R_2 > 1.5$) do not jump, partly due to loss of momentum transfer in the direction normal to the surface. The inability for droplets to jump at any radius mismatch[28-36] required us to implement a mismatch constraint in the simulations, which required that the population based standard deviation of the coalescing droplets is 5X (based on two droplet coalescence analogy) less than their average. In order to determine whether the droplet mismatch constraint affected our steady state criteria, we plotted $R_{\max}$ as a function of time for both low (N_s =10^3 sites/mm^2) and high (N_s =10^5 sites/mm^2) nucleation site

densities. We compared the results to the cases where droplet mismatch was not considered (Fig. 4.8), with simulations performed for N_0 = 1,000, 5,000, and 10,000 sites. Figure 4.8(a) shows that for N_s = 10^3 sites/mm^2, $R_{\max}$ kept growing over time. This behavior was not observed for higher number densities (N_s = 10^5 sites/mm^2, Fig. 4.8b). The results indicated that droplet mismatch can hinder the simulation from achieving steady state at low number densities (< 10^3 sites/mm^2) as large droplet spacing allows for droplets to reach large sizes (≈50 μm) compared to the jumping radius (≈1 μm) resulting in large mismatch being more likely to occur during coalescence. At higher number densities (> 10^5 sites/mm^2) the continued $R_{\max}$ growth behavior disappeared since the maximum droplet size (< 6 μm) was comparable to the jumping radius of 1 μm. The results indicated that steady state is achieved if $R_{\max}/R_{\text{jump,min}}$ < 50. For realistic number densities during jumping droplet condensation ($N_s >$ 50,000 sites/mm^2), steady state was easily achieved, and the remainder of the study will focus on the distribution density function of simulated cases representing realistic conditions.

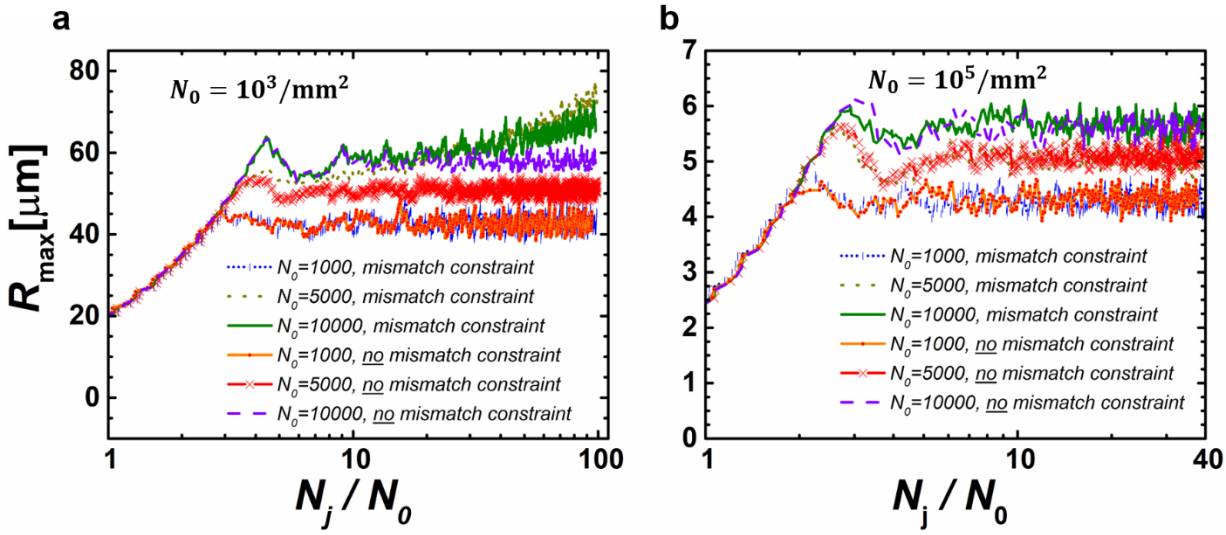

Figure 4.8. Effect of the droplet mismatch criterion on steady state behavior of jumping droplet condensation for nucleation site density of (a) $\mathbf{N_s}$ = 10^3 sites/mm^2 and (b) $\mathbf{N_s}$ = 10^5 sites/mm^2. Each graph shows the maximum droplet radius $\mathbf{R_{max}}$ as a function of time, as represented by the number of jumps normalized by the number of nucleation sites simulated ($\mathbf{N_j/N_0}$). For $\mathbf{N_s}$ = 10^3 sites/mm^2, the mismatch constraint led to $\mathbf{R_{max}}$ continuously growing and hence

preventing the achievement of steady state in cases where $\mathbf{R_{max}}$ > 50 μm. For $\mathbf{N_s}$ = 10^5 sites/mm^2, the mismatch constraint did not affect the achievement of steady state and $\mathbf{R_{max}}$ matched with the case of no mismatch constraint applied (Fig. 4.6).

4.5. Droplet Size Distribution Function

After determining the criteria for achieving steady-state, we performed simulations with N_0 = 1,000 sites. Using steady state defined as $N_j/N_0 > 20$ for $N_s \geq 10^4$ sites/mm^2, we simulated jumping droplet condensation to study the droplet size distribution for a variety of conditions.

4.5.1. Effect of Nucleation Site Density

Figure 4.9 shows the droplet size distribution (f) as a function of droplet radius for varying nucleation site densities (N_s). To achieve a more physical comparison, we non-dimensionalized the curves by normalizing the droplet radius (R) by the characteristic length scale (s) and the distribution function by N_s/s. Figure 4.9 shows that the droplet population has a fractal-like behavior. While the curves for N_s = 10^4 and 10^5 sites/mm^2 show similar behavior in terms of their decay characteristics, distributions with larger nucleation densities increasingly deviated from the norm (Fig. 4.9, inset). For N_s = 10^4 and 10^5 sites/mm^2, the left side of the distribution function (R/s < 0.1) asymptoted to a constant value. However, for N_s = 10^6 and 10^7 sites/mm^2, the asymptotic behavior was not attained since the coalescence radius (s) approached the critical nucleation radius (R_{min}). The tail of the distribution also changed at higher droplet densities due to the minimum jumping radius criteria. To gain more insight into the distribution, we plotted the normalized maximum radius (R_{max}/s) as a function of the number of jumps (N_j) (figure 4.10). We observed that increasing the nucleation site density from 10^4 to 10^6 sites/mm^2 slightly increased the coalescence based growth rate (slope of the straight line [12]). Furthermore, the increase in nucleation site density tended to decrease R_{max}/s, as expected, due to the decreasing standard

deviation of site spacing (Eq. 4.1-d). The highest nucleation density (10^7 sites/mm^2) revealed a different regime that will be explored in the next section.

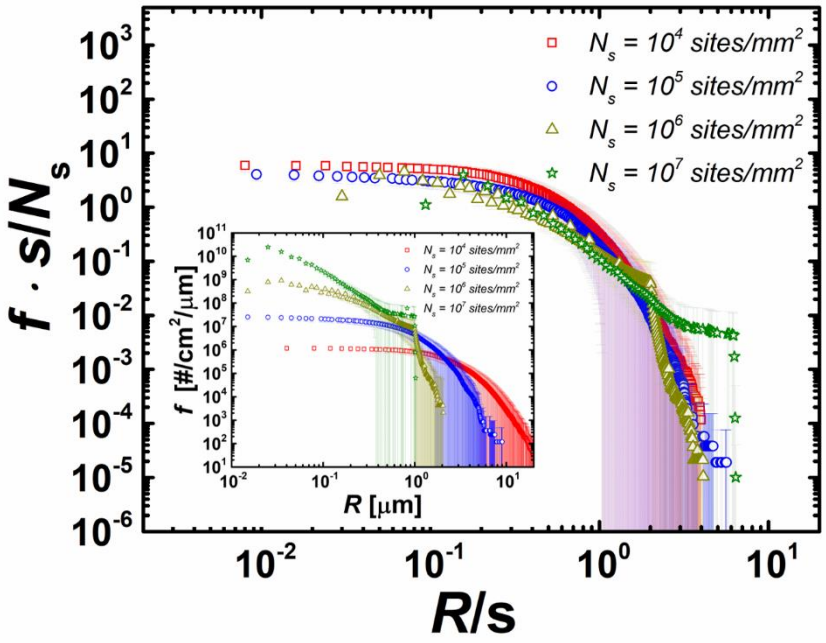

Figure 4.9. Non-dimensional droplet size distribution ($\boldsymbol{f}$) as a function of normalized droplet radius ($\boldsymbol{R/s}$). Inset: Dimensional droplet size distribution functions as a function of droplet radius ($\boldsymbol{R}$) prior to non-dimensionalization. Error bars arise due to the random error (standard deviation) obtained by repeating the simulation 50 times and have been made partially transparent for clarity.

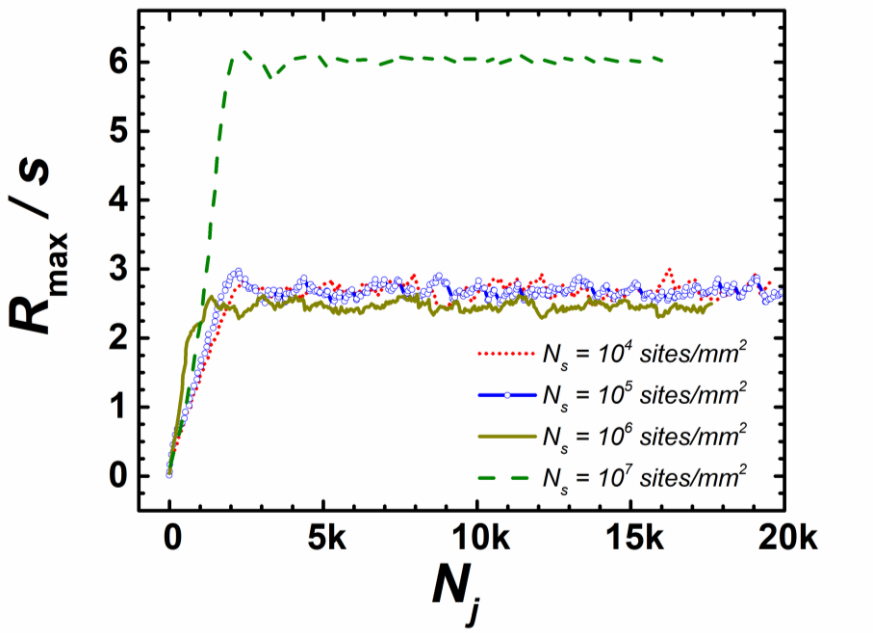

Figure 4.10. Normalized maximum droplet radius ($\boldsymbol{R_{max}/s}$) as a function of the number of jumps ($\boldsymbol{N_j}$) for different nucleation site densities ($\boldsymbol{N_s}$). The number of simulated sites was set to $\boldsymbol{N_0}$ = 1000 droplets for all simulations. The increase in $\boldsymbol{N_s}$ from 10^4 to 10^6 sites/mm^2 slightly increased the coalescence based growth rate (slope of the straight line). The highest nucleation density ($\boldsymbol{N_s}$ = 10^7 sites/mm^2) revealed a different regime.

4.5.2. Effect of Minimum Jumping Droplet Radius

The minimum jumping droplet radius ($R_{\text{jump,min}}$) was varied in order to study how it effects the droplet size distribution. Physically, $R_{\text{jump,min}}$ has been shown to depend on the droplet-surface adhesion, manifested macroscopically by the contact angle hysteresis on the condensing surface. Experimentally, the minimum jumping droplet departure radius for water has been shown to be as low as $R_{\text{jump,min}}$ = 375 nm, and as high as $R_{\text{jump,min}}$ = 100 μm[37]. Theory reveals that inertial-capillary forces govern droplet coalescence even at nanometric length scales[37,38]. It is important to note that as droplet radii approach 300 nm, jumping ceases to happen after coalescence due to viscous effects starting to dominate inertial-capillary forces in the coalescing bridge at small length scales[8].

For N_s = 10^5 sites/mm^2 with N_0 = 1000 sites, we ran simulations for $R_{\text{jump,min}}$ = 0.1, 1, 3, 6 and 10 μm, with an average droplet spacing s = 1.6 μm. Figure 4.11 shows the jumping droplet

distribution as a function of droplet radius for varying $R_{\mathrm{jump,min}}$. The results show that the right side of the distribution flattens for large $R_{\mathrm{jump,min}}$ (> 6 μm) similarly to the curve for large number density (N_s=10^7/mm^2), indicating that curve flattening was due to the average spacing between droplets becoming small compared to the minimum jumping radius. For N_0 = 1000 sites, we observed that the maximum radius of droplets residing on the surface at steady state reached approximately three times the average spacing between droplets ($\approx 3s$, Fig. 4.6). However if the maximum droplet radius exceeded the jumping radius, then the maximum radius on the surface became the jumping radius, as given by the equation:

$$R_{\max} = \min\left(C_{\mathrm{m}} \cdot s\,,\; C_{\mathrm{g}} \cdot R_{\mathrm{jump,min}}\right), \tag{4.9}$$

where C_{m} is a constant depending on the number of droplet simulated. For N_0 = 1000, $C_{\mathrm{m}} \approx 3$. However, for N_0 = 10^4, $C_{\mathrm{m}} \approx 3.9$ (Fig. 4.6) and can increase further at a decreasing rate for higher N_0. The increase of C_{m} as a function of N_0 was observed to mitigate at higher droplet densities. The factor C_{g} ($0 < C_{\mathrm{g}} < 1$) represents the ratio of pre-to-post coalescence radius and depends on the average size mismatch between coalescing droplets. The factor C_{g} can be obtained from the conservation of volume at a constant condensate density. For n equally sized coalescing droplets, $C_{\mathrm{g}} = 1/n^{1/3}$, (≈0.8 for n = 2). For the cases simulated here, $C_{\mathrm{g}} \approx 1$ showing that droplets close to the minimum jumping radius merged with smaller droplets on average. Hence, the distribution flattening can be explained by the fact that all droplets were well beyond their natural maximum spacing and would jump as soon as they reach the jumping radius. The curve flattening was observed to initiate at $R \approx 2s$, increasing as the difference between $C_{\mathrm{m}} \cdot s$ and $R_{\mathrm{jump,min}}$ increased, as seen from the cases of $R_{\mathrm{jump,min}}$ = 3 and 6 μm. The case of $R_{\mathrm{jump,min}}$ = 3 μm shows

a transient regime where the $R_{\max}$ approaches the value of 3 μm expressed by $R_{\text{jump,min}}$. A clear cut-off in the tail of the droplet distribution appears for $R_{\max}$ = 6 μm and $R_{\max}$ = 10 μm.

4.5.3. Effect of Maximum Jumping Droplet Radius

The radius at which droplets coalesce and jump need not be fixed, and can exhibit a range of values[35]. One way to modify $R_{\text{jump,max}}$ is by microstructuring the surface to pin droplets between pre-designed structures such as pillars. In our simulations, for values where $R_{\text{jump,max}}$ was higher than the maximum droplet radius on the surface at steady state, changing $R_{\text{jump,max}}$ had no effect on the droplet distribution. If, however, $R_{\text{jump,max}}$ was lowered to a value below the maximum radius on the surface ($C_{\text{m}} \cdot s$), then steady state was not reached as droplets existed on the surface that would not jump.

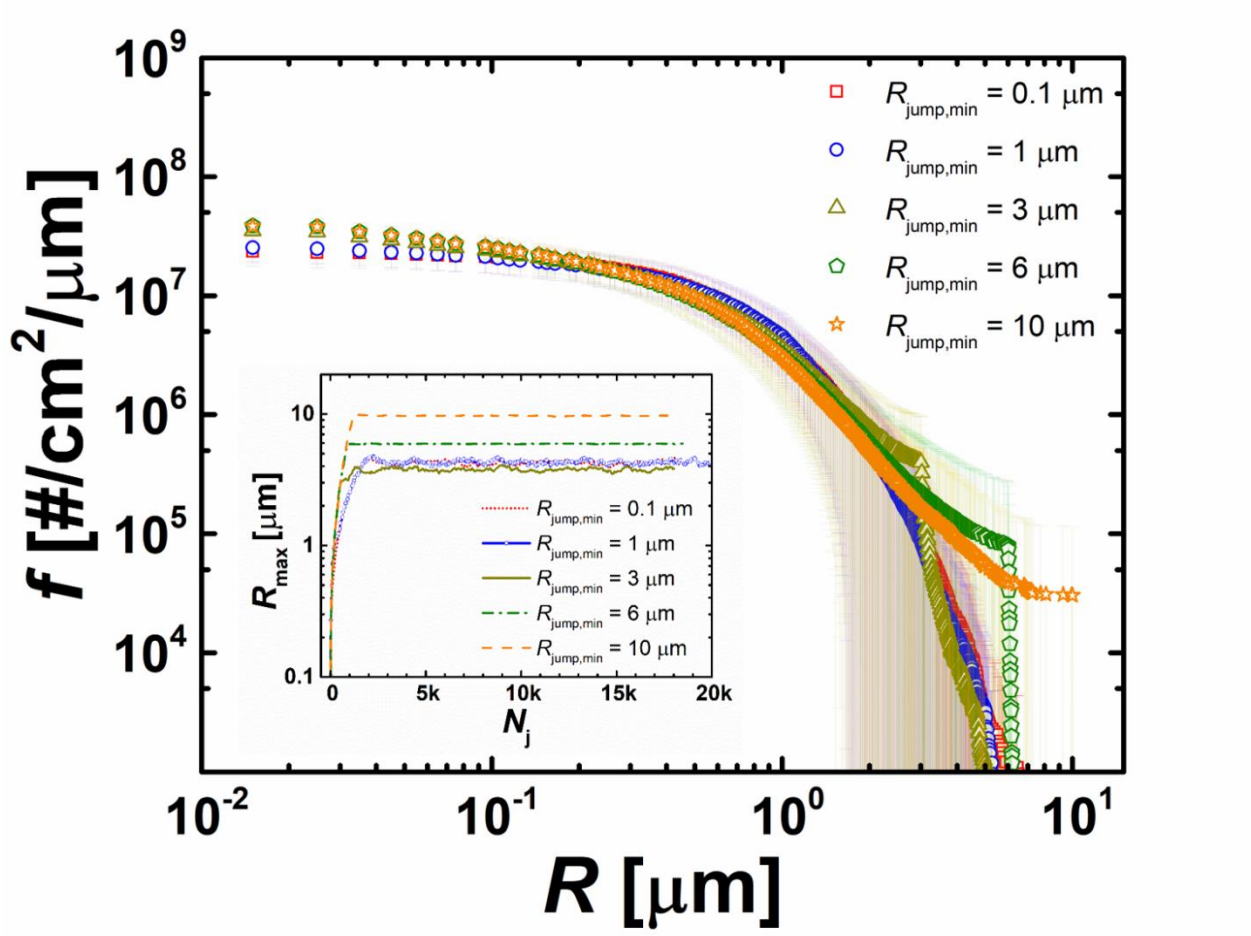

Figure 4.11. Droplet size distribution as a function of droplet radius for varying minimum jumping radius ($\boldsymbol{R_{jump,min}}$). As $\boldsymbol{R_{jump,min}}$ increased from 0.1, 1, 3, 6 to 10 μm, the distribution tail flattened. The flattening behavior explained the trends observed in Figures 4.8 and 4.9 for large droplet densities. Inset: Maximum droplet radius on the condensing surface ($\boldsymbol{R_{max}}$) as a function of time represented by the number of jumping events ($\boldsymbol{N_j}$). Error bars have been made partially transparent for clarity.

4.5.4. Effect of Contact Angle

The contact angle affects both the droplet growth rate (Eqns. 4.6, 4.8), and droplet coalescence due to the 3D geometry of droplets in the superhydrophobic state. Figure 4.12 shows the distribution function for apparent advancing contact angles of $\boldsymbol{\theta}$ = 150°,160° and 175° while keeping all other parameters constant ($\boldsymbol{N_s}$ = 10^5 sites/mm^2, $\boldsymbol{N_0}$ = 1000 sites). It is important to note, although the apparent advancing contact angle is used here for simulations due to droplets

residing in the advancing state during growth[39], the apparent receding contact angle is of equal importance as it is a macroscopic measure of whether jumping occurs (adhesion)[37,40]. Our simulations incorporate the contact angle hysteresis through the specification of $\boldsymbol{R_{jump,min}}$, i.e. the lower $\boldsymbol{R_{jump,min}}$, the lower the hysteresis. The inset of Figure 4.12 depicts the maximum droplet radius for the simulated scenarios, showing that the distribution is negligibly altered at the tail end of the distribution ($\boldsymbol{R}$ > 2 μm, $\boldsymbol{s}$ = 1.6 μm). The results show that the maximum droplet radius residing on the surface increases from 3.8 μm to 4.2 μm (≈10%) when the apparent advancing contact angle increases from 150° to 175°. The increase in maximum radius can be explained by the increased coalescence beneath large droplets at elevated contact angles[41]. Small droplets coalescing with large droplets "feed" the large droplets without any subsequent jumping (large size mismatch, figure 4.5-d). However, this shadowed coalescence phenomenon does not perturb the distribution significantly. The lack of distribution change is observable in figure 4.13 where the normalized covered surface area ($\boldsymbol{A_c/L^2}$), projected surface area ($\boldsymbol{A_p/L^2}$) and their ratio are plotted as a function of the apparent advancing contact angle. The values ($\boldsymbol{A_c/L^2}$) and ($\boldsymbol{A_p/L^2}$) are calculated by integrating the distribution function times the base area and projected area respectively. The ratio $\boldsymbol{A_p/A_c}$ follows the square of the ratio of the droplet radius to base radius ($\boldsymbol{1/\,sin\theta}$), a consequence of the invariance of the distribution with apparent advancing contact angle. Although the apparent advancing contact angle directly affects 3D coalescence effects, it also plays a large effect on individual droplet growth rate.

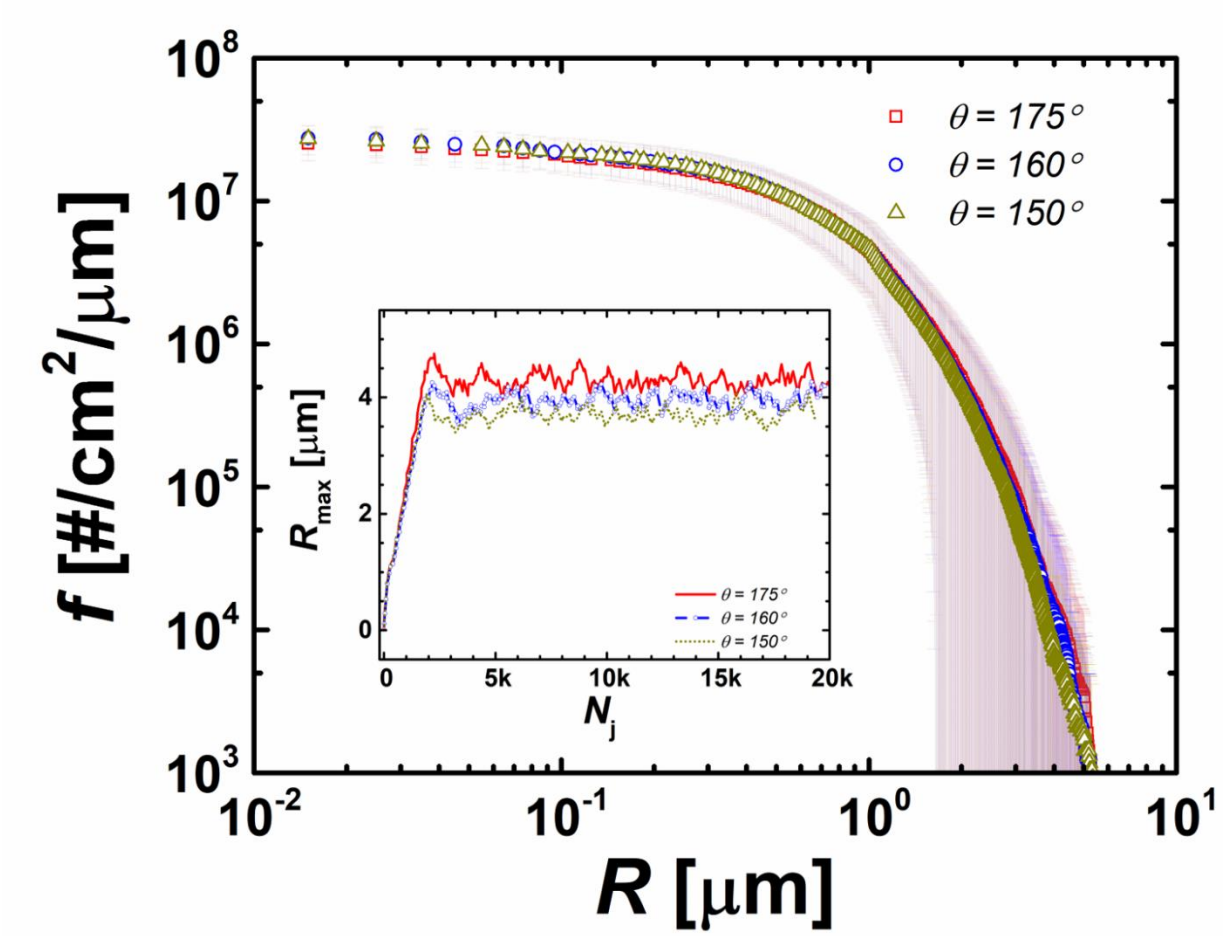

Figure 4.12. Droplet distribution as a function or droplet radius for varying apparent advancing contact angles $\boldsymbol{\theta}$. Inset: maximum droplet radius ($\boldsymbol{R_{max}}$) as a function of time as expressed by the number of droplet jumping events ($\boldsymbol{N_j}$) on the surface. Simulation parameters: $\boldsymbol{N_0}$ = 1000 sites, $\boldsymbol{N_s}$ = 10^5 sites/mm^2. Larger apparent advancing contact angles cause a slight increase in the droplet size for $\boldsymbol{R}$ > 2 μm due to increased coalescence with smaller droplets within their geometric shadow. Error bars have been made partially transparent for clarity.

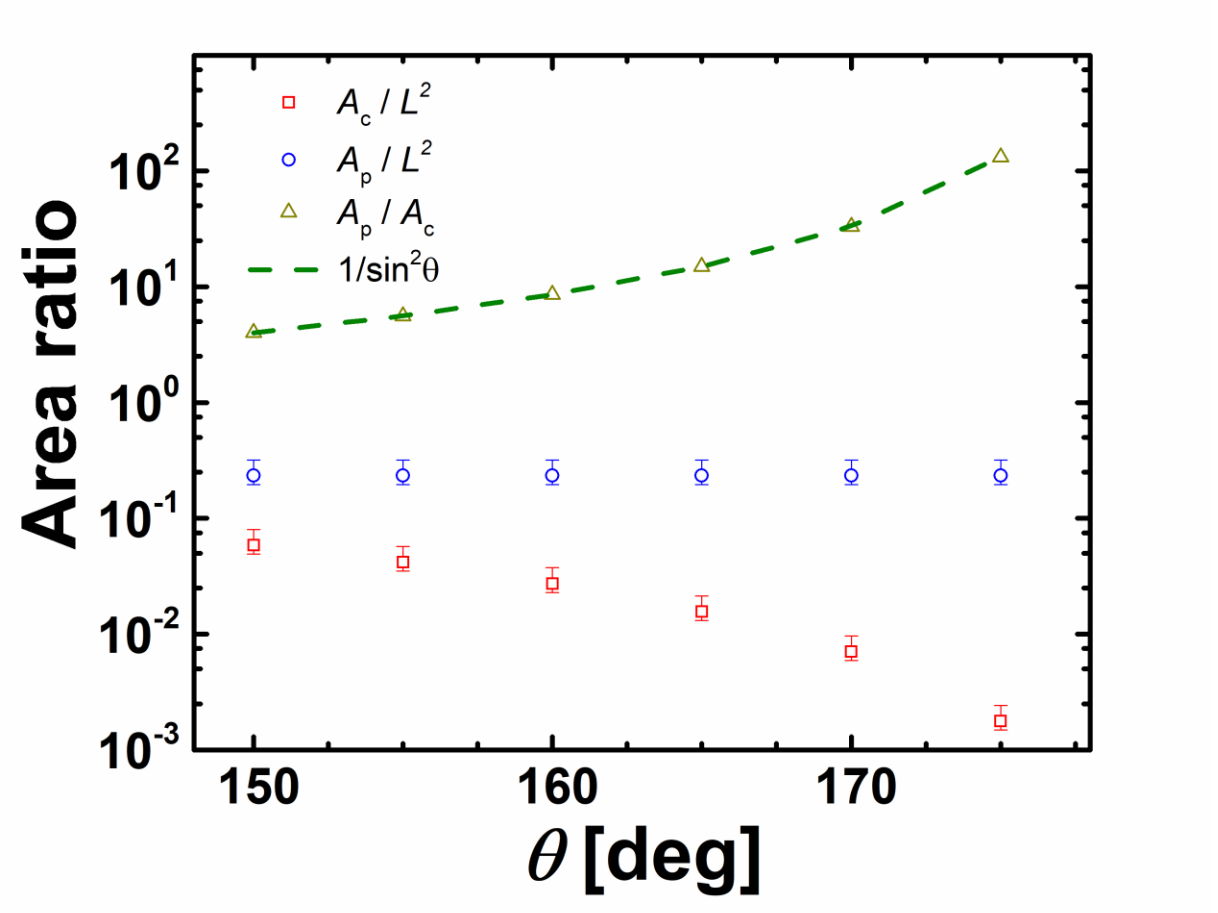

Figure 4.13. Normalized covered surface area ($\boldsymbol{A_c/L}$) , projected surface area ($\boldsymbol{A_p/L}$) and their ratio as a function of apparent advancing contact angle ($\boldsymbol{\theta}$). The values are calculated by integrating the distribution function ($\boldsymbol{f}$) times the base and projected areas, respectively. The Ratio $\boldsymbol{A_p/A_c}$ follows the square of the ratio of the droplet radius to the base radius ($\boldsymbol{R/R\,sin\,\theta}$), which is a consequence of the invariance of the distribution with the apparent advancing contact angle.

4.5.5. Effect of Droplet Growth Rate

Although the magnitude of the growth rate varies as a function of apparent advancing contact angle (eq. 4.8), the previous section showed that the contact angle did not significantly affect the distribution function. To reconcile the effect of individual droplet growth rate on the distribution function, we conducted additional simulations with differing growth rate functions. Although the growth rate of a condensing droplet in pure saturated vapor is well defined, additional thermal and

mass transfer resistances can change the experimentally observed growth rate of individual droplets[20,42,43]. We perform simulations for different growth rate functions with respect to the droplet radius R. The growth rate obtained from the droplet heat transfer analysis was fitted with a quadratic curve ($\log f \sim (\log R)^2$) that captures the shape closely, a linear curve ($\log f \sim (\log R)$) and a constant value (fig. 4.14). A different hydrophobic coating thickness (δ = 1 nm), which acted to change the growth rate by more than an order of magnitude, was also investigated. Despite the growth rate changes, the distribution did not alter in any considerable way. The results are in agreement with past studies of dropwise condensation on smooth surfaces which have shown the droplet distribution to be invariant with surface heat flux or droplet growth rate dynamics[44,45].

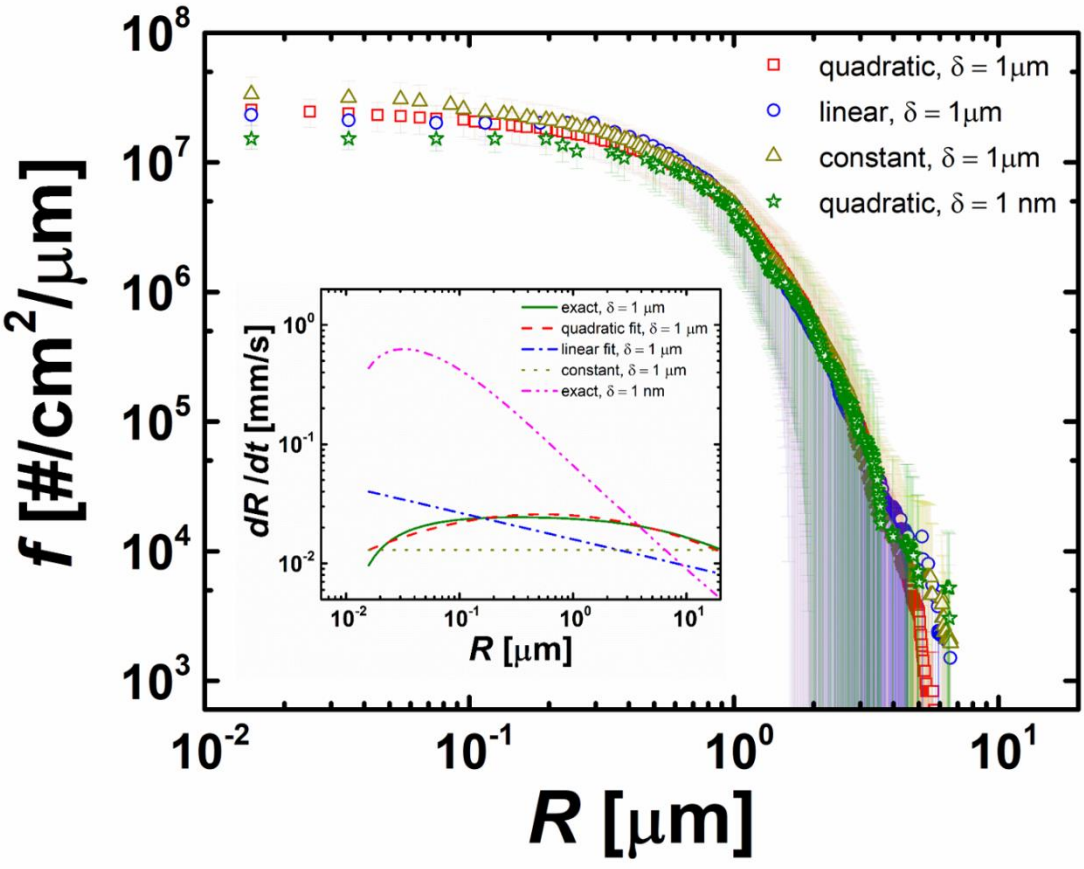

Figure 4.14. Condensate droplet size distribution as for varying individual droplet growth rates. Quadratic ($\log f \sim (\log R)^2$), linear ($\log f \sim (\log R)$) and constant growth curves were simulated. A different coating thickness ($\boldsymbol{\delta}$ = 1 nm) was also investigated. Error bars have been made partially transparent for clarity.

4.5.6. Suggested Droplet Size Distribution Fit

Based on the aforementioned results, we suggest the following curve fit for the non-dimensional droplet size distribution during jumping droplet condensation (Fig. 4.15) for realistic number densities ($N_s > 10^5$ mm^{-2}) with an overall correlation coefficient $r^2 > 0.995$.

$$Y = \begin{cases} -0.25X^4 - 1.37X^2 - 2.88X^2 - 2.84X - 0.61 & | \quad X \leq 0.15 \\ -3.18X^2 - 3.67X - 0.73 & | \quad X > 0.15 \end{cases}, \tag{4.9}$$

where $X = \log_{10}(R/s)$, and $Y = \log_{10}(fs/N_s)$.

4.6. 2D vs 3D coalescence

The high contact angles (θ>150°) observed on superhydrophobic surfaces create a 3D aspect for the coalescence that is not present on hydrophobic surfaces ($\theta \approx$90°). We highlight this effect by counting, at steady state, the number of coalescences that would have been counted if the simulation were 2D ($N_{coa,2D}$) and the number of coalescences that are effectively happening in 3D, ($N_{coa,3D}$). The ratio of the latter to the former is plotted for several nucleation densities when the growth rate is taken for δ =1 μm, θ=175° and L = 1 mm (fig. 4.15). The 3D coalescence is highlighted further as we plot the ratio of the base areas associated with the 3D and 2D coalescences respectively, $A_{coa,3D}/A_{coa,2D}$. The error bars arise from the repeated (10) measurements on snapshots taken at steady state. The results reveal the paramount importance of 3D coalescence as $N_{coa,3D}/N_{coa,2D}$ reaches values of ≈10% and $A_{coa,3D}/A_{coa,2D}$ ≈5% for nucleation site densities $N_s > 10^4$ mm^{-2}, which results in a very large error if the simulation was performed in 2D instead of 3D. The inset in figure 4.15 reveals the case where a 2D coalescence is present but a 3D coalescence is not ($\theta \approx$160°).

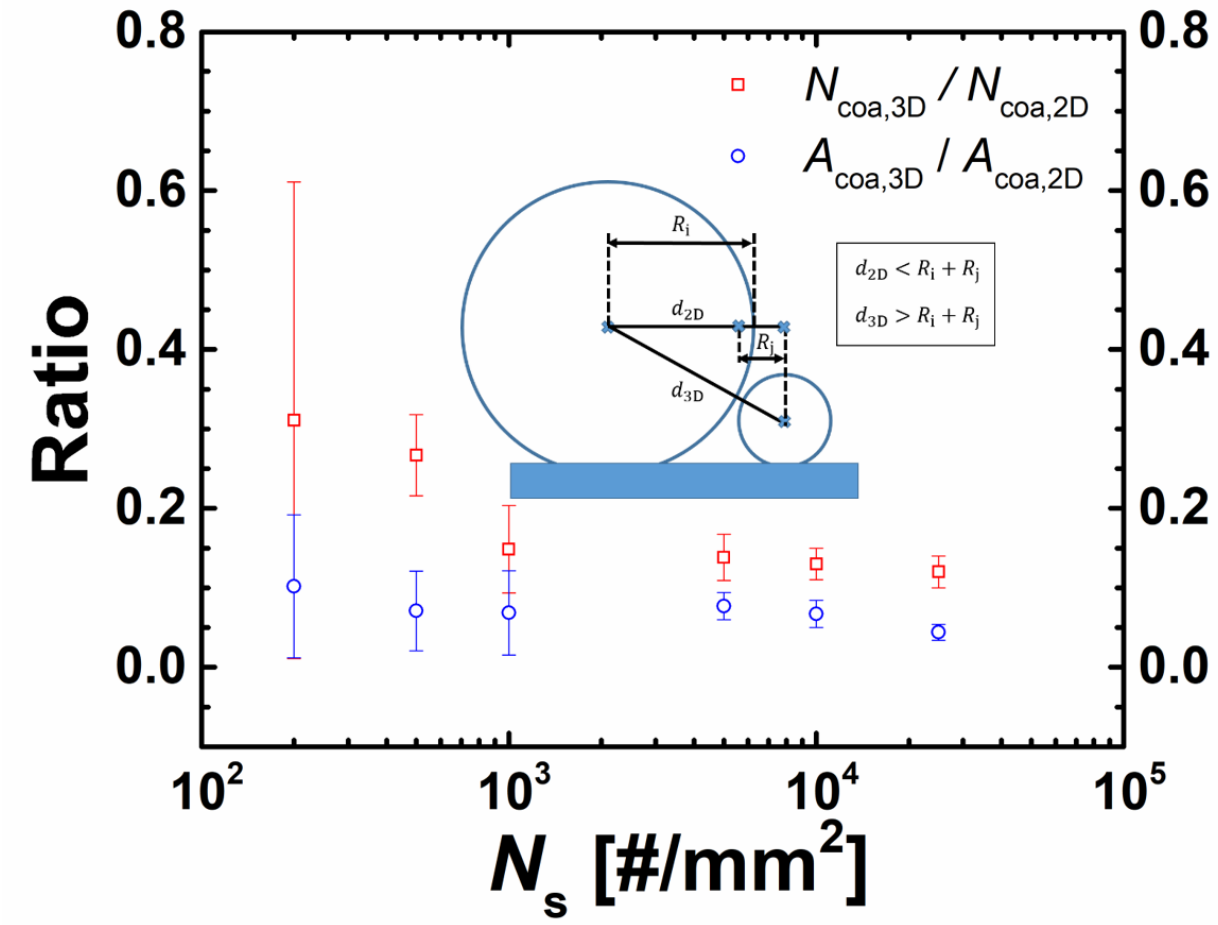

Figure 4.15. Ratio of the number of 3D coalescence events ($\mathbf{N_{coa,3D}}$), and the corresponding base area of coalescing droplets ($\mathbf{A_{coa,3D}}$), to the number of 2D coalescence events ($\mathbf{N_{coa,2D}}$) and its corresponding base area ($\mathbf{A_{coa,2D}}$) at steady state as a function of the nucleation site density ($\mathbf{N_s}$). The inset depicts the schematic of a 2D coalescence that is not a 3D coalescence of 2 droplets.

4.7. Heat Transfer

The main purpose of quantifying the droplet distribution function was to predict the overall (average) condensation heat transfer on the surface. The overall heat flux q can be obtained by:

$$q = \int_{R_{\min}}^{\infty} q_{\mathrm{d}} f \,\mathrm{d}R \,. \tag{4.10}$$

The value of the overall heat flux was plotted as a function of apparent advancing contact angle for four different coating thicknesses (δ = 1 μm, 100 nm, 10 nm, and 1 nm) with a nucleation site density N_s = 10^5 mm^{-2} (figure 4.16). The results reveal a diminishing overall heat flux as a function of increasing apparent advancing contact angle due to the increased droplet conduction thermal resistance for more spherical droplet geometries. Numerically, the results make sense as the droplet distribution is not changed significantly with increasing apparent advancing contact angle (fig. 4.12), while the droplet base area is decreased. The simulations reveal that the overall heat flux can reach values approaching 80 W/cm^2 for thin coatings (δ = 1 nm) with condensation heat transfer coefficient of 80 kW/m^{2}K (ΔT = 10 K) which is consistent with previous experimentally measure values [6].

To gain a better understanding of physical mechanisms governing jumping droplet condensation heat transfer, the cumulative heat flux fraction (q''_{cumul}/q'') was calculated as a function of droplet radius R, for N_s = 10^5 mm^{-2} and $\theta = 175°$ (figure 4.17, right axis). Figure 4.17 (left axis) shows the droplet distribution function (f), heat transfer per droplet (q_d), heat transfer per droplet size (fq_d), and total area per droplet size (fR^2) as a function of condensing droplet radius. All variables were normalized by their maximum over the plotted range for ease of visualization. The results show that the biggest contributors to the overall heat flux are droplets in the size range 800 nm < R < 1.2 μm. The peak observed for the heat transfer per droplet size matches well with the peak in total area covered by this size range, indicating that the area covered by droplets residing in this size range (800 nm < R < 1.2 μm) is the largest amongst other size ranges, hence contributing most to the overall heat transfer.

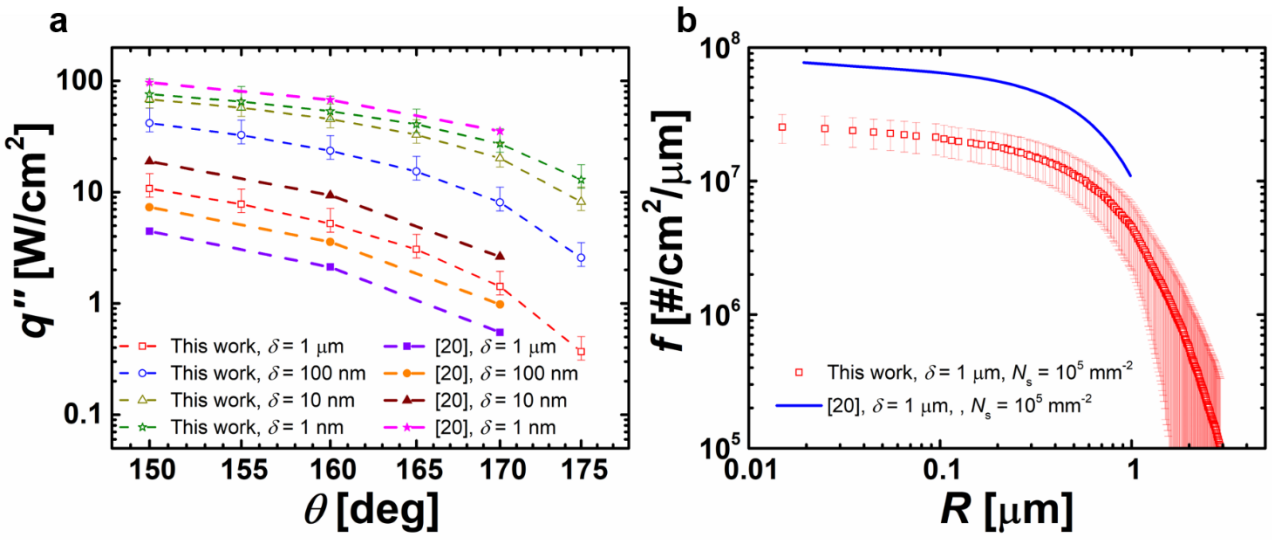

Figure 4.16. (a) Overall condensation heat flux (***q***") as a function of apparent advancing contact angle (***θ***) for varying hydrophobic coating thickness for N_s=10^5 mm-2. To compare the simulation results to analytical theory, a previously developed analytical model[20] was used to calculate the heat flux.

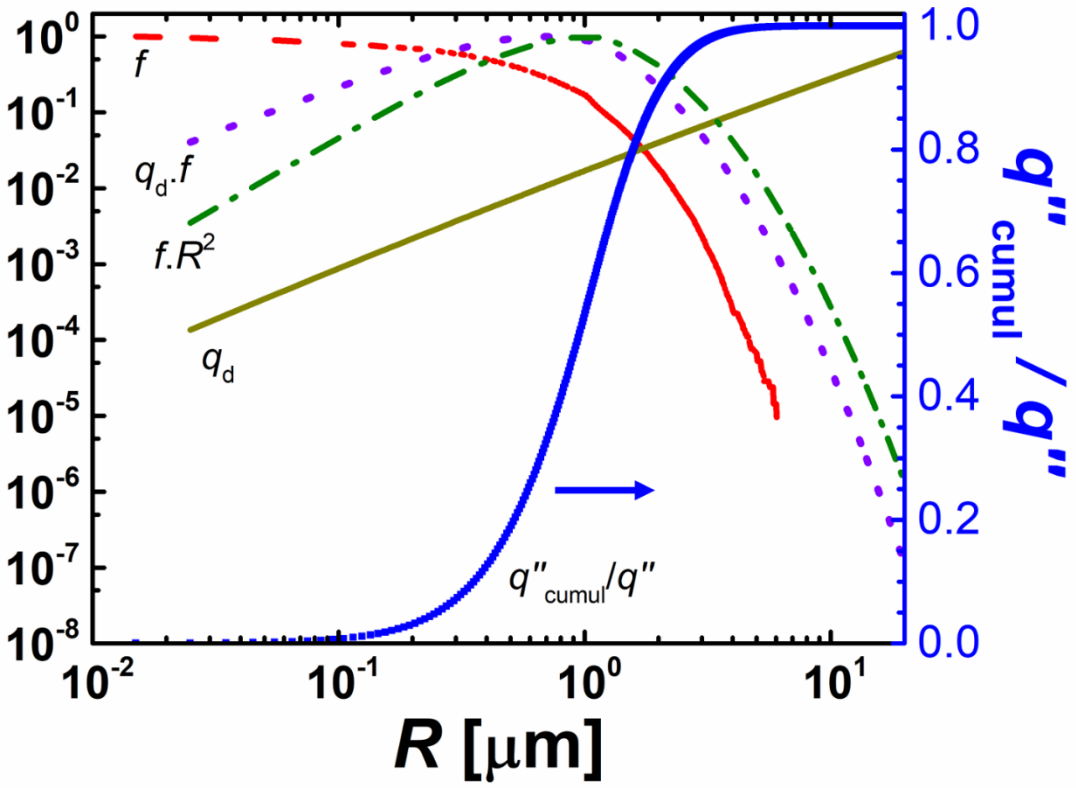

Figure 4.17. Jumping droplet heat transfer parameters as a function of individual droplet radius (***R***). The left axis plots the labeled normalized heat transfer variables. The variables have been

normalized by their maximum over the plotted range and represent: 1) the droplet size distribution $\boldsymbol{f}$, 2) the total heat transfer per droplet $\boldsymbol{q_d}$, 3) the total heat transfer per droplet radius, $\boldsymbol{q_d f}$, and 4) the total area covered by droplets of finite size, $\boldsymbol{f R^2}$. On the right axis (blue), the cumulative fraction of the total heat flux ($\boldsymbol{q''_{cumul}/q''}$) is plotted on a linear scale. The cumulative plot is the integral of the heat transfer per droplet size, $\boldsymbol{q_d f}$.

4.8. Discussion

The simulations provided in this work from the first complete 3D framework that enable modeling of condensation heat transfer on superhydrophobic surfaces with jumping-droplets. Prior modeling work[9] suggest that the distribution of droplets below the coalescence radius is governed by the population balance theory which does not agree the current results. In addition, a recent numerical simulation performed by Meng et. al. [46] does obtain the distribution for jumping droplet condensation on vertical surfaces, by assuming non ideal behavior of the jumping droplets (droplets can grow until they become large enough to be swept from the surface), while this model assumes no defect on the surface and provides a clear study of the achievement of steady state for jumping droplet distributions. The model provided by Meng et. al. does not include any 3D behavior which is critical in determining droplet growth (fig. 4.15), while it has been studied separately in other works for dropwise condensation with no jumping[47]. Hence our work represents the first comprehensive model with 3D coalescence and jumping droplet physics. In addition to the latter contributions, we generalize the mismatch dynamics for multiple droplet coalescence and investigate the effects of parameters such as the number of droplets simulated, droplet growth rate, contact angle, minimum and maximum jumping radius and different nucleation site densities. We provide a numerical correlation depicting the non-dimensional distribution for the expected range of nucleation site densities.

Future work

This work provides a framework for potential avenues still to be explored in modeling of jumping droplet condensation.

1. It would be physically significant to implement contact angle hysteresis and droplet jumping physics from the standpoint of droplet coalescence and the different regimes it involves (). Although right now the model just makes droplet disappear and relies on empirical evidence for jumping criteria (i.e. minimum size, maximum size mismatch), in the future, it would be good to implement all of this together in one unified code. This may require iteration between a finite element software such as ANSYS and our Matlab/C++ code. This will enable a better fundamental understanding of the mismatch effect for multiple droplets that has been lumped as one parameter in this study.
2. It would be good to implement this algorithm for dropwise condensation to validate the previously derived Rose distribution[12] and population balance[16] in one continuous distribution. This would require optimization of the algorithm to be able to handle a large size range of droplets. The algorithm can be enhanced with the use of parallelization for the simulated domain.
3. The current code does not consider vapor side effects which can significantly be altered due to jumping. It would be useful to use our code to develop a boundary condition for a coupled vapor side code to see the effects in terms of mass transfer enhancement. The droplet jumping does perturb the vapor flow and this effect is still to be modeled, in terms of the hydrodynamic and thermal boundary layers

mixing, and potential concentration boundary layers for condensation in the presence of non-condensable gases.

4. Droplet return to the surface is not considered in this paper. In the future, it would be interesting to determine the effect of droplet return to the surface due to the drag exerted by the vapor flow, of gravity depending on the orientation, droplet size and heat flux[24].

4.9. Conclusions

In this study, we provide a numerical simulation of jumping-droplet condensation on horizontal surfaces, in order to determine the steady-state time-averaged droplet size distribution on the condensing surface. In order to characterize steady state, we track the maximum radius on the surface. At steady-state, the maximum radius oscillates around an average value in time. The achievement of steady state requires that $R_{\max}/R_{\text{jump,min}} < \approx 50$, which is satisfied for typical nucleation site densities ($N_s \sim 5\text{x}10^4$ mm^{-2}). The droplet size distribution is obtained in its non dimensional form, and effects of the minimum jumping radius (0.1μm – 10 μm), maximum jumping radius, contact angle (150° – 175°), and droplet growth rate are provided. The minimum jumping radius flattens the tail of the distribution only if it reaches high enough values (> ≈ 3X average spacing), whereas the maximum jumping radius is not shown to modify the distribution unless it drops below (≈ 3X average spacing), where it prohibits the achievement of steady state. The contact angle and growth rate are shown to have negligible effect on the distribution. In this study, we provide a suggested numerical fit for the droplet size distribution with an overall correlation coefficient greater than 0.995. The heat transfer performance is evaluated with the derived distribution and is highly sensitive to contact angle and coating thickness as dictated by

the droplet growth rate. The obtained heat fluxes agree well with previous studies of jumping droplet condensation.

4.10. References:

[4.1] Schmidt, E.; Schurig, W.; Sellschopp, W. Versuche über die Kondensation von Wasserdampf in Film- und Tropfenform. *Forsch. Ingenieurwes* **1930,** *1* (2), 53–63.
[4.2] Miljkovic, N.; Enright, R.; Wang, E. N. Growth Dynamics During Dropwise Condensation on Nanostructured Superhydrophobic Surfaces. *3rd Micro/Nanoscale Heat & Mass Transfer International Conference* **2012**.
[4.3] Ma, X. H.; Rose, J. W.; Xu, D. Q.; Lin, J. F.; Wang, B. X. Advances in dropwise condensation heat transfer: Chinese research. *Chemical Engineering Journal* **2000,** *78* (2-3), 87-93.
[4.4] Enright, R.; Miljkovic, N.; Dou, N.; Nam, Y.; Wang, E. N. Condensation on Superhydrophobic Copper Oxide Nanostructures. *J Heat Transf* **2013,** *135* (9), 091304.
[4.5] Le Fevre, E. J.; Rose, J. W. Heat-Transfer Measurements During Dropwise Condensation of Steam. *International Journal of Heat and Mass Transfer* **1964,** *7*, 272-273.
[4.6] Miljkovic, N.; Enright, R.; Nam, Y.; Lopez, K.; Dou, N.; Sack, J.; Wang, E. N. Jumping-droplet-enhanced condensation on scalable superhydrophobic nanostructured surfaces. *Nano Lett* **2013,** *13* (1), 179-87.
[4.7] Wen, R.; Xu, S.; Ma, X.; Lee, Y.-C.; Yang, R. Three-Dimensional Superhydrophobic Nanowire Networks for Enhancing Condensation Heat Transfer. *Joule* **2018,** *2* (2), 269-279.
[4.8] Enright, R.; Miljkovic, N.; Sprittles, J.; Nolan, K.; Mitchell, R.; Wang, E. N. How Coalescing Droplets Jump. *ACS Nano* **2014,** *8* (10), 10352-10362.
[4.9] Miljkovic, N.; Enright, R.; Wang, E. N. Modeling and Optimization of Superhydrophobic Condensation. *J Heat Trans-T Asme* **2013,** *135* (11).
[4.10] Enright, R.; Miljkovic, N.; Alvarado, J. L.; Kim, K.; Rose, J. W. Dropwise Condensation on Micro- and Nanostructured Surfaces. *Nanosc Microsc Therm* **2014,** *18* (3), 223-250.
[4.11] Miljkovic, N.; Wang, E. N. Condensation heat transfer on superhydrophobic surfaces. *Mrs Bull* **2013,** *38* (5), 397-406.
[4.12] Rose, J. W.; Glicksma.Lr. Dropwise Condensation - Distribution of Drop Sizes. *International Journal of Heat and Mass Transfer* **1973,** *16* (2), 411-425.
[4.13] Glicksman, L. R.; Hunt, A. W. Numerical Simulation of Dropwise Condensation. *International Journal of Heat and Mass Transfer* **1972,** *15* (11), 2251-+.
[4.14] Mei, M. F.; Yu, B. M.; Cai, J. C.; Luo, L. A fractal analysis of dropwise condensation heat transfer. *International Journal of Heat and Mass Transfer* **2009,** *52* (21-22), 4823-4828.
[4.15] Kim, S.; Kim, K. J. Dropwise Condensation Modeling Suitable for Superhydrophobic Surfaces. *J Heat Trans-T Asme* **2011,** *133* (8).
[4.16] AbuOrabi, M. Modeling of heat transfer in dropwise condensation. *International Journal of Heat and Mass Transfer* **1998,** *41* (1), 81-87.
[4.17] Tanasawa, I. Advances in Condensation Heat Transfer. In *Advances in Heat Transfer*, Hartnett, J. P.; Irvine, T. F.; Cho, Y. I., Eds.; Elsevier, 1991; Vol. 21, pp 55-139.
[4.18] Clark, P. J.; Evans, F. C. Distance to Nearest Neighbor as a Measure of Spatial Relationships in Populations. *Ecology* **1954,** *35* (4), 445-453.
[4.19] Schrage, R. W. A theoretical study of interphase mass transfer. Thesis, Columbia University.1953.
[4.20] Chavan, S.; Cha, H.; Orejon, D.; Nawaz, K.; Singla, N.; Yeung, Y. F.; Park, D.; Kang, D. H.; Chang, Y. J.; Takata, Y.; Miljkovic, N. Heat Transfer through a Condensate Droplet on

Hydrophobic and Nanostructured Superhydrophobic Surfaces. *Langmuir* **2016,** *32* (31), 7774-7787.
[4.21] Miljkovic, N.; Preston, D. J.; Enright, R.; Wang, E. N. Electrostatic charging of jumping droplets. *Nat Commun* **2013,** *4*.
[4.22] Xie, F. F.; Lu, G.; Wang, X. D.; Wang, B. B. Coalescence-Induced Jumping of Two Unequal-Sized Nanodroplets. *Langmuir* **2018,** *34* (8), 2734-2740.
[4.23] He, M.; Zhou, X.; Zeng, X. P.; Cui, D. P.; Zhang, Q. L.; Chen, J.; Li, H. L.; Wang, J. J.; Cao, Z. X.; Song, Y. L.; Jiang, L. Hierarchically structured porous aluminum surfaces for high-efficient removal of condensed water. *Soft Matter* **2012,** *8* (25), 6680-6683.
[4.24] Birbarah, P.; Li, Z. E.; Pauls, A.; Miljkovic, N. A Comprehensive Model of Electric-Field-Enhanced Jumping-Droplet Condensation on Superhydrophobic Surfaces. *Langmuir* **2015,** *31* (28), 7885-7896.
[4.25] Birbarah, P.; Miljkovic, N. External Convective Jumping-Droplet Condensation on a Flat Plate. *International Journal of Heat and Mass Transfer* **2017,** *107*, 74-88.
[4.26] Miljkovic, N.; Preston, D. J.; Enright, R.; Wang, E. N. Electric-Field-Enhanced Condensation on Superhydrophobic Nanostructured Surfaces. *ACS Nano* **2013,** *7* (12), 11043-11054.
[4.27] Shahriari, A.; Birbarah, P.; Oh, J.; Miljkovic, N.; Bahadur, V. Electric Field-Based Control and Enhancement of Boiling and Condensation. *Nanosc Microsc Therm* **2017,** *21* (2), 102-121.
[4.28] Chen, X. M.; Patel, R. S.; Weibel, J. A.; Garimella, S. V. Coalescence-Induced Jumping of Multiple Condensate Droplets on Hierarchical Superhydrophobic Surfaces. *Sci Rep-Uk* **2016,** *6*.
[4.29] Chen, X.; Wu, J.; Ma, R.; Hua, M.; Koratkar, N.; Yao, S.; Wang, Z. Nanograssed Micropyramidal Architectures for Continuous Dropwise Condensation. *Advanced Functional Materials* **2011,** *21*, 4617–4623.
[4.30] Wang, K.; Li, R. X.; Liang, Q. Q.; Jiang, R.; Zheng, Y.; Lan, Z.; Ma, X. H. Critical size ratio for coalescence-induced droplet jumping on superhydrophobic surfaces. *Appl Phys Lett* **2017,** *111* (6).
[4.31] Cha, H.; Chun, J. M.; Sotelo, J.; Miljkovic, N. Focal Plane Shift Imaging for the Analysis of Dynamic Wetting Processes. *Acs Nano* **2016,** *10* (9), 8223-8232.
[4.32] Wasserfall, J.; Figueiredo, P.; Kneer, R.; Rohlfs, W.; Pischke, P. Coalescence-induced droplet jumping on superhydrophobic surfaces: Effects of droplet mismatch. *Physical Review Fluids* **2017,** *2* (12).
[4.33] Rykaczewski, K.; Paxson, A. T.; Anand, S.; Chen, X.; Wang, Z.; Varanasi, K. K. Multimode Multidrop Serial Coalescence Effects during Condensation on Hierarchical Superhydrophobic Surfaces. *Langmuir* **2013,** *29* (3), 881–891.
[4.34] Mittal, N.; Ansari, F.; Gowda.V, K.; Brouzet, C.; Chen, P.; Larsson, P. T.; Roth, S. V.; Lundell, F.; Wågberg, L.; Kotov, N. A.; Söderberg, L. D. Multiscale Control of Nanocellulose Assembly: Transferring Remarkable Nanoscale Fibril Mechanics to Macroscale Fibers. *ACS Nano* **2018,** *12* (7), 6378-6388.
[4.35] Kim, M. K.; Cha, H.; Birbarah, P.; Chavan, S.; Zhong, C.; Xu, Y. H.; Miljkovic, N. Enhanced Jumping-Droplet Departure. *Langmuir* **2015,** *31* (49), 13452-13466.
[4.36] Zhang, P.; Maeda, Y.; Lv, F.; Takata, Y.; Orejon, D. Enhanced Coalescence-Induced Droplet-Jumping on Nanostructured Superhydrophobic Surfaces in the Absence of Microstructures. *ACS Applied Materials & Interfaces* **2017,** *9* (40), 35391-35403.

[4.37] Cha, H.; Xu, C.; Sotelo, J.; Chun, J. M.; Yokohama, Y.; Enright, R.; Miljkovic, N. Coalescence-Induced Nanodroplet Jumping. *Physical Review Fluids* **2016,** *In press*.
[4.38] Mulroe, M. D.; Srijanto, B. R.; Ahmadi, S. F.; Collier, C. P.; Boreyko, J. B. Tuning Superhydrophobic Nanostructures To Enhance Jumping-Droplet Condensation. *Acs Nano* **2017,** *11* (8), 8499-8510.
[4.39] Enright, R.; Miljkovic, N.; Al-Obeidi, A.; Thompson, C. V.; Wang, E. N. Condensation on Superhydrophobic Surfaces: The Role of Local Energy Barriers and Structure Length Scale. *Langmuir* **2012,** *28* (40), 14424-14432.
[4.40] Yan, X.; Zhang, L.; Sett, S.; Feng, L.; Zhao, C.; Huang, Z.; Vahabi, H.; Kota, A. K.; Chen, F.; Miljkovic, N. Droplet Jumping: Effects of Droplet Size, Surface Structure, Pinning, and Liquid Properties. *ACS Nano* **2019**.
[4.41] Rykaczewski, K.; Scott, J. H. J.; Rajauria, S.; Chinn, J.; Chinn, A. M.; Jones, W. Three dimensional aspects of droplet coalescence during dropwise condensation on superhydrophobic surfaces. *Soft Matter* **2011,** *7* (19), 8749-8752.
[4.42] Tanner, D. W.; Pope, D.; Potter, C. J.; West, D. Heat Transfer in Dropwise Condensation at Low Steam Pressures in Absence and Presence of Non-Condensable Gas. *International Journal of Heat and Mass Transfer* **1968,** *11* (2), 181-&.
[4.43] Minkowycz, W. J.; Sparrow, E. M. Condensation Heat Transfer in Presence of Noncondensables Interfacial Resistance Superheating Variable Properties and Diffusion. *International Journal of Heat and Mass Transfer* **1966,** *9* (10), 1125-+.
[4.44] Rose, J. W. Dropwise condensation theory and experiment: a review. *P I Mech Eng a-J Pow* **2002,** *216* (A2), 115-128.
[4.45] Weisensee, P. B.; Wang, Y. B.; Qian, H. L.; Schultz, D.; King, W. P.; Miljkovic, N. Condensate droplet size distribution on lubricant-infused surfaces. *International Journal of Heat and Mass Transfer* **2017,** *109*, 187-199.
[4.46] Meng, K.; Fan, W.; Wang, H. Dynamic scenario simulation of dropwise condensation on a superhydrophobic surface with droplet jumping. *Applied Thermal Engineering* **2019,** *148*, 316-323.
[4.47] Xu, W.; Lan, Z.; Liu, Q. C.; Du, B. G.; Ma, X. H. Droplet size distributions in dropwise condensation heat transfer: Consideration of droplet overlapping and multiple re-nucleation. *International Journal of Heat and Mass Transfer* **2018,** *127*, 44-54.

Chapter 5 – Jumping-Droplet Electronics Hot Spot Cooling

5.1. Introduction

Recent advances in electronic materials and circuit architectures have catalyzed an increase in power density (power-to-volume ratio) and the specific power (power-to-weight ratio) of both stationary and mobile systems.[1, 2] The trend of replacing bulky pneumatic and mechanical systems with smaller electrical systems in more-electric and fully-electric vehicles ranging from automobiles to aircrafts has created a demand for lighter and more compact power electronics. Yet, the ability to remove heat from internal hot spots constrains the design of converters and inverters.[3] Phase change heat transfer offers a platform to efficiently remove heat from electronic devices and transfer it via the generated vapor phase (evaporation in heat pipes and vapor chambers) to the outside environment.[4] However, recent advances utilizing wide bandgap semiconductors have shown that the majority of heat can be generated locally near spatially distributed hot spots.[3, 5] Traditional cooling schemes can also be stymied by the temporal variation in hot spot locations concurrent with electro-thermal optimization and novel circuit architectures.[6]

In this work, we experimentally demonstrated jumping droplet-based active cooling of electronics hot spots with nanoengineered superhydrophobic surfaces. Recent studies have shown that when small water droplets (≈1-100 μm in diameter) merge on superhydrophobic nanostructured surfaces, droplets can spontaneously eject via the release of excess surface energy irrespective of gravity.[7-9] A number of works have since fabricated superhydrophobic nanostructured surfaces to achieve spontaneous droplet removal for a variety of applications including self-cleaning,[10, 11] condensation heat transfer enhancement,[12-16] thermal diodes,[17] vapor chambers,[18] electrical energy harvesting,[19] and anti-icing.[20] Furthermore,

we recently discovered that these jumping droplets are positively charged (≈10–100 fC), due to electric-double-layer charge separation at the hydrophobic coating/condensate interface,[21] and can be manipulated with electric fields.[21-23] Here, we take advantage of this unique droplet-charging phenomenon to demonstrate electric-field-enhanced (EFE) jumping-droplet hot spot cooling, where the charged droplets jump between superhydrophobic copper oxide (CuO) condensers and either single or multiple high power gallium nitride (GaN) transistors acting as local hot spots to remove heat via droplet evaporation. We experimentally demonstrated spatially and temporally-controllable jumping-droplet based cooling of ≈1 W/cm^2 and describe near term approaches to increase heat fluxes to 120 W/cm^2.

The utilization of droplet-jumping and active electric fields to locally cool mobile hot spots builds on state-of-the-art vapor chamber designs with several significant advantages as follows: (i) The electronics act directly as the evaporator and minimize thermal resistance as typically observed through the utilization of thermal-interface-materials and channel walls.[24] If integrated into a jumping-droplet vapor chamber geometry due to electrical isolation concerns, the mass flow rate of the liquid inside the jumping-droplet vapor chamber is not dictated by the height of the wick structure, but by the jumping frequency since the condenser liquid is returned through the vapor space.[18] (ii) Spatial and temporal control of the jumping droplet motion is possible with electrostatic fields such that mobile hot spots can be sensed and cooled as needed.[22] (iii) The low Bond number of the jumping droplets (Bo ~ 10^{-3}) allows operation independent of gravitational orientation. (iv) The out-of-plane jumping return is scalable and particularly suitable for planar systems, unlike conventional vapor chambers with capillary return along wicked walls, where longer liquid return paths are expected for devices of larger areas.[18]

5.2. Experiment and Results

To investigate jumping-droplet electronics cooling, a printed circuit board (PCB) with a single active integrated GaN field effect transistor (FET, EPC2034)[25] was positioned above the nanostructured superhydrophobic CuO surface. The circuit board was placed on top in order to test the worst case scenario of droplet jumping against gravity (Figure 5.1(a)-(c)). The CuO nanostructures (Fig. 5.1(d), inset) were grown on commercially purchased 800 μm thick Cu tabs with overall dimensions of 50 x 50 mm. Each tab was cleaned in an ultrasonic bath with acetone for 10 min and rinsed with ethanol, isopropyl alcohol, and deionized (DI) water. The tabs were then dipped into a 2.0M hydrochloric acid solution for 10 min to remove the native oxide film on the surface, then triple rinsed with DI water and dried with clean nitrogen gas. Nanostructured CuO films were formed by immersing one of the cleaned tabs into a hot (≈ 98°C) alkaline solution composed of $NaClO_2$, NaOH, $Na_3PO_4 \cdot 12H_2O$, and DI water (3.75: 5: 10: 100 wt. %).[26] During the oxidation process, a thin (≈300 nm) Cu_2O layer was formed that then re-oxidized to form sharp, knife-like CuO oxide structures with heights of $h \approx 1$ μm, a solid fraction $\varphi \approx 0.02$ and a roughness factor $r \approx 10$. To render the CuO tabs superhydrophobic, a C_4F_8 hydrophobic coating was applied with chemical vapor deposition. This process allowed for the development of a highly conformal (≈50-nm thick) polymer layer on the CuO surface. Goniometric measurements (MCA-3, Kyowa Interface Science) of ≈ 300 nl droplets on a smooth C_4F_8-coated silicon wafer surface showed advancing and receding contact angles of θ_a = 121 ± 5.1° and θ_r = 105 ± 9°, respectively. Meanwhile, the advancing and receding contact angles on the superhydrophobic CuO surface were measured to be θ_a^{app} = 166 ± 6° and θ_r^{app} = 156 ± 7°, respectively.

To initiate jumping-droplet hot spot cooling, the temperature of the CuO tab was reduced to ≈ 5°C via a cooling water flow (Fig. 5.1(a,c)) until jumping-droplet-condensation occurred. To

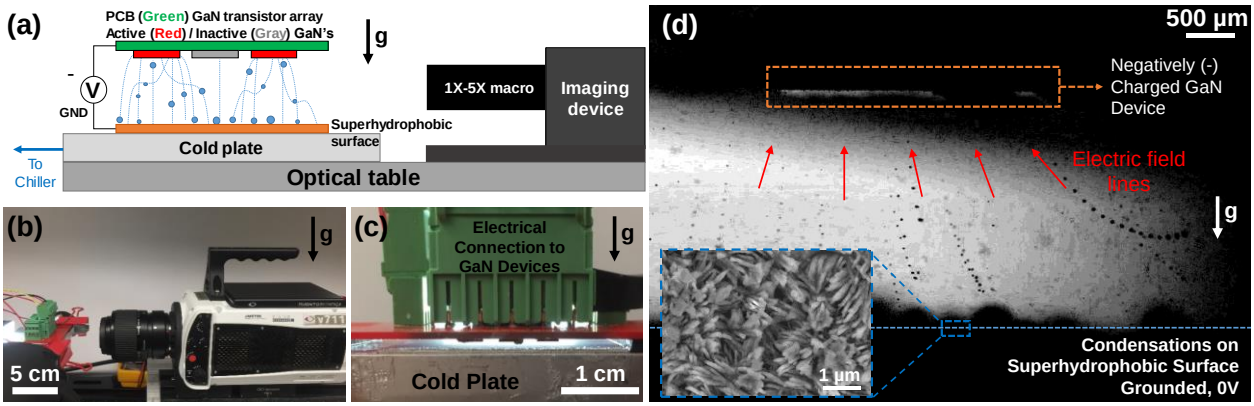

Figure 5.1. (a) Side view schematic and (b) photograph of the experimental setup for characterizing jumping droplet cooling of GaN transistors. (c) Side view image of the experimental setup showing the GaN electrical contact (green), the PCB with GaN devices (red), and superhydrophobic surface resting on the cold plate. (d) Composite image of several successive frames from a high speed video of electric-field-enhanced jumping-droplet condensation toward a GaN transistor. Electric field lines are depicted by red arrows. The droplet trajectories clearly follow (are influenced by) the electric field lines, which are depicted by red arrows. Inset: top-view scanning electron micrograph of a C_4F_8 functionalized (≈50 nm) superhydrophobic CuO surface used in these experiments.

visualize the behavior, a gap between the parallel devices was observed with a high speed camera. Due to electric-double-layer charge separation at the liquid-hydrophobic coating interface,[21] the jumping droplets departed the surface with a droplet radius dependent electrostatic charge (~10 fC). The jumping droplets travelled from the CuO surface to the circuit board, resulting in evaporative cooling of the hot GaN FET. In order to quantify cooling, EFE jumping droplet condensation for a single GaN device for cases with and without an external electric field of -100 V for the guard ring or the source pin potential of the GaN FET was studied.

Using rear lighting and long exposure time imaging, images and videos of jumping droplet phenomena in the gap were obtained. In the no-field condition, droplets jumping with insufficient inertia fall back to the superhydrophobic surface. In contrast, an external electric provides sufficient force to guide droplet's with insufficient inertia along electric field lines to the GaN device as depicted in Figure 5.1(d). The unique parabolic path in the right hand side of Figure

5.1(d) also reveals how the droplet accelerate toward the power devices due to the presence of an electric field. Accelerations between 3 and 6 m/s^2 for the droplets attracted by the electric fields were observed from measurements when a -100 V potential was applied across a 3 mm spacing between the cold plate and the GaN transistor, thus, enhancing the cooling capability by improving the rate and the number of droplets that reach the GaN FET. The applied fields (200 – 300 V/cm) are very similar to the critical fields needed to overcome gravity and drag forces as shown in previous studies.[23]

Steady-state infrared imaging (Fig. 5.2(a)) of the active GaN FET (Fig. 5.2(b)) as well as transient time-lapse liquid crystal thermography (Fig. 5.2(c)) were able to provide qualitative information about the GaN device temperature and its high temperature localization (hot spots) and to highlight how heat spread in the PCB (see Supplementary Material, section S2). Yet, the inability to view the device while integrated with the superhydrophobic surface required the use of thermocouples. By attaching thermocouples to the transistor and the cold plate, quantification of the GaN FET steady-state temperature for various spacings (2 – 4 mm) between the circuit and cold superhydrophobic sample was studied. Figure 5.2(d) shows the thermal circuit corresponding to the experimental setup. The GaN device was assumed to have a uniform temperature, T_{G} due to the low Biot number (Bi ~ 10^{-2}) for the cooling conditions and geometry studied here. Joule heating of 1.57 W was generated inside the GaN transistor at a rate of RI^2 where R = 7 mΩ is the internal electrical resistance of the GaN FET, and I = 15 A is the DC current flowing through the device. The heat is dissipated either to the backside (through the board, then to ambient air, T_{amb} = 23 ± 0.5°C), or to the front side (towards the superhydrophobic sample, T_{s} = 5 ± 0.5°C). Miscellaneous losses to ambient air have been lumped into a thermal resistance, R_{losses}, which was determined through calibration during the no-jumping condition .

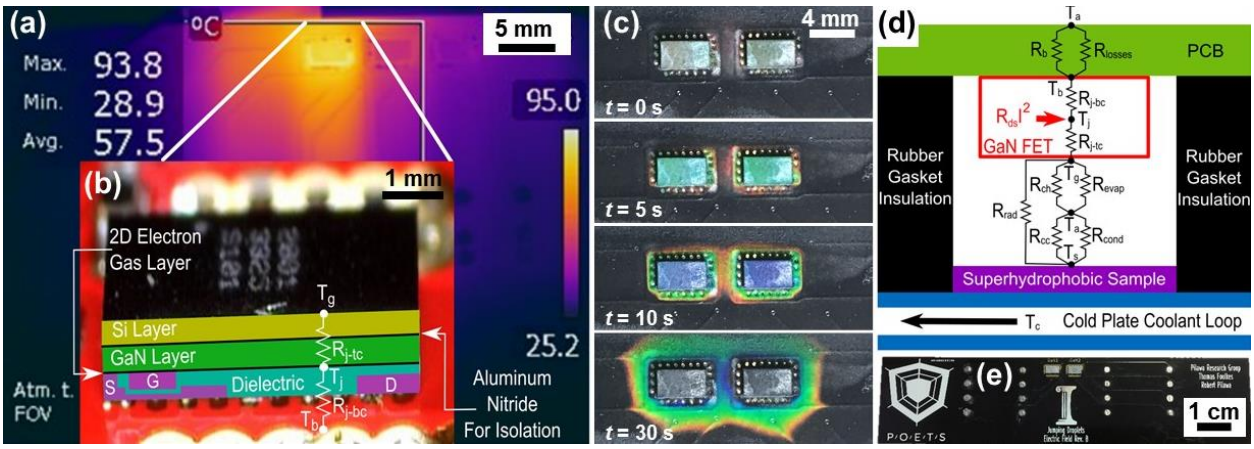

Figure 5.2. (a) Thermal infrared image of GaN FET with (b) detailed device structure. (c) Top view time-lapse liquid crystal thermographic images of the two GaN device during startup. Thermal steady-state was reached at 30 seconds. Red corresponds to 70°C and violet corresponds to 90°C. For infrared and liquid crystal thermography experimental details, please see Supplementary Material, section S2. (d) Thermal resistance network of experimental setup. For a detailed model description, please see Supplementary Material, section S1. (e) Top view photograph of the two-GaN PCB.

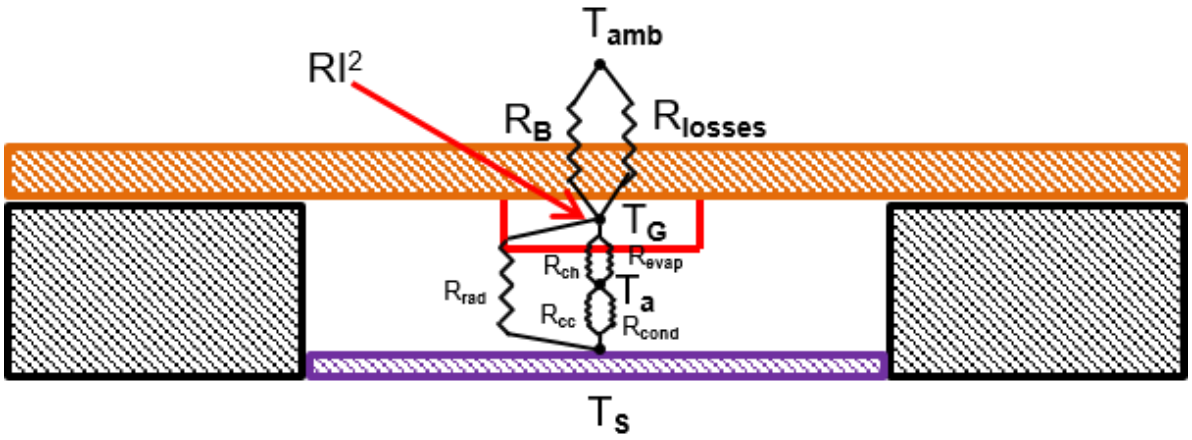

Figure 5.3. Thermal Circuit for GaN transistor cooling

Figure 5.3. shows the thermal circuit corresponding with the experimental setup. The GaN transistor is considered with a lumped temperature T_G. Joule heating is generated inside the GaN at a rate of RI^2 where $R = 0.007 \pm 0.002\ \Omega$ is the internal electrical resistance of the GaN transistor, and $I = 15$ A is the current running through the transistor. The heat is dissipated either to the backside (through the board, then to ambient air, $T_{amb} = 23 \pm 1$°C), either to the front side

(towards the superhydrophobic sample, $T_s = 5 \pm 1$°C). Miscellaneous losses to ambient air have been lumped into a thermal resistance R_{losses}. Table 5.1. summarizes the parameters used.

Table 5.1. Parameters used in the thermal resistance network

Symbol / Equation	Thermal Resistance	Value (K/W)
$R_B = R_{sp} + R_{nat}$	Backside resistance	79.2
R_{sp}	Spreading resistance within the PCB	47.2
$R_{nat} = \frac{1}{h_{nat} A_{PCB}}$	Natural convection on the PCB	32
R_{losses}	Miscellaneous thermal losses to ambient air	-
$R_{ch} = \frac{1}{h_{ch} A_G}$	Natural convection at the hot side	4806
$R_{cc} = \frac{1}{h_{cc} A_s}$	Natural convection at the cold side	80
$R_{evap} = \frac{1}{h_{evap} A_G}$	Evaporation of jumping droplets	-
$R_{cond} = \frac{1}{h_{cond} A_s}$	Condensation on the superhydrophobic sample	0.4
$R_{rad} = \frac{1}{h_{rad} A_G}$	Radiation thermal resistance	1114

Where the heat transfer coefficients and areas are as expressed in Table 5.1., and :

$h_{rad} = \sigma({T_G}^2 + {T_S}^2)(T_G + T_S)$, $\sigma =$ 5.67x10-8 W/m^{2}K^4 is Stephan-Boltzmann's constant, $A_{PCB} = 62$ cm^2 is the PCB backside surface area

The spreading resistance was found by :

$$R_{sp} = \frac{\tan^{-1}\left[\frac{a+b}{c} - \frac{\pi}{4}\right]}{\pi c k_{PCB}} \tag{5.1}$$

Where a = 1.6 mm and b = 5.2 cm are thickness and width of PCB, respectively, and c = 1.8 mm represents the radius of the GaN if it were a circular spot. The thermal conductivity of the PCB, k_{PCB}, is found by

$$k_{\mathrm{PCB}} = f_t k_{\mathrm{PCB},t} + (1 - f_t) k_{\mathrm{PCB},n} \tag{5.2}$$

$$k_{\mathrm{PCB},t} = \frac{k_{\mathrm{FR4}} t_{\mathrm{FR4}} + k_{\mathrm{Cu}} t_{\mathrm{Cu}}}{t_{\mathrm{FR4}} + t_{\mathrm{Cu}}} \tag{5.3}$$

$$k_{\mathrm{PCB},n} = \left(\frac{t_{\mathrm{FR4}}}{t_{\mathrm{FR4}} + t_{\mathrm{Cu}}} \frac{1}{k_{\mathrm{FR4}}} + \frac{t_{\mathrm{Cu}}}{t_{\mathrm{FR4}} + t_{\mathrm{Cu}}} \frac{1}{k_{\mathrm{Cu}}} \right)^{-1} \tag{5.4}$$

$t_{\mathrm{Cu}} = 140$ μm is the thickness of copper layers, t_{FR4} =302.5 μm is the thickness of FR4 layers, $k_{\mathrm{PCB},t}$ is tangential thermal conductivity weighted by f_t and $k_{\mathrm{PCB},n}$ is normal thermal conductivity, which has been weighted to 95% as most of the spreading was normal in this geometry.

In order to determine the value of the miscellaneous losses in our system, we plotted the results of h_{evap} in terms of the GaN temperature for different values of R_{losses}, as shown in figure 5.4:

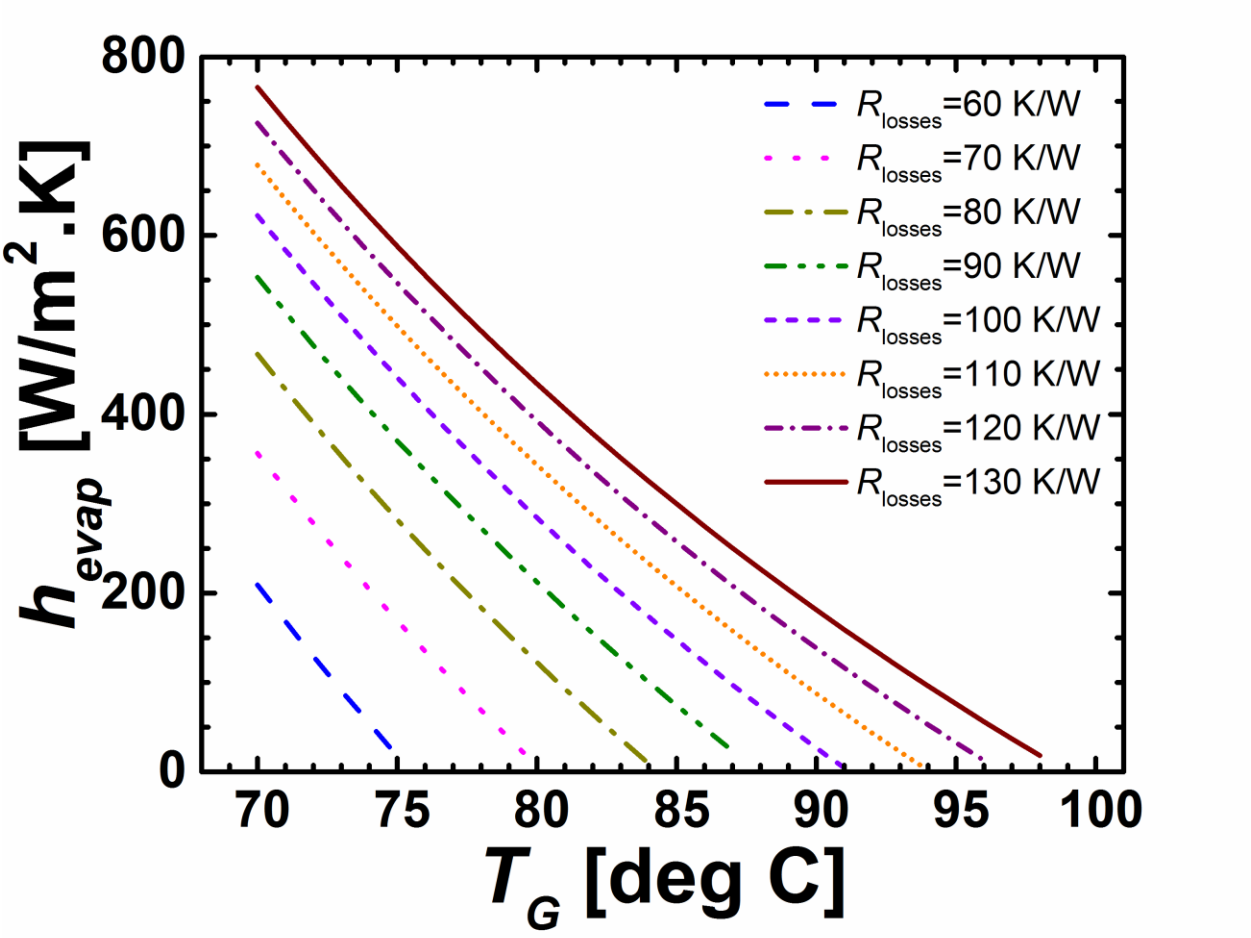

Figure 5.4. Evaporation heat transfer coefficient in terms of the GaN temperature for different values of $\mathbf{R}_{losses}$.

Experimentally, without jumping droplets ($h_{\text{evap}} = 0$), the temperature of the GaN was determined to be 90 ± 1 °C which results in R_{losses}= 100 ±5 K/W. With this value of R_{losses}, we can determine the value of h_{evap} for different GaN temperatures.

Using the cross-sectional area of the GaN FET (A_{GaN} = 0.12 cm^2),[25] a total heat flux of 13.2 W/cm^2 was dissipated. The cooling benefit can be separated into its contributing factors of radiation, convection, conduction through the back of the PCB, and heat removed via jumping droplet condensation and subsequent evaporation from the GaN device.

Table 5.2 summarizes the measured and calculated performance, showing that although only modest GaN FET temperature decreases (~ 2°C) were obtained by jumping droplet cooling, EFE condensation enhances the heat transfer from the hot spot by ≈ 200% and 20% when compared to cooling without jumping and non-EFE jumping, respectively.

Table 5.2. Quantitative thermal breakdown for the key single-GaN experiment parameters. H.T.C. stands for heat transfer coefficient.

Parameters	**Symbol [Units]**	**(a) no jumping**	**(b) jumping**	**(c) EFE jumping**
Heat generated	q **[W]**	1.6 ± 0.4		
Sample temperature	T_s **[°C]**	5 ± 0.5		
GaN area	A_G **[cm^2]**	0.12 ± 0.01		
Sample area	A_s **[cm^2]**	25 ± 0.1		
Nat. convection H.T.C.	h_{nat} **[W/m^{2}K]**	2 - 5		
Radiation H.T.C.	h_{rad} **[W/m^{2}K]**	7.60	7.52	7.48
Condensation H.T.C.	h_{cond} **[W/m^{2}K]**	100 - 1000		
GaN temperature	T_{GaN} **[°C]**	90 ± 1	88 ± 1	87 ± 1
Evaporation H.T.C.	h_{evap} **[W/m^{2}K]**	≈ 0	100 ± 25	150 ± 25
Heat removed from front	q_f **[W]**	0.036 ± 0.03	0.082 ± 0.03	0.105 ± 0.03
Heat flux from front	q_f'' **[W/cm^2]**	0.3 ± 0.25	0.69 ± 0.25	0.92 ± 0.25

The relatively low heat fluxes dissipated by our device was mainly due to the presence of non-condensable gases (NCGs) in the vapor environment. The condensation of water vapor leaves behind NCGs (air) that blanket the superhydrophobic surface and act as a diffusion barrier for water vapor.[27, 28] The counter diffusion of water vapor to the surface, coupled with the diffusion

of NCGs away from the surface, significantly deteriorate the condensation heat transfer process, and hence decrease the effective surface-to-vapor temperature difference.

To investigate the possibility of using jumping-droplet EFE condensation to achieve dynamic spatial-temporal control of cooling for mobile hot spots, we repeated the experiments with a modified two transistor circuit having two GaN devices spaced 3 mm apart in the horizontal direction (Fig 5.2(e)). By observing droplet trajectories through high speed imaging, we were able to plot the trajectories of droplets from the superhydrophobic surface to the GaN devices with no-field, EFE condensation with the electric field biased towards only one GaN FET (GaN1) or the electric field biased towards the other GaN FET (GaN2) (Fig. 5.5).

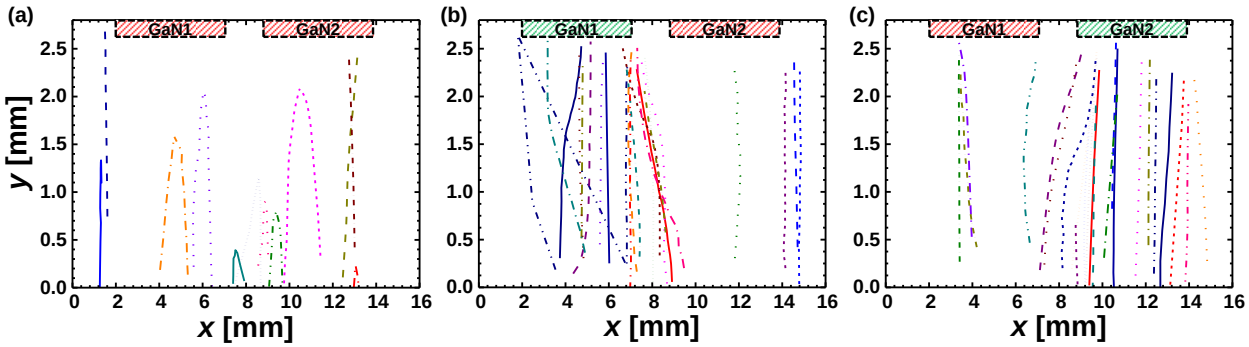

Figure 5.5. Droplet trajectories (a) without electric field (shaded red), (b) electric field applied to the left GaN transistor (shaded green), and (c) electric field applied to the right GaN transistor (shaded green). Gap spacing, voltage, and electric field strength were: 2.5 mm, -100 V, and -40 V/mm. E-Field is pointing toward the GaN devices as described in Figure 5.2. In addition to directing jumping droplets to the active transistor, the electric field also prevented droplet return due to gravitational forces as well as vapor flow entrainment back to the condensing surface.

In contrast to Figure 5.5(a) where no external electric fields are employed, Figures 5.5(b) and 3(c) underscore how an external electric field dramatically increases the average number of droplet trajectories directed toward a specific GaN transistor, and demonstrates spatially controllable cooling. The droplet trajectories in Fig. 5.5(c), which appear to stop before reaching the GaN FET, are a good example of droplets leaving the plane of focus for the high resolution video camera. In this case, the droplets will reach the GaN device due to the external electric field. The droplet's

initial velocity, as measured from the videos, did not show a significant deviation from the inertial-capillary scaling, consistent with previous works on jumping droplets[8, 21, 22] that have deduced that the separation of charge on the superhydrophobic surface happens as a result of jumping, which leads to electrostatic interaction contributions only after the jump. The frequency of jumping was also not increased with the application of electric fields during the experiment. However, we expect that on the long run, the reduced average droplet size on the surface will result in an increase in the number of droplets that are within the jumping range, causing an increased jumping frequency as an indirect effect of the applied field. Electrically floating the source pin was found experimentally to direct the droplets closer to the GaN transistor than the external guard ring. Since the source pin approach involves electrically floating pins underneath approximately half of the total device surface as shown in Fig. 5.2(b), the electric field lines attract all of the droplets directly toward the GaN FET. In contrast, some of the droplets attracted by the external guard ring would have to wick from the guard ring toward the package of the GaN device.

5.3. Discussion

To provide insight into the experimental results and to project the maximum potential of jumping-droplet cooling, we estimated the maximum possible thermal concentration of droplets that could reach a GaN FET using the image processing techniques coupled to previous condensation heat transfer measurements in pure vapor environments.[29] Assuming that all of the departing droplets leave the superhydrophobic surface and reach the GaN device, the maximum jumping-droplet cooling heat flux can be calculated as $q'' = q_c''A_C/A_{GaN}$, where q_c'' is the critical flooding heat flux for CuO superhydrophobic surfaces having conformal hydrophobic polymer coatings ($\approx 13 W/cm^2$ from h=10,000 W/m^2K & $\Delta T = 10^oC$), and A_C is the effective condenser area which is able to provide jumping droplets that move laterally from their jumping location to the

GaN device ($A_c = L^2$, where L is the maximum horizontal distance from which jumping droplets will travel to the device). Analyzing figures analogous to Figure 5.5(d) to estimate L during EFE condensation ($A_C \approx 9A_{GaN}$), our analysis suggests that heat fluxes of $q'' \approx 120 W/cm^2$ should be attainable in pure vapor environments for gap spacings of 3 mm and the GaN FET geometries studied here. We note that in a closed system, no heat flux limitation is present due to wicking as in conventional heat pipes and vapor chambers[18, 30]. Our analysis suggests that increasing in the charge per droplet is the most important parameter to obtain enhanced heat flux since the effect of the electric field attrition force and area ratio can be increased ($A_C \sim L^2$). A secondary and more practical approach to increase the hot spot heat flux is to optimize the condenser-to-FET spacing or applied EFE voltage in order to attract more droplets. The experiments conducted here were limited to -100 V due to safety considerations; however, higher applied voltages are possible in closed systems.[16]

The EFE jumping droplet cooling method demonstrated here is similar to but fundamentally different from the jumping-droplet vapor chamber.[18] In the jumping droplet vapor chamber, spatial and temporal control of droplet motion is not possible, whereas in our device, active sensing of hot spots can be used as a feedback to locally direct droplets using electric fields. Furthermore, active application of electric fields may not be necessary, as the EFE concept developed here has future possibility of exploiting the inherent electric fields generated by the high voltage switching action (dv/dt) from power semiconductor devices to tailor the electric field to provide localized, directed cooling for the power devices. In addition to improved cooling, this effect may also realize a method to better equalize temperatures, a key design challenge for power sharing among parallel-connected devices. In the future, it would be interesting to investigate the performance of the device in pure vapor environments in vacuum due to: (i) the significant condensation thermal

resistance added by NCGs, and (ii) the potential for droplet charge dissipation in the presence of NCGs. Indeed, a scaling analysis using previous EFE condensation visualization studies in pure vapor environments[22] indicates that the thermal concentration ratio (A_C/A_{GaN}) can be well over 100 for gap spacing of the same order of magnitude studied here (5 mm), inferring that $q'' = q_c''A_C/A_{GaN} \approx$ 1kW/cm^2 can be achieved.

5.4. Conclusions

In summary, we demonstrated jumping-droplet hot spot cooling, whereby charged droplets jump between superhydrophobic copper oxide condensers and electrical circuits to cool local hot devices actively with evaporation. Through experiments and modeling, we demonstrated heat flux dissipations of 1 W/cm^2, which can be improved in the near-term to 120 W/cm^2. Future enclosed devices with pure vapor environments, and optimized geometrical designs have the potential to achieve higher active cooling rates approaching 1 kW/cm^2. However, for a reliable practical application, it is crucial to investigate the durability of the superhydrophobic surfaces, determining their possible mechanical degradation within months or years. This work not only demonstrates EFE condensation based electronics cooling for the first time, but also provides a framework for the development of active jumping droplet based vapor chambers and heat pipes capable of spatial and temporal thermal dissipation control.

5.5. References

[1] P.T. Krein, Elements of power electronics, Oxford University Press, New York, 1998.

[2] J.G. Kassakian, T.M. Jahns, Evolving and Emerging Applications of Power Electronics in Systems, Ieee J Em Sel Top P, 1(2) (2013) 47-58.

[3] Y. Lei, C. Barth, S. Qin, W. Liu, I. Moon, A. Stillwell, D. Chou, T. Foulkes, Z. Ye, Z. Liao, R.C. Pilawa-Podgurski, A single-phase, 7-level, gan inverter with an active energy buffer achieving 216 w/in3 power density and 97.6% peak efficiency, in: IEEE (Ed.) Applied Power Electronics Conference and Exposition (APEC), IEEE, Long Beach, CA, 2016.

[4] A. Faghri, Heat pipe science and technology, 2nd ed., Global Digital Press, Columbia, MO, 2010.

[5] C.B. Barth, T. Foulkes, W. Chung, T. Modeer, P. Assem, Y. Lei, R.C.N. Pilawa-Podgurski, Design and control of a GaN-based, 13-level, flying capacitor multilevel inverter, in: IEEE (Ed.) 2016 IEEE 17th Workshop on Control and Modeling for Power Electronics (COMPEL), IEEE, Trondheim, Norway, 2016, pp. 1-6.

[6] J. Doty, K. Yerkes, L. Byrd, J. Murthy, A. Alleyne, M. Wolff, S. Heister, T.S. Fisher, Dynamic Thermal Management for Aerospace Technology: Review and Outlook, J Thermophys Heat Tr, 0(0) (2016) 1-13

[7] J.B. Boreyko, C.H. Chen, Self-Propelled Dropwise Condensate on Superhydrophobic Surfaces, Phys Rev Lett, 103(18) (2009).

[8] R. Enright, N. Miljkovic, J. Sprittles, K. Nolan, R. Mitchell, E.N. Wang, How Coalescing Droplets Jump, ACS Nano, 8(10) (2014) 10352-10362.

[9] H. Cha, C. Xu, J. Sotelo, J.M. Chun, Y. Yokoyama, R. Enright, N. Miljkovic, Coalescence-Induced Nanodroplet Jumping, Physical Review Fluids, 1(064102) (2016).

[10] G.S. Watson, M. Gellender, J.A. Watson, Self-propulsion of dew drops on lotus leaves: a potential mechanism for self cleaning, Biofouling, 30(4) (2014) 427-434.

[11] R.L. Chavez, F.J. Liu, J.J. Feng, C.H. Chen, Capillary-inertial colloidal catapults upon drop coalescence, Appl Phys Lett, 109(1) (2016).

[12] R. Enright, N. Miljkovic, J.L. Alvarado, K. Kim, J.W. Rose, Dropwise Condensation on Micro- and Nanostructured Surfaces, Nanosc Microsc Therm, 18(3) (2014) 223-250.

[13] D. Attinger, C. Frankiewicz, A.R. Betz, T.M. Schutzius, R. Ganguly, A. Das, C.-J. Kim, C.M. Megaridis, Surface engineering for phase change heat transfer: A review, MRS Energy & Sustainability, 1 (2014).

[14] N. Miljkovic, E.N. Wang, Condensation heat transfer on superhydrophobic surfaces, Mrs Bull, 38(5) (2013) 397-406.

[15] H.J. Cho, D.J. Preston, Y. Zhu, E.N. Wang, Nanoengineered materials for liquid–vapour phase-change heat transfer, Nature Reviews Materials, 2(16092) (2016).

[16] A. Shahriari, P. Birbarah, J. Oh, N. Miljkovic, V. Bahadur, Electric-field-based control and enhancement of boiling and condensation, Journal of Nanoscale and Microscale Thermophysical Engineering, (2016).

[17] J.B. Boreyko, Y.J. Zhao, C.H. Chen, Planar jumping-drop thermal diodes, Appl Phys Lett, 99(23) (2011).

[18] J.B. Boreyko, C.H. Chen, Vapor chambers with jumping-drop liquid return from superhydrophobic condensers, International Journal of Heat and Mass Transfer, 61 (2013) 409-418.

[19] N. Miljkovic, D.J. Preston, R. Enright, E.N. Wang, Jumping-droplet electrostatic energy harvesting, Appl Phys Lett, 105(1) (2014).

[20] J.B. Boreyko, P.C. Collier, Delayed Frost Growth on Jumping-Drop Superhydrophobic Surfaces, Acs Nano, 7(2) (2013) 1618-1627.

[21] N. Miljkovic, D.J. Preston, R. Enright, E.N. Wang, Electrostatic charging of jumping droplets, Nat Commun, 4 (2013).

[22] N. Miljkovic, D.J. Preston, R. Enright, E.N. Wang, Electric-Field-Enhanced Condensation on Superhydrophobic Nanostructured Surfaces, ACS Nano, 7(12) (2013) 11043-11054.

[23] P. Birbarah, Z.E. Li, A. Pauls, N. Miljkovic, A Comprehensive Model of Electric-Field-Enhanced Jumping-Droplet Condensation on Superhydrophobic Surfaces, Langmuir, 31(28) (2015) 7885-7896.

[24] R. Prasher, Thermal interface materials: Historical perspective, status, and future directions, P Ieee, 94(8) (2006) 1571-1586.

[25] E.E.P. Conversion, EPC2304 – Enhacement Mode Power Transistor, 2016.

[26] Y. Nam, Y.S. Ju, A comparative study of the morphology and wetting characteristics of micro/nanostructured Cu surfaces for phase change heat transfer applications, Journal of Adhesion Science and Technology, 27(20) (2013) 2163-2176.

[27] W.J. Minkowycz, E.M. Sparrow, Condensation Heat Transfer in Presence of Noncondensables Interfacial Resistance Superheating Variable Properties and Diffusion, International Journal of Heat and Mass Transfer, 9(10) (1966) 1125-+.

[28] S. Chavan, H. Cha, D. Orejon, K. Nawaz, N. Singla, Y.F. Yeung, D. Park, D.H. Kang, Y.J. Chang, Y. Takata, N. Miljkovic, Heat Transfer through a Condensate Droplet on Hydrophobic and Nanostructured Superhydrophobic Surfaces, Langmuir, 32(31) (2016) 7774-7787.

[29] N. Miljkovic, R. Enright, Y. Nam, K. Lopez, N. Dou, J. Sack, E.N. Wang, Jumping-Droplet-Enhanced Condensation on Scalable Superhydrophobic Nanostructured Surfaces, Nano Letters, 13(1) (2013) 179-187.

[30] J.B. Boreyko, Y.J. Zhao, C.H. Chen, Planar jumping-drop thermal diodes, Appl Phys Lett, 99(23) (2011) 234105.

Chapter 6 – Water Immersion Cooling of Electronics

6.1. Introduction

Thermal management of power electronic systems is a key bottleneck to power densification [1-7]. Single phase cooling is limited to low heat transfer coefficients [8] (< 2000 W/m2K) while two-phase cooling such as flow boiling suffers from hydrodynamic instabilities [9]. Immersion cooling has emerged as a potential solution to overcome these barriers by enabling the boiling of a cooling fluid directly from the electronics module, thereby removing thermal interface materials [10, 11] and packaging constraints. Except for the use of treated, deionized water for some systems [12], state of the art (SOA) immersion cooling systems [13] utilize non-conductive dielectric heat transfer liquids due to electrical considerations [14, 15]. The use of these fluids presents three fundamental disadvantages: 1) the low boiling point of non-polar fluids at atmospheric pressure means that electronics components cannot exceed the boiling temperature (≈ 50°C) by an appreciable amount due to the formation of a vapor blanket and critical heat flux. 2) The maximum heat flux attainable in the system is equal to the critical heat flux of the working fluid, which for non-polar dielectric fluids is much smaller (< 20 W/cm^2) than what is needed for next generation high power density systems (> 100 W/cm^2). 3) The dielectric fluid has relatively poor thermophysical properties such as thermal conductivity, latent heat, and surface tension, when compared to ideal conducting fluids such as water.

In this study, we propose using water as the immersion fluid which has significant advantages over SOA systems in addition to the increased availability and reduced cost. The ultra-high latent heat of phase change (2.4 MJ/kg for water-glycol vs. 0.3 MJ/kg for oil) and surface tension (50 to 73 mN/m for water-glycol mixtures vs. 5 mN/m for oil) of water and water-glycol mixtures enable

highly efferent pool boiling heat transfer that has an order of magnitude increase in crucial heat flux when compared to dielectric liquids. Furthermore, operating temperatures of electronics at atmospheric pressures could be extended to 100°C for water or higher for water glycol mixtures (107°C for water-ethylene glycol mixture of 50%-50% by volume).Water based fluids are currently utilized in many applications such as automotive cooling and hence would eliminate the need for additional working fluids for immersion cooling of electronics. The main challenge of implementing water immersion cooling is the electrical conduction of water due to its polar nature and the ionization it induces. To solve this problem, we first coat the electronic components such as Gallium Nitride (GaN) transistors on a PCB with an ultra-thin (≈1-25 μm) and ultra-conformal high dielectric constant [16] (78 V/μm) Parylene C coating, hence electrically passivating and isolating these components from the working fluid. Here, we demonstrate the capability of a 5 μm layer of ParyleneC to insulate the board and run up to 20 A of current through a GaN transistor without any short circuit occurring. We extract the heat transfer characteristics of the system (q vs ΔT and h vs ΔT) for water, water-glycol mixture (50% by volume) and dielectric fluids, and demonstrate an enhancement in the heat dissipated before transistor failure. This study not only demonstrates immersion cooling in water and water-glycol mixtures of high-power density electronics, but develops the design guidelines for cooling of electronic components through the use of novel coatings.

6.2. Immersion cooling vs forced air cooling

Prior to the experiments, we motivate the study with a comparison between forced air cooling of electronics and immersion cooling. In figure 1, we consider a standard geometry of a finned heat sink designed for the cooling of an intel Core 2 Quad processor. The geometry considered is used for quantifying the fin resistance: 10 square fins (5cm x 5cm) with a 2 mm thickness cover the

PCB area (5 cm x 5 cm), with a fin spacing of 3 mm. Underneath the heat sink, is a gap pad (1 mm thick) that is made of a rubber-like material with an advanced thermal conductivity of k_{pad}=17 W/(m.K), a state of the art thermal conductivity for gap pads. The gap pad and the heat sink sit on top of the PCB and air is blown towards the heat sink, with a convection coefficient h. The heat sink is assumed to be made of copper k_{Cu}=385 W/(m.K). We calculate the fin resistance associated with this configuration and plot the total thermal resistance of the forced air cooling strategy (figure 2-a), and compare it to water immersion with a insulating layer of Parylene C (k_{p}=0.1 W/(m.K)), and immersion in a dielectric fluid (figure 2-b). Water boiling is assumed to have a 100,000 W/m^{2}K heat transfer coefficient with the dielectric boiling one order of magnitude below that.

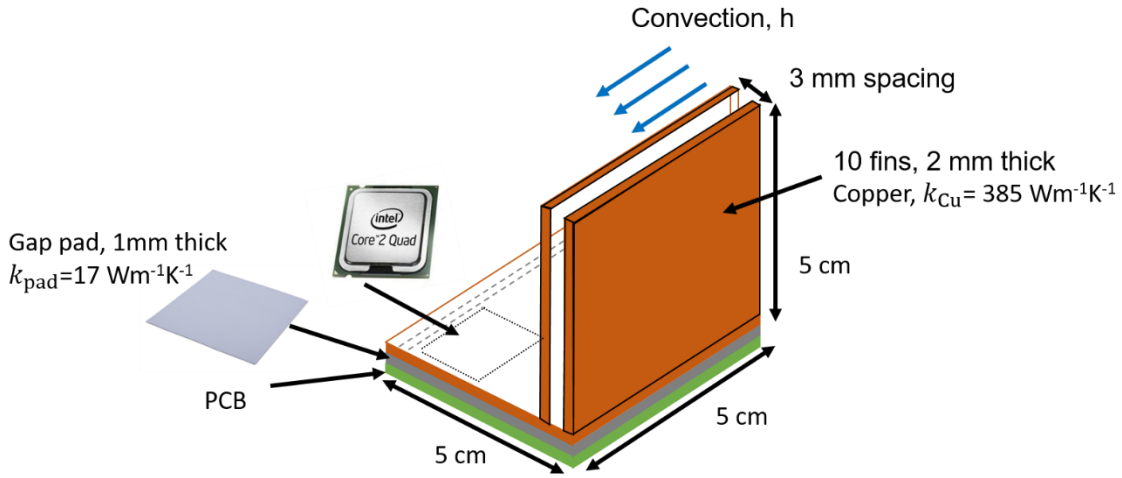

Figure 6.1. Standard heat sink design for forced air cooling of an intel Core 2 Quad CPU.

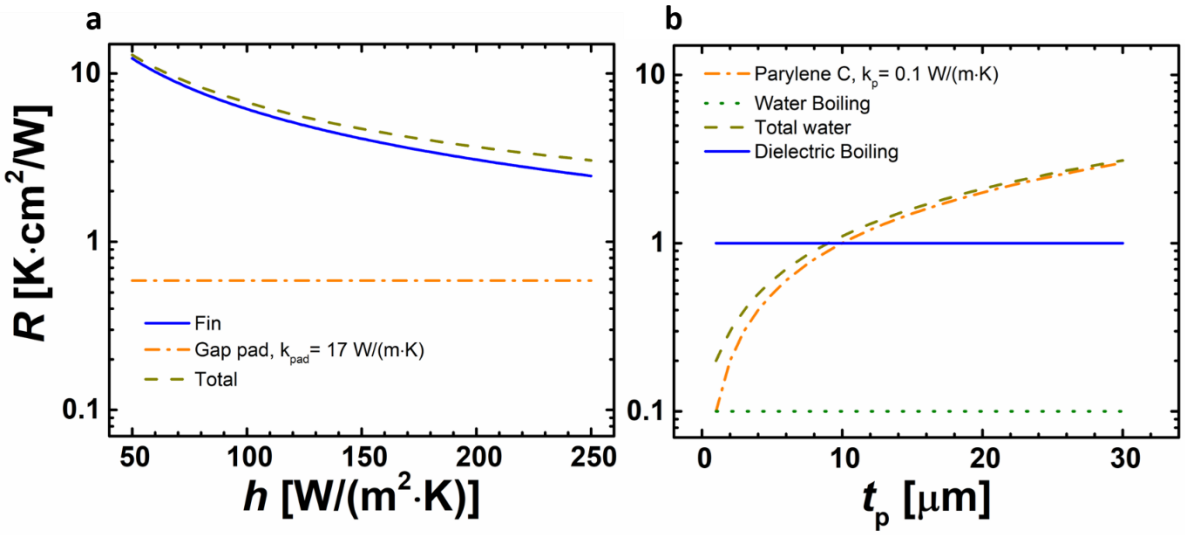

Figure 6.2. Thermal resistance (R) analysis of (a) forced air cooling for electronics cooling as a function of the convection coefficient h, and (b) immersion cooling in a dielectric fluid and in water with a Parylene C coating for electrical insulation as a function of the Parylene thickness t_p.

6.3. Experimental setup and procedure

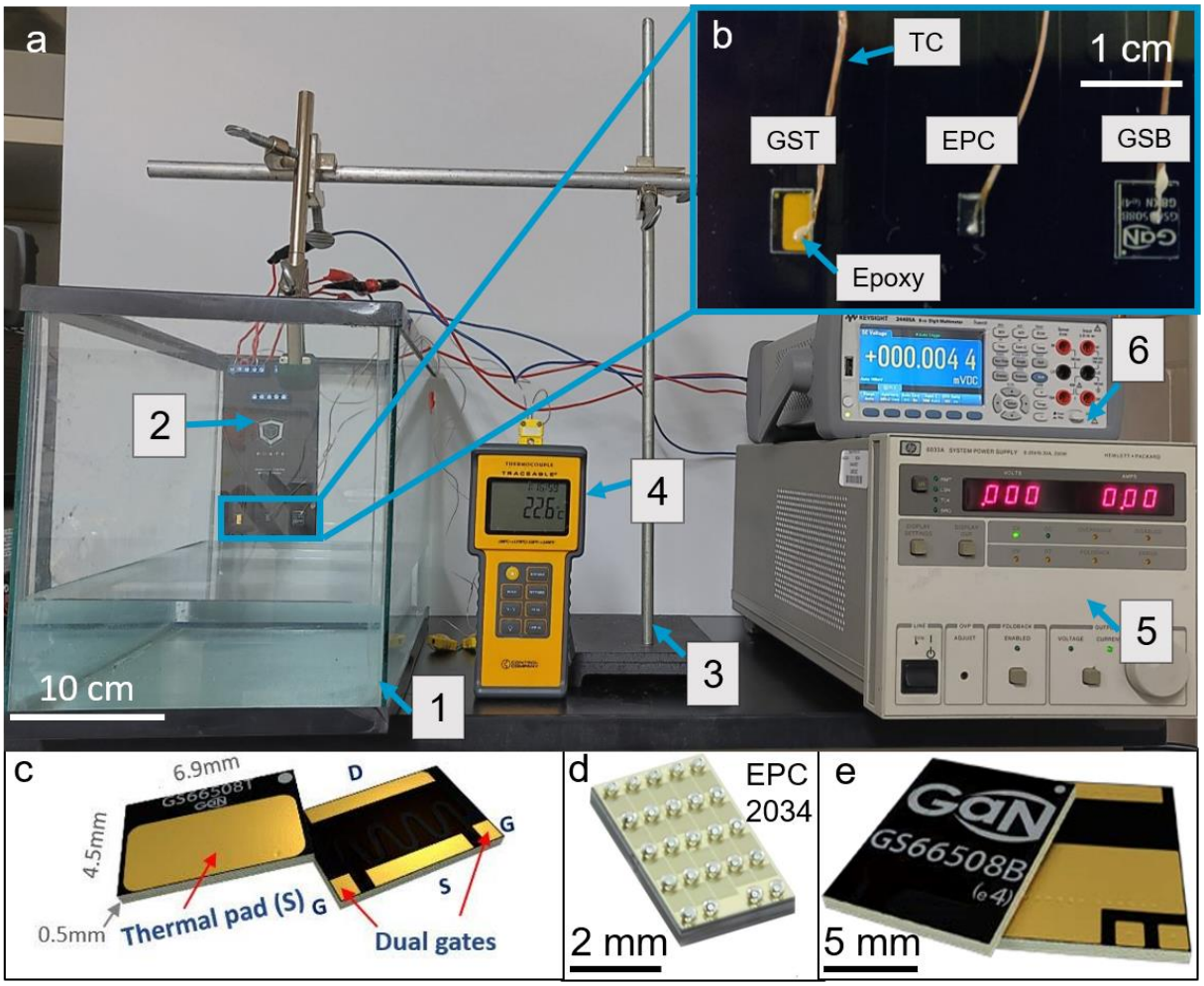

Figure 6.3. (a) Experimental setup for immersion cooling. 1: Glass immersion tank, 2: Printed circuit board, 3: Support for PCB, 4: thermocouple reader, 5: Power supply, 6: digital multimeter. (b) Zoom-in picture of transistors: GaN Systems top cooled (GST), GaN Sys Systems bottom cooled (GSB) and EPC 2034 (EPC). Thermocouples (TC) are attached to the surface of the transistors via epoxy. (c), (d) and (e) Dimensions and footprints of GST, EPC and GSB respectively

Figure 3-a represents the setup that is used for the immersion cooling of the transistors. The printed circuit board (PCB) is immersed in a glass tank that holds the immersion fluid. The PCB is held vertically with a clamp that is attached to an aluminum rod support structure with screw clamps, giving freedom of operation in the vertical plane and in the horizontal inclination. The support structure itself stabilizes through the base weight and can be easily repositioned. We use an

HP6033A power supply to apply the constant voltage to the transistors that operate in diode mode (gate-source shorted, V_{SD} >0). The diode regime enables us to dissipate enough heat to induce boiling of the immersion fluid, as opposed to pure conduction mode ($V_{GS} = 5V$, i_{DS}> 0) that is characterized by little thermal losses as the on-state resistance varies from $R_{ds,ON}$=10 mΩ (EPC 2034) to 50 mΩ (GS66508B, GS66508T). The voltage drop across the drain and source is measured via a Keysight 34465A digital multimeter, through Kelvin connections that provide direct access to the drain and source eliminating the error due to voltage drop across the connecting wires[16].

Standard FR-4 printed circuit boards (PCBs) are used, with all exposed copper coated with gold to prevent oxidation. The FR4 layer is 1.6 mm thick, sandwiched between two 71.12 μm thick copper layers (2 oz. Cu). In order to constrain the heat near the transistors, the copper leads on the PCB were designed thin (≈1 mm wide) as compared to the leads further away from the transistors on the PCB (≈5 mm wide) in oder to generate less heat in the wires and decrease the thermal resistance simultaneously. For the bottom-cooled GaN Systems devices, open plated through-hole vias are added to drive heat to the thermal pads created on the bottom copper layer. They are spaced 0.64 mm apart, both vertically and horizontally, with a diameter equal to 0.3 mm, as recommended for preventing solder wicking through the vias[17].

On the surface of the transistor, we mount a PFA insulated K type thermocouple with a diameter of 80 μm and fix it via a pre-mixed epoxy paste (Duralco 128) that is left 24 hours to cure at room temperature. The epoxy is deposited to form a small drop (<1mm x 1mm, fig.3-b) in order to minimize the error on the temperature measurement while providing enough adhesion for the thermocouple. However, the temperature error can still be high for high heat flux, which was depicted in some of our error bars.

Three types of transistors are used in the experiments (figure 3). EPC2034 is a top-cooled transistor with solder balls on its back (PCB side) that are used for soldering purposes. The EPC2034 is rated for a drain-source voltage V_{DS}=200V, drain current i_{D}=48 A, with an ON state resistance $R_{\mathrm{DS,ON}}$=10 mΩ. The EPC2034 is used for high frequency DC-DC conversion, motor drive, industrial automation, class-D audio and other[18]. On the other hand, the two transistors provided by GaN Systems, GS66508B (bottom-cooled) and GS66508T (top cooled), are surface-mount devices that are placed directly on the surface of the PCB. For the bottom-cooled device, thermal vias (spacing and diameter) are added to the footprint in order to route the heat generated into the thermal pad located on the back of the board. In the case of top-cooled transistors, heat is dissipated to the fluid through the top thermal pads that are added by the manufacturer. They are both rated for V_{DS}=650V, drain current i_{D}=30 A, with $R_{\mathrm{DS,ON}}$=50 mΩ, with applications in high efficiency and high power density power conversion (AC-DC and DC-DC), uninterruptable power supplies, and other[19, 20].

As for the immersion fluid, we use two distinct dielectric fluids (3M Novec 72DE[21], 3M Novec 7300[22]) in addition to tap water and a mixture of water and ethylene glycol 50% -50% by volume. The properties of the fluids are depicted in table 1[21-28]. For water and water-ethylene glycol mixtures we had to add a few drops of a commercial non-ionic surfactant (Plex Mate) to eliminate the adhesion of pre-dissolved air on the transistor as the temperature increases and the solubility of air decreases in the fluid.

Table 6.1. Properties of the immersion fluids at ambient temperature and at saturation temperature at atmospheric pressure.

Property	**T = 25 °C**				**$T = T_b$ (boiling temperature)**			
	Novec 72DE	**Novec 7300**	**Water**	**50/50 WEG**	**Novec 72DE**	**Novec 7300**	**Water**	**50/50 WEG**
T_b	-	-	-	-	43	98	100	107.3
c_p [kJ/kg·K]	≈1.1	1.14	4.173	3.412	≈1.1	1.14	4.217	3.65
h_{fg} [kJ/kg]	≈235	92	2438	≈1500	217.6	≈84.2	2257	≈1380
ρ_l [kg/m^3]	1280	1645	997	1079	≈1143	1467	957.8	1030
ρ_v [kg/m^3]	2.19	1.06	0.025	≈0.02	≈27.38	13.2	0.6	≈0.02
k [W/m·K]	≈0.06	0.063	0.6	≈0.37	≈0.06	0.063	0.68	≈0.4
σ [mN/m]	19	14.15	72	57	≈11.65	8.64	58.9	45
μ x10^6 [Pa·s]	450	1000	855	2800	≈190.7	423	279	700
Pr	≈8.25	18.78	5.95	≈25.8	≈ 3.37	7.65	1.76	6.38
βx10^6 [K^{-1}]	≈ 1300	1300	276	210	-	-	-	-

Prior to testing with water and water-glycol mixture, the boards are coated with a thin (1-25 µm) coating of dielectric (Parylene C, E_s=78 V/m, $k_{parylene}$ =0.1 W/m.K) via chemical vapor deposition (CVD, Specialty Coating Systems corporation). The coating is conformal and is tested in tap water prior to experimentation for current leakage through the PCB. The gate is connected

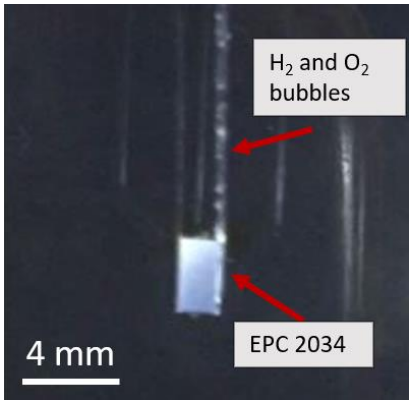

Figure 6.4. Hydrolysis of tap water for transistor in reverse diode mode.

to the source without any activation voltage, and the voltage between drain and source is increased up to 200 V without any observed current or hydrolysis of the water. Without any coating, bubbles

are observed rising from the transistors due to hydrolysis (Fig. 4), demonstrating that the coating was the inhibitor of hydrolysis.

6.4. Thermal performance of different immersion fluids

6.4.1. Experimental Results

The immersion heat transfer performance is evaluated for the different fluids considered (Novec 72DE, Novec 7300, tap water and water-ethylene glycol 50%-50% by volume). For conductive fluids (water and water-glycol mixture), we conduct experiments for the 3 different thicknesses of Parylene C (1μm, 5μm and 25 μm). We plot the power dissipated per transistor as a function of the temperature potential between the surface temperature of the transistor and the ambient fluid. In addition, we compare the performance of two different topologies for top-cooled transistors (EPC 2034 and GST). In figure 5-a we plot the results for the EPC2034 transistor. The power in the transistor was increased until the device failed. The curves depict the regime of single phase natural convection as well as the boiling regime. For the dielectric fluids, a critical heat flux is reached and leads to device failure. The power dissipated does not exceed 14 W and critical heat flux is achieved at ΔT ≈60°C or T_s ≈80°C (T_{amb} ≈ 20°C) for Novec 72DE (T_b=43°C) and at T_s ≈120°C for Novec 7300 (T_b=98°C). As for water and water-glycol mixture, the device failure occurs in the nucleate boiling regime due to the junction temperature exceeding its rated value (150 °C). The boiling curve should not theoretically vary for the different parylene thicknesses for a given fluid, since the heat flow would not change for a given heat transfer coefficient and the same temperature difference between the surface of the transistor and the ambient temperature. This is in good agreement with the experimental curves showing little variation within the same fluid, except that the maximum power obtained can vary greatly between thicknesses, which relates to the overall resistance (including the parylene thermal resistance). The maximum power

dissipated per device is shown in table 2 for the different curves plotted in figure 5-a. As for the transfer coefficient (figure 5-b), there is some difficulty in determining exactly its value since the area through which the heat is being dissipated is greater than the footprint area due to heat spreading in the PCB. For that reason, we plot the area-multiplied heat transfer coefficient (hA) in terms of ΔT, and a corresponding heat transfer coefficient based on the footprint area on the right axis. The observed heat transfer coefficients are summarized in table 3.

The error on the temperature is obtained by repeating the experiment for at least two different boards (2-5 experiments per curve), while accounting for the error on the thermocouple (± 1℃). The error in the heat dissipated is minimal as the voltage $V_{\mathrm{DS}}$was measured with Kelvin connections and did not include any losses from the wires. The error on the power was on average less than 0.5 W. While the power error bars were insignificant, some temperature error bars observed were relatively large (50°C). This is due to the small variation (<0.5 mm) in the thickness of the epoxy used (k_{epoxy}=2.88 W/mK) to attach the thermocouple. In figure 6, we plot the temperature drop across the epoxy for a heat flux ranging from 1 to 100 W/cm^2 (which is roughly the critical heat flux for water that has not been reached in the experiments), when the epoxy thickness t_{epoxy} takes on values of 0.1 mm, 0.25 mm and 0.5 mm. The estimation relied on the 1-dimensional linear thermal resistance of the epoxy. The maximum temperature drops range from 35K for t_{epoxy}=0.1 mm to 170K for t_{epoxy}=0.5 mm, which explains the error bars observed, and is a limitation of the temperature measurement technique employed.

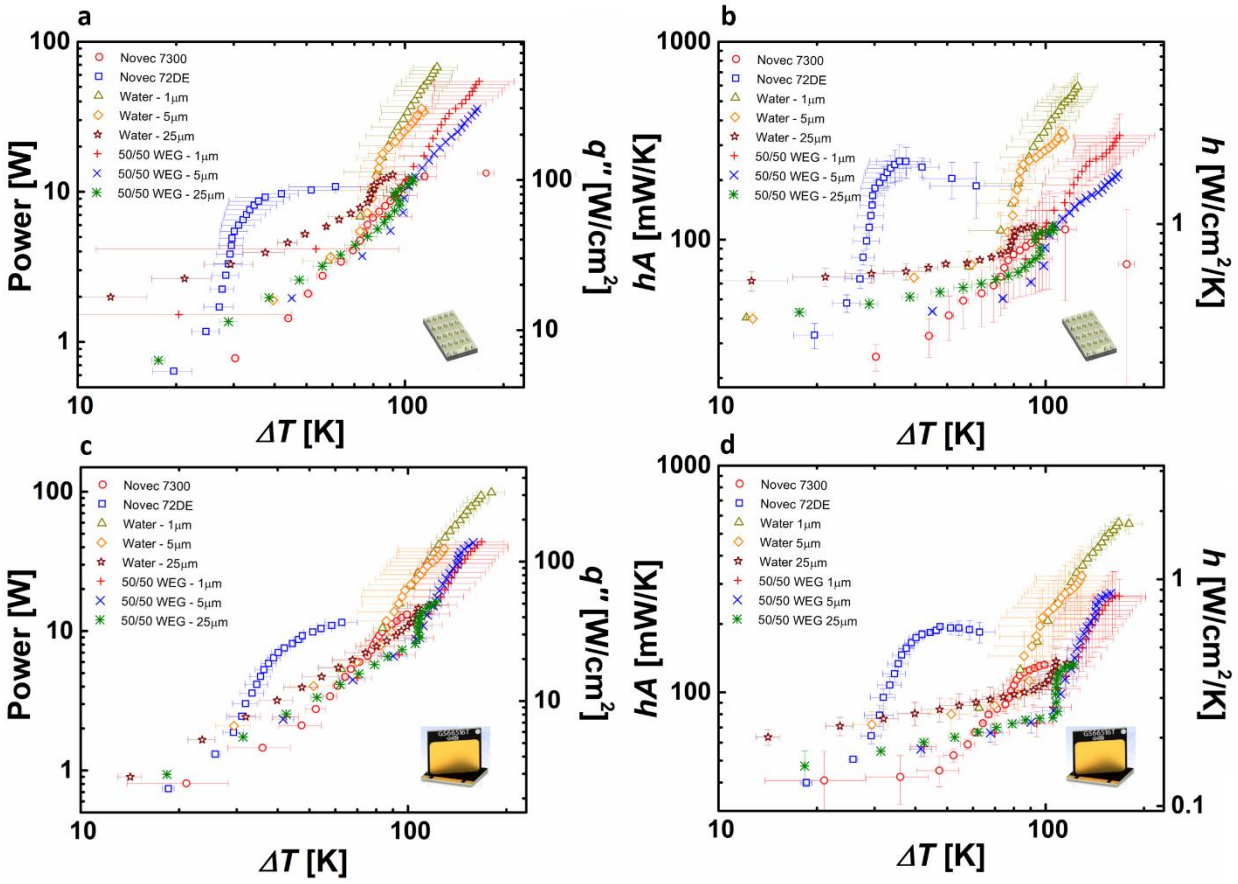

Figure 6.5. (a) Power dissipated per transistor (EPC2034) as a function of the temperature difference **ΔT** between the top surface of the transistor and the ambient fluid temperature. On the left axis is plotted the power per footprint area (12.5 mm^2),$\mathbf{q''}$. (b) Overall area-multiplied heat transfer coefficient (UA) as a function of **ΔT**. Experiments are conducted for two dielectric fluids (Novec 72DE and Novec 7300) as well as for water and water-ethylene glycol mixture for 3 different thicknesses of dielectric Parylene C coating (1 μm, 5 μm and 25 μm). (c) and (d) Power-ΔT and UA-ΔT for GST.

Table 6.2. Maximum power dissipated per footprint area of transistors during immersion.

Device	Maximum Power Dissipated per footprint area [W/cm²]							
	72DE	7300	50/50 WEG			Water		
	-	-	25 μm	5 μm	1 μm	25 μm	5 μm	1 μm
EPC2034(12 mm²)	90	111	103	298	452	108	299	562
GST(31.5 mm²)	37	42	49	124	314	51	136	139

Table 6.3. Experimental heat transfer coefficient (based on footprint area) for natural convection and nucleate boiling for the immersion fluids considered for the EPC2034 (12mm^2 footprint area)

Fluid	*h* [kW/m^{2}K] – based on footprint area	
	Natural convection	Nucleate Boiling
Novec 72DE	2±0.34 – 5.4±0.54	5.4±0.54 – 20.8±4.2
Novec 7300	1.9±0.05 – 4.2±1.17	4.2±1.17 – 9.7±4.9
50/50 WEG	2.5±0.11 – 7±0.36	7.0±0.36 – 27.9±7.83
Water	3.3±0.25 – 9.2±2.08	9.2±2.08 – 49.2±8.16

Table 6.4. Experimental heat transfer coefficient (based on footprint area) for natural convection and nucleate boiling for the immersion fluids considered for the GST (31.5 mm^2 footprint area)

Fluid	*h* (kW/m^{2}K) – based on footprint area	
	Natural convection	Nucleate Boiling
Novec 72DE	1.27±0.06 – 2.4±0.21	2.4±0.21 - 6.2±0.44
Novec 7300	1±0.19 – 2±0.086	2±0.086 – 4.2±0.11
50/50 WEG	1.5±0.22 – 2.3±0.29	2.3±0.29 – 8.6±2.57
Water	2.1±0.32 – 3.2±0.46	3.2±0.46 – 17.8±1.37

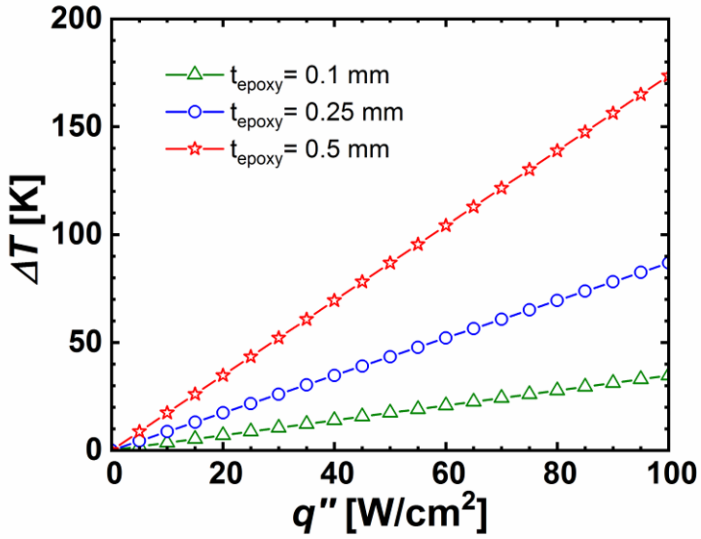

Figure 6.6. Temperature drop across the epoxy as a function of heat flux for different epoxy thicknesses. One dimensional linear thermal resistance is assumed for the estimation of temperature drop.

6.4.2. Comparison with Literature

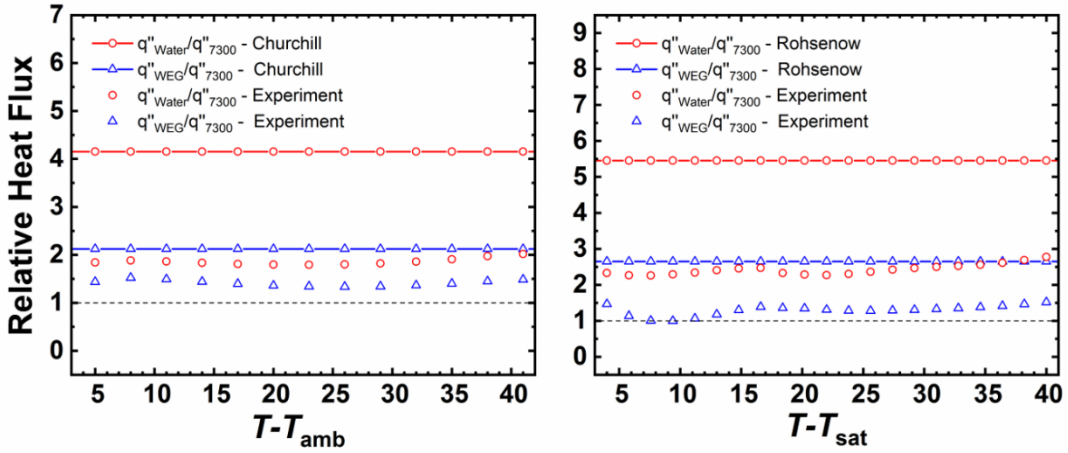

Figure 6.7. (a) Relative heat flux comparison for several fluids as a function of the temperature difference $\mathbf{T - T_{amb}}$ for natural convection from the current experiment and previous correlations[29]. (b) Nucleate boiling relative heat flux from current experiment and Rohsenow model[30]

In order to compare the relative performance of the fluids in both the single phase (natural convection) regime and the two-phase (boiling) regime with existing literature, we refer to the well-known Churchill correlation[29] for laminar natural convection (Eq. 1) and the well-known Rohsenow model (Eq. 3)[30].

$$Nu = \frac{hD}{k} = 0.68 + \frac{0.67Ra^{1/4}}{\left[1 + (0.492/Pr)^{\frac{9}{16}}\right]^{4/9}}, \quad Ra < 10^9 \tag{6.1}$$

$$Ra = \frac{g\beta(T_s - T_{amb})L^3}{\nu\alpha} \tag{6.2}$$

$$q'' = \mu h_{fg}\left[\frac{g(\rho_l - \rho_v)}{\sigma}\right]^{1/2}\left(\frac{1}{C_{sf}}\right)^{1/r} Pr^{-s/r}\left[\frac{c_p(T_w - T_{sat})}{h_{fg}}\right]^{1/r} \tag{6.3}$$

r=0.33, s=1 for water and s=1.7 for other fluids. The surface coefficient C_{sf}=0.013 for water, 0.0022 alcohol (water-glycol) and 0.0049 for n-Pentane (dielectric fluids).

The results are plotted in figure 7. We can see that the experimental relative thermal performance of the fluids is qualitatively as expected both for natural convection and for the boiling regime.

The quantitative discrepancy (2X) for natural convection is due to the assumption of a one dimensional heat transfer for the vertical plate, which is not the case in the experimental setup that includes spreading in 2D. As for the boiling regime, the Rohsenow model is very sensitive to the surface coefficient. This coefficient has been employed for copper whereas in reality the contact surface is parylene C for the water and water-glycol 50%-50% by volume whereas the contact surface is the outer-package of the transistor for the dielectric and these coefficients need to supplied for such surfaces for a better accuracy.

6.5. Onset of boiling on the EPC2034

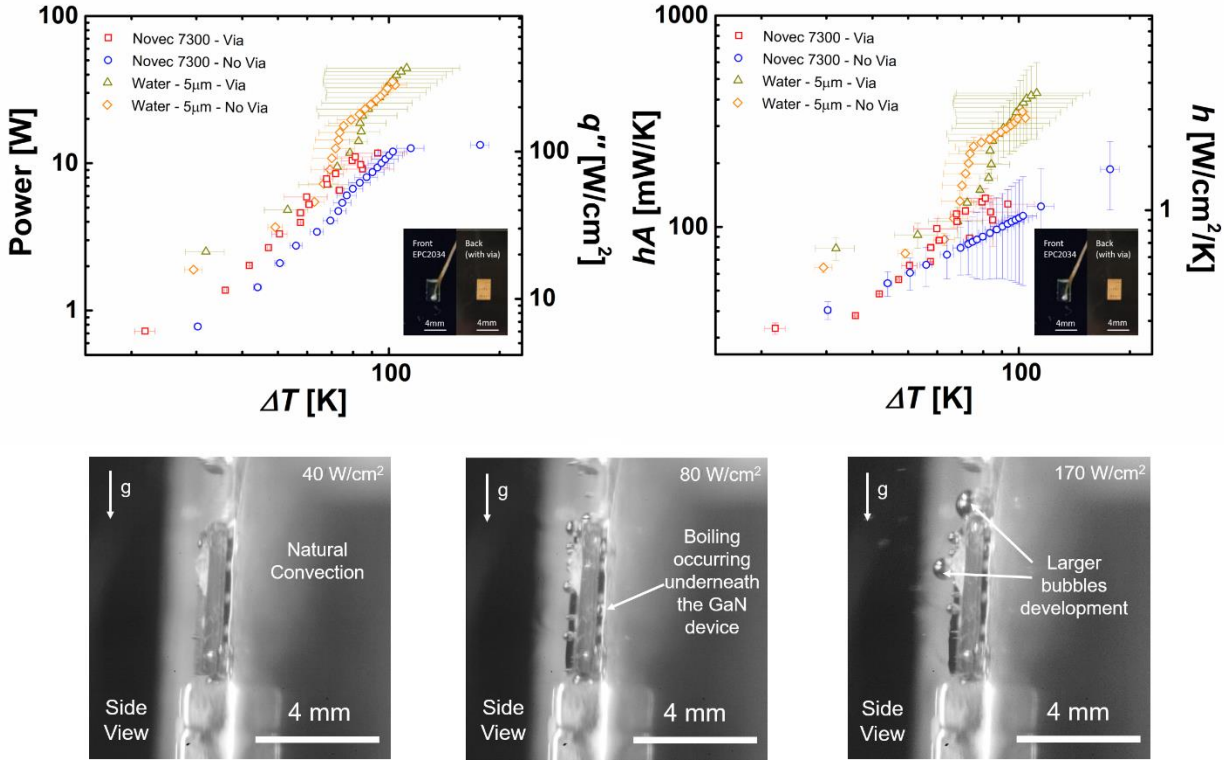

Figure 6.8.(a) and (b) Effect of through-PCB copper via and back gold pad on the heat performance of the top cooled EPC2034 transistor. (c) and (d) Snapshot (side view) of bubble generation underneath the EPC device and on the top surface (taken from high speed camera (Photron Mini AX200)

Experiments with the EPC top-cooled transistors showed that boiling starts underneath the device, where the solder balls are located and then appears on the top after the power is increased above a certain level. This can be considered as a peculiar result for top-cooled devices since the thermal

resistance from the junction is 9X larger to the board than it is to the case[18]. We suspect this behavior to be the result of the confinement of the liquid under the device which induces higher temperatures for the fluid around the solder balls and favors boiling to start in this region.

The schematic in figure 9 shows the thermal resistance network used to compare the temperature at the top surface of the EPC with that at the solder balls. The heat generated at the junction is the sum of two heat flows that can be written at steady state as follows:

$$q_{\mathrm{Top}} = \frac{T_{\mathrm{J}} - T_{\mathrm{amb}}}{R_{\mathrm{T}} + R_{\mathrm{C}}} = \frac{T_{\mathrm{J}} - T_{\mathrm{S}}}{R_{\mathrm{T}}} \tag{6.4}$$

$$q_{\mathrm{Bot}} = \frac{T_{\mathrm{J}} - T_{\mathrm{amb}}}{R_{\mathrm{B}} + R_{\mathrm{eq}}} = \frac{T_{\mathrm{J}} - T_{\mathrm{SB}}}{R_{\mathrm{B}}} \tag{6.5}$$

Dividing these two equations and rearranging leads to the following relation:

$$\frac{T_{\mathrm{J}} - T_{\mathrm{S}}}{T_{\mathrm{J}} - T_{\mathrm{SB}}} = \frac{R_{\mathrm{T}}}{R_{\mathrm{B}}} \times \frac{R_{\mathrm{B}} + R_{\mathrm{eq}}}{R_{\mathrm{C}}} \tag{6.6}$$

R_{eq} is the equivalent resistance that takes into account the PCB, convection and confinement thermal resistances. Since the spacing between the transistor and the PCB is small, the cross-sectional area for heat flow is small which leads to a high R_{eq} value and hence, a ratio $\frac{T_{\mathrm{J}} - T_{\mathrm{S}}}{T_{\mathrm{J}} - T_{\mathrm{SB}}}$ larger than 1 even though $\frac{R_{\mathrm{T}}}{R_{\mathrm{B}}} = 0.115$ [datasheet]. This means that the temperature T_{SB} at the solder balls is higher than T_{S}, that at the surface of the device, because a high confinement resistance R_{conf} makes the temperature at the solder balls less influenced by the ambient temperature and more biased to that at the junction, so to speak. Thus, boiling starts underneath the top-cooled transistor and not on its top surface like with the top-cooled GaN Systems SMD transistor.

To investigate this hypothesis, we prepared boards where the EPC footprint is supplemented with 17 0.3 mm-diameter non-filled thermal vias routing heat to a 24 mm^2 thermal pad on the back of the board where it can be dissipated easier. According to the thermal resistance analysis described

above, reducing R_{eq} sufficiently might lead to a higher temperature at the surface of the device and boiling starts there. In this respect, we chose to add thermal vias to the footprint which reduces the equivalent resistance R_{eq} and increases T_S with respect to T_{SB}. The experiments were performed in Novec 7300 and water with a 5 μm thickness Parylene coating for the boards submerged in the latter. The devices with thermal vias were able to handle 1.23X higher power levels in the case of water (figure 8a). This is due to the increased area of interface with the ambient fluid that the back thermal pad provides. Moreover, the vias added were not sufficient to initiate boiling on the surface. The number of vias was limited by the small footprint of the device, especially that these should be added only to the source copper pad. Future work should consider putting more filled thermal vias as a way to switch the location where boiling starts.

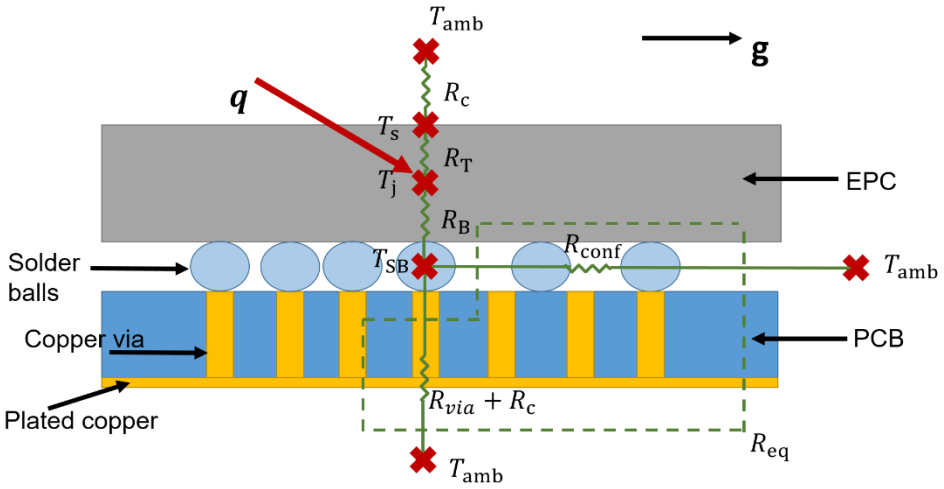

Figure 6.9. Thermal resistance network of the immersion cooling of EPC2034

6.6. Effect of thermal pad size for bottom-cooled transistors

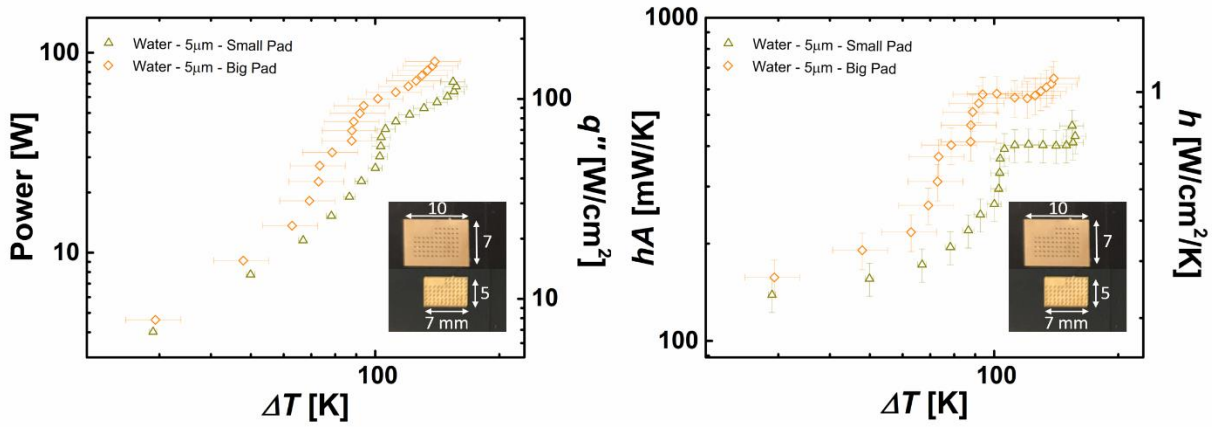

Figure 6.10. Effect of pad size on the heat transfer performance of the bottom cooled GaN transistor (GS66508B). The source-connected gold pads on the back of the PCB were varied in size from 5mm x 7mm (small pad) to 7mm x 10 mm (big pad).

Bottom-cooled transistors were used to study the effect of the thermal pad area on cooling performance. Two sets of boards were prepared for this purpose with bottom thermal pad areas equal to 35 mm^2 and 70 mm^2 respectively. Experiments were performed in water with boards coated with a 5 μm layer of Parylene C. Natural convection cooling started at low power levels followed by boiling, which happened initially at the bottom thermal pad. The graphs in figure 10b show a jump in the convection coefficient that is due to the initiation of boiling on the top side of the transistor with increased power. This enhancement in the cooling performance is substantial that it can keep the temperature of the transistor nearly the same even with a 2X increase in the power level in the case of large pads (figure 10a) creating a thermal buffer. This is due to the formation of new boiling nucleation sites on the top of the transistor with higher power, which compensates for the higher heat generation with a higher convection coefficient. Furthermore, this buffer zone is followed by a plateau in the power dissipated. The plateau is followed by a further increase in power as new nucleation sites are activated.

6.7. Conclusions

This work provides an experimental investigation of water immersion cooling for electronics. Immersion of individual Gallium Nitride (GaN) transistors is achieved in tap water and water-ethylene glycol mixture (50% by volume), and benchmarked against dielectric fluids. The boards were coated with three different thicknesses (1 μm, 5 μm and 25 μm) of dielectric coating (Parylene C) before immersion in water or water-glycol mixture. Large heat flux (based on footprint area) dissipations are observed for water (up to 562 W/cm^2) and for water glycol mixture (452 W/cm^2) as compared to dielectric fluids (up to 111 W/cm^2), as a result of subcooled boiling in a room temperature bath. The device failed before the achievement of critical heat flux in both water and water-glycol mixture, whereas critical heat flux was attained for dielectric fluids. We compare the natural convection results and boiling results with the well known Churchill and Rohsenow correlations, respectively, with discrepancies up to 300%, showing the inability of these models to capture 2D physics for natural convection and the surface interactions for the boiling on a PCB with and without Parylene. In addition, we investigate the onset of boiling on the EPC2034 transistor used in power conversion, and discover that boiling is initiated at the solder balls (PCB side) although the transistor is rated for top side cooling, relating to confinement of the fluid and local temperature increase of the fluid at the PCB interface. Furthermore, we investigate the effect of the thermal pad on the power dissipation of a bottom cooled transistor (surface mounted on the PCB) and show an increase in heat transfer proportional to the increased area.

6.8. References

[6.1] A.L. Moore, L. Shi, Emerging challenges and materials for thermal management of electronics, Materials Today, 17(4) (2014) 163-174.
[6.2] A.S. Shanmuga, R. Velraj, Thermal management of electronics: A review of literature., Thermal Science, 12(2) (2008) 5-26.
[6.3] Y.T. Lei, C. Barth, S.B. Qin, W.C. Liu, I. Moon, A. Stillwell, D. Chou, T. Foulkes, Z.C. Ye, Z.T. Liao, R.C.N. Pilawa-Podgurski, A 2-kW Single-Phase Seven-Level Flying Capacitor Multilevel Inverter With an Active Energy Buffer, Ieee T Power Electr, 32(11) (2017) 8570-8581.
[6.4] T. Modeer, C.B. Barth, N. Pallo, W.H. Chung, T. Foulkes, R.C.N. Pilawa-Podgurski, Design of a GaN-based, 9-level Flying Capacitor Multilevel Inverter with Low Inductance Layout, Appl Power Elect Co, (2017) 2582-2589.
[6.5] C. Barth, T. Foulkes , W.H. Chung, T. Modeer, P. Assem, Y. Lei, R.C.N. Pilawa-Podgurski, Design and Control of a GaN-based, 13-level, Flying Capacitor Multilevel Inverter, in: 2016 IEEE 17th Workshop on Control and Modeling for Power Electronics (COMPEL), Trondheim, Norway, 2016.
[6.6] N. Pallo, T. Foulkes , T. Modeer, S. Coday, R.C.N. Pilawa-Podgurski, Power-Dense Multilevel Inverter Module using Interleaved GaN-Based Phases for Electric Aircraft Propulsion, in: IEEE Applied Power Electronics Conferenece and Exposition (APEC), San Antonio, TX, USA, 2018.
[6.7] A. Stillwell, M.E. Blackwell, R.C.N. Pilawa-Podgurski, Design of a 1 kV bidirectional DC-DC converter with 650 V GaN transistors, in: IEEE Applied Power Electronics Conference and Exposition (APEC), San Antonio, TX, USA, 2018.
[6.8] H.R. Upadhye, S.G. Kandlikar, Extending the heat flux limit with enhanced microchannels in direct single-phase cooling of computer chips, in: Semiconductor Thermal Measurement and Management Symposium, 2005 IEEE Twenty First Annual, San Jose, CA, USA, 2005.
[6.9] W.L. Qu, I. Mudawar, Measurement and prediction of pressure drop in two-phase micro-channel heat sinks, International Journal of Heat and Mass Transfer, 46(15) (2003) 2737-2753.
[6.10] F. Sarvar, D.C. Whalley, P.P. Conway, Thermal Interface Materials - A review of the State of the Art, in: Electronics System Integration Technology Conference, 1st. IEEE, Dresden, Germany, 2006.
[6.11] S. Narumanchi, Thermal Interface Materials for Power Electronics Applications, in: Itherm, Orlando, FL, USA, 2008.
[6.12] L. Zhu, R.F. Boehm, Y.P. Wang, C. Halford, Y. Sun, Water immersion cooling of PV cells in a high concentration system, Sol Energ Mat Sol C, 95(2) (2011) 538-545.
[6.13] E. Baker, Liquid Immersion Cooling of Small Electronic Devices, Microelectron Reliab, 12(2) (1973) 163-173.
[6.14] P.J. Marto, V.J. Lepere, Pool Boiling Heat-Transfer from Enhanced Surfaces to Dielectric Fluids, J Heat Trans-T Asme, 104(2) (1982) 292-299.
[6.15] T.L. Chen, S.V. Garimella, Measurements and high-speed visualizations of flow boiling of a dielectric fluid in a silicon microchannel heat sink, Int J Multiphas Flow, 32(8) (2006) 957-971.
[6.16] M. Heaney, Electrical Conductivity and Resistivity, CRC Press, 2003.
[6.17] G. Systems, PCB Thermal Design Guide for GaN Enhancement Mode Power Transistors, in.
[6.18] EPC, EPC2034 - Enhancement Mode Power Transistor, in, pp. EPC 2034 Datasheet.

[6.19] Gansystems, GS66508T 650V Enhancement Mode GaN Transistor, in.
[6.20] Gansystems, GS66508B 650V Enhancement Mode GaN Transistor, in.
[6.21] 3M, 3M Novec 72DE Engineered Fluid, in.
[6.22] 3M, 3M Novec 7300 Engineered Fluid, in.
[6.23] D. Bohne, S. Fischer, E. Obermeier, Thermal-Conductivity, Density, Viscosity, and Prandtl-Numbers of Ethylene Glycol-Water Mixtures, Ber Bunsen Phys Chem, 88(8) (1984) 739-742.
[6.24] N.G. Tsierkezos, I.E. Molinou, Thermodynamic properties of water plus ethylene glycol at 283.15, 293.15, 303.15, and 313.15 K, J Chem Eng Data, 43(6) (1998) 989-993.
[6.25] G.I. Egorov, D.M. Makarov, A.M. Kolker, Volumetric properties of the water-ethylene glycol mixtures in the temperature range 278-333.15 K at atmospheric pressure, Russ J Gen Chem+, 80(8) (2010) 1577-1585.
[6.26] M.H. Rausch, L. Kretschmer, S. Will, A. Leipertz, A.P. Froba, Density, Surface Tension, and Kinematic Viscosity of Hydrofluoroethers HFE-7000, HFE-7100, HFE-7200, HFE-7300, and HFE-7500, J Chem Eng Data, 60(12) (2015) 3759-3765.
[6.27] 3M, Heat transfer applications using 3M Novec Engineering Fluids, in.
[6.28] 3M, Cool Under Fire - Dielectric heat transfer fluid solutions for military and aerospace applications, in.
[6.29] F.P. Incropera, D.P. DeWitt, Fundamentals of heat and mass transfer, 5th ed., J. Wiley, New York, 2002.
[6.30] V.P. Carey, Liquid-vapor phase-change phenomena : an introduction to the thermophysics of vaporization and condensation processes in heat transfer equipment, 2nd ed., Taylor and Francis, New York, 2008.

Chapter 7 – Conclusions

This thesis has worked on enhanced jumping droplet condensation and cooling strategies for high power density electronics. Starting from a single droplet modeling, we have developed a comprehensive physical model of external and internal convective jumping-droplet condensation. A boundary layer approach was used to model the vapor flow over the plate and inside the pipe with condensation modeled as a suction at the wall. The jumping droplet trajectories were simulated accounting for the Saffman lift force of the shear flow. The results indicated that a delicate balance between drag, lift and gravitational force leads to optimum trajectories in terms of both height and distance traveled for a droplet radius of ≈ 30 μm. The condensation heat flux acts to shortens the trajectory of the droplet as it leads to an increased suction, however it can have the opposite effect for very small (∼1 μm) or very big droplets (∼100 μm) as it can cause a downward shift of the horizontal velocity profile and greater transverse momentum transfer. For a pipe, the dynamics can vary. Using our individual droplet model, we then incorporated multi-hop jumping, showing that multi-hop jumping droplet condensation has the potential to increase the total travel distances along the plate or the pipe. The present analysis outlines a condensation methodology to delay progressive flowing and enable the steady heat transfer coefficients of >100 kW/m^2K at low supersaturations. The findings presented here have significant relevance to the applications of convective jumping-droplet condensation for efficient phase change heat transfer applications. Furthermore, the developed boundary layer based modeling approach presents a design framework for future models and designs of jumping droplet condensers having more complex geometries, flow conditions, and heat fluxes.

Transitioning to multiple droplets modeling, we provide a numerical simulation of jumping-droplet condensation on horizontal surfaces, in order to determine the steady-state time-averaged droplet size distribution on the condensing surface. In order to characterize steady state, we track the maximum radius on the surface. At steady-state, the maximum radius oscillates around an average value in time. The achievement of steady state requires that $R_{\max}/R_{\text{jump,min}} <$ ≈50, which is satisfied for typical nucleation site densities (N_s~5x10^4 mm^{-2}). The droplet size distribution is obtained in its non dimensional form, and effects of the minimum jumping radius (0.1μm – 10 μm), maximum jumping radius, contact angle (150° – 175°), and droplet growth rate are provided. The minimum jumping radius flattens the tail of the distribution only if it reaches high enough values (> ≈ 3X average spacing), whereas the maximum jumping radius is not shown to modify the distribution unless it drops below (≈ 3X average spacing), where it prohibits the achievement of steady state. The contact angle and growth rate are shown to have negligible effect on the distribution. In this study, we provide a suggested numerical fit for the droplet size distribution with an overall correlation coefficient greater than 0.995. The heat transfer performance is evaluated with the derived distribution and is highly sensitive to contact angle and coating thickness as dictated by the droplet growth rate. The obtained heat fluxes agree well with previous studies of jumping droplet condensation.

The second portion of the thesis was related to the thermal management of electronics. We demonstrated jumping-droplet hot spot cooling, whereby charged droplets jump between superhydrophobic copper oxide condensers and electrical circuits to cool local hot devices actively with evaporation. Through experiments and modeling, we demonstrated heat flux dissipations of 1 W/cm^2, which can be improved in the near-term to 120 W/cm^2. Future enclosed devices with pure vapor environments, and optimized geometrical designs have the potential to achieve higher active cooling rates approaching 1 kW/cm^2. However, for a reliable practical application, it is crucial to investigate the durability of the superhydrophobic surfaces, determining their possible mechanical degradation within months or years. This work not only demonstrates EFE condensation based electronics cooling for the first time, but also provides a framework for the development of active jumping droplet based vapor chambers and heat pipes capable of spatial and temporal thermal dissipation control.

For higher heat flux applications (>50 W/cm^2), we propose the use of water immersion cooling for electronics. Immersion of individual Gallium Nitride (GaN) transistors is achieved in tap water and water-ethylene glycol mixture (50% by volume), and benchmarked against dielectric fluids. The boards were coated with three different thicknesses (1 μm, 5 μm and 25 μm) of dielectric coating (Parylene C) before immersion in water or water-glycol mixture. Large heat flux (based on footprint area) dissipations are observed for water (up to 562 W/cm^2) and for water glycol mixture (452 W/cm^2) as compared to dielectric fluids (up to 111 W/cm^2), as a result of subcooled boiling in a room temperature bath. The device failed before the achievement of critical heat flux in both water and water-glycol mixture, whereas critical heat flux was attained for dielectric fluids. We compare the natural convection results and boiling results with the well known Churchill and Rohsenow correlations, respectively, with discrepancies up to 300%, showing the inability of these

models to capture 2D physics for natural convection and the surface interactions for the boiling on a PCB with and without Parylene. In addition, we investigate the onset of boiling on the EPC2034 transistor used in power conversion, and discover that boiling is initiated at the solder balls (PCB side) although the transistor is rated for top side cooling, relating to confinement of the fluid and local temperature increase of the fluid at the PCB interface. Furthermore, we investigate the effect of the thermal pad on the power dissipation of a bottom cooled transistor (surface mounted on the PCB) and show an increase in heat transfer proportional to the increased area.